PNNL-14895

Pacific Northwest
National Laboratory
Operated by Battelle for the
U.S. Department of Energy

Three-Dimensional Modeling of DNAPL in the Subsurface of the 216-Z-9 Trench at the Hanford Site

M. Oostrom
M. L. Rockhold
P. D. Thorne
G. V. Last
M. J. Truex

October 2004

Prepared for the U.S. Department of Energy
under Contract DE-AC05-76RL01830

DISCLAIMER

PACIFIC NORTHWEST NATIONAL LABORATORY
operated by
BATTELLE
for the
UNITED STATES DEPARTMENT OF ENERGY
under Contract DE-AC06-76RL01830

Printed in the United States of America

Available to DOE and DOE contractors from the
Office of Scientific and Technical Information,
P.O. Box 62, Oak Ridge, TN 37831-0062;
ph: (865) 576-8401
fax: (865) 576-5728
email: reports@adonis.osti.gov

Available to the public from the National Technical Information Service,
U.S. Department of Commerce, 5285 Port Royal Rd., Springfield, VA 22161
ph: (800) 553-6847
fax: (703) 605-6900
email: orders@ntis.fedworld.gov
online ordering: http://www.ntis.gov/ordering.htm


This document was printed on recycled paper.
(8/00)

PNNL-14895

Three-Dimensional Modeling of DNAPL in the Subsurface of the 216-Z-9 Trench at the Hanford Site

M. Oostrom
M. L. Rockhold
P. D. Thorne
G. V. Last
M. J. Truex

October 2004

Prepared for
the U.S. Department of Energy
under Contract DE-AC05-76RL01830

Pacific Northwest National Laboratory
Richland, Washington 99352

Executive Summary

Carbon tetrachloride (CT) was discharged to waste sites that are included in the 200-PW-1 Operable Unit in Hanford 200 West Area. Fluor Hanford, Inc. is conducting a Comprehensive Environmental Response, Compensation, and Liability Act (CERCLA) remedial investigation/feasibility study (RI/FS) for the 200-PW-1 Operable Unit. The RI/FS process and remedial investigations for the 200-PW-1, 200-PW-3, and 200-PW-6 Operable Units are described in the Plutonium/Organic-Rich Process Condensate/Process Waste Groups Operable Unit RI/FS Work Plan. As part of this overall effort, Pacific Northwest National Laboratory was contracted to improve the conceptual model of how CT is distributed in the Hanford 200 West Area subsurface through use of numerical flow and transport modeling. This work supports the U.S. Department of Energy's (DOE's) efforts to characterize the nature and distribution of CT in the 200 West Area and subsequently select an appropriate final remedy.

Three-dimensional modeling was conducted to enhance the conceptual model of CT distribution in the vertical and lateral direction beneath the 216-Z-9 trench. Simulations targeted migration of dense, nonaqueous phase liquid (DNAPL) consisting of CT and co-disposed organics in the subsurface beneath the 216-Z-9 trench as a function of the properties and distribution of subsurface sediments and of the properties and disposal history of the waste. The geological representation of the computational domain was extracted from a larger Earthvision™ geologic model of the 200 West Area subsurface developed during fiscal year 2002. Simulations of CT migration were conducted using the Subsurface Transport Over Multiple Phases (STOMP) simulator, a multi-fluid flow and transport code developed by Pacific Northwest National Laboratory.

A total of 23 three-dimensional simulations were conducted to examine infiltration and redistribution of CT in the subsurface prior to implementation of remediation activities in 1993. The simulations consisted of one Base Case simulation and 22 sensitivity analysis simulations. The sensitivity simulations investigated the effects of variations in 1) fluid composition; 2) disposal rate, area, and volume; 3) fluid retention; 4) permeability; 5) anisotropy; 6) sorption; 7) porosity; and 8) residual saturation formation on the movement and redistribution of DNAPL. Additional simulations were conducted to investigate the effect of soil-vapor extraction (SVE) on the distribution of CT in the subsurface of the 216-Z-9 trench.

The simulation results indicate that the Cold Creek unit accumulated CT and has a large impact on DNAPL movement and the resulting distribution of CT in the subsurface. The Cold Creek unit is a relatively thin, laterally continuous unit comprised of a silt layer and a cemented carbonaceous layer located about 40 m below ground surface and about 50 m above the water table. The simulations also show that the lateral extent of the vapor-phase plume in the vadose zone was much more extensive than the lateral extent of the DNAPL. Density-driven vapor flow caused the CT vapor to move downward until the plume contacted relatively impermeable units (e.g., the Cold Creek unit) or the water table. At these interfaces, the vapor plume moved laterally. The vapor plume also partitioned into the water and onto the solid phase as it moved. The CT present in the Cold Creek unit can continue to volatilize over time and move downward to layers where it could be removed by SVE or deeper where groundwater contamination could take place. The simulation results also clearly demonstrated that DNAPL CT has not moved laterally away from the footprint of the disposal facility. In most simulations, CT was predicted to

enter the water table as a separate phase or in the aqueous phase directly beneath the disposal area or through gaseous transport and subsequent partitioning into the aqueous phase over a wide-spread area.

In summary, the modeling results led to the following conclusions that can be used to update the conceptual model of CT distribution in the subsurface.

- *Where is CT expected to accumulate?* CT DNAPL accumulates in the finer-grain layers of the vadose zone but does not appear to pool on top of these layers.

- *Where would continuing liquid CT sources to groundwater be suspected?* Migration of DNAPL CT tends to be preferentially vertically downward below the disposal area. Lateral movement of DNAPL CT is not likely. However, significant lateral migration of vapor CT occurs.

- *Where would DNAPL contamination in groundwater be suspected?* Sufficient CT and co-disposed liquids were introduced to the subsurface for DNAPL CT to migrate at least through the Cold Creek unit and, in some sensitivity cases, to migrate across the water table. For the Base Case simulation, 43% of the original DNAPL inventory (450,000 kg) was still present in the vadose zone as a DNAPL in 1993. Most of this DNAPL was located just above and within the Cold Creek units. At 1993, about 27,000 kg (6% of the inventory) of DNAPL had moved across the water table.

- *What is the estimated distribution and state of CT in the vadose zone?* The amount of DNAPL CT that accumulated in the vadose zone by 1993 ranges from 19% to 65% of the total disposed in the sensitivity simulations. The majority of the mass at 1993 was typically a DNAPL or sorbed phase. The center of mass for CT in the vadose zone was typically directly beneath the disposal area and within the Cold Creek unit.

- *How does SVE affect the distribution of CT in the vadose zone?* SVE effectively removes CT from the permeable layers of the vadose zone. SVE previously applied in the 216-Z-9 trench area has likely removed a large portion of CT initially present in the permeable layers within the large radius of influence of the extraction wells. Finer grain layers with more moisture content are less affected by SVE and contain the CT remaining in the vadose zone.

Contents

Figures

Tables

1.0 Introduction

Plutonium recovery operations within the Z-Plant aggregate area (Plutonium Finishing Plant [PFP]) of the Hanford Site resulted in organic and aqueous wastes that were disposed at several cribs, tile fields and French drains. The organic wastes consisted of carbon tetrachloride (CT) mixed with lard oil, tributyl phosphate (TBP), and dibutyl butyl phosphonate (DBBP). The main disposal areas were the 216-Z-9 trench, the 216-Z-1A tile field, and the 216-Z-18 crib. The three major disposal facilities received a total of about 13,400,000 L of liquid waste containing 363,000 to 580,000 L of CT. Assuming a maximum solubility of 800 mg/L and a fluid density of 1.59 g/cm^3, the 13,400,000 L of liquid waste would be able to contain approximately 6,700 L of CT in dissolved form. This indicates the majority of the CT entered the subsurface as an organic liquid.

Last and Rohay (1993) conducted a rough order-of-magnitude estimate of the discharge inventory and they computed that 21% of the CT might have been lost to the atmosphere, 12% is retained in the vadose zone (dissolved in water, sorbed to the solid phase, and as a component of the gas phase), and 2% is dissolved in the saturated zone. The remaining 65% has not been accounted for and might have been initially present as residual liquid saturation in the vadose zone. Although a considerable amount of the disposed CT is assumed to remain in the vadose zone as a residual liquid, the physical processes describing the formation of residual dense, nonaqueous phase liquid (DNAPL) in the vadose zone are not well understood and have not previously been incorporated into multi-fluid flow simulators.

Two remediation technologies have been applied. Between 1992 and 2000, about 76,500 kg (48,100 L) of CT has been removed using a soil-vapor extraction (SVE) system in the vadose zone. In addition, a pump-and-treat system for the unconfined aquifer removed 4,570 kg (2,870 L) of CT from groundwater between 1996 and 2000.

Interestingly, between 1996 and 2000, dissolved CT concentrations increased at several groundwater extraction wells located in the northern part of the PFP complex. The persistence of the contamination suggests that a continuing DNAPL source may be present in the vadose zone or groundwater. Further remedial action decisions require the identification of any continuing sources of CT beneath the PFP (DOE 2001).

Several conceptual models have been proposed to explain the behavior of CT mixtures in the subsurface. The conceptual models are summarized as follows (DOE 2001):

1. Downward migration of CT through disposal facilities and underlying soil column to groundwater, with lateral migration of groundwater to the PFP.

2. Downward migration of CT through disposal facilities and underlying soil column to the Cold Creek unit, with lateral migration along the top of the unit toward the PFP. In addition, CT also moves vertically to the groundwater and laterally to the PFP.

3. Downward migration from an unknown source.

4. Vapor migration from major disposal sites to groundwater, followed by lateral movement to the PFP.

5. A combination of option 1 through 4.

Numerical modeling was conducted to simulate CT flow and transport. This work supports the remedial investigation/feasibility study (RI/FS) for 200-PW-1 Operable Unit. The three-dimensional multi-fluid flow modeling focused on the subsurface near the 216-Z-9 trench. This work builds on Piepho's (1996) two-dimensional simulations of the same site. The modeling will provide information relevant to answering the following questions:

a) Where is CT expected to accumulate?
b) Where would continuing liquid CT sources to groundwater be suspected?
c) Where would DNAPL contamination in groundwater be suspected?
d) What is the estimated distribution and state of CT in the vadose zone?
e) How does SVE affect the distribution of CT in the vadose zone?

The numerical model was configured using available information regarding the hydrogeology of the modeled area, measured fluid properties for the likely mixtures of disposed organic liquid (e.g., mixtures of CT, lard oil, TBP, and DBBP) and estimates of hydrologic boundary conditions. The hydrogeologic setting was configured by assembling a geologic model based on interpretations of borehole geologic information at the regional and local scale. The geologic model was constructed using the EarthVision™ software to provide a means for three dimensional interpolation of borehole geologic information and to establish an electronic format for the geologic model that enabled porous media properties to be readily mapped to the numerical model grid. Fluid properties for relevant organic liquid mixtures were determined in the laboratory as part of the U.S. Department of Energy's (DOE's) Science and Technology Program. Additional work under this program provided the basis for an updated theory of non-aqueous phase liquid (NAPL) residual saturation formation that was incorporated into the model for selected simulations. Hydraulic boundary conditions were determined based on the information regarding fluid discharges in the 200 Area. Simulation results of water flow from a regional scale model were used to establish the boundary conditions for the local model that was used to simulate DNAPL movement. Appropriate ranges for organic liquid and water disposal conditions for the local model were established based on a thorough review of historical information. Based on the above information, a numerical model was configured using the Subsurface Transport Over Multiple Phases (STOMP) code (White and Oostrom 2003). A series of three-dimensional multi-fluid flow simulations were conducted to examine the impact of parameter variation on the migration of CT in the subsurface beneath the 216-Z-9 disposal area over the period from initial disposal until 1993 when SVE was initiated in the area. Additional simulations that included a model of the SVE process were conducted for the period from 1993 to 2004.

This report is organized into seven sections. Section 1 is the introduction. Section 2 provides an overview of the STOMP code used for the numerical modeling. Section 3 is a description of the geologic model and how it was developed. The numerical model configuration is presented in Section 4. Section 5 describes the simulation scenarios. Section 6 presents the simulation results. Conclusions from this modeling effort are discussed in Section 7.

2.0 STOMP Simulator and Constitutive Relations

The water-oil-air operational mode of the STOMP simulator (White and Oostrom 2003) was used to simulate multi-fluid flow and transport beneath the 216-Z-9 trench. The fully implicit integrated finite difference code has been used to simulate a variety of multi-fluid systems (e.g., Oostrom et al. 1997, 1999; Oostrom and Lenhard 1998; Schroth et al. 1998). The applicable governing equations are the component mass-conservation equations for water, organic compounds, and air, expressed as, respectively:

$$\frac{\partial}{\partial t}\left[n_D \omega_l^w \rho_l s_l\right] = -\nabla F_l^w + \dot{m}^w \tag{2.1a}$$

$$\frac{\partial}{\partial t}\left[\sum_{\gamma=l,n}\left(n_D \omega_\gamma^o \rho_\gamma s_\gamma\right) + \left((1-n_T)\omega_s^o \rho_s\right)\right] = -\sum_{\gamma=l,n}\left\{\nabla F_\gamma^o + \nabla J_\gamma^o\right\} + \dot{m}^o \tag{2.1b}$$

$$\frac{\partial}{\partial t}\left[\sum_{\gamma=l,g}\left(n_D \omega_\gamma^a \rho_\gamma s_\gamma\right)\right] = -\sum_{\gamma=l,g}\left\{\nabla F_\gamma^a + \nabla J_\gamma^a\right\} + \dot{m}^a \tag{2.1c}$$

where

$$F_\gamma^w = -\frac{\omega_\gamma^w \rho_\gamma k_{rl} k}{\mu_\gamma}\left(\nabla P_\gamma + \rho_\gamma g z\right) \text{ for } \gamma = \text{l,g,(2-1d)}$$

$$F_\gamma^o = -\frac{\omega_\gamma^o \rho_l k_{r\gamma} k}{\mu_\gamma}\left(\nabla P_\gamma + \rho_\gamma g z\right) \text{ for } \gamma = \text{l,n,g} \tag{2.1e}$$

$$F_\gamma^a = -\frac{\omega_\gamma^a \rho_\gamma k_{r\gamma} k}{\mu_\gamma}\left(\nabla P_\gamma + \rho_\gamma g z\right) \text{ for } \gamma = \text{l,g} \tag{2.1f}$$

$$J_\gamma^w = -\tau_\gamma n_D \rho_\gamma s_\gamma \frac{M^w}{M_\gamma} D_\gamma^w \nabla \chi_\gamma^w \text{ for } \gamma = \text{l,g} \tag{2.1g}$$

$$J_\gamma^o = -\tau_\gamma n_D \rho_\gamma s_\gamma \frac{M^o}{M_\gamma} D_\gamma^o \nabla \chi_\gamma^o \text{ for } \gamma = \text{l,n,g} \tag{2.1h}$$

$$J_\gamma^a = -\tau_\gamma n_D \rho_\gamma s_\gamma \frac{M^a}{M_\gamma} D_\gamma^a \nabla \chi_\gamma^a \text{ for } \gamma = \text{l,g} \tag{2.1i}$$

The subscripts l, n, g, and s denote aqueous, NAPL, gas and solid phase, respectively; the superscripts w, o, and a denote water, organic compound, and air components, respectively; t is time (s), n_D is the diffusive porosity, n_T is the total porosity, ω is the component mass fraction, ρ is the density (kg/m^3), s is the actual liquid saturation, V is the volumetric flux (m/s), J is the diffusive-dispersive mass flux vector (kg/m^2s), m is the component mass source rate (kg/m^3s), k is the intrinsic permeability (m^2), $k_{r\gamma}$ is the relative permeability of phase γ, μ is the viscosity (Pa s), P is the pressure (Pa), gz is the gravitational vector (m/s^2), τ is the tortuosity, M is the molecular weight (kg/mole), D is the diffusive-dispersive tensor (m^2/s), and $\underline{X}$ is the component mole fraction. The partitioning between the aqueous and solid phases is described by a linear exchange isotherm through a constant distribution coefficient.

The governing partial differential equations (Equations 2.1a, 2.1b, and 2.1c), are discretized following the integrated-volume finite difference method by integrating over a control volume. Using Euler backward time differencing, yielding a fully implicit scheme, a series of nonlinear algebraic expressions is derived. The algebraic forms of the nonlinear governing equations are solved with a multi-variable, residual-based Newton-Rhapson iterative technique where the Jacobian coefficient matrix is composed of the partial derivatives of the governing equations with respect to the primary variables.

Assuming the aqueous phase never disappears, the primary variable for the water equation is always the aqueous pressure. For the oil equation, the primary variable is P_n when free NAPL is present, s_n when only entrapped NAPL is present, and the component mole fraction when no NAPL is present. For the air equation, the primary variable is P_a. The algebraic expressions are evaluated using upwind interfacial averaging to fluid density, mass fractions, and relative permeability. User specified weights (i.e., arithmetic, harmonic, geometric, upwind) are applied to the remaining flux components. For the simulations described in these papers, harmonic averages were used for all other flux components, while the maximum number of Newton-Rhapson iterations was sixteen, with a convergence factor of 10^{-6}.

Secondary variables, those parameters not directly computed from the solution of the governing equations, are computed from the primary variable set through the constitutive relations. A complete overview of these relations can be found in White and Oostrom (2000). In this section, only the relations between relative permeability, fluid saturation, and capillary pressure (k-S-P) pertinent to the conducted simulations are described. The used k-S-P relations consist of the Brooks and Corey (1964) S-P relations in combination with the k-S relations derived from the Burdine (1953) or Mualem (1976) model. In these relations, the effects of fluid entrapment and residual saturation formation have been included.

The k-S-P relations distinguish between actual, effective, and apparent saturations. Actual saturations are defined as the ratio of fluid volume to diffusive pore volume. Effective saturations represent normalized actual saturations based on the pore volumes above the irreducible or minimum saturation of the wetting fluid (i.e., aqueous phase liquid). Effective saturations for the aqueous phase, NAPL, and gas phase and total liquid, are defined according to Equation (2.2):

$$\bar{s}_l = \frac{s_l - s_{rl}}{1 - s_{rl}} \qquad (2.2a)$$

$$\bar{s}_n = \frac{s_n}{1 - s_{rl}} \tag{2.2b}$$

$$\bar{s}_g = \frac{s_g}{1 - s_{rl}} \tag{2.2c}$$

$$\bar{s}_t = \frac{s_l + s_n - s_{rl}}{1 - s_{rl}} \tag{2.2d}$$

where s_{rl} is the irreducible aqueous phase saturation. Apparent saturations are defined in terms of effective saturations. Apparent saturations represent the effective saturation of the fluid plus the effective saturations of fluids of lesser wettability entrapped within the wetting fluid. In the simulator, it is assumed that fluid wettability follows the sequence: water > NAPL > air (Leverett 1941). Fluids of lesser wettability can potentially be trapped by NAPL or aqueous phase and NAPL can be entrapped by the aqueous phase.

In a three-phase system, the apparent total-liquid saturation is considered to be a function of the air-NAPL capillary pressure, and the apparent aqueous phase saturation a function of the NAPL-water capillary pressure, as follows:

$$\bar{\bar{s}}_t = \left[\frac{P_d}{\beta_{gn} P_{gn}} \right]^{\lambda} \quad \text{for} \quad \beta_{gn} P_{gn} > P_d \tag{2-3a}$$

$$\bar{\bar{s}}_t = 1 \quad \text{for} \quad \beta_{gn} P_{gn} \le P_d \tag{2-3b}$$

$$\bar{\bar{s}}_l = \left[\frac{P_d}{\beta_{nl} P_{nl}} \right]^{\lambda} \quad \text{for} \quad \beta_{nl} P_{nl} > P_d \tag{2-3c}$$

$$\bar{\bar{s}}_l = 1 \quad \text{for} \quad \beta_{nl} P_{nl} \le P_d \tag{2-3d}$$

where P_d is the air-entry pressure, P_{gn} the gas phase – NAPL capillary pressure, P_{nl} the NAPL – aqueous phase capillary pressure, γ is a pore-size distribution factor, and β_{gn} and β_{nl} are interfacial tension dependent scaling factors, defined as $\beta_{gn} = (\sigma_{gn} - \sigma_{nl}) / \sigma_{gn}$ and $\beta_{nl} = (\sigma_{gn} - \sigma_{nl}) / \sigma_{nl}$, respectively. The nature of these relations is discussed by Lenhard (1994). For aqueous-gas phase systems, Equation (2.3) is replaced by

$$\bar{\bar{s}}_l = \left[\frac{P_d}{P_{gl}} \right]^{\lambda} \quad \text{for} \quad P_{gl} > P_d \tag{2.4a}$$

$$\bar{\bar{s}}_l = 1 \quad \text{for} \quad P_{gl} \le P_d \tag{2.4b}$$

Modeling the subsurface behavior of contaminants can be a cost-effective tool to aid in cleaning up and managing contaminated sites. Before models can be the tools of choice, they must be able to accurately predict contaminant behavior and assess the level of uncertainty associated with the predictions. One shortcoming of multi-fluid flow and transport codes is their inability to accurately predict the retention of NAPL in the vadose zone after long drainage periods. Conceptually, this NAPL is present in small pores, pore wedges, bypassed pores, and as thin films or lenses on water surfaces.

The inability to accurately predict NAPL distribution in the vadose zone is a consequence of deficiencies in the multi-fluid air-NAPL-water constitutive theory (relations among relative permeabilities, saturations, and pressures) employed in numerical simulators. It is common to assume that all NAPL is mobile unless it is occluded (surrounded) by water and exists as ganglia. However, experimental investigations (Hofstee et al. 1998; Oostrom and Lenhard 2003; Oostrom et al. 2003) have shown that non-water-occluded NAPL is retained in the vadose zone after NAPL drainage has ceased. It is postulated that this non-water-occluded NAPL remains in the vadose zone because it exists in forms that are immobile or negligibly mobile. Such forms include films or lenses on water surfaces, NAPL in small or 'dead-end' pore channels and pore wedges, and NAPL in bypassed pores. By accounting for these immobile forms of non-water-occluded NAPL in relative permeability-saturation-pressure (k-S-P) relations, it should be possible to predict the NAPL saturation that does not drain from the vadose zone after long drainage periods. Vadose-zone hydrologists have used the term 'residual NAPL' to describe non-water-occluded NAPL that does not drain from the vadose zone after long drainage periods.

The Hanford Science and Technology program has funded an effort to develop an experimentally validated theory, based on pore-scale physics, to describe the formation of residual NAPL saturation formation. The initial theory is described by Lenhard et al. (2004). The implementation of the initial phases of the theory into the STOMP simulator has been discussed by White et al. (2004). Although the theory is still in development, two of the sensitivity simulations have been conducted using the new constitutive theory. A brief description of this new theory is in Appendix A.

3.0 Geologic Model

Development of a geologic model for the 216 Z-9 trench was completed in three stages, each covering successively smaller domains nested inside the previous one (Figure 3.1). First, a regional-scale geologic model was developed to support groundwater flow modeling and set the boundary conditions for the more detailed local models. Then a more detailed local-scale geologic model was developed to support groundwater modeling of the primary source area (i.e., the major carbon tetrachloride disposal facilities). Finally, a highly detailed site-specific scale geologic model was developed to support detailed flow and transport simulations of a single disposal site, the 216-Z-9 trench.

The boundaries of the regional geologic model domain were set to include primary recharge or discharge areas, thereby acting as logical hydrologic boundaries. The boundaries include important liquid disposal areas: the 216-U-14 ditch to the east, the 216-U-pond to the south, the 200-ZP-1 injection wells to the west, and the old 216-T-4 pond to the north. Geologic data collection for the regional geologic model domain was focused primarily on data from groundwater wells. Initially, 172 groundwater wells were identified within this model domain.

Geologic data for the local geologic model domain considered data from all boreholes (i.e., groundwater wells, dry wells, and soil borings). Initially, 215 boreholes were identified within the local geologic model domain identified on Figure 3.1. To support very detailed high-resolution modeling of the subsurface beneath the 216-Z-9 trench, geologic data from 21 boreholes in the immediate vicinity of the 216-Z-9 trench was incorporated into the site-specific geologic model.

3.1 Geologic Data

The first effort in developing the geologic model was to build a database of geologic contacts. Existing published tabulated data (e.g., Rohay et al. 1994) and/or other data sets extracted from lithologic log summaries or published maps (e.g., Connelly et al. 1992) were compiled. A complicating factor was that these existing data sets all use a different set of stratigraphic unit definitions. To create a consistent database of geologic contacts, all pertinent data sets were mapped to a single set of stratigraphic units. These stratigraphic units have also been mapped to the new Standardized Stratigraphic Nomenclature (DOE 2002). Figure 3.2 illustrates how the various stratigraphic interpretations relate to each other and how mapping was accomplished.

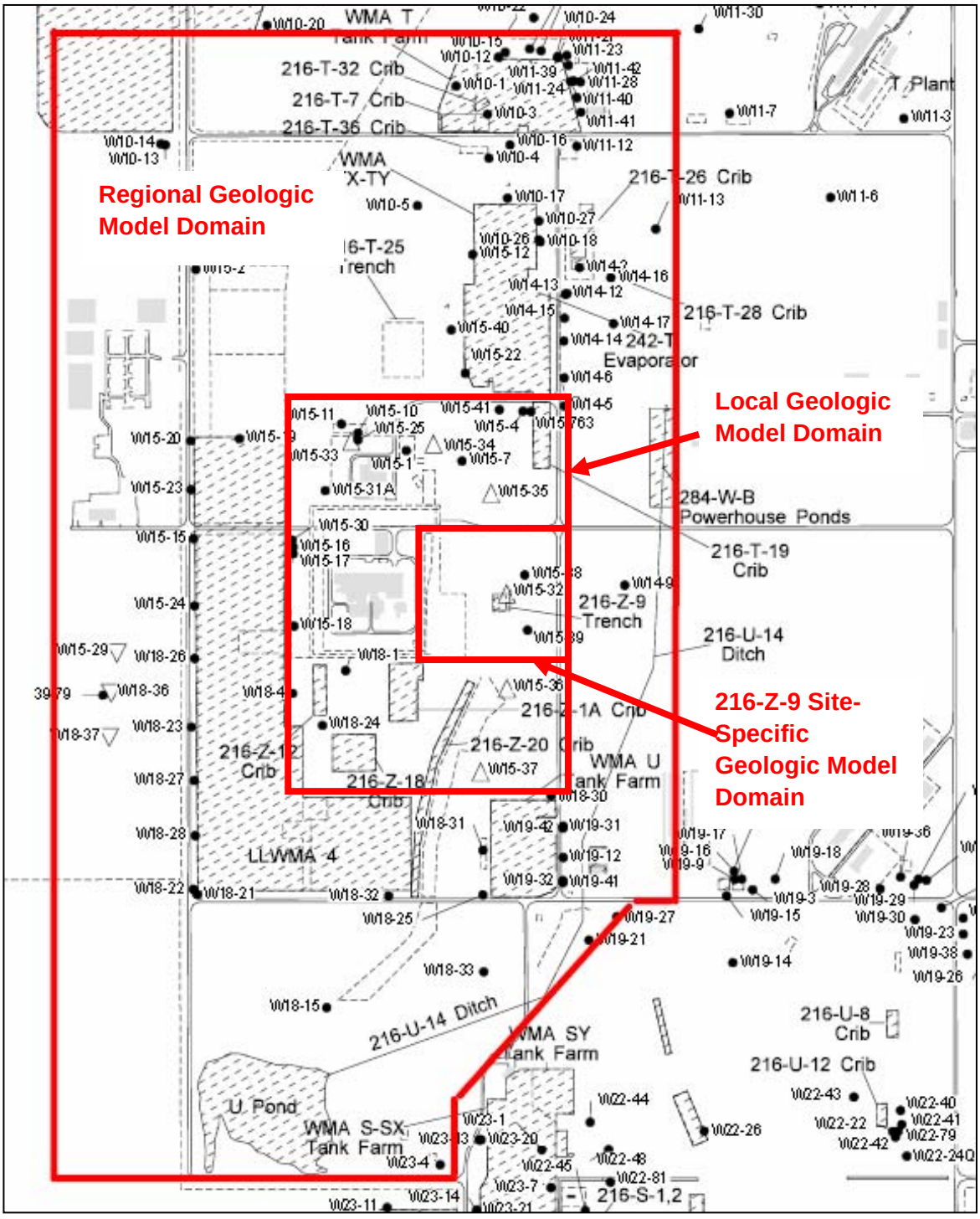

Figure 3.1. Outline of Regional, Local, and 216-Z-9 Trench-Specific Geologic Model Domains

	Price et. al. 1979	Kasper 1982	Last et. al. 1989	Lindsey, et. al. 1991.	Connelly et. al. 1992	Last and Rohay, 1993	Rohay, et. al. 1993	Rohay, Swett, and Last, 1994	Lindsey et. al. 1994a & b	Rohay, 2002	Williams et. al. 2002	Stratigraphic Units Used in this report
Holocene	Backfill	Backfill				Backfill	Backfill	Backfill	Backfill	Backfill		Backfill
		Eolian Silt	Eolian Deposits	Eolian Deposits	Eolian Sheet Sands	Sand	Eolian Material	Sand	Eolian Deposits	Sand		Holocene Sand (HDf[msw-ws] to HDm[xbed-ws])
Hanford	Fine to Very Fine Sand		Coarse-Grained Sequence	Coarse-Grained Sequence	Coarse-Grained Sequence	Upper Sand	Upper Fine	Upper Fine	Unit H1a	Upper Fine	Unit 1	Hanford Upper Fine (HF-SD)
	Sandy Coarse to Fine Pebble	Coarse Sandy Pebble				Upper Gravel	Upper Coarse	Upper Coarse	Unit H1	Upper Coarse		Hanford Upper Coarse (HF-GD)
	Very Coarse to Medium Sand	Coarse Sand										
		Medium to Fine Sand										
	Sandy Coarse to Fine Pebble	Silty Sandy Gravel										
	Medium to Fine Sand	Fine Sand				Lower Fine A	Fine	Fine	Unit H2	Fine		Hanford Fine (HF-SD)
									Unit H2a			
	Pebbly Very Coarse to Medium Sand	Coarse Sandy Pebble				Lower Gravel	Lower Coarse	Lower Coarse	Unit H3	Lower Coarse		Hanford Lower Coarse (HF-GD)
	Silty Medium to Fine Sand		Basal Slackwater Sequence	Fine-Grained Sequence	Fine-Grained Sequence	Lower Sand	Lower Fine	Lower Fine	Unit H4	Lower Fine		Hanford Lower Sand (HF-SD)
						Lower Fine B						
Cold Creek Unit (formerly Plio-Pleistocene Unit)	Eolian Silt (Sandy Silt)	Early Palouse Soil	Early Palouse Soil	Early Palouse Soil	Early Palouse Soil	Early Palouse Soil	Early Palouse Soil	Plio-Pleistocene	Plio-Pleistocene	Plio-Pleistocene	Unit 2 (Early Palouse Soil)	Cold Creek Unit Silt (CCUf[lam-msv]))
	Caliche Horizons		Plio-Pleistocene	Plio-Pleistocene	Pedogenic Calcrete	Plio-Pleistocene	Plio-Pleistocene				Unit 3	Cold Creek Unit Carbonate (CCUc-f[calc])
					Basalt Detritus							
Ringold	Upper	Upper	Upper	Upper Unit	Upper Unit	Upper Unit		Upper	Member of Taylor Flat	Upper	Unit 4	Upper Ringold (Ru)
	Middle	Middle	Middle	Unit E	Unit E	Unit E	Unit E	Unit E	Unit E Member of Wooded Island	Unit E	Unit 5	Ringold Unit E (Re)
											Unit 7	
	Lower		Lower	Lower Mud	Lower Mud	Lower Mud		Lower Mud		Lower Mud	Unit 6	Ringold Lower Mud
											Unit 8	
			Basal Fine	Unit A	Unit A	Unit A		Unit A		Unit A	Unit 9	Ringold Unit A
			Basal Coarse									
Saddle Mtns.			Basalt	Elephant Mtn. Basalt	Elephant Mtn. Basalt	Elephant Mtn. Basalt		Elephant Mtn. Basalt		Elephant Mtn. Basalt		Elephant Mtn. Basalt

= Existing Tabulated Data Set

Figure 3.2. Mapping of Existing Data Sets to a Common Set of Stratigraphic Units

Where discrepancies were found between multiple data sets, and/or where large gaps existed in the spatial distribution of the data, efforts were made to determine the geologic contacts by reviewing/ evaluating the raw borehole data. These data include driller's logs, geologist's logs, summaries of the driller's or geologist's logs in as-built drawings from the Hanford Well Information System (HWIS), particle size data, calcium carbonate data, moisture content data, and geophysical logs. An example of the data used and the interpretations made is show in Figure 3.3.

This figure provides a table of the driller's description of the geologic materials penetrated, along with particle size data, the Folk/Wentworth sediment classification, and the calcium carbonate concentration for the upper portion of borehole 299-W15-95. Note that samples were taken nearly every foot from this borehole. Juxtaposed to this table are plots of the average particle size distribution (in phi), the calcium carbonate concentration, and the gross gamma log. Three correlations lines are provided to illustrate the lithologic changes and define the geologic contacts between the backfill (B), the Hanford Upper Gravel Dominated (GD) unit, the Hanford fine (SD) unit, and the Hanford lower fine (SD) unit.

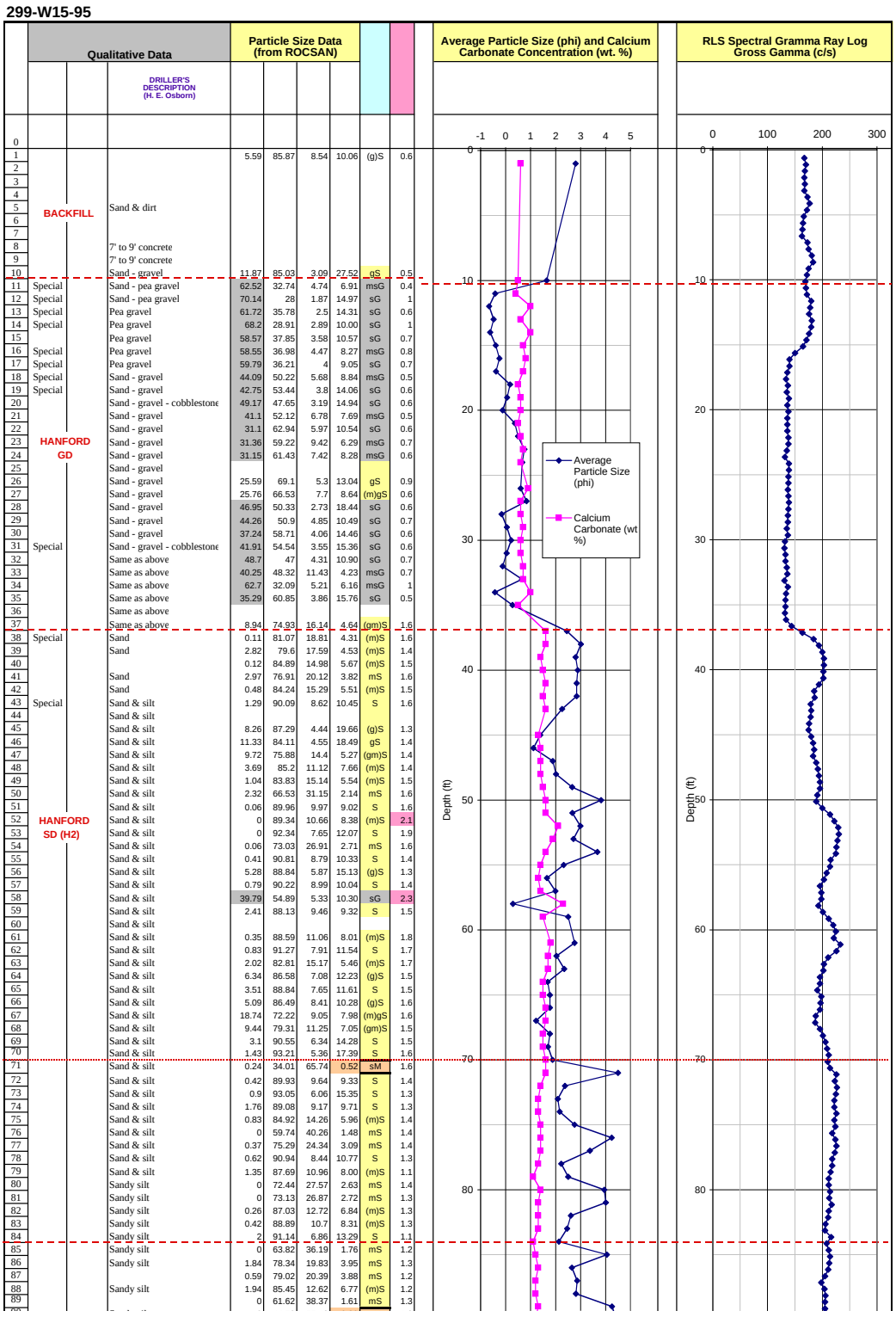

Figure 3.3. Interpretation of Geologic Contacts from Raw Data

Figure 3.4 (modified from Last and Rohay 1993) illustrates the dominant grain size, calcium carbonate content, and gross gamma activity for the principal geologic units. Note that the Hanford Upper Gravel Dominated (GD) unit (equivalent to the Hanford H1 unit) as represented by this sample contained over 50% gravel, had low calcium carbonate content, and low gross gamma activity. However, a sample of the fine-grained, laminated to massive facies of the Cold Creek unit (equivalent to the Cold Creek silt [PPlz]), contained 62% mud (silt+clay), had high calcium carbonate content, and high gamma activity.

Formation/ Unit	Lithofacies or Facies Association	Symbol *	Borehole /Depth (m)	Folk Classification/Description	Gravel >2 mm Wt. %	Very Coarse Sand 1-2 mm Wt. %	Coarse Sand 0.5-1 mm Wt. %	Medium Sand 0.25-0.5 mm Wt. %	Fine Sand 0.125-0.25 mm Wt. %	Very Fine Sand 0.063-0.125 Wt. %	Mud (Silt + Clay) <0.063 Wt. %	CaCO3 Content Wt. %	Relative Gross Gamma Activity
Holocene Deposits (HD)	Backfill	B	299-W15-95 3.0 m	gravelly medium SAND	11.9	0.6	16.8	52.5	11.9	3.3	3.1	0.5	Low - Moderate
	Sand (Fine-Grained, Massive, Well Sorted)	HDf(msv-ws)	299-W15-5 3.0 m	slightly muddy, fine to very fine SAND	0.0	0.7	4.9	13.1	30.9	33.9	16.5	0.5	Moderate
Hanford formation (HF)	Upper Fine, H1a (Sand Dominated)	HF-SD(Sh[c])	299-W18-85 4.6 m	gravelly, very coarse to coarse SAND	20.5	39.0	20.0	7.1	4.5	3.0	5.9	0.5	Low
	Upper Coarse, H1 (Gravel Dominated)	HF-GD(Gm)	299-W18-85 12.2 m	sandy GRAVEL	50.1	24.6	15.9	4.3	1.8	1.1	2.1	0.6	Low
	Fine, H2 (Sand Dominated)	HF-SD(Sh[c])	299-W15-95 19.8 m	coarse to medium SAND	3.5	14.0	30.5	29.1	10.4	4.8	7.7	1.5	Low - Moderate
	Lower Coarse, H3 (Gravel Dominated)	HF-GD(Gm)	299-W18-85 36.6 m	muddy, sandy, GRAVEL	46.7	17.8	9.0	6.9	5.1	3.7	10.8	1.1	Low
	Lower Sand, H4 (HF-SD)	HF-SD(Sh[c])	299-W15-95 26.8 m	slightly muddy, medium to fine SAND	1.9	4.8	9.8	21.2	35.6	14.0	12.6	1.2	Low-Moderate
	Interbedded sand and mud		299-W15-95 27.1 m	sandy MUD	0.0	0.1	0.4	2.4	11.8	46.9	38.4	1.3	
Cold Creek Unit (CCU)	Silt (Fine-Grained, Laminated, to Massive)	CCUf[lam-msv])	299-W15-85 42.7 m	sandy MUD	0.5	1.4	6.0	10.1	6.3	13.3	62.3	2.5	High
	Carbonate (Coarse to Fine-Grained, Carbonate Cemented)	CCUc-f(calc)	299-W15-5 38.1 m	calcareous, gravelly, muddy, SAND	21.6	10.6	7.6	8.8	9.2	9.9	32.4	12.8	Moderate to High
Ringold	Upper	Ru	299-W15-5 45.7 m	slightly muddy, slightly gravelly, coarse to medium SAND	7.3	8.3	22.5	30.5	10.3	6.7	14.5	4.0	Low
	Unit E	Re	299-W15-5 56.4 m	muddy, sandy, GRAVEL	58.7	12.4	4.0	7.9	7.3	3.8	5.9	0.3	Low-Moderate
	Lower Mud		299-W15-5 137.2 m	muddy, medium to fine SAND	0.9	2.4	5.5	21.4	21.6	14.0	34.3	1.6	Moderate to High
	Unit A		299-W15-5 147.8 m	sandy GRAVEL	40.1	33.4	17.1	4.5	1.2	1.2	2.6	0.3	Low-Moderate

* After DOE 2002

Figure 3.4. Typical Particle-Size, Calcium Carbonate, and Gamma Log Activity for the Principle Stratigraphic Units Beneath the Carbon Tetrachloride Disposal Area (after Rohay et al. 1994)

Analysis of the initial EarthVision™ geologic model constructed based on geologic contact database created for this study, identified several anomalous areas where adjacent boreholes had markedly different geologic contact elevations, creating large peaks or basins of unexplained paleogeomorphologic character. Thus, efforts were made to re-evaluate the raw geologic data in these areas, make new estimates (or confirm existing estimates) of the geologic contacts, and resolve these anomalies. As these new changes were input to the EarthVision™ model and new results were made available, additional refinements to the database were made.

Assignment of flow and transport properties to the stratigraphic units defined in the geologic model was accomplished by mapping these units to various soil/sediment classes for which hydraulic property data is available (e.g., Khaleel and Freeman 1995). Figure 3.5 illustrates how this process was used to

map these units to the hydraulic property data sets used in the initial assessments conducted with the System Assessment Capability, Rev. 0.

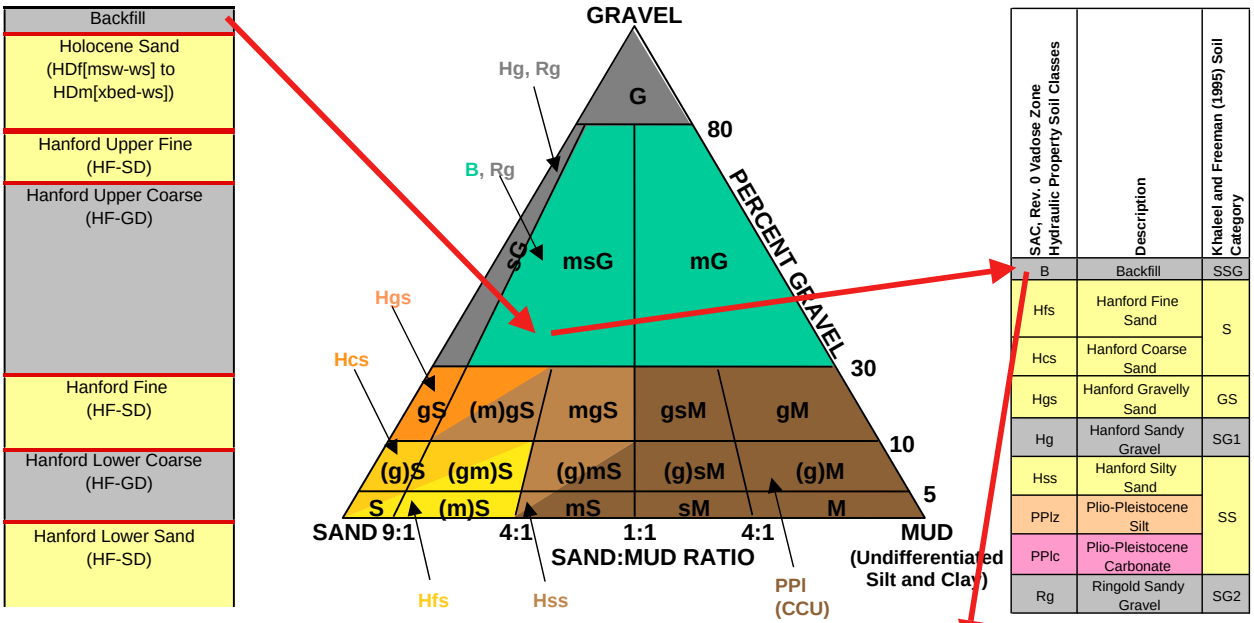

Table 1. Approximation for the distribution function for **soil type "B" (backfill)** based on **Khaleel and Freeman (1995) soil category SSG** (sand and gravel mixed with finer fraction).

B		Raw					Transformed (normal distribution)				Beta Distribution		Truncation Limits	
Parameter	Number of samples	Low	High	Mean	Standard Deviation	Stochastic Distribution	Low	High	Mean	Standard Deviation	A	B	Lower	Upper
θ_s	6	0.187	0.375	0.262	0.072	Normal							0.149	0.942
θ_R	6	0	0.064	0.03	0.029	Normal							0.150	0.879
s_r	7	0	0.212952381	0.101598768	0.089458717	Beta					1.0572	9.3483	0.000	0.213
α (1/cm)	6	0.003	0.103	0.032	0.036	Lognormal			-3.957	1.166			0.100	0.926
n	6	1.256	1.629	1.4	0.131	Normal							0.136	0.960
K_s (cm/s)	6	2.76E-05	6.80E-02	1.50E-02	2.70E-02	Log Ratio	-10.854	2.995	-5.262	5.499			0.010	0.990
Longitudinal Dispersivity[1] (m)	NA	0.027	0.178	0.09		Uniform								
Bulk Density[2]	NA			1.94		Constant								
Particle Density (g/cm^3)				2.65		Constant								

[1] Taken from Ho, et. al., 1999 [Stochastic Parameter Development for PORFLOW Simulations of the Hanford AX Tank Farm]
[2] Taken from Khaleel, et. al. 2000 (Modeling Data Package for S-SX Field Investigation Report (FIR) [DRAFT])

Figure 3.5. Example of the Soil Property Mapping Process

In an effort to better represent the small, site-specific scale geologic controls, and to support very detailed high-resolution modeling of the subsurface beneath the 216-Z-9 trench, the study analyzed data from 21 boreholes in the immediate vicinity of the 216-Z-9 trench. This analysis was conducted by assembling raw data sets for each well, consistent with that used for the prototype Hanford Borehole Geologic Information System (HBGIS; Last et al. 2002). These datasets include image files (e.g., links to scanned images of the as built diagrams, driller's logs), text (e.g., summarized descriptions extracted from the driller's logs or geologist's logs), and numerical data (e.g., particle-size, calcium carbonate content, moisture content, geophysical log data). The actual data types included in a particular borehole dataset are dependent on the types of data available. The datasets were originally prepared as a series of Excel spreadsheets/tables, with electronic links to other databases. Twenty of the 21 datasets were also entered into a relational database developed in Access to facilitate data processing and reporting.

Once the raw data sets were assembled, some manipulation of the data sets was conducted to derive additional data sets (e.g., the sand: mud ratio, average particle size), adjust for differences in reference

elevations (e.g., account for stickup where the reference datum was top of casing rather than ground surface), and/or graphically portray the data. Selected data sets were then plotted side-by-side in Borehole Correlation Charts to aid synergistic interpretation of all data sets for a given borehole.

New capabilities were added to generate automated reports and graphic plots directly from the new HBGIS. Examples of an automated report and graphic plot for well 299-W15-8 are provided in Figures 3.6 and 3.7, respectively. Other capabilities were also added to export data to log analysis and presentation software (i.e., LogPlot). Detailed cross sections were prepared to evaluate the cross borehole correlations for all 21 boreholes.

The prototype HBGIS and the new log analysis software provide the capability to synergistically interpret key borehole datasets to identify and record lithologic/facies changes and define the geologic contacts (picks). Capabilities within the prototype HBGIS also record the geologic picks (and subsequent changes to the picks) to another database table for export to other geologic analysis and visualization software (e.g., RockWare, EarthVision™) for creating cross sections, fence diagrams, contour maps, and solid models.

Once the data for individual boreholes was synergistically interpreted (via the log plots) in coordination with cross-borehole correlations (via the cross sections), and the geologic contacts (picks) database refined, these data were then exported to the EarthVision™ software for three-dimensional (solid model) analysis. Geologic interpretation of the EarthVision™ model also leads to re-interpretation of some of the raw data sets, and subsequent adjustments to the geologic contacts database. As the geologic contacts were adjusted and new solid models generated, the need for additional adjustments became obvious. Thus, several iterations were made to re-interpret the raw borehole data in context with the two-dimensional and three-dimensional geologic interpretation.

During the initial phases of this work, several observations/recommendations were made regarding uncertainties in the geologic data and interpretations. Some of the factors contributing to the uncertainty were 1) quality of survey control, 2) the lack of geophysical logs some key wells, 3) quality of lithologic descriptions, 4) inconsistent level of detail/scale of geologic data, and 5) the ad hoc methods of mapping geologic lithofacies to hydrologic property distributions. To better resolve these uncertainties, nearly every borehole/well in the site-specific domain was resurveyed using a state of the art global positioning system. These new survey data were then incorporated into the geologic contacts database. Recommendations were made to incorporate borehole geophysical logging of key wells into the sampling and analysis plan for upcoming investigations. Efforts were planned to visually inspect and log archived samples; however, these efforts have been delayed by the on going efforts to move the Hanford Geotechnical Library. Essentially all raw data from all 21 boreholes/wells in the immediate vicinity of the 216-Z-9 trench were entered into the prototype HBGIS and synergistically interpreted using the graphical log plots. Considerable efforts were made to correlate hydraulic properties with particle size data and lithofacies.

WELL: 299-W15-8

DEPTH	Drill/Sample Method	Moistur	Driller's Description	Total Gravel %	Total Sand %	Total Mud %	Sand/Slit Ratio	Litho Class	CACO3
			Qualitative Data		**Particle Size Data (from**				
0									
5	H			6.7	72.9	20.4	3.6	(g)mS	0.9
10	H			9.7	69.9	20.4	3.4	(g)mS	0.9
15	H								
20	H			10.4	70.6	19.0	3.7	mgS	1.2
25	H		Gravel and sand - caves and looses water	56.9	42.7	0.5	89.1	sG	0.5
30	H		Gravel and sand - caves and looses water	48.4	51.3	0.2	241.0	sG	0.3
35	H		Gravel and sand - caves and looses water	32.6	67.0	0.5	138.7	sG	0.3
40	H		Gravel and sand - caves and looses water						
45	H		Gravel and sand - caves and looses water	32.4	52.4	15.3	3.4	msG	0.5
50	H		Gravel and sand - caves and looses water	42.6	46.1	11.3	4.1	msG	0.4
55	H		2 ft. gravel - 3 ft. sand and light silt	22.5	76.7	0.7	104.0	gS	0.9
60	H		Sand - some silt - caves	16.3	75.5	8.2	9.2	gS	1.2
65	H		Sandy silt - caves	6.0	82.6	11.4	7.2	(gm)S	1.5
70	H		Sandy silt - caves	2.9	83.8	13.3	6.3	(m)S	1.6

WELL: 299-W15-8

DEPTH	Drill/Sample Method	Moistur	Driller's Description	Total Gravel %	Total Sand %	Total Mud %	Sand/Slit Ratio	Litho Class	CACO3
			Qualitative Data		**Particle Size Data (from**				
75	H		Sandy silt - caves	3.4	88.0	8.7	10.2	S	1.7
80	H		Sandy silt	4.6	87.3	8.1	10.8	S	1.4
85	H		Sandy silt	2.4	83.6	14.0	6.0	(m)S	1.4
90	H		Sandy silt	1.4	82.3	16.3	5.1	(m)S	1.4
95	H		Sandy silt	0.4	77.2	22.4	3.4	mS	1.3
100	H		Sandy silt	0.8	78.3	21.0	3.7	mS	1.5
105				0.9	76.6	22.5	3.4	mS	1.4
107	H		Sandy silt						
113	DB?		107-113' - No record						
120	DB?		113-120' - Sand & silt, gravel, caliche						
125	H		120-125' - Cobbles						
129	H		125-129' - Cobbles						
135	H		129-135' - Cobbles						
140	H		135-140' - Cobbles, gravel						
150	H		140-150' - Cobbles, gravel						
152	DB		150-152' - Cobbles, gravel						
155	H		152-155' - Gravel, silt, boulders						

Figure 3.6. Borehole Geologic Data Report for Well 299-W15-8 (first two pages only)

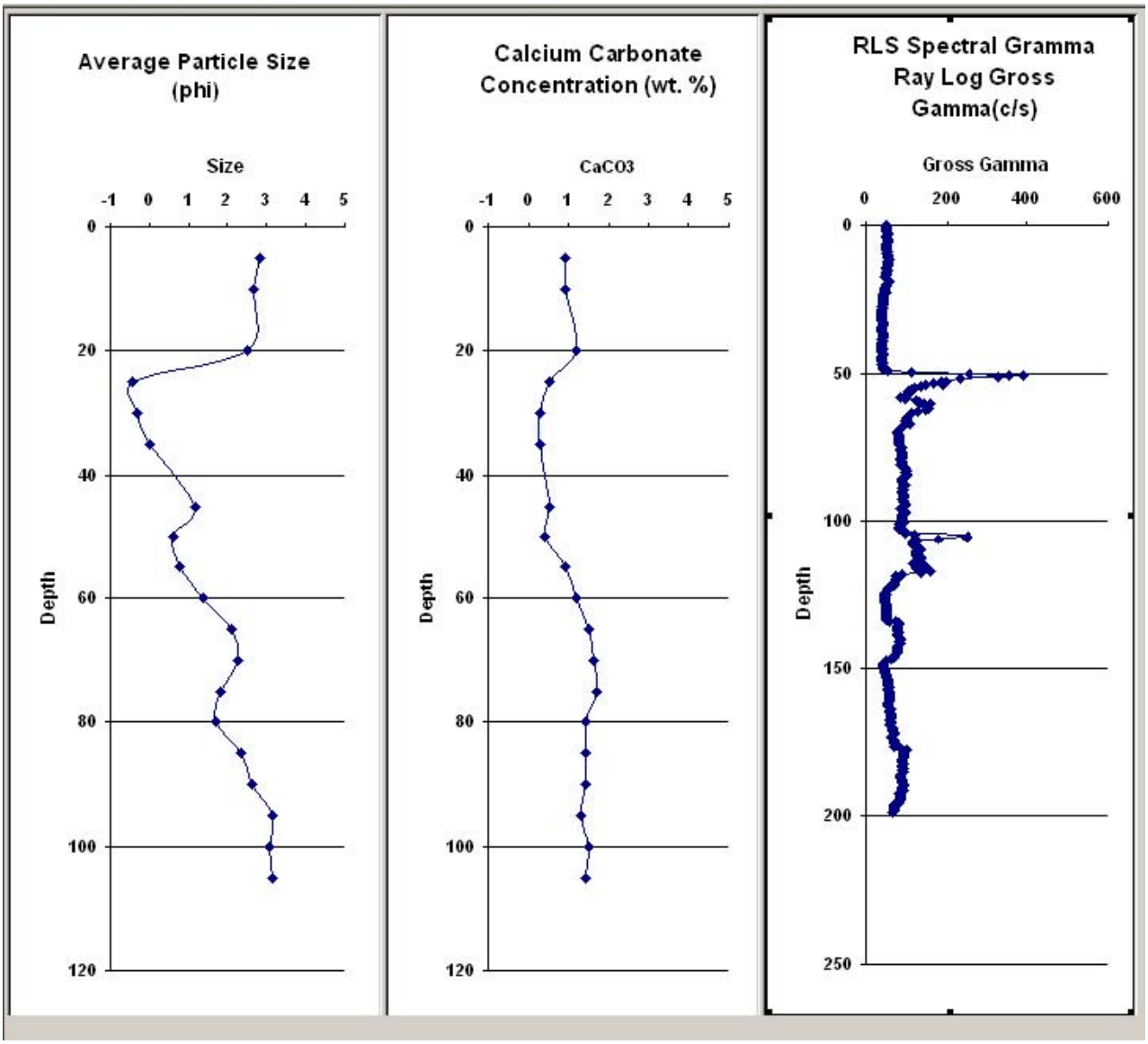

Figure 3.7. Graphic Borehole Report for Well 299-W15-8

To aid initial groundwater flow and transport simulations of the 216-Z-9 trench, the geologic framework was simplified into a layered sequence of five main stratigraphic units and a number of subordinate units. From oldest to youngest, the main stratigraphic units are the : 1) Saddle Mountains Formation (of Miocene age), 2) Ringold Formation (of Miocene/Pliocene age), 3) Cold Creek unit (Pliocene-Pleistocene), 4) Hanford Formation (Pleistocene), and 5) undifferentiated Holocene Deposits. Table 3.1 provides the stratigraphic template and associated hydraulic property distributions used in the initial numerical simulations. A brief description of each the stratigraphic units is presented on page 3.13.

Table 3.1. Hydraulic Property Distributions for the 216-Z-9 Trench Soil Classes

Vadose Zone Hydraulic Property Distributions (After Khaleel's Sept. 2000 White Paper, and Khaleel and Freeman, 1995)

Table 1. Approximation for the distribution function for **soil type "B" (backfill)** based on **Khaleel and Freeman (1995) soil category SSG** (sand and gravel mixed with finer fraction).

B		Raw					Transformed (normal distribution)				Beta Distribution		Truncation Limits	
Parameter	Number of samples	Low	High	Mean	Standard Deviation	Stochastic Distribution	Low	High	Mean	Standard Deviation	A	B	Lower	Upper
θ_S	6	0.187	0.375	0.262	0.072	Normal							0.149	0.942
θ_R	6	0	0.064	0.03	0.029	Normal							0.150	0.879
s_r	7	0	0.21295238	0.10159877	0.08945872	Beta					1.0572	9.3483	0.000	0.213
α (1/cm)	6	0.003	0.103	0.032	0.036	Lognormal			-3.957	1.166			0.100	0.926
n	6	1.256	1.629	1.4	0.131	Normal							0.136	0.960
K_s (cm/s)	6	2.76E-05	6.80E-02	1.50E-02	2.70E-02	Log Ratio	-10.854	2.995	-5.262	5.499			0.010	0.990
Longitudinal Dispersivity[1] (m)	NA	0.027	0.178	0.09		Uniform								
Bulk Density[2]	NA			1.94		Constant								
Particle Density[3] (g/cm^3)				2.65		Constant								

[1] Taken from Ho, et. al., 1999 [Stochastic Parameter Development for PORFLOW Simulations of the Hanford AX Tank Farm]

[2] Taken from Khaleel, et. al. 2000 (Modeling Data Package for S-SX Field Investigation Report (FIR) [DRAFT])

Table 2. Approximation for the distribution function for **soil type "Hfs"** (Hanford fine sand) based on **Khaleel and Freeman (1995) soil category S** (sand). As modified by Freeman (2001)[3].

Hfs		Raw					Transformed (normal distribution)				Beta Distribution		Truncation Limits	
Parameter	Number of samples	Low	High	Mean	Standard Deviation	Stochastic Distribution	Low	High	Mean	Standard Deviation	A	B	Lower	Upper
θ_S	25	0.2663	0.4431	0.3653	0.05	Normal							0.024	0.940
θ_R	25	0	0.0608	0.0309	0.0166	Normal							0.031	0.964
s_r	25	0	0.1837	0.0857	0.0464	Normal							0.032	0.983
α (1/cm)	25	0.004	0.7417	0.0448	0.0767	Lognormal			-3.79E+00	1.37E+00			0.103	0.990
n	25	1.1928	4.77	2.3553	0.9811	Normal							0.118	0.990
K_s (cm/s)	22	1.38E-05	4.42E-02	5.85E-04	1.61E+00	Lognormal			-7.45E+00	2.05E+00			0.100	0.982
Longitudinal Dispersivity[1] (m)	NA	0.183	0.223	0.203		Uniform								
Bulk Density[3] (g/cm^3)	21	1.44	1.97	1.609	0.113	Normal							0.067	0.999
Particle Density[3] (g/cm^3)	21	2.35	2.71	2.6343	0.0921	Normal							0.001	0.794

[1] Taken from Ho, et. al., 1999 [Stochastic Parameter Development for PORFLOW Simulations of the Hanford AX Tank Farm]

[2] Taken from Khaleel, et. al. 2000 (Modeling Data Package for S-SX Field Investigation Report (FIR) [DRAFT])

[3] Taken from Freeman's e-mail to George Last, dated 12/27/01 (finetex1a.doc and HStex1.doc).

Table 3. Approximation for the distribution function for **soil type "Hcs"** (Hanford coarse sand) based on **Khaleel and Freeman (1995) soil category S** (sand). As modified by Freeman (2001)[3]

Hcs		Raw					Transformed (normal distribution)				Beta Distribution		Truncation Limits	
Parameter	Number of samples	Low	High	Mean	Standard Deviation	Stochastic Distribution	Low	High	Mean	Standard Deviation	A	B	Lower	Upper
θ_S	41	0.1968	0.519	0.3359	0.0806	Normal							0.042	0.988
θ_R	41	0	0.0994	0.0251	0.0178	Normal							0.079	0.990
s_r	41	0	0.2078	0.0762	0.0481	Normal							0.057	0.990
α (1/cm)	41	0.0131	0.8612	0.1338	0.1806	Lognormal			-2.53E+00	1.02E+00			0.100	0.990
n	41	1.2658	4.1695	2.0475	0.7149	Normal							0.137	0.990
K_s (cm/s)	40	2.10E-05	5.80E-02	1.87E-03	1.48E+00	Lognormal			-6.28E+00	1.96E+00			0.100	0.960
Longitudinal Dispersivity[1] (m)	NA	0.183	0.223	0.203		Uniform								
Bulk Density[3] (g/cm^3)	30	1.46	1.8	1.6203	0.0826	Normal							0.026	0.985
Particle Density[3] (g/cm^3)	30	2.65	2.65	2.65	0	Constant								

Table 3.1. (contd)

Table 4. Approximation for the distribution function for **soil type "Hgs"** (Hanford gravelly sand) based on **Khaleel and Freeman (1995) soil category GS.**

Hgs		Raw					Transformed (normal distribution)				Beta Distribution		Truncation Limits	
Parameter	Number of samples	Low	High	Mean	Standard Deviation	Stochastic Distribution	Low	High	Mean	Standard Deviation	A	B	Lower	Upper
θ_S	10	0.203	0.334	0.272	0.048	Normal							0.075	0.902
θ_R	10	0.01	0.069	0.04	0.019	Normal							0.057	0.937
s_r	9	0.0296472	0.24368552	0.1570079	0.07134004	Beta					3.9262	21.0801	0.030	0.244
α (1/cm)	10	0.004	0.074	0.027	0.023	Normal							0.159	0.979
n	10	1.529	2.537	1.994	0.315	Normal							0.070	0.958
K_s (cm/s)	10	5.43E-05	8.00E-03	3.00E-03	3.00E-03	Log Ratio			-1.569	3.582			0.010	0.990
Longitudinal Dispersivity[1] (m)	NA	0.0468	0.134	0.088		Uniform								
Bulk Density[2]	NA			2.07		Constant								
Particle Density[3] (g/cm^3)				2.65		Constant								

[1] Taken from Ho, et. al., 1999 [Stochastic Parameter Development for PORFLOW Simulations of the Hanford AX Tank Farm]

[2] Taken from Khaleel, et. al. 2000 (Modeling Data Package for S-SX Field Investigation Report (FIR) [DRAFT]). Same as SG1.

Table 5. Approximation for the distribution function for **soil type "Hg"** (Hanford sandy gravel) based on **Khaleel and Freeman (1995) soil category SG1** (sandy gravel with gravel fraction < 60%).

Hg		Raw					Transformed (normal distribution)				Beta Distribution		Truncation Limits	
Parameter	Number of samples	Low	High	Mean	Standard Deviation	Stochastic Distribution	Low	High	Mean	Standard Deviation	A	B	Lower	Upper
θ_S	25	0.113	0.26	0.166	0.036	Normal							0.070	0.990
θ_R	25	0	0.062	0.023	0.015	Normal							0.063	0.990
s_r	26	0	0.38707654	0.13146178	0.09252076	Beta					1.6221	10.7165	0.000	0.387
α (1/cm)	25	0.002	0.919	0.083	0.204	Lognormal			-4.086	1.55			0.100	0.990
n	25	1.262	2.947	1.66	0.355	Lognormal			0.489	0.184			0.100	0.990
K_s (cm/s)	24	1.90E-07	3.70E-02	5.00E-03	9.00E-03	Lognormal			-7.932	3.322			0.100	0.919
Longitudinal Dispersivity[1] (m)	NA	0.027	0.178	0.09		Uniform								
Bulk Density[2]	NA			2.07		Constant								
Particle Density[3] (g/cm^3)				2.65		Constant								

[1] Taken from Ho, et. al., 1999 [Stochastic Parameter Development for PORFLOW Simulations of the Hanford AX Tank Farm]. Same as SSG

[2] Taken from Khaleel, et. al. 2000 (Modeling Data Package for S-SX Field Investigation Report (FIR) [DRAFT]). Same as SG-1.

Table 6. Approximation for the distribution function for **soil type "PPlz"** (Plio-Pleistocene-silt) based on **Khaleel and Freeman (1995) soil category SS** (sand mixed with finer fraction). As modified by Freeman (2001)[3].

PPlz		Raw					Transformed (normal distribution)				Beta Distribution		Truncation Limits	
Parameter	Number of samples	Low	High	Mean	Standard Deviation	Stochastic Distribution	Low	High	Mean	Standard Deviation	A	B	Lower	Upper
θ_S	7	0.34	0.5331	0.4238	0.0812	Normal							0.151	0.911
θ_R	7	0.02	0.06	0.041	0.0143	Normal							0.071	0.908
s_r	7	0.0537	0.1125	0.0883	0.0229	Normal							0.065	0.855
α (1/cm)	7	0.001	0.0069	0.00519	0.0047	Lognormal			-5.56E+00	7.74E-01			0.100	0.775
n	7	1.5218	2.815	2.0671	0.5053	Normal							0.140	0.931
K_s (cm/s)	6	4.12E-07	2.00E-04	1.48E-05	1.12E+00	Lognormal			-1.11E+01	2.56E+00			0.100	0.845
Longitudinal Dispersivity[1] (m)	NA	0.0279	0.0341	0.031		Uniform								
Bulk Density[3] (g/cm^3)	7	1.46	1.781	1.6129	0.1323	Normal							0.124	0.898
Particle Density[3] (g/cm^3)	7	2.62	2.69	2.6657	0.0264	Normal							0.042	0.821

[1] Taken from Ho, et. al., 1999 [Stochastic Parameter Development for PORFLOW Simulations of the Hanford AX Tank Farm].

[2] Taken from Khaleel, et. al. 2000 (Modeling Data Package for S-SX Field Investigation Report (FIR) [DRAFT]).

[3] Taken from Freeman's e-mail to George Last, dated 12/27/01 (finetex1a.doc and HStex1.doc).

Table 3.1. (contd)

Table 7. Approximation for the distribution function for **soil type "PPlc"** (Plio-Pleistocene-carbonate) based on **Khaleel and Freeman (1995) soil category SS** (sand mixed with finer fraction). As modified by Freeman (2001)[3].

PPlc		Raw					Transformed (normal distribution)				Beta Distribution		Truncation Limits	
Parameter	Number of samples	Low	High	Mean	Standard Deviation	Stochastic Distribution	Low	High	Mean	Standard Deviation	A	B	Lower	Upper
θ_S	13	0.1933	0.6306	0.3203	0.119	Normal							0.143	0.990
θ_R	13	0.023	0.2412	0.0785	0.06116	Normal							0.182	0.990
s_r	13	0.0962	0.4445	0.223	0.1032	Normal							0.110	0.984
α (1/cm)	13	0.0039	0.0728	0.01726	0.0182	Lognormal			-4.43E+00	8.69E-01			0.100	0.981
n	13	1.2618	2.5367	1.7705	0.3515	Normal							0.074	0.985
K_s (cm/s)	13	2.60E-07	6.80E-02	6.72E-04	1.99E+00	Lognormal			-7.31E+00	3.59E+00			0.100	0.901
Longitudinal Dispersivity[1] (m)	NA	0.0279	0.0341	0.031		Uniform								
Bulk Density[3] (g/cm^3)	12	1.39	1.9	1.6475	0.1444	Normal							0.037	0.960
Particle Density[3] (g/cm^3)	12	2.62	2.74	2.6667	0.0345	Normal							0.088	0.983

[1] Taken from Ho, et. al., 1999 [Stochastic Parameter Development for PORFLOW Simulations of the Hanford AX Tank Farm].

[2] Taken from Khaleel, et. al. 2000 (Modeling Data Package for S-SX Field Investigation Report (FIR) [DRAFT]).

[3] Taken from Freeman's e-mail to George Last, dated 12/27/01 (finetex1a.doc and HStex1.doc).

Table 8. Approximation for the distribution function for **soil type "Hss"** (Hanford silty fine sand) based on **Khaleel and Freeman (1995) soil category SS** (sand mixed with finer fraction). As modified by Freeman (2001)[3].

Hss		Raw					Transformed (normal distribution)				Beta Distribution		Truncation Limits	
Parameter	Number of samples	Low	High	Mean	Standard Deviation	Stochastic Distribution	Low	High	Mean	Standard Deviation	A	B	Lower	Upper
θ_S	37	0.3208	0.6772	0.4478	0.0699	Normal							0.035	0.990
θ_R	37	0.019	0.2705	0.0779	0.04607	Normal							0.101	0.990
s_r	37	0.0472	0.3388	0.161	0.059	Normal							0.027	0.990
α (1/cm)	37	0.0008	0.387	0.0107	0.0138	Lognormal			-5.03E+00	9.93E-01			0.100	0.990
n	37	1.2598	3.2652	1.9229	0.4652	Normal							0.077	0.990
K_s (cm/s)	28	1.40E-08	8.88E-04	5.98E-05	1.16E+00	Lognormal			-9.72E+00	2.42E+00			0.100	0.868
Longitudinal Dispersivity[1] (m)	NA	0.0279	0.0341	0.031		Uniform								
Bulk Density[3] (g/cm^3)	10	1.33	1.72	1.576	0.1164	Normal							0.017	0.892
Particle Density[3] (g/cm^3)	10	2.65	2.66	2.651	0.0032	Normal							0.377	0.998

[1] Taken from Ho, et. al., 1999 [Stochastic Parameter Development for PORFLOW Simulations of the Hanford AX Tank Farm].

[2] Taken from Khaleel, et. al. 2000 (Modeling Data Package for S-SX Field Investigation Report (FIR) [DRAFT]).

[3] Taken from Freeman's e-mail to George Last, dated 12/27/01 (finetex1a.doc and HStex1.doc).

Table 9. Approximation for the distribution function for **soil type "Rg"** (Ringold sandy gravel) based on **Khaleel and Freeman (1995) soil category SG2** (sandy gravel with gravel fraction >60%).

Rg		Raw					Transformed (normal distribution)				Beta Distribution		Truncation Limits	
Parameter	Number of samples	Low	High	Mean	Standard Deviation	Stochastic Distribution	Low	High	Mean	Standard Deviation	A	B	Lower	Upper
θ_S	11	0.056	0.107	0.077	0.016	Lognormal			-2.59	0.216			0.100	0.950
θ_R	11	0	0.0197	0.01	0.007	Normal							0.077	0.917
s_r	50	0	0.22853087	0.14323863	0.08069021	Beta					2.5566	15.2920	0.000	0.229
α (1/cm)	11	0.003	0.028	0.009	0.009	Lognormal			-5.008	0.882			0.182	0.948
n	11	1.347	1.885	1.621	0.178	Normal							0.062	0.931
K_s (cm/s)	10	2.83E-05	1.30E-01	1.40E-02	4.10E-02	Lognormal			-7.137	2.332			0.100	0.986
Longitudinal Dispersivity[1] (m)	NA	0.027	0.178	0.09		Uniform								
Bulk Density[2]	NA			2.07		Constant								
Particle Density[3] (g/cm^3)				2.65		Constant								

[1] Taken from Ho, et. al., 1999 [Stochastic Parameter Development for PORFLOW Simulations of the Hanford AX Tank Farm]. Same as SSG.

[2] Taken from Khaleel, et. al. 2000 (Modeling Data Package for S-SX Field Investigation Report (FIR) [DRAFT]). Same as SG-1.

1. **Saddle Mountains Formation**. The Saddle Mountains Formation forms the bedrock beneath the site. Its upper most member, the Elephant Mountain Member lies at a depth of approximately 161 m, and slopes to southwest at a rate of about 0.015 (or 15 m/100 m). This medium- to fine-grained tholeiitic basalt essentially acts as a no-flow boundary at the floor of the unconfined aquifer

2. **Ringold Formation**. The basalt bedrock is overlain by the Ringold Formation, a sedimentary sequence of fluvial-lacustrine clay, silt, sand, and granule to cobble gravel deposited by the ancestral Columbia River. Beneath the 216-Z-9 trench, the Ringold Formation has been sub-divided into three subordinate units. From oldest to youngest, these are: 1) Unit A – fluvial sandy gravel; 2) the Lower Mud Unit – a sequence of paleosols and lake deposits, consisting of muddy medium to fine sand; and 3) Unit E – semi-indurated fluvial muddy sand gravel.

3. **Cold Creek Unit**. Overlying the Ringold Formation is the Cold Creek unit. Locally, this unit is differentiated into the Cold Creek carbonate layer and the Cold Creek silt layer. The Cold Creek carbonate layer, formerly described as the caliche (or calcrete), is a fine- to coarse-grained, calcium-carbonate cemented paleosol that developed on top of the Ringold Formation. Overlying the Cold Creek carbonate layer is the Cold Creek silt layer formally referred to as the "Early Palouse Soil." This unit consists of cohesive, compact, massive to laminated and stratified fine-grained sand and silt (e.g., Sandy Mud).

4. **Hanford Formation**. The Hanford formation has been locally subdivided into three main units (from oldest to youngest): 1) a sequence of interbedded sand and mud (e.g., slightly muddy medium to fine sand to sandy mud), equivalent to the Hanford H4 unit; 2) a sequence of coarse to medium sand, equivalent to the Hanford H2 unit; and 3) a sequence of sandy gravel, equivalent to the Hanford H1 unit.

5. **Backfill**. The 216-Z-9 trench was excavated in to the underlying Holocene Sand and Hanford sandy gravel units. The stockpiles of these sediments have been used as backfill in pipeline trenches and other excavations in the vicinity of the 216-Z-9 trench. These backfill materials are described as gravelly medium sand.

To create a consistent database of geologic contacts, all pertinent data sets were mapped to a single set of hydrostratigraphic units. These hydrostratigraphic units have also been mapped to the new Standardized Stratigraphic Nomenclature (DOE 2002). To enhance the level of detail, the 5 main hydrostratigraphic units were subsequently divided into 14 units for the 216-Z-9 trench domain. The units are Backfill, Holocene Sand, Hanford Upper Fine, Hanford 1, Hanford 2, Hanford Lower Gravel, Hanford Lower Sand, Cold Creek silt, Cold Creek carbonate, Upper Ringold, Ringold E, Ringold Lower Mud, Ringold A, and Elephant Mtn. Basalt. Table 3.1 provides the hydraulic property distributions of the hydrostratigraphic units. Figure 3.5 illustrates the method that has been used to assign the properties to the units.

3.2 EarthVision Geologic Model

EarthVision™ software was used to create a three-dimensional model of the geologic units. The EarthVsion™ model consists of a "faces" file that represents each unit as a zone within a solid three-dimensional block. The surface of each unit is defined by an XYZ grid with XY spacing of 5 m. The model domain is 440 m wide and 540 m long. Figure 3.1 shows the model domain and also shows the location of the PFP, the three major carbon tetrachloride disposal cribs, U Pond, and the 216-U-14 ditch. The faces file can be sampled using utilities provided in the EarthVision™ software to create input files for numerical flow models. Fourteen units were originally defined for the EarthVision™ model. However, based on revised geological interpretations, the Hanford lower-fines (b-fines) were combined with the Hanford lower-sand unit. The uppermost unit is "backfill," which only occurs in a few locations. The unit below this, which is the first extensive unit, includes both the Holocene Sand and the Hanford Upper Fine units. These units were lumped together into the Hanford 1A unit because they are texturally similar.

The following procedure was used to build and revise the geologic model:

1. Grids representing the tops of extensive units (present over most of the model domain) were created based on the elevation picks from wells. Control points were added in areas where data were sparse, particularly on the edges of the model domain to control extrapolation.

2. Thickness (isopach) grids were calculated for less extensive geologic units based on the thickness measured at wells and zero thickness for the not present (NP) flags in the well data. For these less extensive units, it was assumed that the unit was not present in areas where there were no data for the unit.

3. Starting from the base of the model, grids for the top elevation of each less extensive geologic unit were calculated by adding the thickness grid to the elevation grid for whichever unit exists below it.

4. The model was examined to determine if any units had incorrectly "pinched-out" because the top of a deeper unit was being extrapolated above the elevation of the well pick. If this occurred, control points were added to control top of the deeper unit.

The geologic modeling procedure was an iterative process because examination of the model identified wells where elevation picks were inconsistent. The geologic data were then reevaluated by reviewing/evaluating the raw borehole data to determine whether the picks were valid.

Analysis of the initial EarthVision™ model results identified several anomalous areas where adjacent boreholes had markedly different geologic contact elevations, creating large peaks or basins of unexplained paleogeomorphologic character. Thus, efforts were made to re-evaluate the raw geologic data in these areas, make new estimates (or confirm existing estimates) of the geologic contacts, and resolve these anomalies. As these new changes were input to the revised EarthVision™ model and new results were made available, additional refinements to the database were made.

The EarthVision™ model is displayed in series of figures. Figure 3.8 shows an overview of the model area. Figure 3.9 shows the three-dimensional geologic model with a cut-out beneath the 216-Z-9 and 216-Z-1A cribs. Figures 3.10 through 3.20 are surface contour maps for each geo-stratigraphic unit of the model except the backfill. Locations of data points are also shown for each unit. Figures 3.21 and 3.22 show north-south and west-east cross-sections, respectively, through the model.

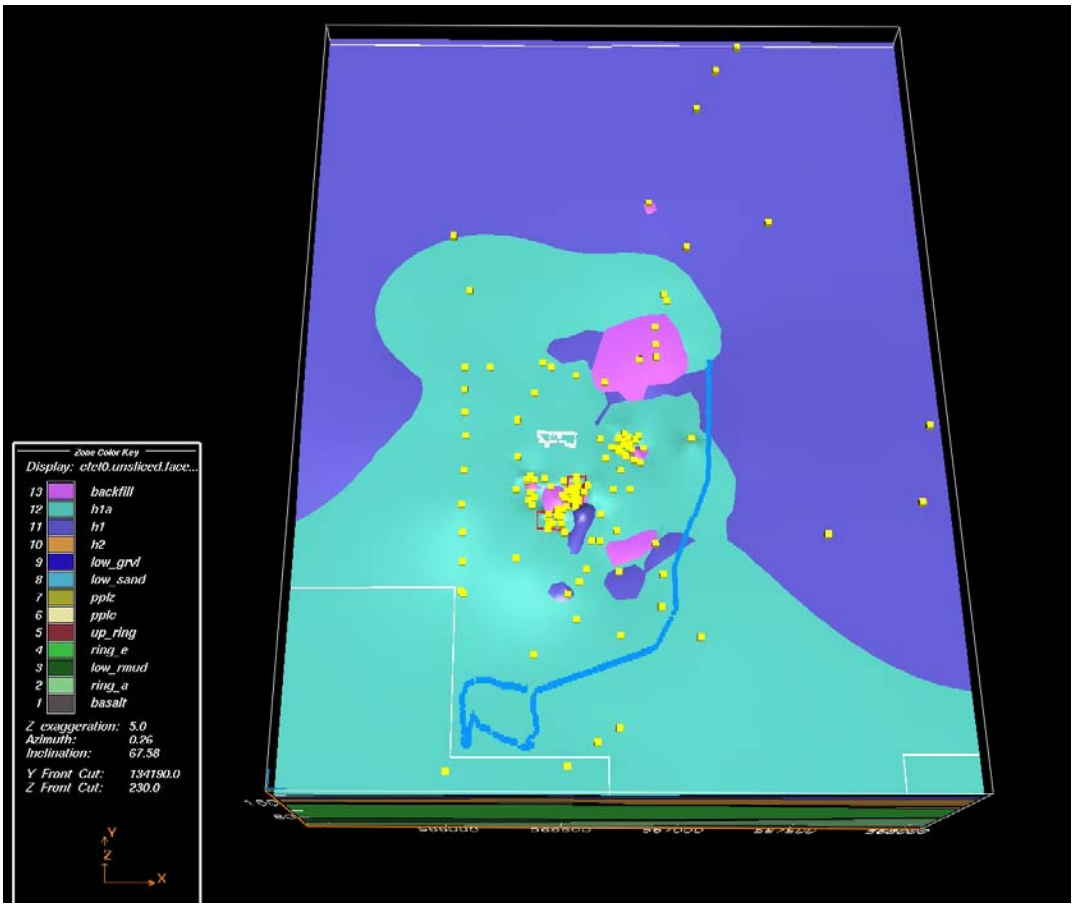

Figure 3.8. Overview of EarthVision™ Model Boundary in Relation to 200-West Area

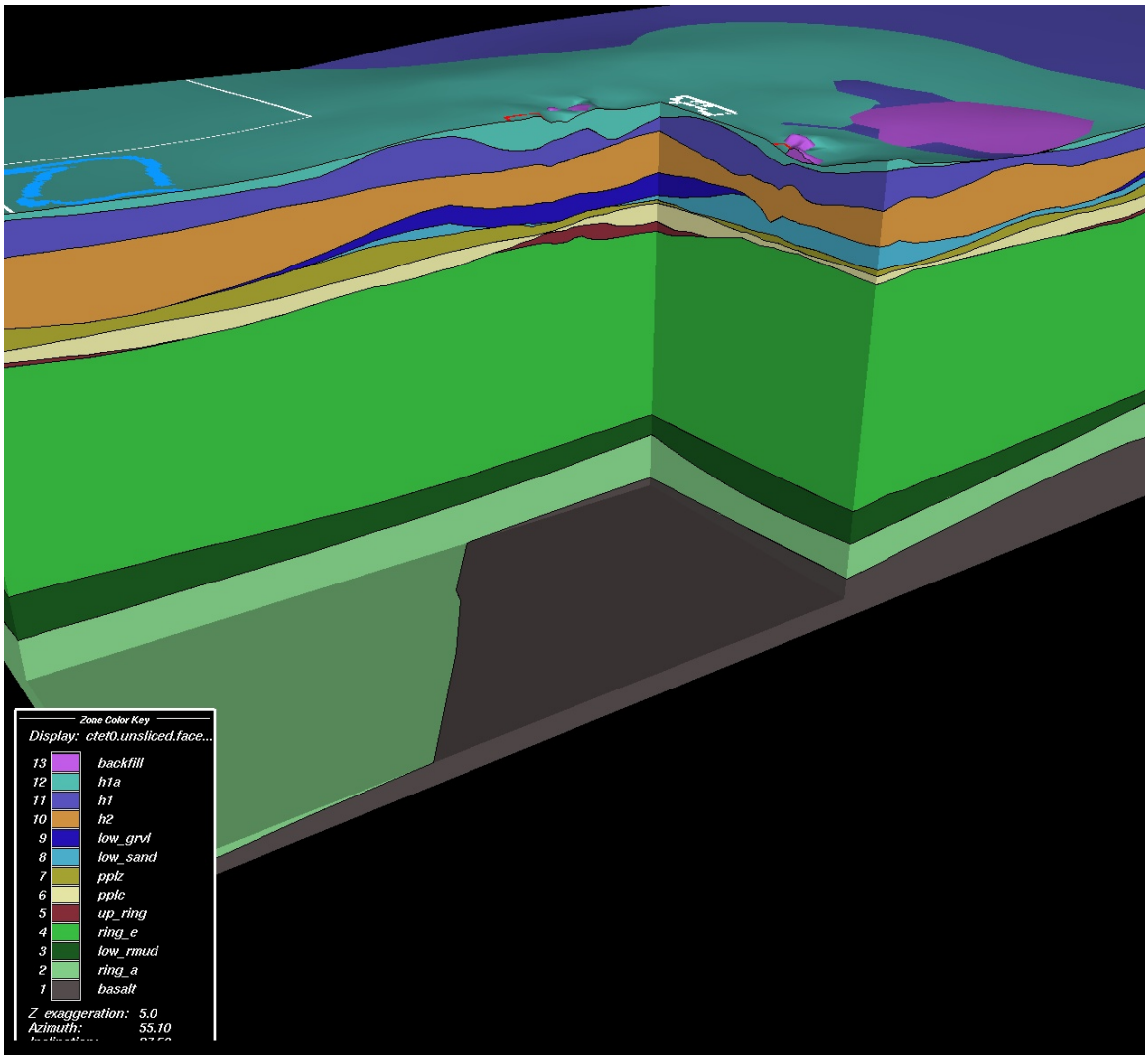

Figure 3.9. Three-Dimensional Geologic Model with a Cut-Out Beneath the 216-Z-9 and 216-Z-1A Cribs

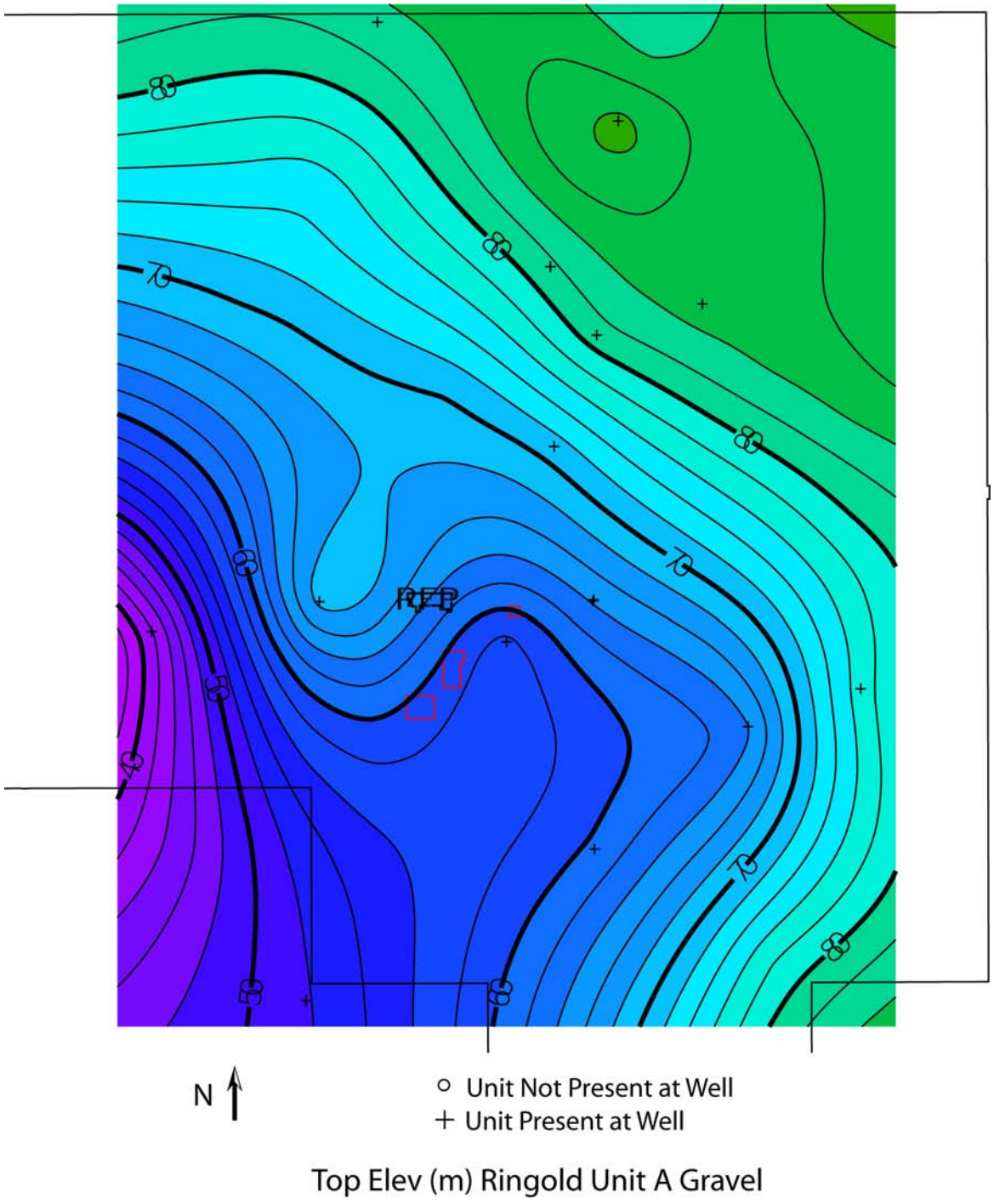

Figure 3.10. Top Elevation of Ringold Unit A Gravel

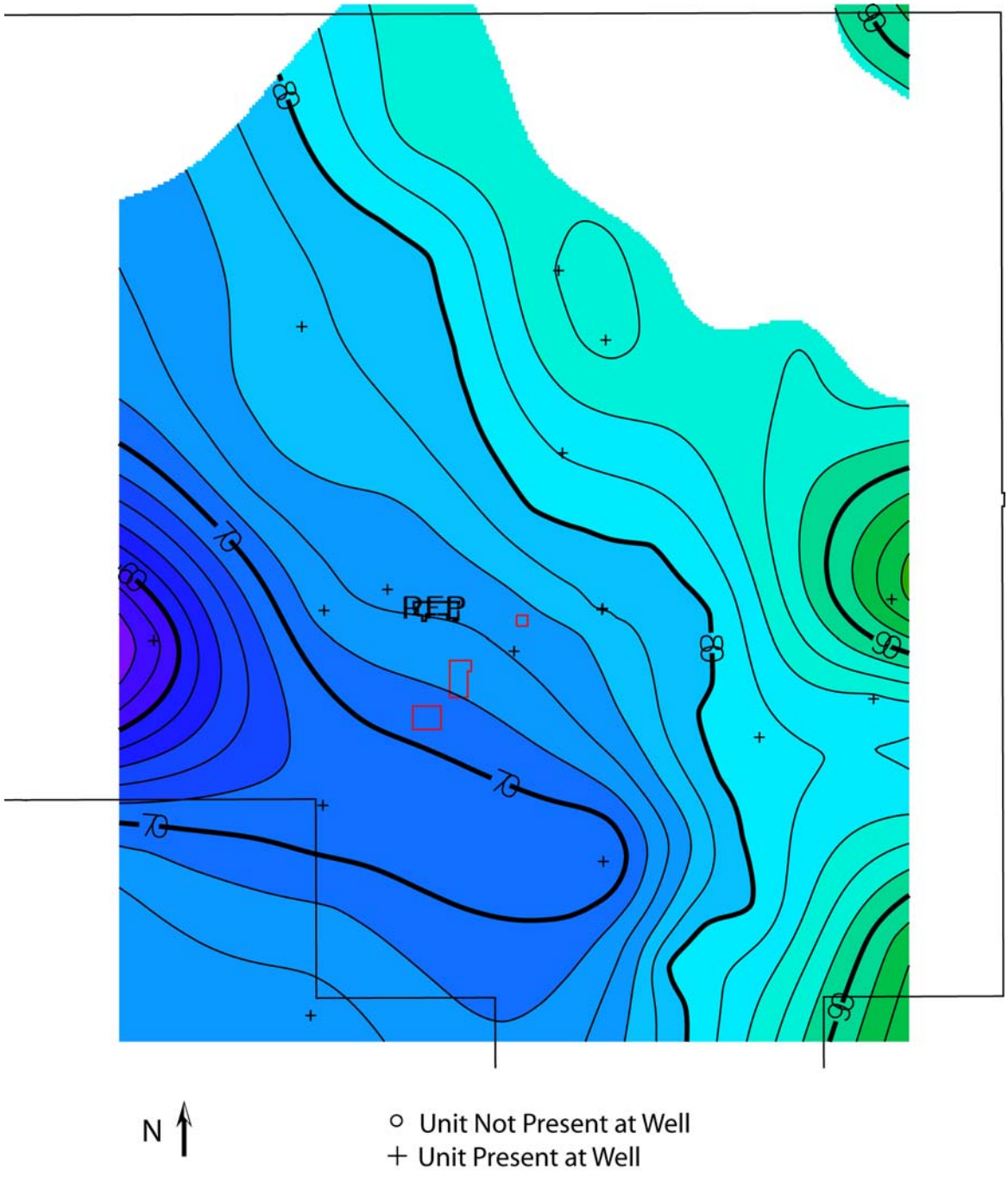

Figure 3.11. Top Elevation of Lower Ringold Mud Unit

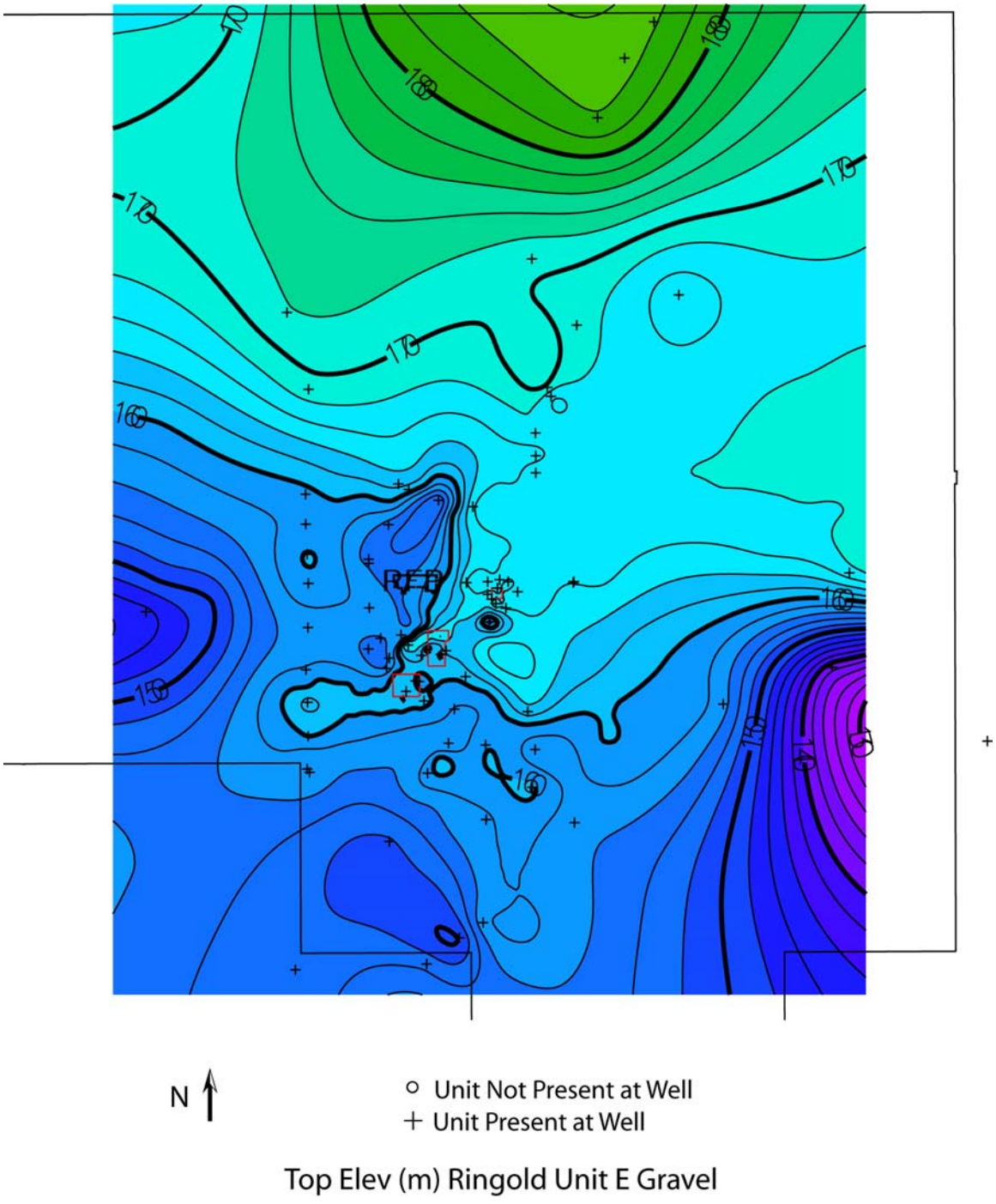

Figure 3.12. Top Elevation of Ringold Unit E Gravel

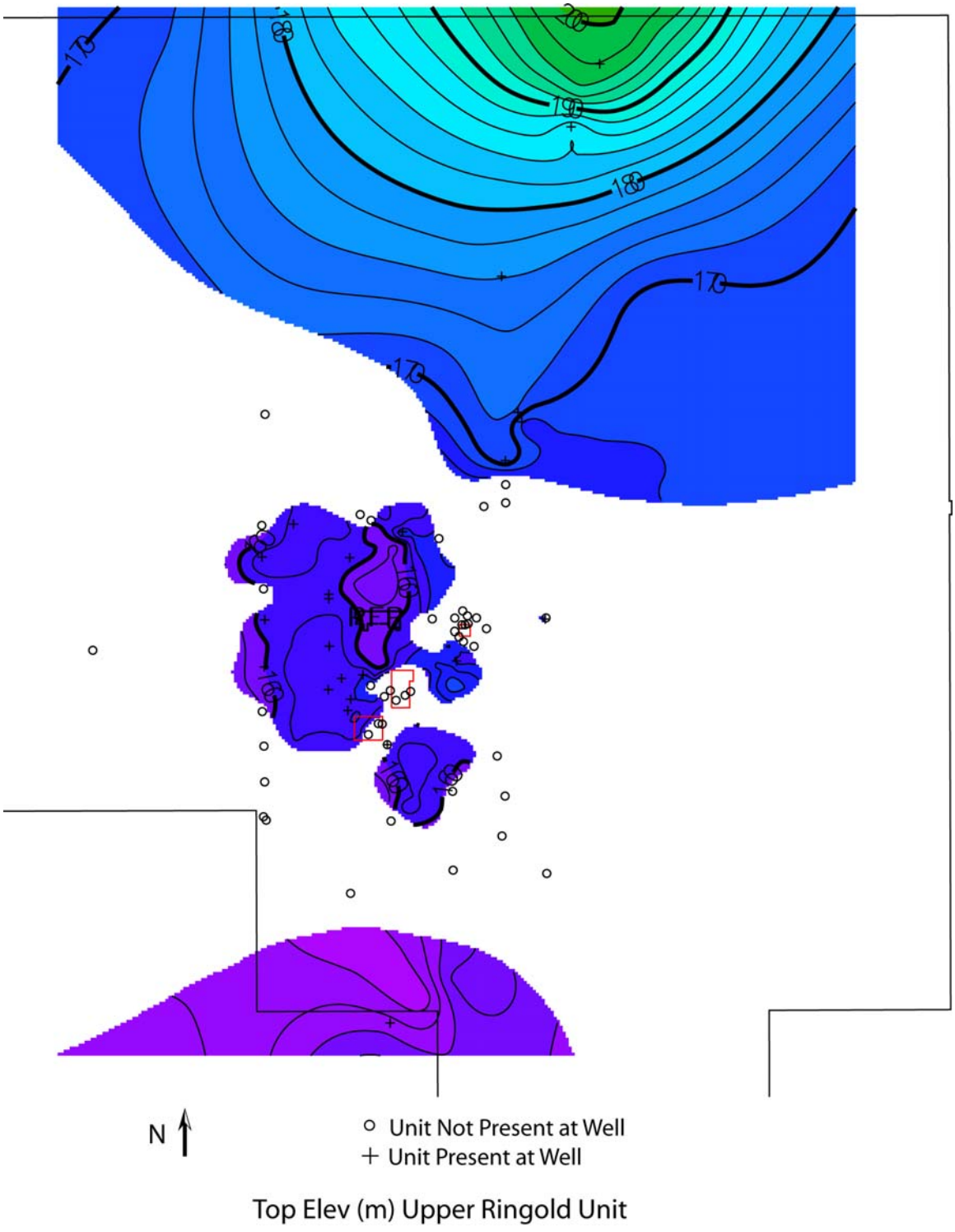

Figure 3.13. Top Elevation of Upper Ringold Unit

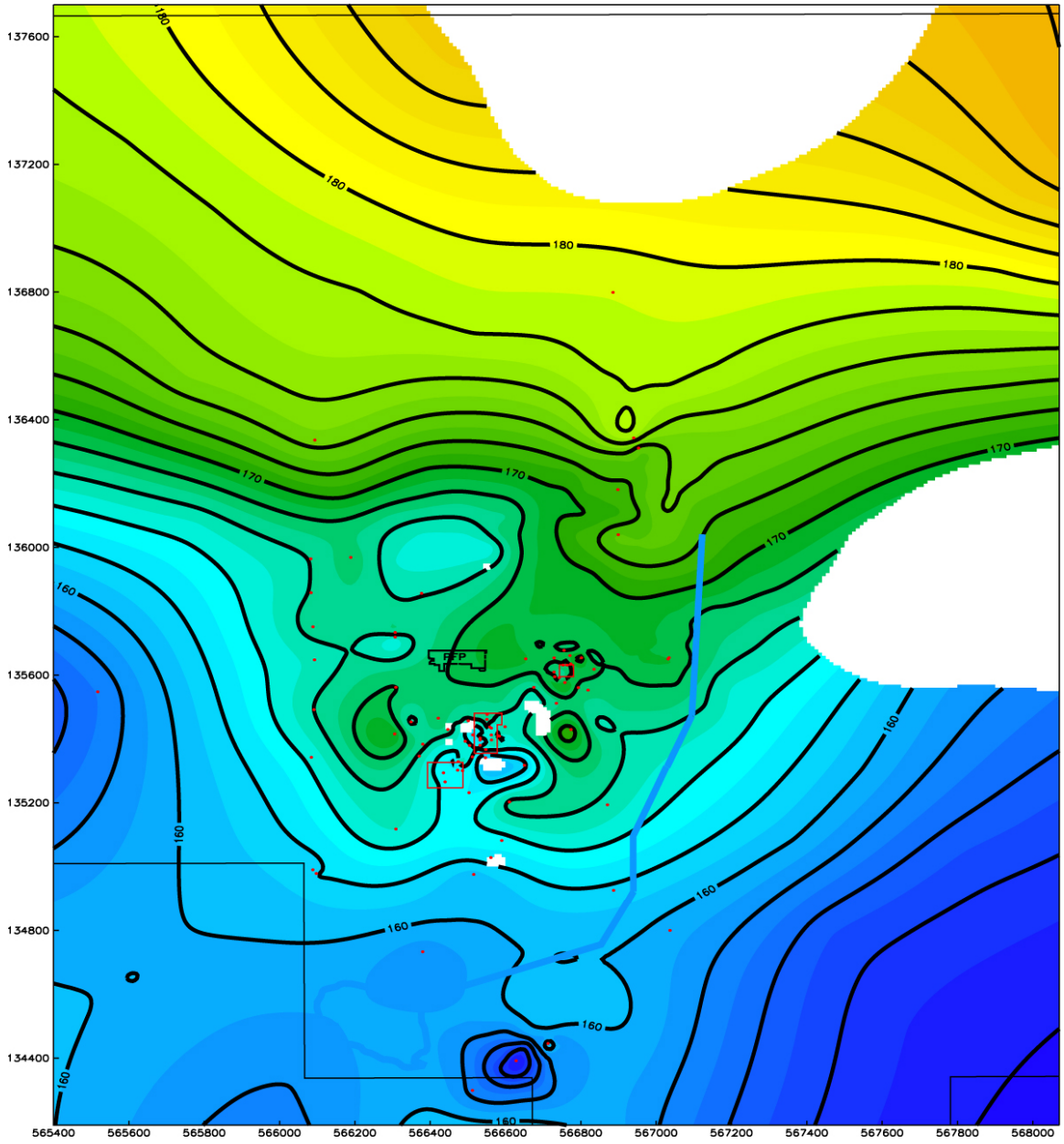

Figure 3.14. Top Elevation of Cold Creek Carbonate Layer

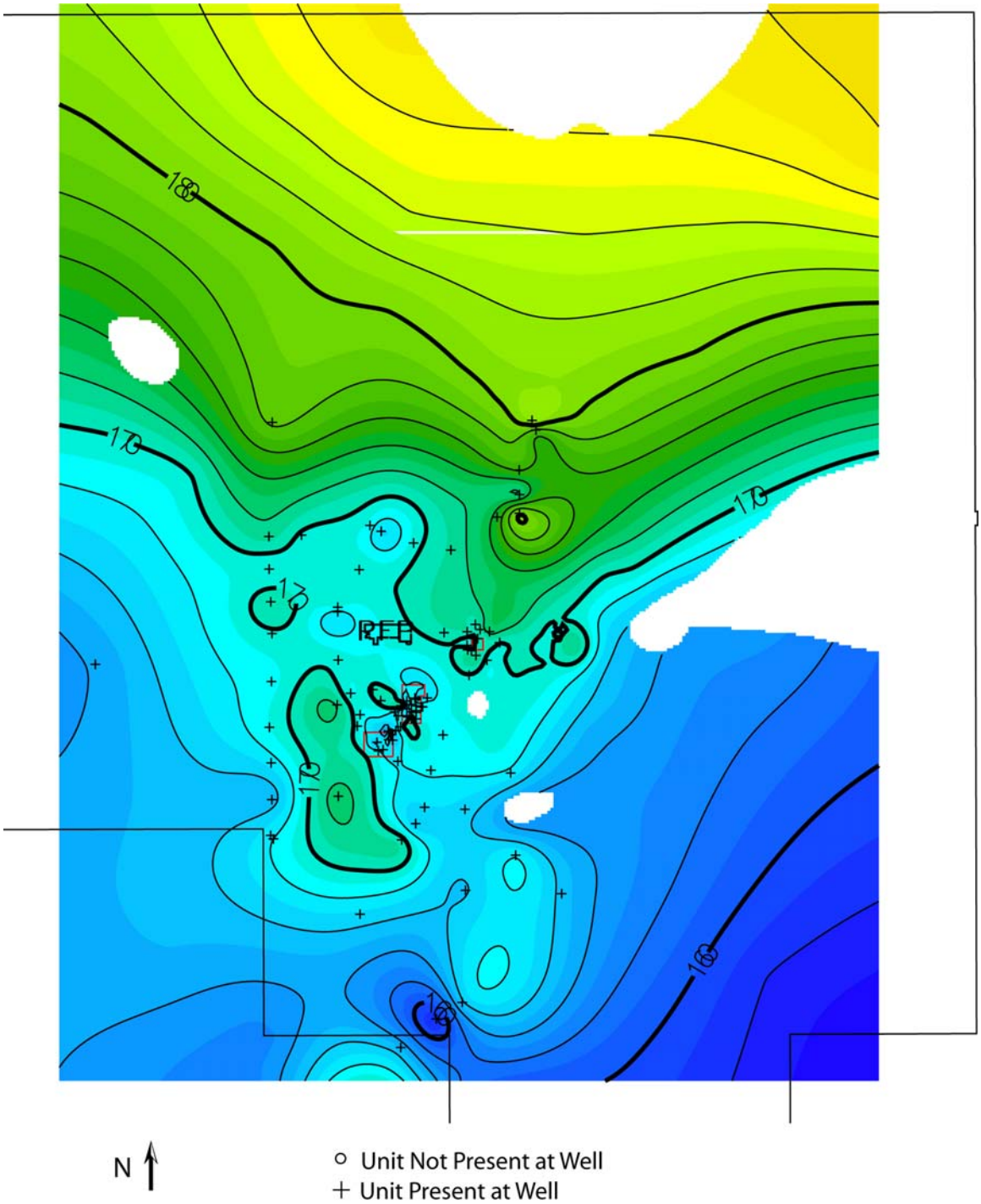

Figure 3.15. Top Elevation of Cold Creek Silt Layer

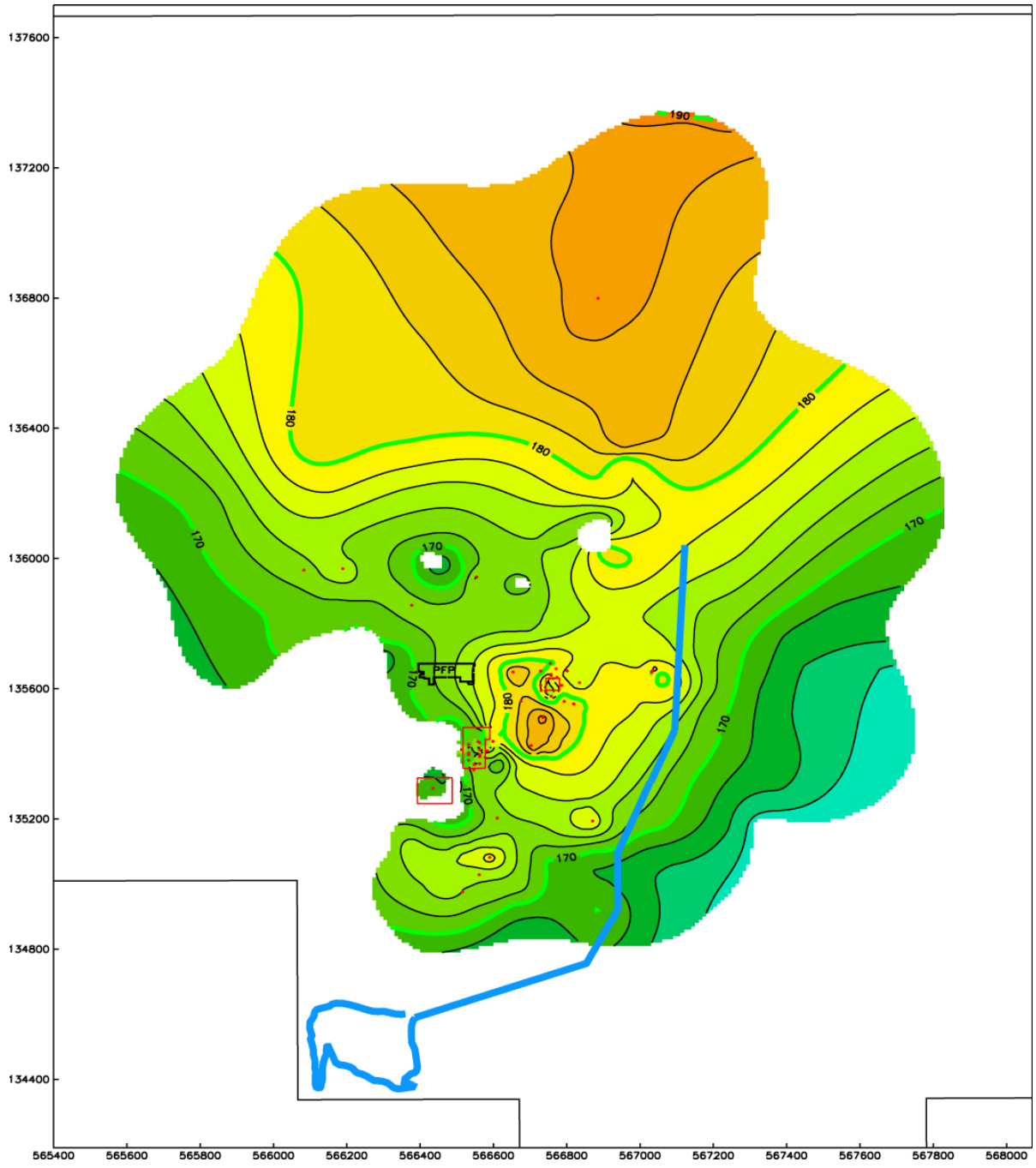

Figure 3.16. Top Elevation of Lower Hanford Sand Unit

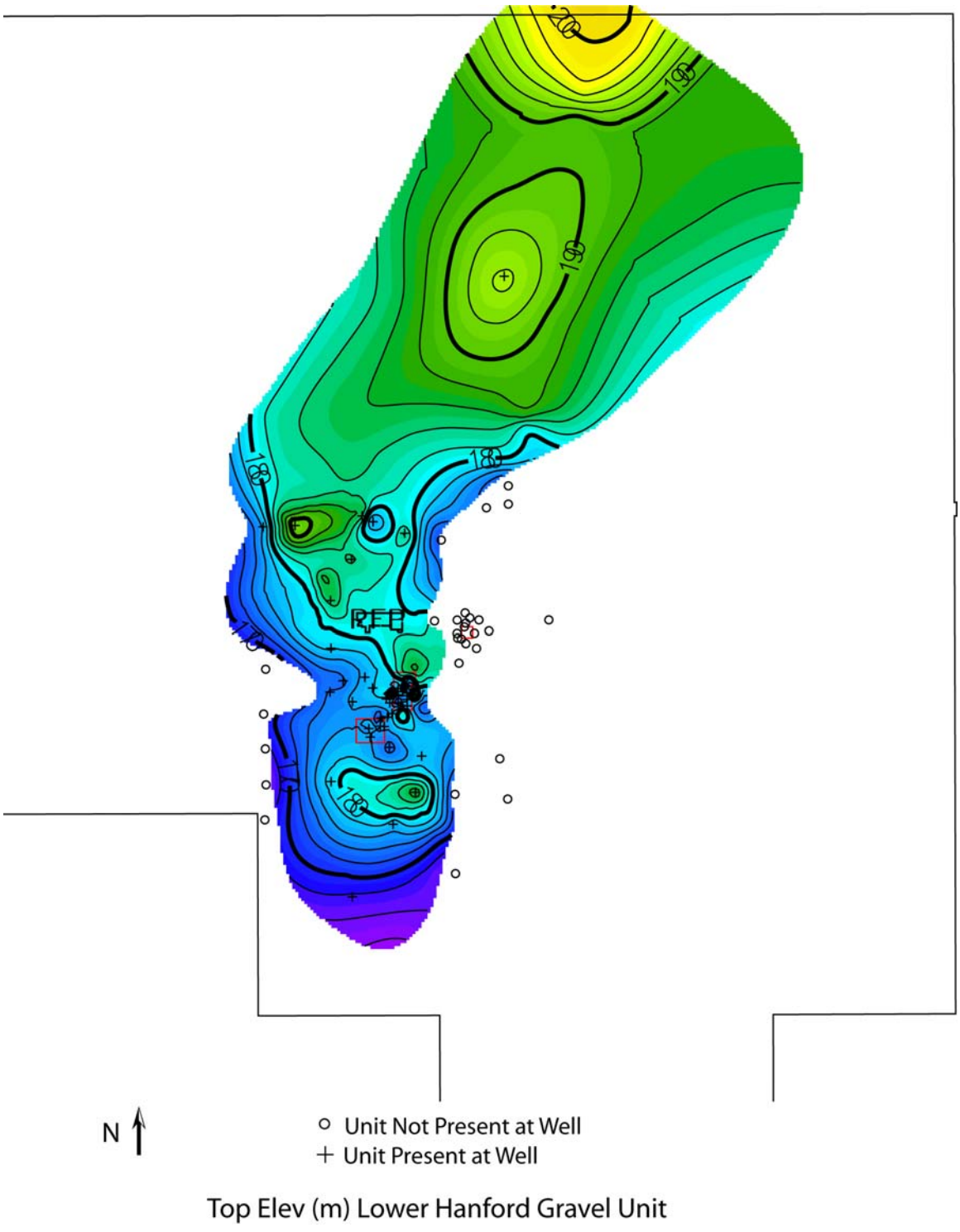

Figure 3.17. Top Elevation of Lower Hanford Gravel Unit

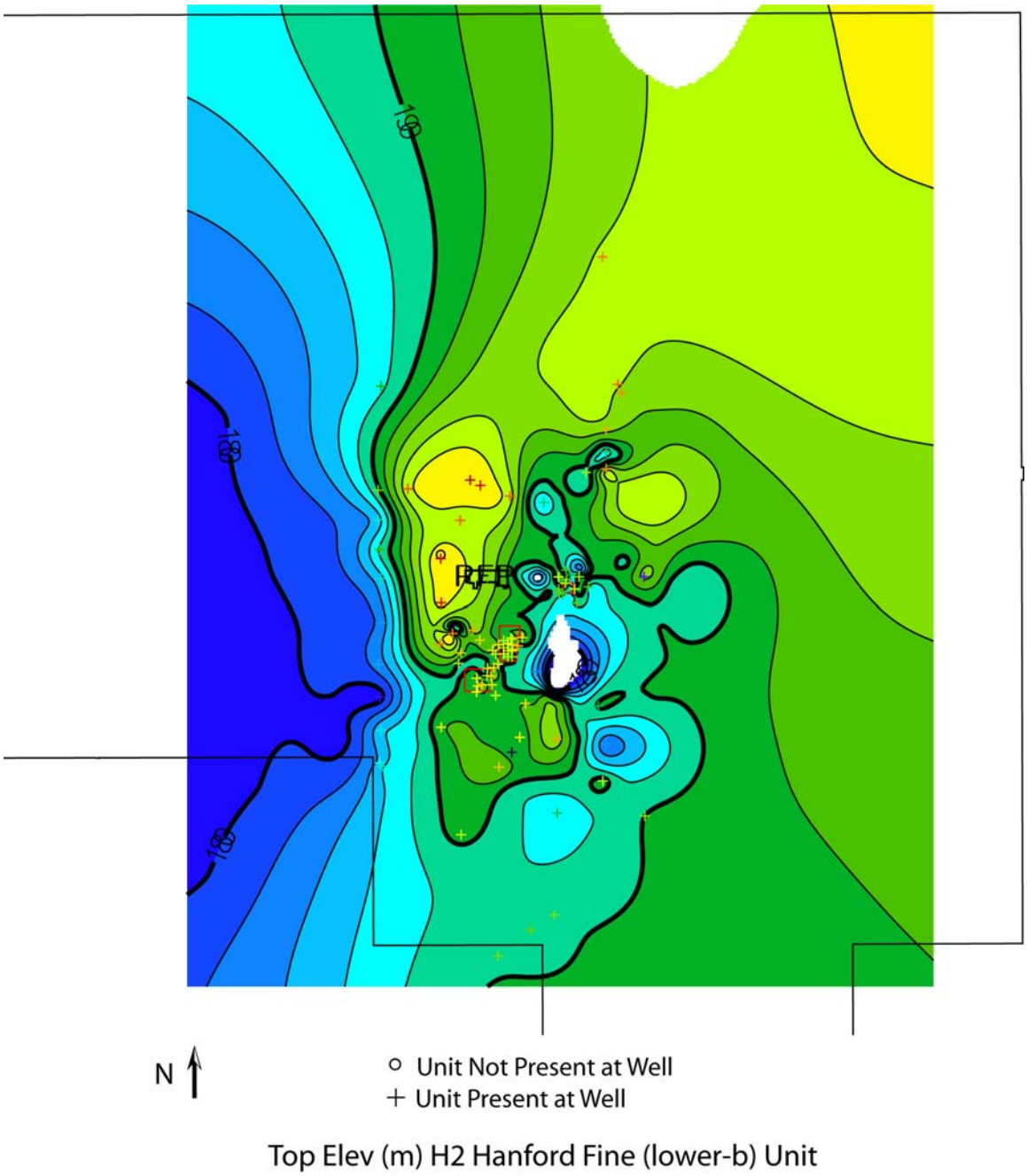

Figure 3.18. Top Elevation of Hanford Fine Unit

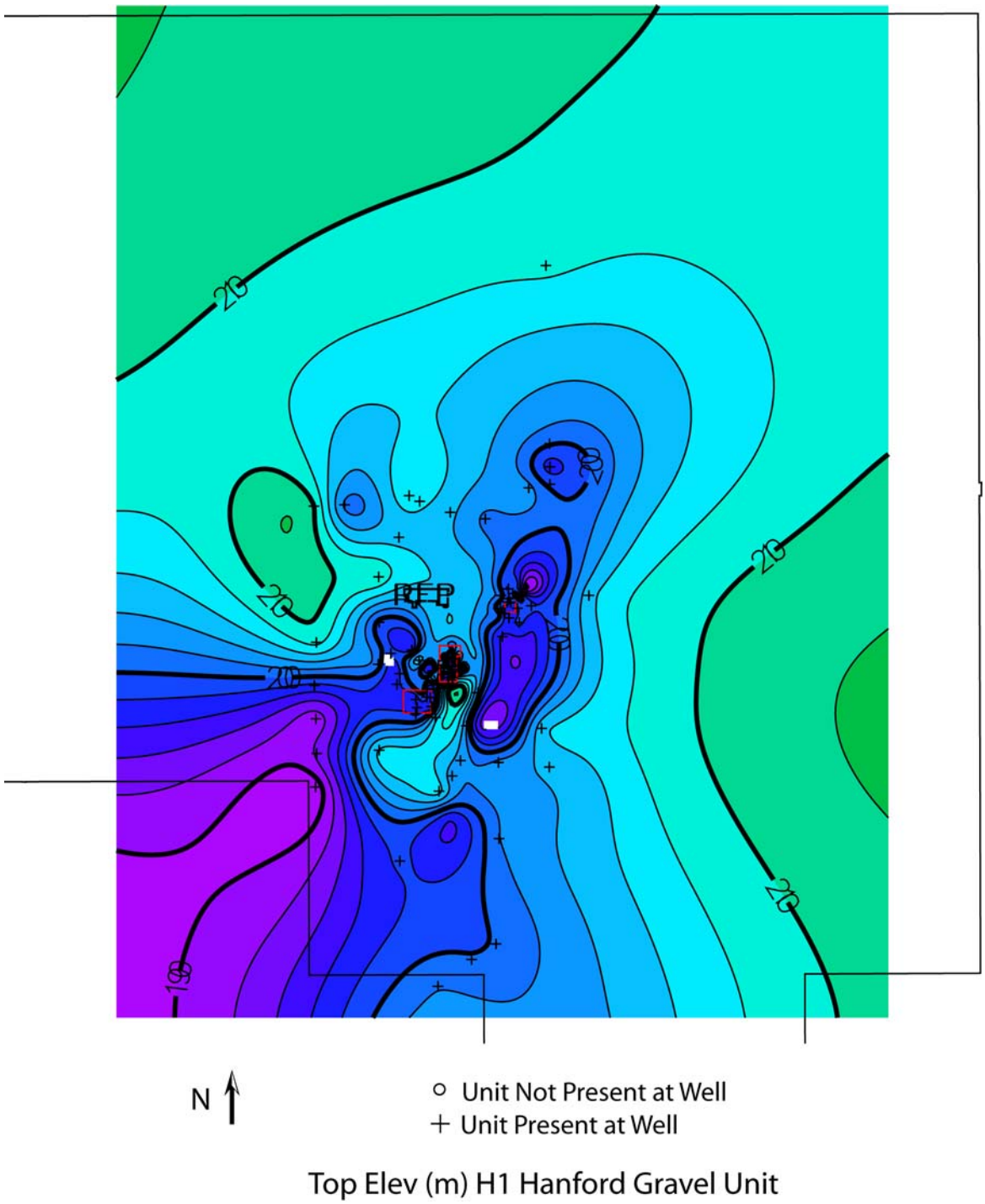

Figure 3.19. Top Elevation of H1 Hanford Gravel Unit

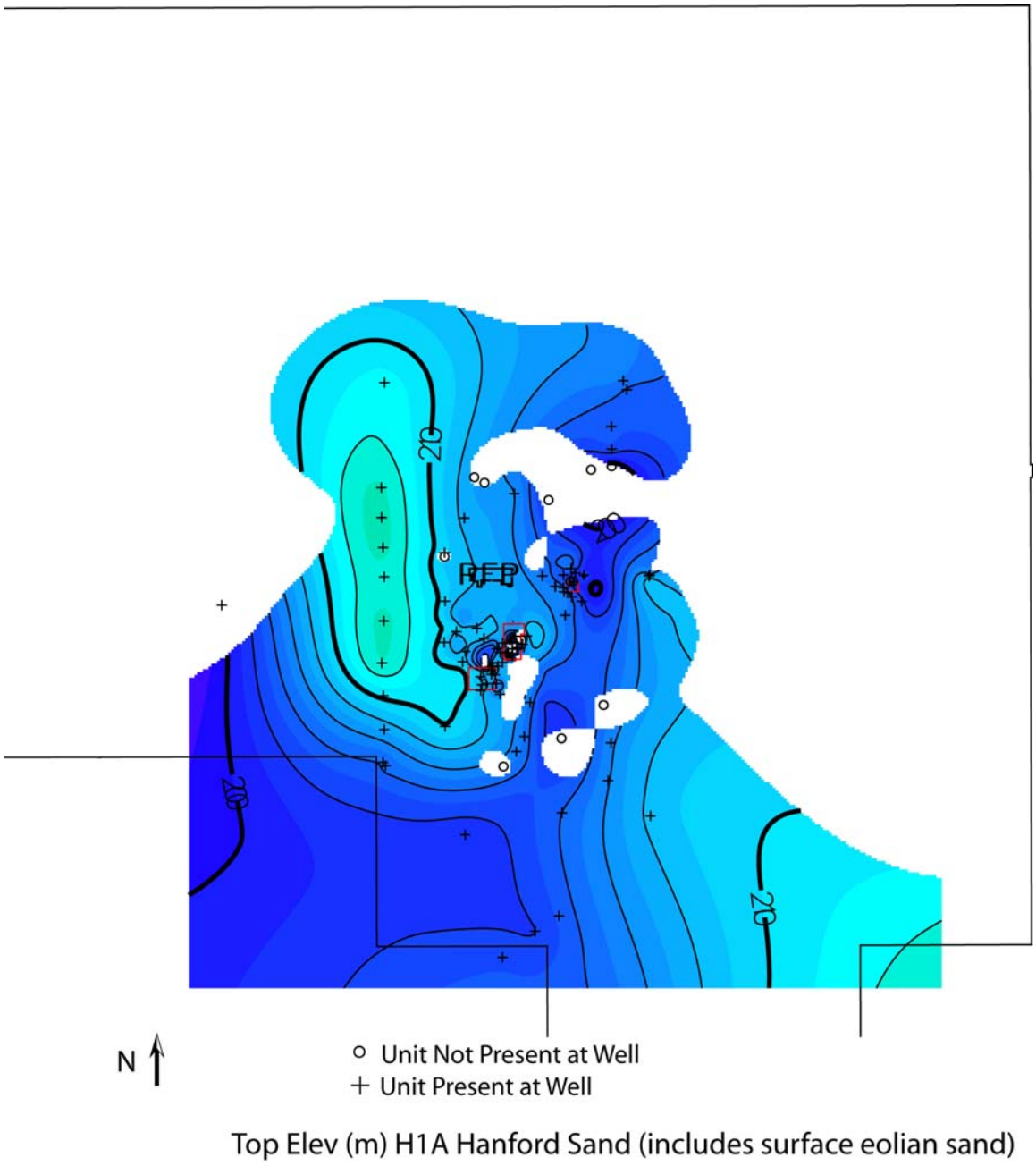

Figure 3.20. Top Elevation of H1A Hanford Sand Unit (includes surface eolian sand)

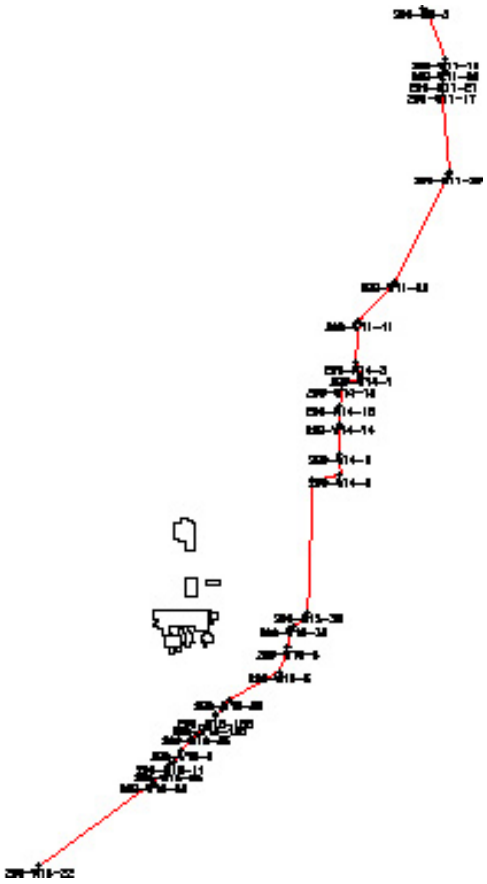

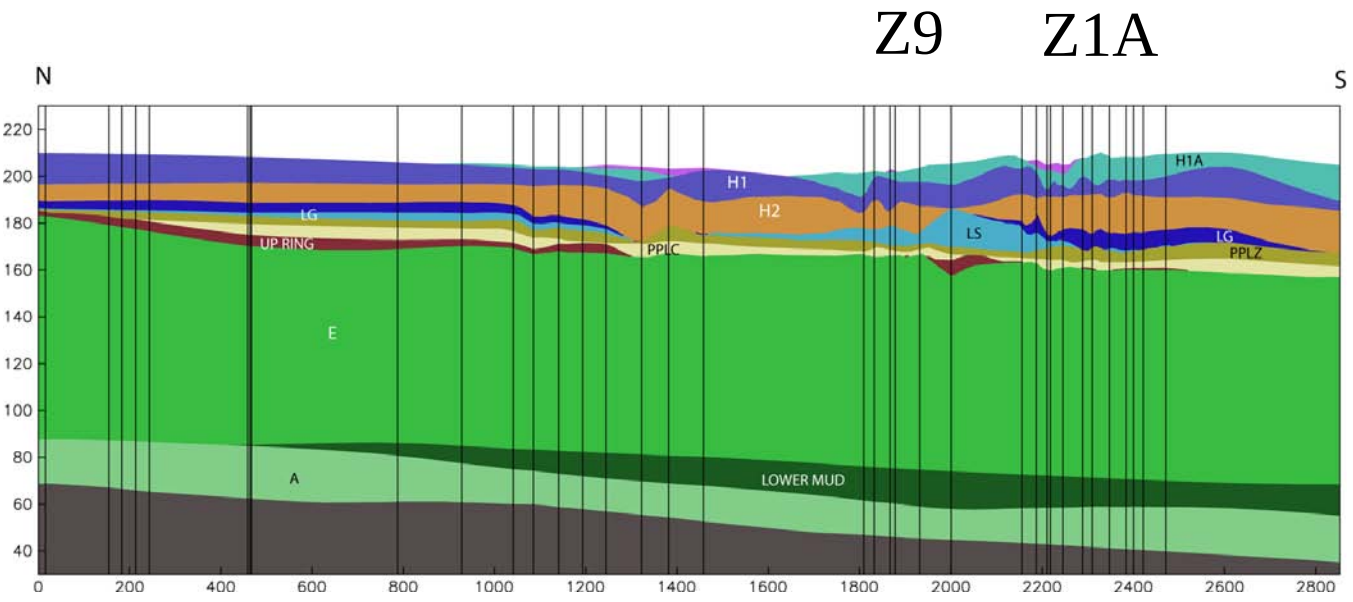

Figure 3.21. Selected North-South Cross Section

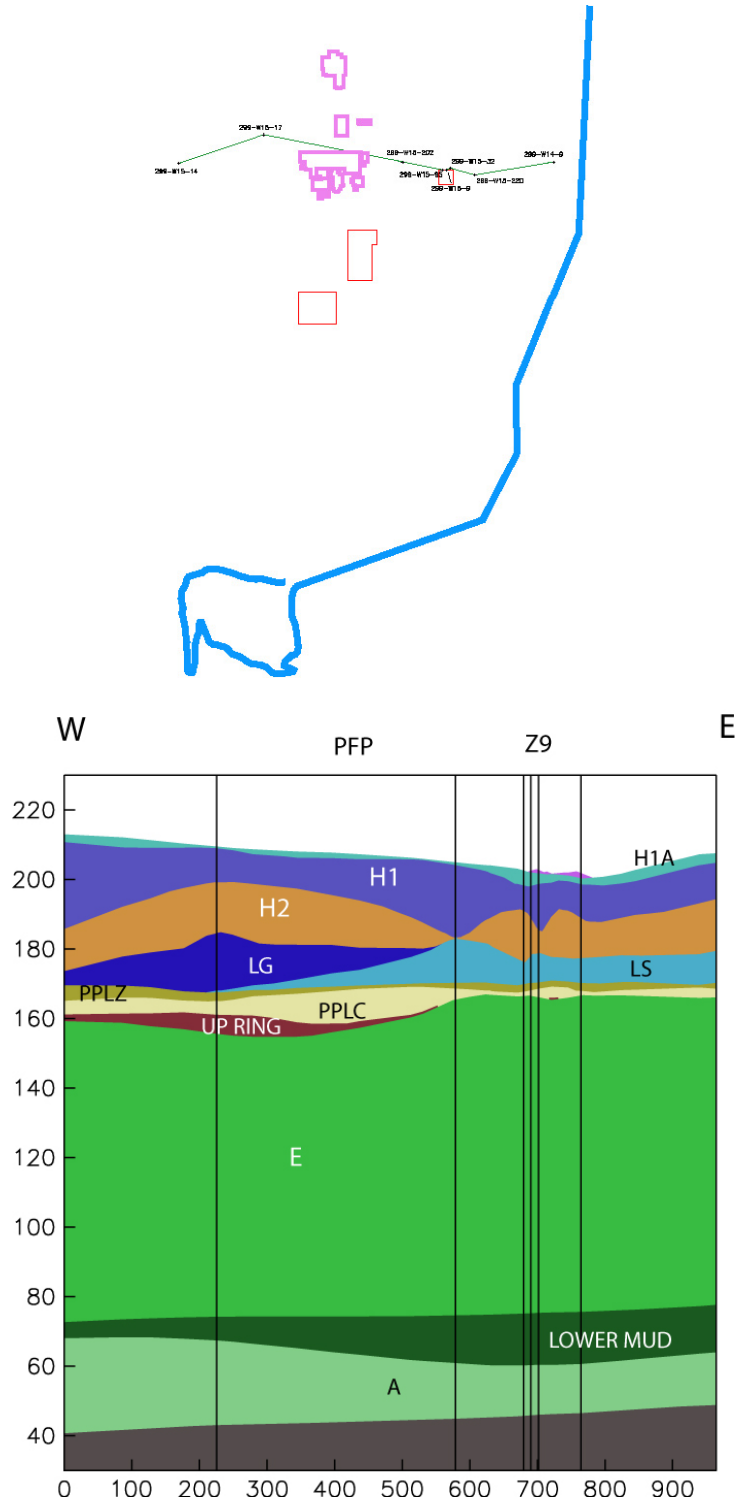

Figure 3.22. Selected West-East Cross Section

4.0 Disposal History

Data on liquid discharges were compiled for the regional area extending from T Tank Farm to U Pond as shown in Figure 3.1. Table 4.1 lists total liquid volumes and periods of operation for the discharge sites. This information is useful to understand the regional context for the modeling and will be of use for future larger scale modeling efforts. This information also includes the discharges that were used to set input parameters for modeling at the 216-Z-9 trench. For most sites, the numbers indicate aqueous phase volumes. For a few sites (e.g., 216-Z-9, 216-Z1-A, 216-Z18), the numbers are the combined volumes of aqueous phase and organic waste volumes. Table 4.2 lists the reference documents from which liquid discharge numbers were obtained. Most discharge information is on a yearly basis and has been evenly split over the duration of the year for which operation was known to occur. Table 4.3 lists geographical/physical information about the discharge sites. The full data sets contain 8,052 records (monthly data) for the 70 discharge sites. Time series information was used in conjunction with the state plane coordinates and site dimensions to determine liquid infiltration fluxes. The actual cross sectional area affected by liquid discharges must be estimated for many sites because of 1) discrepancies in the method of defining site dimensions (e.g., reporting a site boundary instead of the actual site or measuring the top of a crib that has an angled wall and a smaller bottom cross section) and 2) uncertainty about actual practice (e.g., was liquid pumped out of a pipe at the center of a crib versus flooding the whole bottom cross section of the crib; did liquid in a ditch infiltrate prior to reaching the destination pond; how often did a crib receive overflow liquid when connected in a series of cribs).

Volumes of organic waste disposal (carbon tetrachloride mixtures) are listed in Table 4.4 for 216-Z-9, Table 4.5 for 216-Z-1A, and Table 4.6 for 216-Z-18. For the 216-Z-9 trench, the volumes have been listed for both the minimum (8.3E4 L) and maximum (3.0E5 L) estimate of the total carbon tetrachloride inventory. Waste consisted of CT, TBP, DBBP, and lard oil.

Table 4.1. Summary Liquid Release Information for Sites Within the Study Area

Site Name	Earliest Date	Most Recent Date	Completeness	Total Volume (L)
200-W-52	Jan-63	Dec-63	12 out of 12 months	1,896
207-U	Jan-52	Dec-94	516 out of 516 months	13,054.8
216-T-12	Jan-54	Dec-54	12 out of 12 months	5,000,000
216-T-14	Jan-54	Dec-54	12 out of 12 months	1,000,000
216-T-15	Jan-54	Dec-54	12 out of 12 months	1,000,000
216-T-16	Jan-54	Dec-54	12 out of 12 months	1,000,000
216-T-17	Jan-54	Dec-54	12 out of 12 months	785,000
216-T-18	Jan-53	Dec-53	12 out of 12 months	1,000,000
216-T-19	Jan-51	Dec-76	312 out of 312 months	455,266,000
216-T-20	Jan-52	Dec-52	12 out of 12 months	18,900
216-T-21	Jan-54	Dec-54	12 out of 12 months	459,000
216-T-22	Jan-54	Dec-54	12 out of 12 months	1,530,000
216-T-23	Jan-54	Dec-54	12 out of 12 months	1,480,000
216-T-24	Jan-54	Dec-54	12 out of 12 months	1,530,000
216-T-25	Jan-54	Dec-54	12 out of 12 months	3,000,000
216-T-26	Jan-55	Dec-56	24 out of 24 months	12,004,000
216-T-27	Jan-65	Dec-65	12 out of 12 months	7,200,000
216-T-28	Jan-60	Dec-66	84 out of 84 months	42,337,400
216-T-32	Jan-46	Dec-52	84 out of 84 months	28,996,000
216-T-36	Jan-67	Dec-69	36 out of 36 months	523,040
216-T-4	Jan-44	Dec-78	420 out of 420 months	42,526,640,000
216-T-4-2	Jan-72	Dec-96	300 out of 300 months	448,826,000
216-T-5	Jan-55	Dec-55	12 out of 12 months	2,600,000
216-T-7	Jan-48	Dec-55	96 out of 96 months	110,053,000
216-U-10	Jan-44	Dec-96	636 out of 636 months	1.62843E+11
216-U-13	Jan-52	Dec-56	60 out of 60 months	11,376
216-U-14	Jan-76	Dec-96	252 out of 252 months	3,201,402,000
216-U-3	Jan-54	Dec-55	24 out of 24 months	791,200
216-Z-1:2	Jan-49	Dec-69	96 out of 96 months	33,700,996
216-Z-10	Jan-45	Dec-45	12 out of 12 months	1,000,000
216-Z-12	Jan-59	Dec-73	180 out of 180 months	281,344,000

Table 4.1. (contd)

Site Name	Earliest Date	Most Recent Date	Completeness	Total Volume (L)
216-Z-16	Jan-68	Dec-77	120 out of 120 months	101,966,100
216-Z-17	Jan-67	Dec-68	24 out of 24 months	36,790,000
216-Z-18	Jan-69	Dec-73	60 out of 60 months	3,858,000
216-Z-1A	Jan-49	Dec-59	132 out of 132 months	999,530
216-Z-1A-A	Jan-64	Dec-66	36 out of 36 months	1,900,700
216-Z-1A-B	Jan-66	Dec-67	24 out of 24 months	1,900,000
216-Z-1A-C	Jan-67	Dec-69	36 out of 36 months	1,407,700
216-Z-1D	Jan-44	Dec-59	192 out of 192 months	1,000,320
216-Z-20	Jan-79	Dec-96	216 out of 216 months	4,391,800,000
216-Z-3	Jan-52	Dec-59	96 out of 96 months	178,530,000
216-Z-4	Jan-45	Dec-45	12 out of 12 months	11,000
216-Z-5	Jan-45	Dec-47	36 out of 36 months	31,050,000
216-Z-6	Jan-45	Dec-45	12 out of 12 months	98,000
216-Z-7	Jan-47	Dec-66	* 156 out of 240 months *	79,881,030
216-Z-8	Jan-57	Dec-61	60 out of 60 months	9,584.1
216-Z-9	Jan-55	Dec-62	96 out of 96 months	4,090,200
241-T-101	Jan-69	Dec-69	12 out of 12 months	37,800
241-T-103	Jan-74	Dec-74	12 out of 12 months	11,400
241-T-106	Jan-73	Dec-73	12 out of 12 months	434,400
241-TX-107	Jan-77	Dec-77	12 out of 12 months	30,240
241-TY-103	Jan-71	Dec-71	12 out of 12 months	11,400
241-TY-105	Jan-60	Dec-60	12 out of 12 months	132,000
241-TY-106	Jan-58	Dec-58	12 out of 12 months	75,720
241-U-101	Jan-59	Dec-59	12 out of 12 months	114,000
241-U-104	Jan-56	Dec-56	12 out of 12 months	500,400
241-U-110	Jan-75	Dec-75	12 out of 12 months	24,840
241-U-112	Jan-68	Dec-68	12 out of 12 months	32,160
2607-W8	Jan-44	Dec-98	660 out of 660 months	100,375,000
2607-WA	Jan-68	Dec-00	396 out of 396 months	70,290,000
2607-WB	Jan-63	Dec-98	432 out of 432 months	31,323,600
2607-WL	Jan-62	Dec-98	444 out of 444 months	141,081,000
2607-Z	Jan-49	Dec-98	600 out of 600 months	414,400,000

Table 4.1. (contd)

Site Name	Earliest Date	Most Recent Date	Completeness	Total Volume (L)
2607-Z1	Jan-58	Dec-98	492 out of 492 months	38,909,000
284-WB	Jan-79	Dec-96	216 out of 216 months	1,687,800,000
UPR-200-W-135	Jan-54	Dec-54	12 out of 12 months	3,792
UPR-200-W-150	Jan-73	Dec-73	12 out of 12 months	11,400,000
UPR-200-W-151	Jan-74	Dec-74	12 out of 12 months	5,304
UPR-200-W-29	Jan-54	Dec-54	12 out of 12 months	3,792
UPR-200-W-97	Jan-66	Dec-66	12 out of 12 months	999.6

Table 4.2. Sources for Liquid Release Information and Subjective Indication of Data Quality

Site Name	Earliest Date	Most Recent Date	Data Quality Indicator	Reference Source
200-W-52	Jan-63	Dec-63	Unknown	WIDS Database (R. L. Aaberg)
207-U	Jan-52	Dec-94	Unknown	WIDS Database (R. L. Aaberg)
216-T-12	Jan-54	Dec-54	Good	Anderson (1976) (Table 1, page 37)
216-T-12	Nov-54	Nov-54	Avg-Known	Anderson (1976) (Table 1, page 37)
216-T-14	Jan-54	Dec-54	Good	Anderson (1976) (Table 1, page 37)
216-T-15	Jan-54	Dec-54	Good	Anderson (1976) (Table 1, page 38)
216-T-16	Jan-54	Dec-54	Good	Anderson (1976) (Table 1, page 38)
216-T-17	Jan-54	Dec-54	Good	Anderson (1976) (Table 1, page 38)
216-T-17	Feb-54	Jun-54	Avg-Known	Anderson (1976) (Table 1, page 38)
216-T-18	Jan-53	Dec-53	Good	Anderson (1976) (Table 1, page 38)
216-T-19	Jan-51	Dec-75	Avg-Known	Anderson (1976) (Table 1, page 39)
216-T-19	Jan-51	Dec-75	Good	Anderson (1976) (Table 1, page 39)
216-T-19	Jan-76	Apr-76	Good Estimate	Mirabella (1977) (Table 26, page 219) Sum of reported monthly volume plus 1/12 the adjustment volume
216-T-19	May-76	Dec-76	Good Estimate	Mirabella (1977) (Table 26, page 219) Adjustment assumed not to apply to zero discharge months
216-T-20	Jan-52	Dec-52	Good	Anderson (1976) (Table 1, page 39)
216-T-21	Jan-54	Dec-54	Avg-Known	Anderson (1976) (Table 1, page 39)
216-T-21	Jan-54	Dec-54	Good	Anderson (1976) (Table 1, page 39)
216-T-22	Jan-54	Dec-54	Avg-Known	Anderson (1976) (Table 1, page 39)

Table 4.2. (contd)

Site Name	Earliest Date	Most Recent Date	Data Quality Indicator	Reference Source
216-T-22	Jan-54	Dec-54	Good	Anderson (1976) (Table 1, page 39)
216-T-23	Jan-54	Dec-54	Avg-Known	Anderson (1976) (Table 1, page 40)
216-T-23	Jan-54	Dec-54	Good	Anderson (1976) (Table 1, page 40)
216-T-24	Jan-54	Dec-54	Good	Anderson (1976) (Table 1, page 40)
216-T-25	Jan-54	Dec-54	Good	Anderson (1976) (Table 1, page 40)
216-T-26	Jan-55	Dec-56	Avg-Known	Anderson (1976) (Table 1, page 40)
216-T-26	Jan-55	Dec-56	Good	Anderson (1976) (Table 1, page 40)
216-T-27	Jan-65	Dec-65	Avg-Known	Anderson (1976) (Table 1, page 40)
216-T-27	Jan-65	Dec-65	Good	Anderson (1976) (Table 1, page 40)
216-T-28	Jan-60	Dec-66	Avg-Known	Anderson (1976) (Table 1, page 41)
216-T-28	Jan-60	Dec-66	Good	Anderson (1976) (Table 1, page 41)
216-T-32	Jan-46	Dec-52	Avg-Known	Anderson (1976) (Table 1, page 41)
216-T-32	Jan-46	Dec-52	Good	Anderson (1976) (Table 1, page 41)
216-T-36	Jan-67	Dec-69	Avg-Known	Anderson (1976) (Table 1, page 42)
216-T-36	Jan-67	Dec-69	Good	Anderson (1976) (Table 1, page 42)
216-T-4	Jan-44	Oct-44	Good	Anderson (1976) (Table 1, page 36)
216-T-4	Nov-44	Dec-75	Avg-Known	Anderson (1976) (Table 1, page 36)
216-T-4	Jan-76	Apr-76	Good Estimate	Mirabella (1977) (Table 12, page 175) Sum of reported monthly volume plus 1/4 the adjustment volume
216-T-4	May-76	Dec-76	Good	Mirabella (1977) (Table 12, page 175) Removed from service April 1976
216-T-4	Jan-77	Dec-77	Good	Anderson and Poremba (1978) (Table 1-A, page 16) Removed from service April 1976
216-T-4	Jan-78	Dec-78	Good	Anderson and Poremba (1979) (Table 1, page 17) Removed from service April 1976
216-T-4-2	Jan-72	Dec-78		Estimated using 1979 data
216-T-4-2	Jan-79	May-95	Estimate	WHC (1990) (Table 2.19-1) maximum effluent discharge rate
216-T-4-2	Jun-95	Dec-96	Good	Stream connected to 200 Area TEDF on 5/16/95 ('M-17 Phase I and Phase II Streams' list provided by Steve Lowe [WHC])
216-T-5	Jan-55	Dec-55	Good	Anderson (1976) (Table 1, page 36)
216-T-7	Jan-48	Dec-55	Avg-Known	Anderson (1976) (Table 1, page 37)

Table 4.2. (contd)

Site Name	Earliest Date	Most Recent Date	Data Quality Indicator	Reference Source
216-T-7	Jan-48	Dec-55	Good	Anderson (1976) (Table 1, page 37)
216-U-10	Jan-44	Dec-75	Avg-Known	Anderson (1976) (Table 1, page 45)
216-U-10	Jan-44	Dec-75	Good	Anderson (1976) (Table 1, page 45)
216-U-10	Jan-76	Dec-76	Good Estimate	Mirabella (1977) (Table 18, page 193) Sum of reported monthly volume and 1/12 the adjustment volume
216-U-10	Jan-77	Dec-77	Good Estimate	Anderson and Poremba (1978) (Table 19, page 196) Sum of reported monthly volume and 1/12 the adjustment volume
216-U-10	Jan-78	Dec-78	Good Estimate	Anderson and Poremba (1979) (Table 19, page 196) Sum of reported monthly volume and 1/12 the adjustment volume
216-U-10	Jan-79	Dec-79	Good Estimate	Sliger (1980) (Table 19) Sum of reported monthly volume and 1/12 the adjustment volume
216-U-10	Jan-80	Dec-80	Good Estimate	Aldrich and Sliger (1981) (Table 19) Sum of reported monthly volume and 1/12 the adjustment volume
216-U-10	Jan-81	Dec-81	Good Estimate	Sliger (1982) (Table 19) Sum of reported monthly volume and 1/12 the adjustment volume
216-U-10	Jan-82	Dec-82	Good Estimate	Sliger (1983) (Table 16) Sum of reported monthly volume and 1/12 the adjustment volume
216-U-10	Jan-83	Dec-83	Good Estimate	Sliger (1984) (Table 16) Sum of reported monthly volume and 1/12 the adjustment volume
216-U-10	Jan-84	Dec-84	Good Estimate	Aldrich (1985) (Table 17) Sum of reported monthly volume and 1/12 the adjustment volume
216-U-10	Jan-85	Dec-96	Good	Fuchs et al. (1986) (page 27)
216-U-13	Jan-52	Dec-56	Avg-Known	Anderson (1976) (Table 1, page 46)
216-U-13	Jan-52	Dec-56	Good	Anderson (1976) (Table 1, page 46)
216-U-14	Jan-76	Dec-84	Estimate	Feeder ditch to 216-U-10 Pond. Thus, discharges to this release site are reported as discharges to 216-U-10 Pond prior to January 1985.
216-U-14	Jan-85	Dec-85	Good	Aldrich (1986) (Table 15)

Table 4.2. (contd)

Site Name	Earliest Date	Most Recent Date	Data Quality Indicator	Reference Source
216-U-14	Jan-86	Dec-86	Good	Aldrich (1986) (Table 14)
216-U-14	Jan-87	Dec-87	Good	Coony et al. (1988) (Sum of tables C-17 and C-20)
216-U-14	Jan-88	Dec-88	Good	Coony and Thomas (1989) (Table C-26)
216-U-14	Jan-89	Dec-89	Good	Brown et al. (1990) (Table C-27)
216-U-14	Jan-90	Dec-90	Good	Sum of Waste Streams H102 and H122 - Provided by S. P. Thomas (WHC) from the Environmental Release Summary Database and matched to release site using WHC (1992a).
216-U-14	Jan-91	Dec-91	Good	Sum of Waste Streams H102 and H122 - Provided by S. P. Thomas (WHC) from the Environmental Release Summary Database and matched to release site using WHC (1992b).
216-U-14	Jan-92	Dec-93	Good	Waste Stream H102 - Provided by S. P. Thomas (WHC) from the Environmental Release Summary Database and matched to release site using WHC (1993).
216-U-14	Jan-94	Nov-94	Good	Waste Stream H102 - Provided by Brian Gleckler (WHC) from the Environmental Release Summary Database and matched to release site using WHC (1993).
216-U-14	Dec-94	Jun-95	Poor	The last monthly data I have from Brian Gleckler (WHC) is 11/94. Stream was eliminated by 5/16/95 ('M-17 Phase I and Phase II Streams' list provided by Steve Lowe [WHC])
216-U-14	Jul-95	Dec-96	Good	Stream was eliminated by 5/16/95 ('M-17 Phase I and Phase II Streams' list provided by Steve Lowe [WHC])
216-U-3	Jan-54	Dec-55	Avg-Known	Anderson (1976) (Table 1, page 43)
216-U-3	Jan-54	Dec-55	Good	Anderson (1976) (Table 1, page 43)
216-Z-1:2	Jan-49	Dec-69	Avg-Known	Anderson (1976) (Table 1, page 47)
216-Z-1:2	Jan-49	Dec-69	Good	Anderson (1976) (Table 1, page 47)
216-Z-10	Jan-45	Dec-45	Avg-Known	Anderson (1976) (Table 1, page 50)
216-Z-10	Jan-45	Dec-45	Good	Anderson (1976) (Table 1, page 50)
216-Z-12	Jan-59	Dec-73	Avg-Known	Anderson (1976) (Table 1, page 51)
216-Z-12	Jan-59	Dec-73	Good	Anderson (1976) (Table 1, page 51)
216-Z-16	Jan-68	Dec-75	Avg-Known	Anderson (1976) (Table 1, page 51)

Table 4.2. (contd)

Site Name	Earliest Date	Most Recent Date	Data Quality Indicator	Reference Source
216-Z-16	Jan-68	Dec-75	Good	Anderson (1976) (Table 1, page 51)
216-Z-16	Jan-76	Dec-76	Good	Mirabella (1977) (Table 27, page 220)
216-Z-16	Jan-77	Dec-77	Good	Anderson and Poremba (1978) (Table 28, page 223)
216-Z-17	Jan-67	Dec-68	Avg-Known	Anderson (1976) (Table 1, page 51)
216-Z-17	Jan-67	Dec-68	Good	Anderson (1976) (Table 1, page 51)
216-Z-18	Jan-69	Dec-73	Avg-Known	Anderson (1976) (Table 1, page 52)
216-Z-18	Jan-69	Dec-73	Good	Anderson (1976) (Table 1, page 52)
216-Z-1A	Jan-49	Dec-59	Avg-Known	Anderson (1976) (Table 1, page 47)
216-Z-1A	Jan-49	Dec-59	Good	Anderson (1976) (Table 1, page 47)
216-Z-1A-A	Jan-64	Dec-66	Avg-Known	Anderson (1976) (Table 1, page 47)
216-Z-1A-A	Jan-64	Dec-66	Good	Anderson (1976) (Table 1, page 47)
216-Z-1A-B	Jan-66	Dec-67	Avg-Known	Anderson (1976) (Table 1, page 48)
216-Z-1A-B	Jan-66	Dec-67	Good	Anderson (1976) (Table 1, page 48)
216-Z-1A-C	Jan-67	Dec-69	Avg-Known	Anderson (1976) (Table 1, page 48)
216-Z-1A-C	Jan-67	Dec-69	Good	Anderson (1976) (Table 1, page 48)
216-Z-1D	Jan-44	Dec-59	Unknown	WIDS Database (R. L. Aaberg)
216-Z-20	Jan-79	Dec-80	Good	WHC (1990) (page 2.23-1)
216-Z-20	Jan-81	Dec-81	Good	Sliger (1982) (Sum of Tables 29 and 30)
216-Z-20	Jan-82	Dec-82	Good	Sliger (1983) (Sum of Tables 26 and 27)
216-Z-20	Jan-83	Dec-83	Good	Aldrich (1984) (Sum of Tables 27 and 28)
216-Z-20	Jan-84	Dec-84	Good Estimate	Aldrich (1985) (Table 29) plus 1/12th the adjustment volume (see Z20-ADJ.XLS)
216-Z-20	Jan-85	Dec-85	Good Estimate	Aldrich (1986) (Table 30) plus 1/12th the adjustment volume (see Z20-ADJ.XLS)
216-Z-20	Jan-86	Dec-86	Good Estimate	Aldrich (1987) (Table 25) plus 1/12th the adjustment volume (see Z20-ADJ.XLS)
216-Z-20	Jan-87	Dec-87	Good Estimate	Coony et al. (1988) (Table C-15) plus 1/12th the adjustment volume (see Z20-ADJ.XLS)
216-Z-20	Jan-88	Dec-88	Good Estimate	Coony and Thomas (1989) (Table C-22) plus 1/12th the adjustment volume (see Z20-ADJ.XLS)
216-Z-20	Jan-89	Dec-89	Good Estimate	Brown et al. (1990) (Table C-23) plus 1/12th the adjustment volume (see Z20-ADJ.XLS)

Table 4.2. (contd)

Site Name	Earliest Date	Most Recent Date	Data Quality Indicator	Reference Source
216-Z-20	Jan-90	Dec-90	Good Estimate	Waste Stream H103 - Provided by S. P. Thomas (WHC) from the Environmental Release Summary Database plus 1/12 the adjustment volume (see Z20-ADJ.XLS) and matched to release site using WHC (1992a).
216-Z-20	Jan-91	Dec-91	Estimate	Waste Stream H103 - Provided by S. P. Thomas (WHC) from the Environmental Release Summary Database plus 1/12th an average adjustment volume (see Z20-ADJ.XLS) and matched to release site using WHC (1992b).
216-Z-20	Jan-92	Dec-93	Estimate	Waste Stream H103 - Provided by S. P. Thomas (WHC) from the Environmental Release Summary Database plus 1/12th an average adjustment volume (see Z20-ADJ.XLS) and matched to release site using WHC (1993).
216-Z-20	Jan-94	May-95	Estimate	Waste Stream H103 - Provided by Brian Gleckler (WHC) from the Environmental Release Summary Database plus 1/12th an average adjustment volume (see Z20-ADJ.XLS) and matched to release site using WHC (1993).
216-Z-20	Jun-95	Dec-95	Good	Waste Stream H103 - Provided by Brian Gleckler (WHC) from the Environmental Release Summary Database and matched to release site using WHC (1993).
216-Z-20	Jan-96	Dec-96	Good	Waste stream connected to 200 Area TEDF on 5/22/95 ['M-17 Phase I and II Streams' table provided by Steve Lowe (RFSH)]
216-Z-3	Jan-52	Dec-59	Avg-Known	Anderson (1976) (Table 1, page 48)
216-Z-3	Jan-52	Dec-59	Good	Anderson (1976) (Table 1, page 48)
216-Z-4	Jan-45	Dec-45	Good	Anderson (1976) (Table 1, page 48)
216-Z-4	Jun-45	Jun-45	Estimate	Anderson (1976) (Table 1, page 48) "less than"
216-Z-5	Jan-45	Dec-47	Avg-Known	Anderson (1976) (Table 1, page 49)
216-Z-5	Jan-45	Dec-47	Good	Anderson (1976) (Table 1, page 49)
216-Z-6	Jan-45	Dec-45	Good	Anderson (1976) (Table 1, page 49)
216-Z-7	Jan-47	Dec-66	Avg-Known	Anderson (1976) (Table 1, page 49)
216-Z-7	Jan-47	Dec-66	Good	Anderson (1976) (Table 1, page 49)
216-Z-8	Jan-57	Dec-61	Avg-Known	Anderson (1976) (Table 1, page 50)
216-Z-8	Jan-57	Dec-61	Good	Anderson (1976) (Table 1, page 50)

Table 4.2. (contd)

Site Name	Earliest Date	Most Recent Date	Data Quality Indicator	Reference Source
216-Z-9	Jan-55	Dec-62	Avg-Known	Anderson (1976) (Table 1, page 50)
216-Z-9	Jan-55	Dec-62	Good	Anderson (1976) (Table 1, page 50)
241-T-101	Jan-69	Dec-69	Unknown	WIDS Database (R. L. Aaberg)
241-T-103	Jan-74	Dec-74	Unknown	WIDS Database (R. L. Aaberg)
241-T-106	Jan-73	Dec-73	Unknown	WIDS Database (R. L. Aaberg)
241-TX-107	Jan-77	Dec-77	Unknown	WIDS Database (R. L. Aaberg)
241-TY-103	Jan-71	Dec-71	Unknown	WIDS Database (R. L. Aaberg)
241-TY-105	Jan-60	Dec-60	Unknown	WIDS Database (R. L. Aaberg)
241-TY-106	Jan-58	Dec-58	Unknown	WIDS Database (R. L. Aaberg)
241-U-101	Jan-59	Dec-59	Unknown	WIDS Database (R. L. Aaberg)
241-U-104	Jan-56	Dec-56	Unknown	WIDS Database (R. L. Aaberg)
241-U-110	Jan-75	Dec-75	Unknown	WIDS Database (R. L. Aaberg)
241-U-112	Jan-68	Dec-68	Unknown	WIDS Database (R. L. Aaberg)
2607-W8	Jan-44	Dec-98	Fair	WIDS Database (R. L. Aaberg)
2607-WA	Jan-68	Dec-00	Fair	WIDS Database (R. L. Aaberg)
2607-WB	Jan-63	Dec-98	Fair	WIDS Database (R. L. Aaberg)
2607-WL	Jan-62	Dec-98	Fair	WIDS Database (R. L. Aaberg)
2607-Z	Jan-49	Dec-98	Fair	WIDS Database (R. L. Aaberg)
2607-Z1	Jan-58	Dec-98	Fair	WIDS Database (R. L. Aaberg)
284-WB	Jan-79	Dec-83	Good	WHC (1990) (page 2.24-1)
284-WB	Jan-84	May-95	Estimate	WHC (1990) (Table 2.24-1)
284-WB	Jun-95	Dec-95	Good	Stream connected to 200 Area TEDF by 5/26/95 ('M-17 Phase I and Phase II Streams' list provided by Steve Lowe [WHC])
284-WB	Jan-96	Dec-96	Good	Stream connected to 200 Area TEDF by 5/26/95 ('M-17 Phase I and Phase II Streams' list provided by Steve Lowe [RFSH])
UPR-200-W-135	Jan-54	Dec-54	Unknown	WIDS Database (R. L. Aaberg)

Table 4.2. (contd)

Site Name	Earliest Date	Most Recent Date	Data Quality Indicator	Reference Source
UPR-200-W-150	Jan-73	Dec-73	Unknown	WIDS Database (R. L. Aaberg)
UPR-200-W-151	Jan-74	Dec-74	Unknown	WIDS Database (R. L. Aaberg)
UPR-200-W-29	Jan-54	Dec-54	Unknown	WIDS Database (R. L. Aaberg)
UPR-200-W-97	Jan-66	Dec-66	Unknown	WIDS Database (R. L. Aaberg)

Table 4.3. Geographical/Physical Information for Sites Within the Study Area

Site Name	E-W State Plane (m)	N-S State Plane (m)	Site Type	Length (m)	Width (m)	Depth/ Height (m)	Diameter (m)	Area (m^2)
200-W-52	566,741.3	136,656.9	Crib	3.6576	3.6576	7.9248		13.37804
207-U	566,973.3	135,044	Retention Basin	74.9808	37.4904	1.9812		2,832.8
216-T-12	566,992.6	136,737	Trench	4.572	3.048	2.4384		13.93546
216-T-14	566,948.1	136,839	Trench	83.82	3.048			255.4834
216-T-15	566,975.6	136,836	Trench	83.82	3.048			255.4834
216-T-16	567,003	136,836.1	Trench	83.82	3.048			255.4834
216-T-17	567,018.3	136,836.2	Trench	83.82	3.048			255.4834
216-T-18	566,949.4	136,460.2	Crib	9.144	9.144	4.572		83.61274
216-T-19	566,849.4	135,974	Crib	118.872	25.908			3,079.736
216-T-20	567,119.2	136,074.4	Trench	3.048	3.048			9.290304
216-T-21	566,555.3	136,118.7	Trench	73.152	3.048	3.048		222.9673
216-T-22	566,555.3	136,146.1	Trench	73.152	3.048	3.048		222.9673
216-T-23	566,555.2	136,173.6	Trench	73.152	3.048	3.048		222.9673
216-T-24	566,555	136,201	Trench	73.152	3.048	3.048		222.9673
216-T-25	566,545.9	136,228.5	Trench	54.864	3.048	3.048		167.2255
216-T-26	566,932.1	136,398.7	Crib	9.144	9.144	4.572		83.61274
216-T-27	566,932.5	136,372.8	Crib	9.144	9.144	4.572		83.61274
216-T-28	566,932.5	136,347.2	Crib	9.144	9.144	4.572		83.61274
216-T-32	566,719.3	136,696.1	Crib	20.7264	4.2672	7.9248		88.4437

Table 4.3. (contd)

Site Name	E-W State Plane (m)	N-S State Plane (m)	Site Type	Length (m)	Width (m)	Depth/ Height (m)	Diameter (m)	Area (m^2)
216-T-36	566,702	136,596	Crib	48.768	3.048	4.572		148.6449
216-T-4-2	566,758.43	137,042.02	Ditch	533.4	2.4384	1.2192		1,300.643
216-T-4A	566,533.0	137,099.09	Pond	548.64	182.88			100,335.3
216-T-4B	566,522.63	137,271.25	Pond					6,100
216-T-5	566,666.5	136,727.1	Trench	15.24	3.048	3.6576		46.45152
216-T-7	566,685	136,659.6	Crib	94.488	25.6032			2,419.195
216-U-10	566,371.8	134623.9	Pond					121,405.7
216-U-13	566,722.6	135,067.8	Trench	60.96	6.096	5.4864		371.6122
216-U-14	566,945.4	134,891.6	Ditch	1,731.264	2.4384			4,224.27
216-U-3	566,844.8	134,927.9	French Drain			3.6576	1.8288	2.626772
216-Z-1:2	566,547.4	135,469.2	Crib	4.2672	4.2672	6.4008		18.209
216-Z-10	566,566.5	135,897.3	Injection/ Reverse Well			45.72	0.1524	0.018241
216-Z-12	566,365.1	135,422.8	Crib	91.44	6.096	5.7912		557.4183
216-Z-16	566,430.1	135,991.3	Crib	54.864	3.048	4.8768		167.2255
216-Z-17	566,603.4	135,862.6	Trench	60.96	7.9248	2.4384		483.0958
216-Z-18	566,440.1	135,286.5	Crib	63.0936	3.048	5.4864		192.3093
216-Z-1A	566,549	135,418.9	Tilefield	84	35	5.8		2,940
216-Z-1A-A	566,549	135,418.9	Drain/Tile Field	30.48	79.25			
216-Z-1A-B	566,549	135,418.9	Drain/Tile Field	79.25	22.86			
216-Z-1A-C	566,549	135,418.9	Drain/Tile Field	79.25	22.86			
216-Z-1D	566,644.1	135,258.1	Ditch	1295.4	1.2192	0.6096		1,579.352
216-Z-20	566,624	135,299	Crib	462.9912	3.048			1,411.197
216-Z-3	566,576.8	135,459.2	Crib	20.1168	8.42	7.62	1.2192	169.32
216-Z-4	566,586.3	135,920.7	Trench	3.048	3.048	4.572		9.290304
216-Z-5	566,555.2	135,949.2	Crib	4.2672	4.2672	5.4864		18.209
216-Z-6	566,579.1	135,875.8	Crib	15.8496	2.5908	2.4384		41.06314
216-Z-7	566,700.6	135,926.9	Crib	64.008	13.4112	2.1336		858.4241
216-Z-8	566,654.2	135,652.8	French Drain			4.572	0.9144	0.656693

Table 4.3. (contd)

Site Name	E-W State Plane (m)	N-S State Plane (m)	Site Type	Length (m)	Width (m)	Depth/ Height (m)	Diameter (m)	Area (m^2)
216-Z-9	566,758	135,610.6	Trench	36.576	27.432	6.4008		1,003.353
241-T-101	566,837.9	136,764.8	Single-Shell Tank			11.5824	22.86	410.4331
241-T-103	566,776.9	136,764.6	Single-Shell Tank			11.70432	22.86	410.4331
241-T-106	566,777	136,734.1	Single-Shell Tank			11.76528	22.86	410.4331
241-TX-107	566,742.9	136,186.9	Single-Shell Tank			14.7828	22.86	410.4331
241-TY-103	566,773.4	136,415.5	Single-Shell Tank			13.59408	22.86	410.4331
241-TY-105	566,773.4	136,384.4	Single-Shell Tank			13.59408	22.86	410.4331
241-TY-106	566,742.4	136,384.3	Single-Shell Tank			14.0208	22.86	410.4331
241-U-101	566,842	135,103.9	Single-Shell Tank			11.7348	22.86	410.4331
241-U-104	566,842.1	135,073.4	Single-Shell Tank			11.7348	22.86	410.4331
241-U-110	566,842.3	135,012.5	Single-Shell Tank			11.7348	22.86	410.4331
241-U-112	566,781.3	135,012.3	Single-Shell Tank			11.7348	22.86	410.4331
2607-W8	566,568.3	136,003.5	Septic Tank	5.94	1.83	3.66		
2607-WA	566,847.8	135,745.2	Septic Tank					
2607-WB	566,665.9	135,694.2	Septic Tank					
2607-WL	565,892.7	135,866.5	Septic Tank					
2607-Z	566,609.3	135,571.5	Septic Tank	10.97	3.35	7.01		
2607-Z1	566,406	135,600.5	Septic Tank					
284-WB	567,122.4	135,958.7	Pond	182.88	15.24	6.1		
UPR-200-W-135	567,119.2	136,074.4	Unplanned Release	12.192				0.999
UPR-200-W-150	566,773.4	136,415.6	Unplanned Release					0.999

Table 4.3. (contd)

Site Name	E-W State Plane (m)	N-S State Plane (m)	Site Type	Length (m)	Width (m)	Depth/ Height (m)	Diameter (m)	Area (m^2)
UPR-200-W-151	566,742.3	136,415.5	Unplanned Release					0.999
UPR-200-W-29	566,907.9	136,595.6	Unplanned Release	30.48	22.86			696.7728
UPR-200-W-97	566,902.8	136,595.4	Unplanned Release			0.9144		0.999

Table 4.4. Estimated Waste Component Inventory for the 216-Z-9 Trench

Year	CT Volume*	TBP Volume*	DBBP Volume*	Lard Oil Volume*
CT Release = 8.3E4 L				
1955	1.34E3	1.61E2	2.68E2	5.34E1
1956	1.21E4	1.46E3	2.43E3	4.84E2
1957	1.21E4	1.46E3	2.43E3	4.84E2
1958	1.18E4	1.41E3	2.36E3	4.70E2
1959	1.24E4	1.49E3	2.48E3	4.95E2
1960	1.25E4	1.50E3	2.50E3	5.0E2
1961	1.66E4	1.99E3	3.32E3	6.63E2
1962	3.88E3	4.67E2	7.76E2	1.55E2
Total	8.3E4	9.94E3	1.66E4	3.31E3
CT Release = 3.0E5 L				
1955	4.84E3	5.82E2	9.69E2	1.93E2
1956	4.37E4	5.28E3	8.78E3	1.75E3
1957	4.37E4	5.28E3	8.78E3	1.75E3
1958	4.27E4	5.10E3	8.53E3	1.70E3
1959	4.48E4	5.39E3	8.96E3	1.79E3
1960	4.52E4	5.42E3	9.03E3	1.81E3
1961	6.00E4	7.19E3	1.20E4	2.34E3
1962	1.40E5	1.69E3	2.80E3	5.60E2
Total	3.0E5	3.59E4	6.00E4	1.12E4

CT = Carbon tetrachloride.
DBBP = Dibuty butyl phosphonate.
TBP = Tributyl phosphate.
*All volumes are in liters (L).

Table 4.5. Estimated Waste Component Inventory for the 216-Z-1A Tile Field

Year	CT Volume*	TBP Volume*	DBBP Volume*	Lard Oil Volume*
1964	1.44E4	2.02E3	2.33E3	9.29E2
1965	3.02E4	4.23E3	4.86E3	1.94E3
1966	4.93E4	6.90E3	7.93E3	3.17E3
1967	3.92E4	5.48E3	6.31E3	2.52E3
1968	3.28E4	4.60E3	5.29E3	2.11E3
1969	5.09E3	7.13E2	8.19E2	3.27E2
Total	1.71E5	2.39E4	2.75E4	1.71E5

CT = Carbon tetrachloride.
DBBP = Dibuty butyl phosphonate.
TBP = Tributyl phosphate.
*All volumes are in liters (L).

Table 4.6. Estimated Waste Component Inventory for the 216-Z-18 Crib

Year	CT Volume*	TBP Volume*	DBBP Volume*	Lard Oil Volume*
1969	1.63E4	2.42E3	2.83E3	NR
1970	2.28E4	3.38E3	3.96E3	NR
1971	2.52E4	3.74E3	4.38E3	NR
1972	3.53E4	5.25E3	6.14E3	NR
1973	1.04E4	1.55E3	1.81E3	NR
Total	1.10E5	2.39E4	1.91E4	NR

CT = Carbon tetrachloride.
DBBP = Dibuty butyl phosphonate.
NR = Not reported.
TBP = Tributyl phosphate.
*All volumes are in liters (L).

5.0 Overview of Simulations

Simulations were conducted in two phases. The first part of simulations examined the infiltration and redistribution of CT from the time of disposal through 1993, just prior to the initiation of the SVE treatment. The second phase of simulations examined the impact of SVE on the CT distribution in the subsurface over the time period of 1993 to 2004.

5.1 Infiltration/Redistribution Simulations

A total of 23 three-dimensional simulations were conducted. The simulations consist of one Base Case simulation and a sensitivity analysis consisting of 22 simulations. The computational domain was discretized into 27 x 34 x 85 = 78,030 nodes. Since the water-air-oil mode was used, this number of nodes translates into 3 x 78,030 = 234,090 unknowns. The simulations lasted from 1954 – 1993.

5.1.1 Base Case Simulation

The characteristics of the Base Case simulations are as follows:

DNAPL volume:
DNAPL volume = 3.16E5 L

216-Z-9 Trench Area:
The bottom of the trench is 6.4 m below ground surface (bgs).

DNAPL infiltration rates:
1955 (July-Dec) – 0.062 m/yr
1956 – 0.277 m/yr
1957 – 0.277 m/yr
1958 – 0.264 m/yr
1959 – 0.283 m/yr
1960 – 0.286 m/yr
1961 – 0.379 m/yr
1962 (Jan-Jun) – 0.178 m/yr

Aqueous phase infiltration rates:
1955 (July-Dec) – 3.04 m/yr
1956 – 2.47 m/yr
1957 – 2.95 m/yr
1958 – 3.92 m/yr
1959 – 3.07 m/yr
1960 – 4.42 m/yr
1961 – 4.23 m/yr
1962 (Jan-Jun) – 1.98 m/yr

DNAPL properties:
Fluid properties are measured in the laboratory based on average fluid composition of 8.8% TBP, 14.7% DBBP, 2.9% lard oil, and 73.6% CT.
Density: 1,426 kg/m^3
Viscosity: 1.11 x 10^{-3} Pa s
Vapor pressure: 10,830 Pa
Surface tension (air-DNAPL): 25.1 dynes/cm
Interfacial tension (water-DNAPL): 15.2 dynes/cm

Porous media present in domain:
Ringold A
Lower Mud
Ringold E
Upper Ringold
Cold Creek C
Cold Creek Z
Lower Sand
Lower Gravel
Hanford 2
Hanford 1
Hanford 1a
Backfill

Sorption:
A linear K_d of 0.2 mL/g was applied to all porous media.

Hydraulic properties:
Retention parameters, porosities, and hydraulic conductivities were obtained from Khaleel et al. 2001 and Khaleel and Freeman (1995) (Table 5.1). The relative permeability-saturation-pressure parameters were converted to equivalent Brooks-Corey-Burdine parameters using Lenhard et al. (1989). The Brooks-Corey-Burdine relations were used in all simulations except sensitivity Simulation 8, in which the original van Genuchten-Mualem relations were used.

Permeability anisotropy ratio:
10:1

Boundary and initial conditions:
The simulations were conducted for the period 1954–2003. On the top boundary, atmospheric gas pressure was assumed in conjunction with a 0.5 cm/yr water flux. For the south, north, west, and east boundary, fluctuating water table boundary conditions were imposed for the water mass balance equation below the water table and zero-flux boundary conditions were applied above the water table. The time variant boundary conditions for the water mass balance equation at the south and north boundary (water table information) were derived from observed water levels in wells 299-W15-5 and 6 as shown in

Table 5.1. Saturated Hydraulic Conductivity (K_{sat}), Porosity, and Retention Parameter Values (van Genuchten α, n, and irreducible water saturation) of Stratigraphic Units

Stratigraphic Units	K_{sat} (cm/s)	Porosity	Van Genuchten α (1/cm)	Van Genuchten n	S_{rl}
Ringold A	5.73E-3	0.0770	0.0090	1.6210	0.1299
Lower Mud	1.16E-8	0.0770	0.0090	1.6210	0.1299
Ringold E	5.73E-3	0.0770	0.0090	1.6210	0.1299
Upper Ringold	5.73E-3	0.0770	0.0090	1.6210	0.1299
Cold Creek C	6.72E-3	0.3203	0.0173	1.7705	0.2451
Cold Creek Z	1.48E-4	0.4238	0.0052	2.0671	0.0967
Lower Sand	1.87E-2	0.3359	0.1338	2.0475	0.0747
Lower Gravel	3.00E-2	0.2720	0.0270	1.9940	0.1471
Hanford 2	5.85E-3	0.3653	0.0448	2.3553	0.0846
Hanford 1	5.00E-2	0.1660	0.0830	1.6600	0.1386
Hanford 1A	5.98E-4	0.4478	0.0107	1.9229	0.1740
Backfill	1.5E-2	0.2620	0.0320	1.4000	0.3646

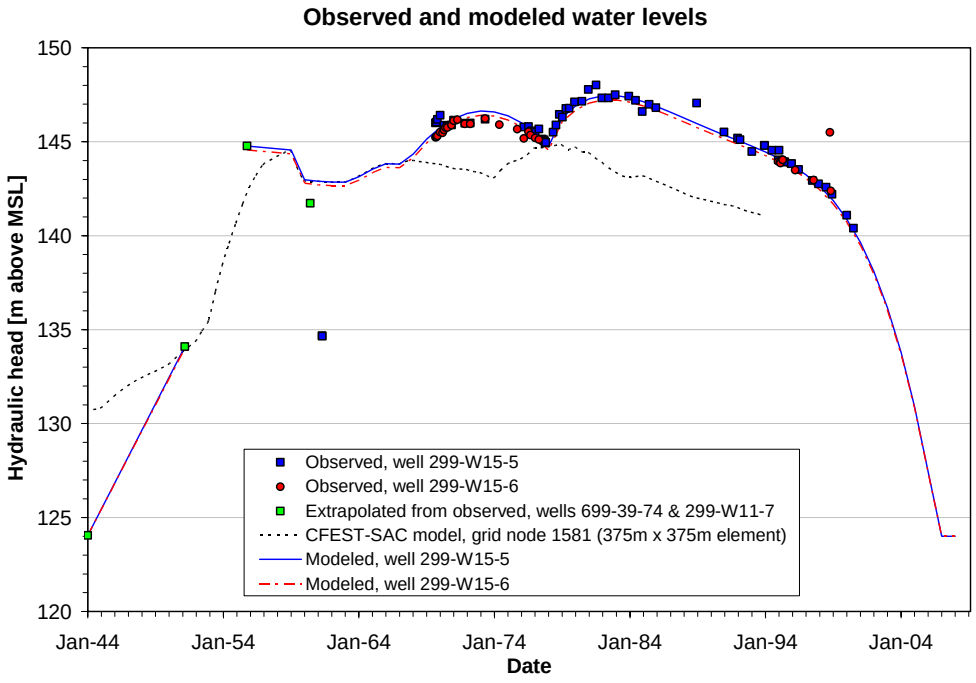

Figure 5.1. Observed and Modeled Water Levels for Aqueous Phase Initial and Boundary Conditions

Figure 5.1. The resulting boundary conditions yielded a ground water flow direction from south to north. Neumann boundary conditions were imposed for water and DNAPL discharges for the 216-Z-9 trench area during the years that these liquids were disposed. The flow rates are listed in the section associated with the specific input parameters for each simulation case. DNAPL was allowed to move freely across all boundaries. The initial gas and aqueous phase pressure distributions in the domain at 1954 were obtained by conducting a 10,000-yr simulation using the interpolated 1954 water levels at the south and north boundary and a recharge rate of 0.5 cm/yr. It was assumed that at 1954, no DNAPL was present in the domain.

5.1.2 Sensitivity Analysis Simulations

A total of 20 sensitivity analysis simulations were conducted. The parameters that were changed from the Base Case for each sensitivity simulation are described below.

1. Total DNAPL volume = 4.07E5 L (maximum estimate) applied as follows:
   1955 (July-Dec) – 0.07983 m/yr
   1956 – 0.35665 m/yr
   1957 – 0.35665 m/yr
   1958 – 0.33991 m/yr
   1959 – 0.36438 m/yr
   1960 – 0.36438 m/yr
   1961 – 0.48798 m/yr
   1962 (Jan-Jun) – 0.22918 m/yr

2. Total DNAPL volume = 1.13E05 L (minimum estimate) applied as follows:
   1955 (July-Dec) – 0.02209 m/yr
   1956 – 0.09867 m/yr
   1957 – 0.09867 m/yr
   1958 – 0.09404 m/yr
   1959 – 0.10081 m/yr
   1960 – 0.10081 m/yr
   1961 – 0.13501 m/yr
   1962 (Jan-Jun) – 0.06341 m/yr

3. Total disposed DNAPL volume equal to total CT volume. Fluid properties of disposed DNAPL equal to properties of pure CT.
   Density: 1594 kg/m^3
   Viscosity: $0.97x10^{-3}$ Pa s
   Vapor pressure: 11950 Pa
   Surface tension (air-DNAPL): 26.2 dynes/cm
   Interfacial tension (water-DNAPL): 40.8 dynes/cm

4. Properties of DNAPL reflecting DNAPL composition of 50% CT, 10% lard oil, 20% DBBP, and 20% TBP. This DNAPL composition reflects the lowest CT percentage of the disposed DNAPL.

Density: 1260 kg/m^3
Viscosity: 1.357×10^{-3} Pa s
Vapor pressure: 8,250 Pa
Surface tension (air-DNAPL): 24.2 dynes/cm
Interfacial tension (water-DNAPL): 11.8 dynes/cm

5. DNAPL infiltration into subsurface through an area 20% of 216-Z-9 footprint. Infiltration rate is constant for each calendar year.

6. DNAPL infiltration rate increased by a factor 4, for one week per month only. Total infiltrated DNAPL volume does not change.

7. Combination of 5 and 6: DNAPL infiltration into subsurface through an area 20% of 216-Z-9 footprint and DNAPL infiltration rate increased by a factor 4, for one week per month. Total infiltrated DNAPL volume does not change.

8. Use of equivalent van Genuchten-Mualem properties.

9. Increase of base case nonwetting fluid entry pressures by a factor of 2.

10. Decrease of base case nonwetting fluid entry pressures by a factor of 2.

11. Increase of base case pore geometry parameter (Brooks and Corey λ) values by a factor of 2.

12. Decrease of base case pore geometry parameter (Brooks and Corey λ) values by a factor of 2.

13. Base case permeability times a factor 10.

14. Base case permeability divided by a factor 10.

15. Anisotropy ratio of 1:1.

16. Anisotropy ration of 20:1.

17. Laboratory measured maximum residual NAPL saturation for Cold Creek silt (0.13), Hanford Sand (0.10), Lower Gravel (0.05), and Ringold E material (0.11). For the other materials, a maximum residual of 0.1 was assumed.

18. Measured and assumed maximum residual NAPL saturation times 1.25

19. Base case porosity times 1.25.

20. Base case porosity times 0.75.

21. A K_d partitioning coefficient of 0.1 mL/g.

22. A K_d partitioning coefficient of 0.4 mL/g.

5.2 SVE Simulations

Rohay (2002) describes the details of the field SVE campaigns for the 200-PW-1 Operable Unit, which includes the 216-Z-9 trench, the 216-A-1A tile field, and the 216-Z-18 crib. There are 46 wells available for SVE in this operable unit, with well diameters ranging from 5 to 20 cm. During the active SVE campaigns, each system extracted soil vapor simultaneously from multiple wells open either above and/or below the Cold Creek unit. In addition to the SVE wells, 126 subsurface monitoring probes were installed to depths of up to 36 m bgs using a cone penetrometer. Up to 87 shallow soil-vapor monitoring probes were also installed at depths ranging from 1.2 to 1.8 bgs. Data from some of these monitoring probes are tabulated in Rohay (2002).

At the 216-Z-9 well field, there are 23 well intervals available for SVE, with 9 of these intervals open below the Cold Creek units. Active SVE operations began at the 216-Z-9 well field in March 1993 (Rohay 2002). Operations were suspended on June 3, 1993, following an overheating incident (Driggers 1994), and then resumed on June 30, 1994. After the overheating incident, all SVE systems were initially operated only during the regular work week, Monday through Friday. The system began operating 24 hr/day and 7 day/week on October 19, 1994 (Rohay 2002). Operations were suspended on November 4, 1996, and then restarted on July 18, 1997, as part of a rebound study (Rohay 1997). All SVE systems then continued to operate until September 30, 1997. Thereafter, the SVE system at the 216-Z-9 well field was only operated for several months each year, from July 7 through September 30, 1998; from March 29 through June 28, 1999; and from July 20 through September 30, 2001. No SVE operations were conducted in FY 2000 due to limited funding. A top view of the well locations within the computational domain is shown in Figure 5.1. Not all of the 23 intervals in the 216-Z-9 well network were connected to the SVE system during its periods of operation. Some of the wells were also modified during the period of SVE operations. Modifications included deepening some wells, perforating new sections of some wells, installing packers, and sealing or plugging the bottoms of some wells. Details regarding flow rates and extracted vapor concentrations for individual wells on selected days are given by Rohay (2002, Table B-3). Daily records of pumping rates for the 216-Z-9 well network, its hours of operation on each day, and the on-line well intervals were provided by Fluor Hanford, Inc.[1] These data were used in conjunction with information on the current screened intervals for each well in the 216-Z-9 well field (also provided by Fluor Hanford, Inc.) to generate time-averaged flow rates which were applied as sink terms to represent SVE in STOMP. No attempt was made in the model simulations to account for any physical changes that might have occurred to any given well during the course of the SVE operations.

On any given day during which the SVE system was operative, the flow rate (m^3/min) for the 216-Z-9 well network was partitioned between the wells and/or well intervals that were on-line during the hours of operation for that day. Time-averaged flow rates were then computed from these data for each operational period (e.g., July 7 to September 30, 1998) and each well interval.

[1] Excel spreadsheet from V. J. Rohay, Fluor Hanford, Inc., Richland, Washington.

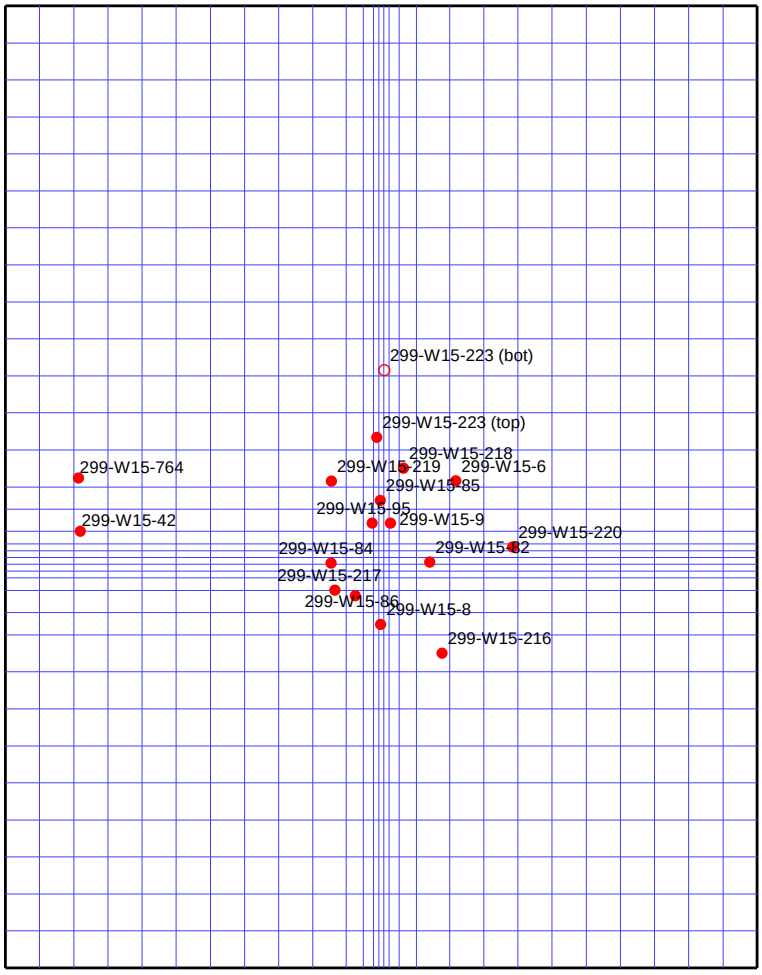

Figure 5.2. Plan View of Model Grid Showing Locations of Soil-Vapor Extraction Wells within the Computational Domain (Note that wells 299-W-15-764 and 299-W15-42 were not in the SVE well network. Well 299-W15-223 was a slant borehole).

Figure 5.3 depicts data from Table B-3 of Rohay (2002) and the time-averaged flow rates used as sink terms in STOMP for two of the SVE wells/intervals. Differences between the time-averaged flow rates and the measured values on selected days are due in part to averaging, especially prior to October 1994, when the SVE well network was turned off for much of the time, and in part to the assumption that the total flow rate was partitioned or divided equally between the number of wells or well intervals that were online. It should also be noted that even during periods when the SVE system was reported to be online 7 days/week and 24 hours/day, the daily records indicate that there were times when the system was actually turned off, or when individual wells or well intervals were taken offline.

In the field, after the overheating incident that occurred in June 1993, a bleeder line was apparently connected to the SVE system for some period of time to dilute the extracted vapor concentrations with fresh air from the surface in order to prevent further overheating. Unfortunately, the relative volumes of fresh air, to air extracted from the subsurface during this period, are unknown. Therefore, there is some

uncertainty in the actual volumes of air that were extracted from the subsurface by the SVE system. For this reason, a limited number of simulations were also conducted with reduced SVE rates to illustrate the sensitivity of the total simulated mass of CT removed to the extraction rates.

Several modifications were made to STOMP to allow it to simulate the process of SVE more accurately and efficiently. These modifications included the addition of a coupled SVE well model to the code and incorporation of a model for a gas-slip phenomenon known as the Klinkenberg effect (Klinkenberg 1941). The well model partitions the volumetric air flow rates that are specified for each well or well interval such that the rate applied to each affected grid block is a fraction of the total flow rate, weighted by product of the gas permeability for the grid block and the length of the portion of the screened interval that overlaps the grid block. The Klinkenberg effect is an experimentally observed phenomenon. At low pressures, such as occur near well bores during SVE, the Klinkenberg effect results in increased gas permeability relative to the gas permeability that would be computed from the intrinsic permeability and fluid properties alone.

Figure 5.4 depicts the ratio of the apparent or observed gas permeability, k_a, to the gas permeability computed from the intrinsic permeability and fluid properties, k, as a function of average gas pressure for several porous media. In general, the Klinkenberg effect is more significant at lower pressures, and in finer-grained porous media.

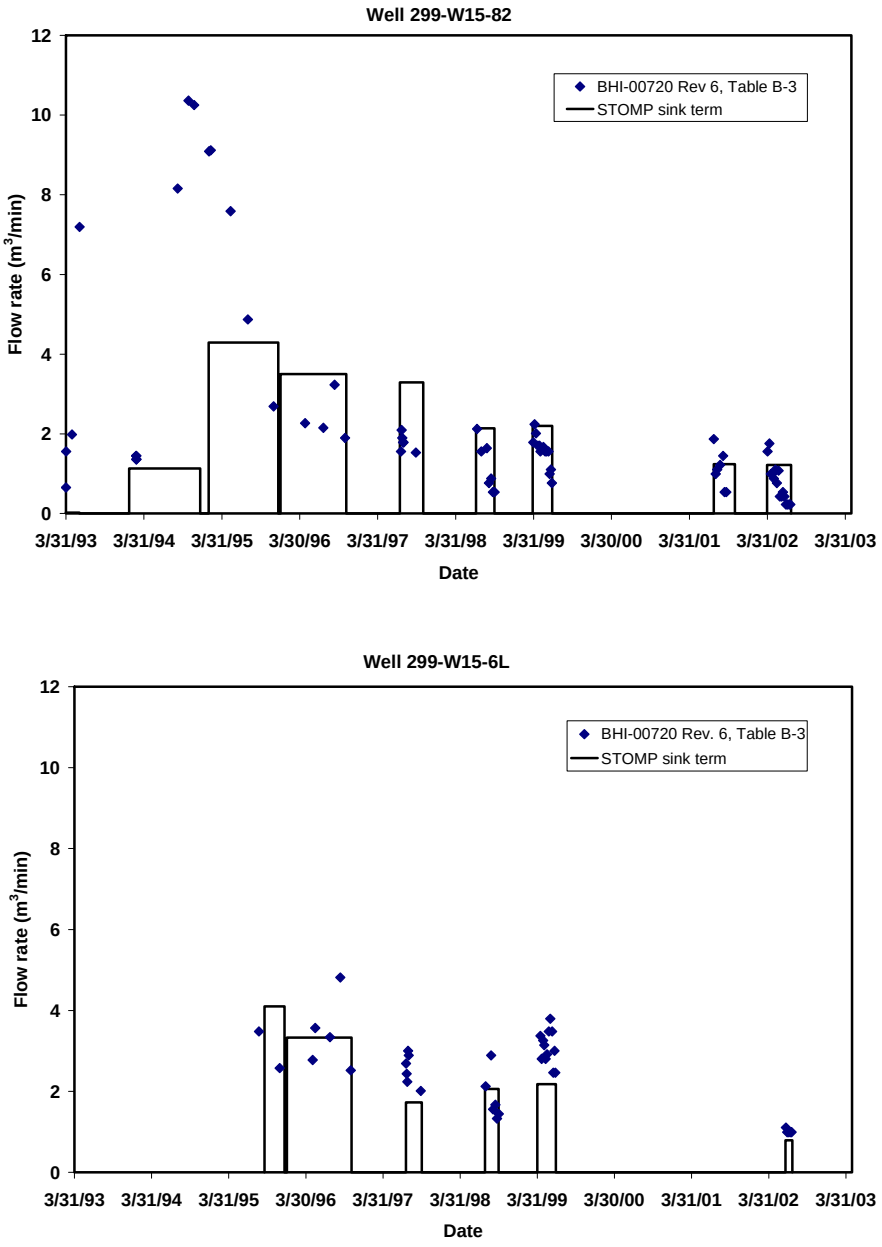

Figure 5.3. Examples of Flow Rates for Individual Wells/Intervals on Selected Days (from Rohay 2002) and Time-Averaged Flow Rates used in STOMP

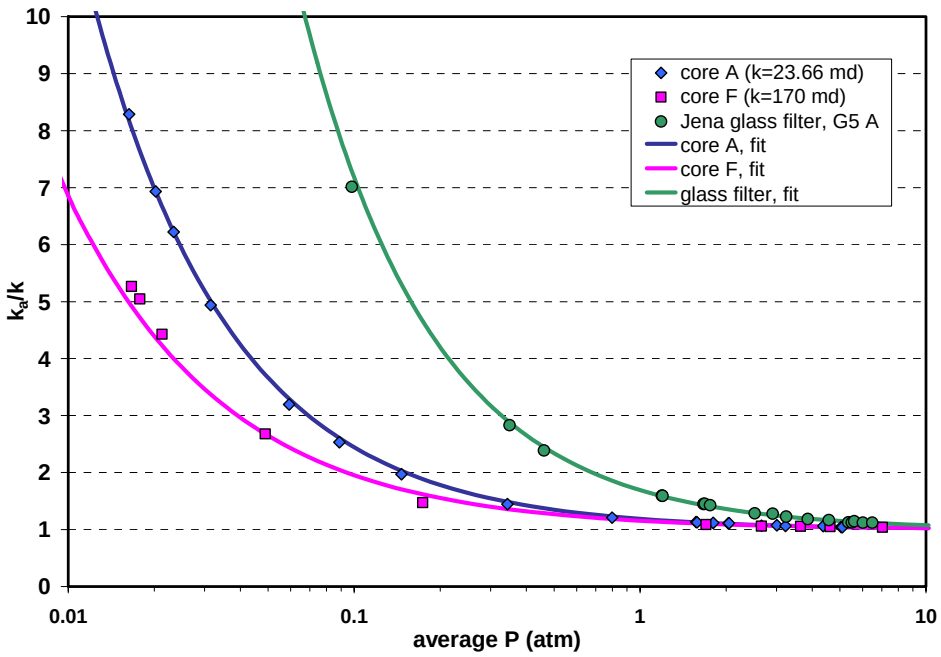

Figure 5.4. Ratio of Apparent (observed) Gas Permeability and Gas Permeability Computed from Intrinsic Permeability and Fluid Properties as a Function of Average Gas Pressure (after Klinkenberg 1941)

6.0 Results and Discussion

6.1 Base Case

Figure 6.1 shows the DNAPL body at 1993 in the Ringold E unit in the subsurface of the 216-Z-9 trench. In Figure 6.2, the Cold Creek silt and carbonate layers have been removed to demonstrate the DNAPL distribution in the unit. Figure 6.3 shows the complete DNAPL body in all units. The black lines in the DNAPL body indicate the interfaces between units. The water table at 1993 is included as a white line in the Ringold E unit. The minimum DNAPL saturation contour is 0.01. These three figures show that the highest DNAPL saturations are located in the Cold Creek silt. The maximum DNAPL saturation in this unit at 1993 is 0.105. Figure 6.3 shows that most DNAPL spreading occurs below the Cold Creek unit in the Ringold E formation. As a result of dissolution in the aqueous phase, the DNAPL body below the water table narrows with increasing depth.

Aqueous phase concentrations in the Ringold E formation are shown in Figure 6.4. In Figure 6.5, the concentrations in the Cold Creek silt and carbonate layers are included, while in Figure 6.6, dissolved concentrations below the Hanford units are shown. The figures show considerable concentrations throughout the horizontal extent of the domain in the vadose zone of the Ringold E. Above and in the Cold Creek unit, the extent of the plume is smaller. Below the water table, dissolved concentrations are near saturated values within the DNAPL body. Downstream of DNAPL, the concentrations decrease as a result of hydrodynamic mixing.

Gas phase concentrations in the Ringold E formation are shown in Figure 6.7. In Figure 6.8, the concentrations in the Cold Creek silt and carbonate layers are included, while in Figure 6.9, dissolved concentrations below the Hanford units are shown. The gas phase concentrations in the unsaturated zone are strongly correlated to the aqueous phase concentrations as both variables are related through Henry's constant. The shape of the gas concentration plume is a strong function of density-driven advection within the gas phase. The DNAPL has a vapor pressure of almost 11,000 Pa and it consists primarily of CT, which has a relatively high molecular weight. As a result, the gas phase containing DNAPL vapors has a density larger than that of ambient gas, resulting in density-driven advection. The dense vapors sink rapidly in the units above the Cold Creek unit and in the unsaturated Ringold E materials between the water table and the Plio-Pleistocene. Since the Cold Creek silt and carbonate layers have fairly high water saturations, the dense vapors are forced to spread laterally on top of these units. This phenomenon is even more pronounced just above the water table. The vapors in the Ringold E are forced to spread in a lateral direction and at 1993, most of the unsaturated Ringold E contains DNAPL vapors. The DNAPL vapors are in contact with the groundwater and through phase partitioning, DNAPL mass is transferred from the gas phase to the aqueous phase. Through this mechanism, the upper part of the saturated zone gets contaminated.

Sorbed concentrations in the Ringold E formation are shown in Figure 6.10. In Figure 6.11, the concentrations in the Cold Creek silt and carbonate layers are included, while in Figure 6.12, sorbed concentrations below the Hanford units are shown. The figures show considerable sorbed amounts throughout the horizontal extent of the domain in the vadose zone of the Ringold E.

Figure 6.13 shows several cumulative mass fluxes as a function of the simulation time. The figure shows four DNAPL mass fluxes (mass into domain, into Cold Creek unit, out of the Cold Creek unit, and across the water table), and volatilized and dissolved mass moving out of the domain. The difference in cumulative fluxes into and out of the Cold Creek unit remains fairly constant at approximately 130,000 kg between 1970 and 1993, indicating that the total DNAPL mass in this unit has been fairly constant during this period. The first kilogram of DNAPL was transported across the water table at 1964.5 years. Until 1993, a total of 26,744 kg was transported across the water table into the aquifer.

Figure 6.14 shows the volatile organic carbon (VOC) mass distribution over the DNAPL, sorbed, aqueous, and gas phases as a function of time. The figure shows that the DNAPL mass has been declining steadily since disposal ceased with an approximate rate of 5,000 kg/year. Until 1993, only 4% of the total inventory has been removed from the computational domain through transport in the gas and aqueous phases. The decreased in DNAPL mass is primarily caused by sorption to the solid phase. Mass partitioning over the various units is shown in Figure 6.15. The figures show that DNAPL at 1993 was draining from the Hanford 2 into the lower sand, and from the lower sand into the Cold Creek unit. The amounts in the Cold Creek unit have been relatively constant since 1965. DNAPL in the Ringold E is disappearing as a result of dissolution below the water table. It is interesting to notice that at 1993, when SVE was initiated, the mass in the lower sand exceeded the combined DNAPL in the Cold Creek silt and carbonate units. The mass in the lower sand is thought to be more readily accessible to SVE than the mass in the Cold Creek unit.

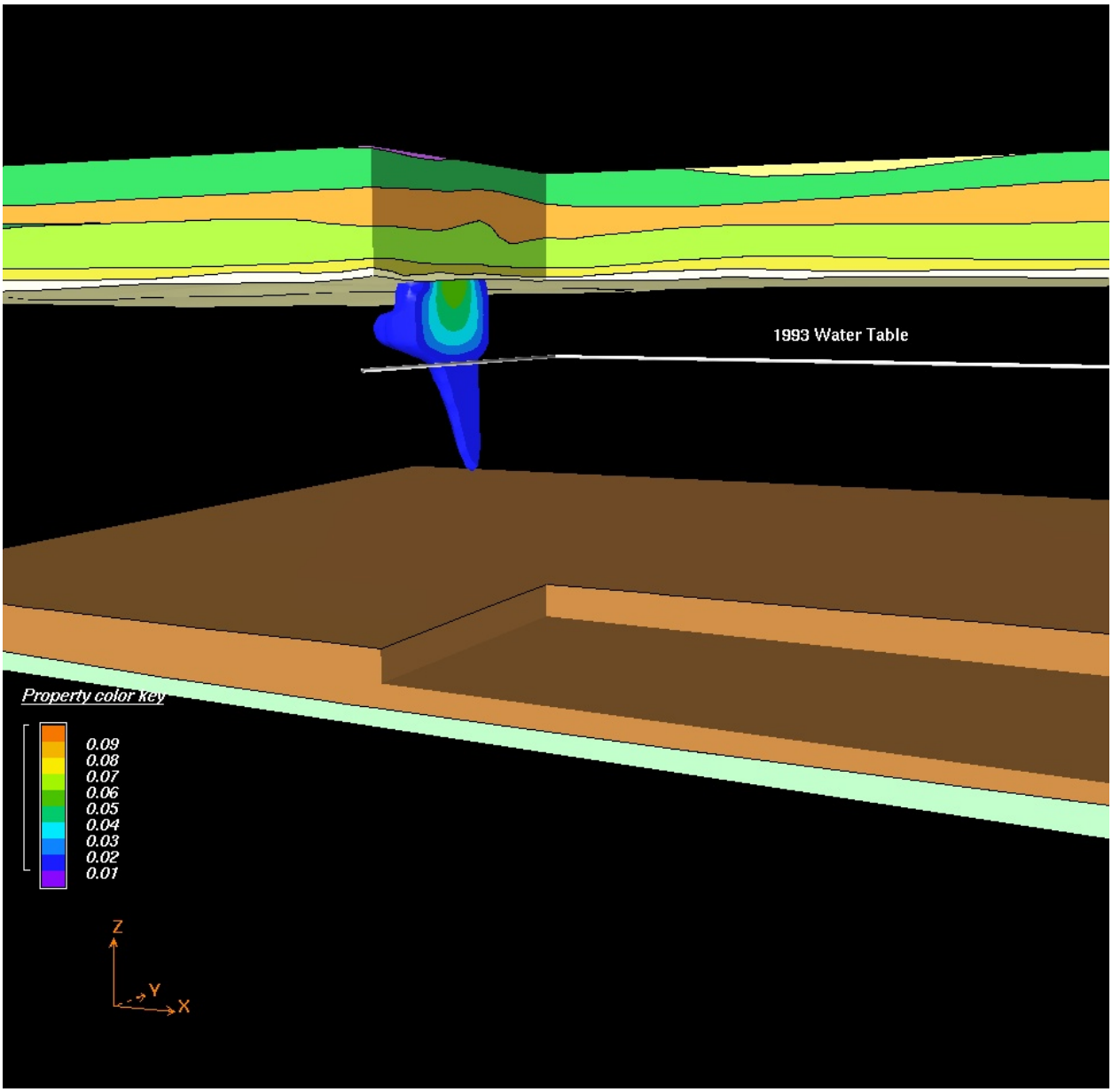

Figure 6.1. DNAPL Body in the Ringold E Unit at 1993 (Base Case)

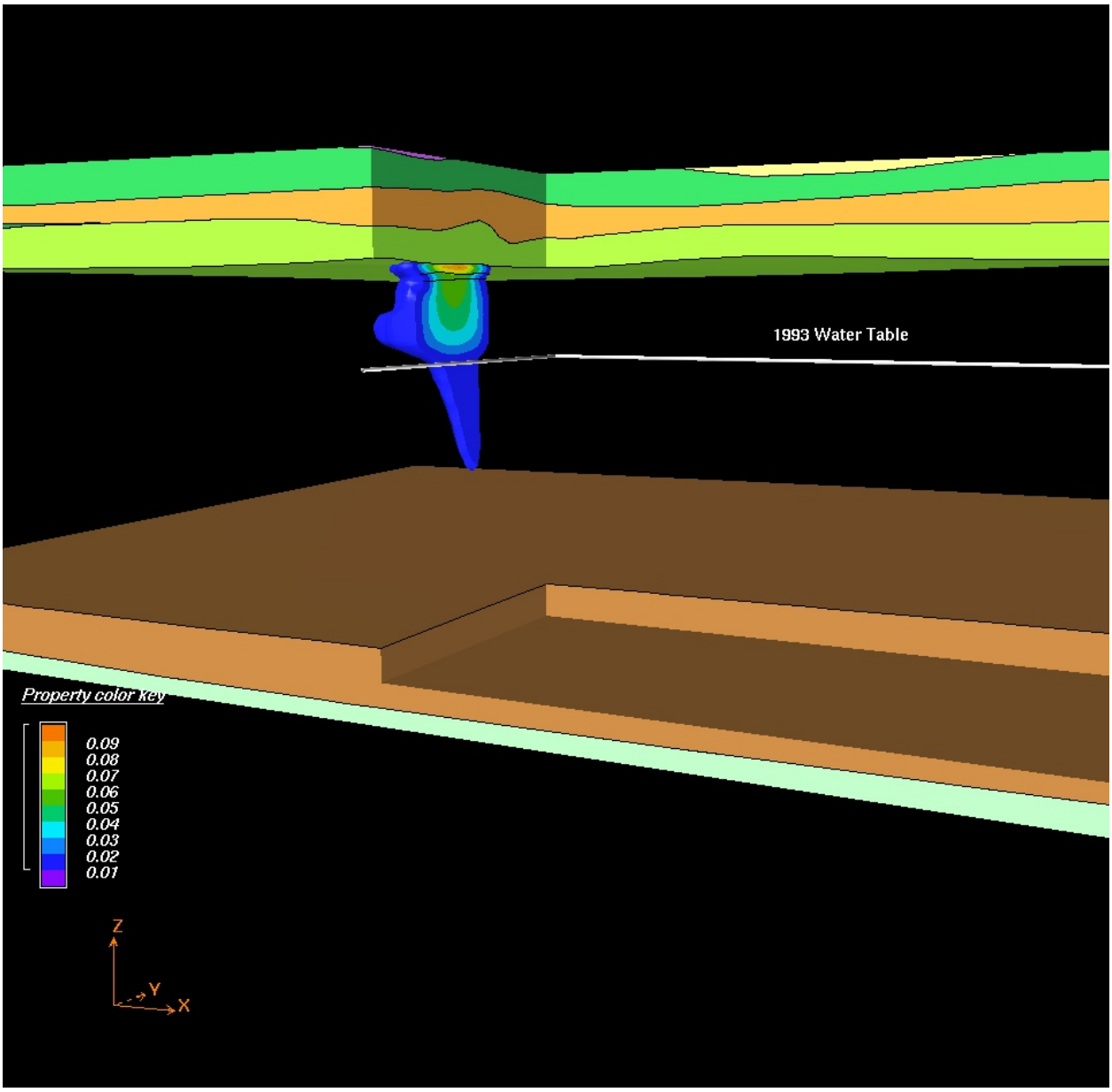

Figure 6.2. DNAPL Body in the Ringold E and Cold Creek Silt and Carbonate Layers at 1993 (Base Case)

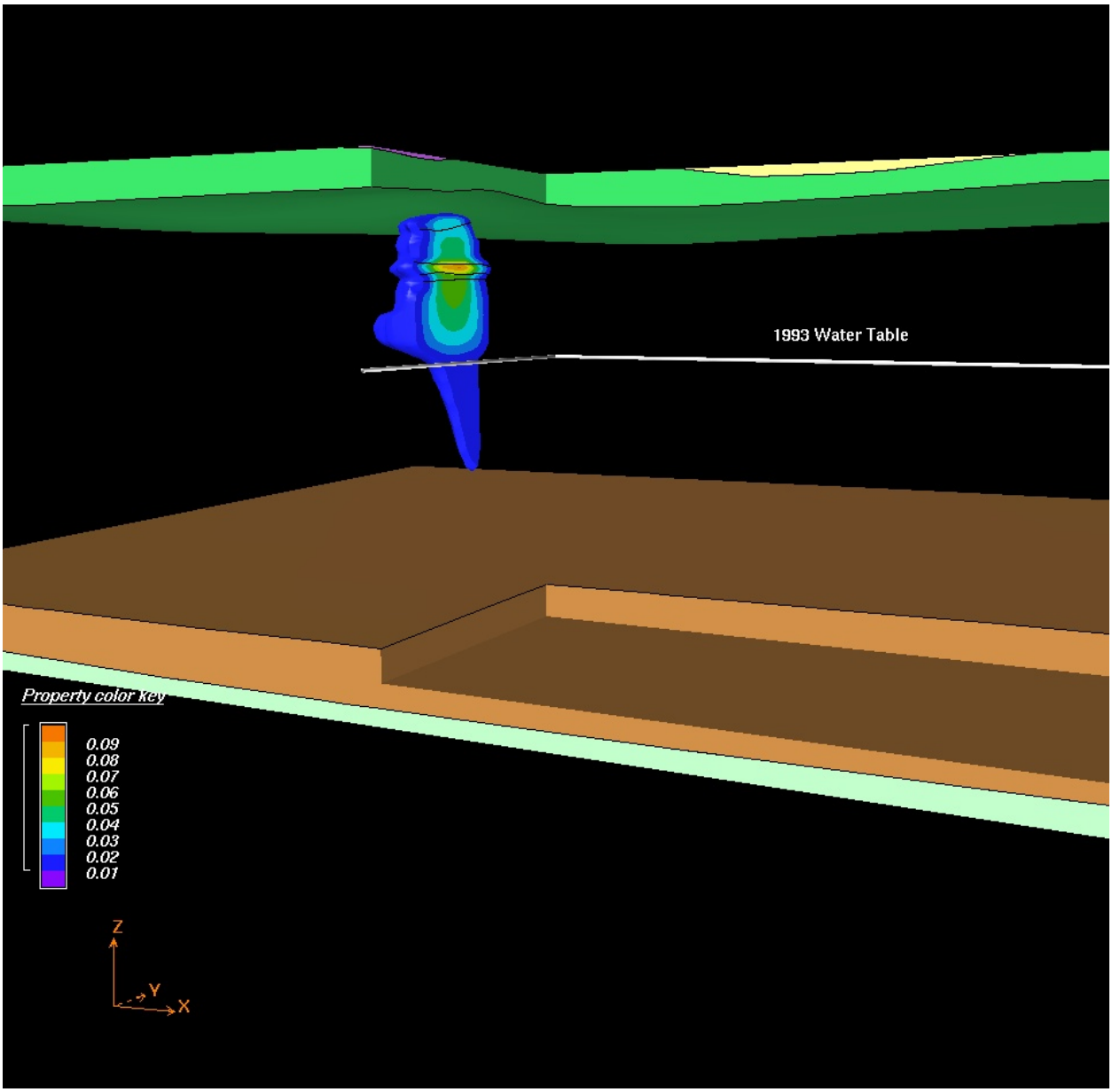

Figure 6.3. DNAPL Body in the Ringold E, Cold Creek, and Hanford Units at 1993 (Base Case)

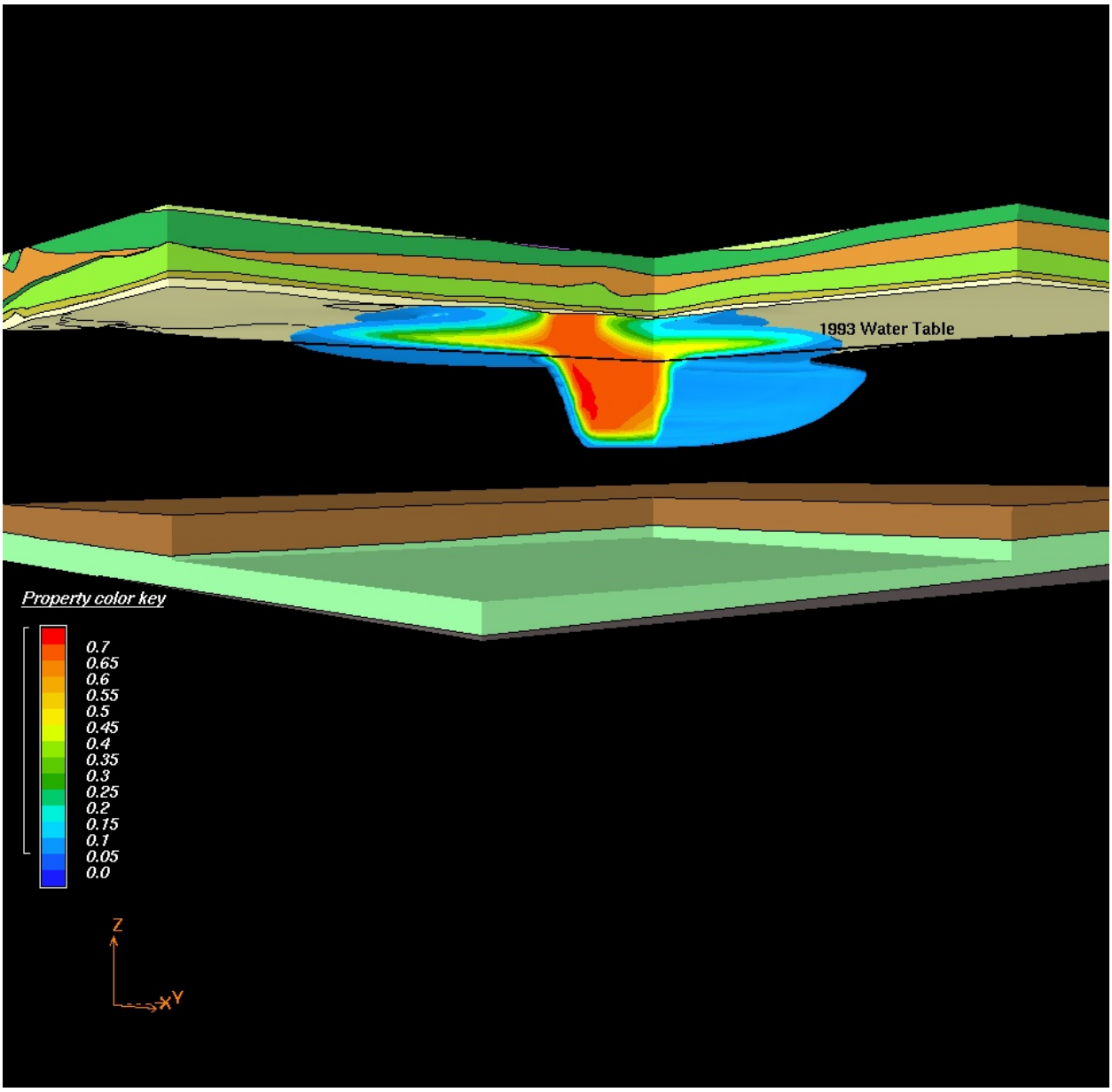

Figure 6.4. Dissolved Aqueous DNAPL Concentrations (g/L) in the Ringold E Unit at 1993 (Base Case)

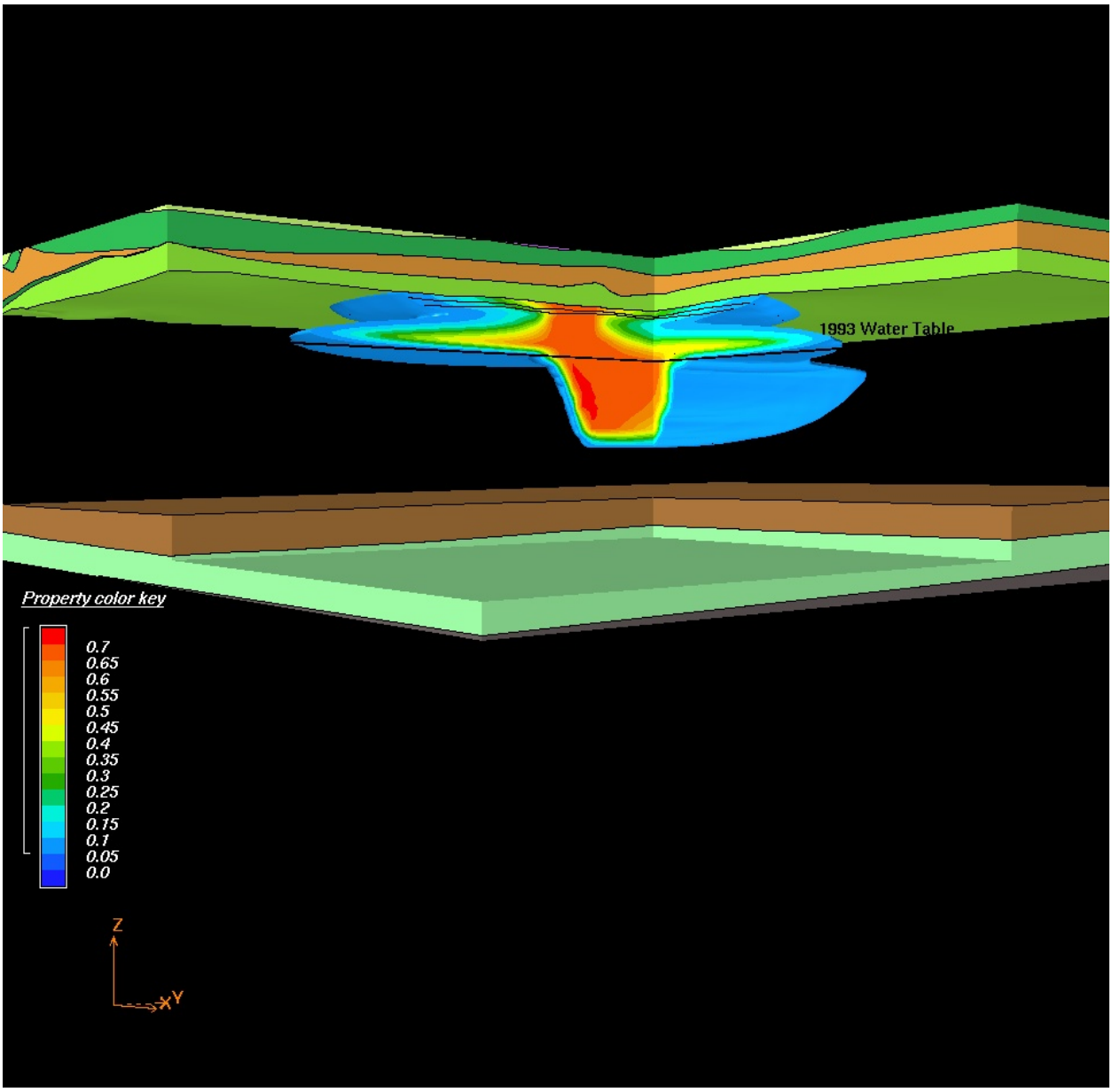

Figure 6.5. Dissolved Aqueous DNAPL Concentrations (g/L) in the Ringold E and Cold Creek Silt and Carbonate Layers at 1993 (Base Case)

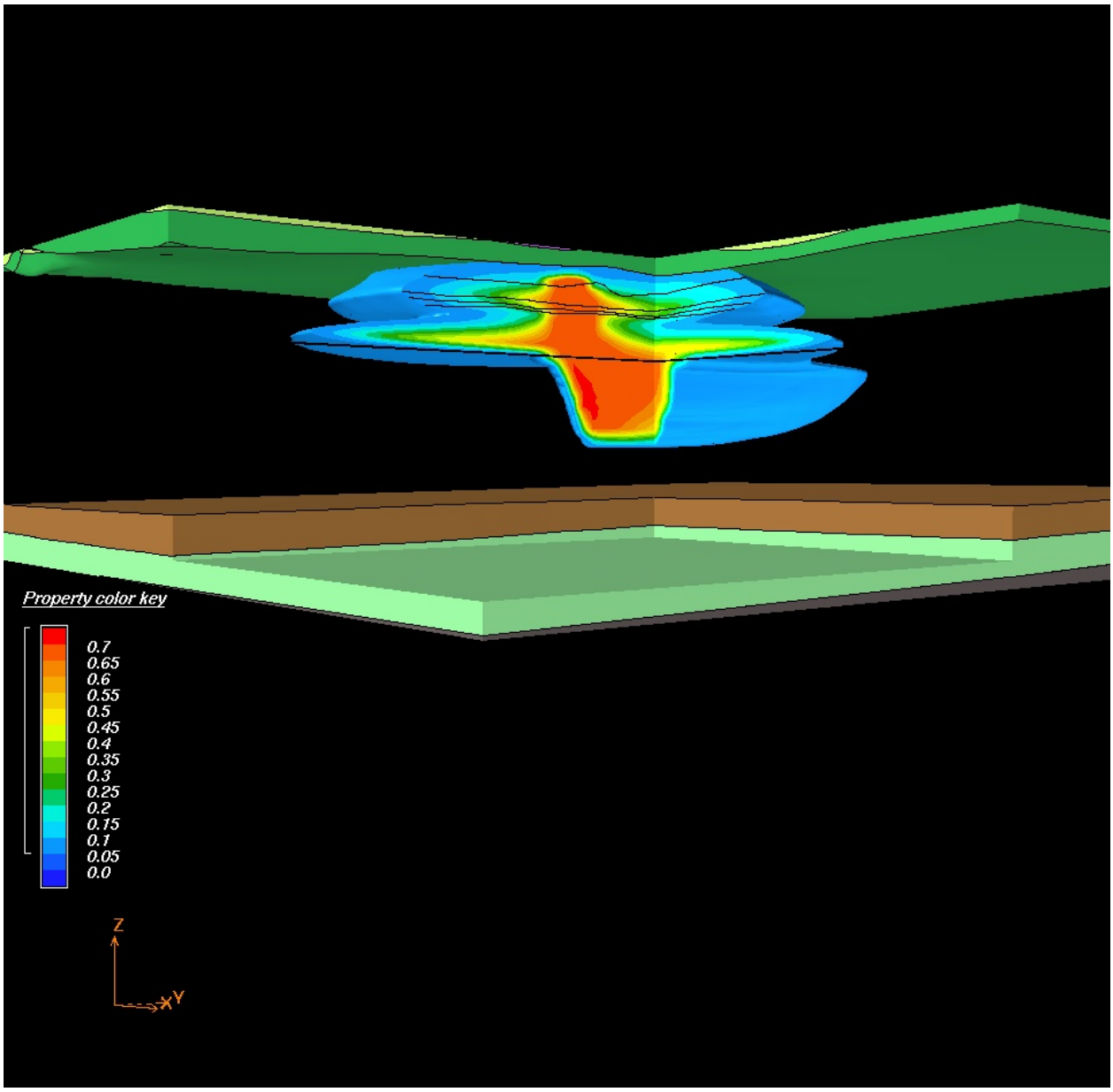

Figure 6.6. Dissolved Aqueous DNAPL Concentrations (g/L) in the Ringold E, Cold Creek, and Hanford Units at 1993 (Base Case)

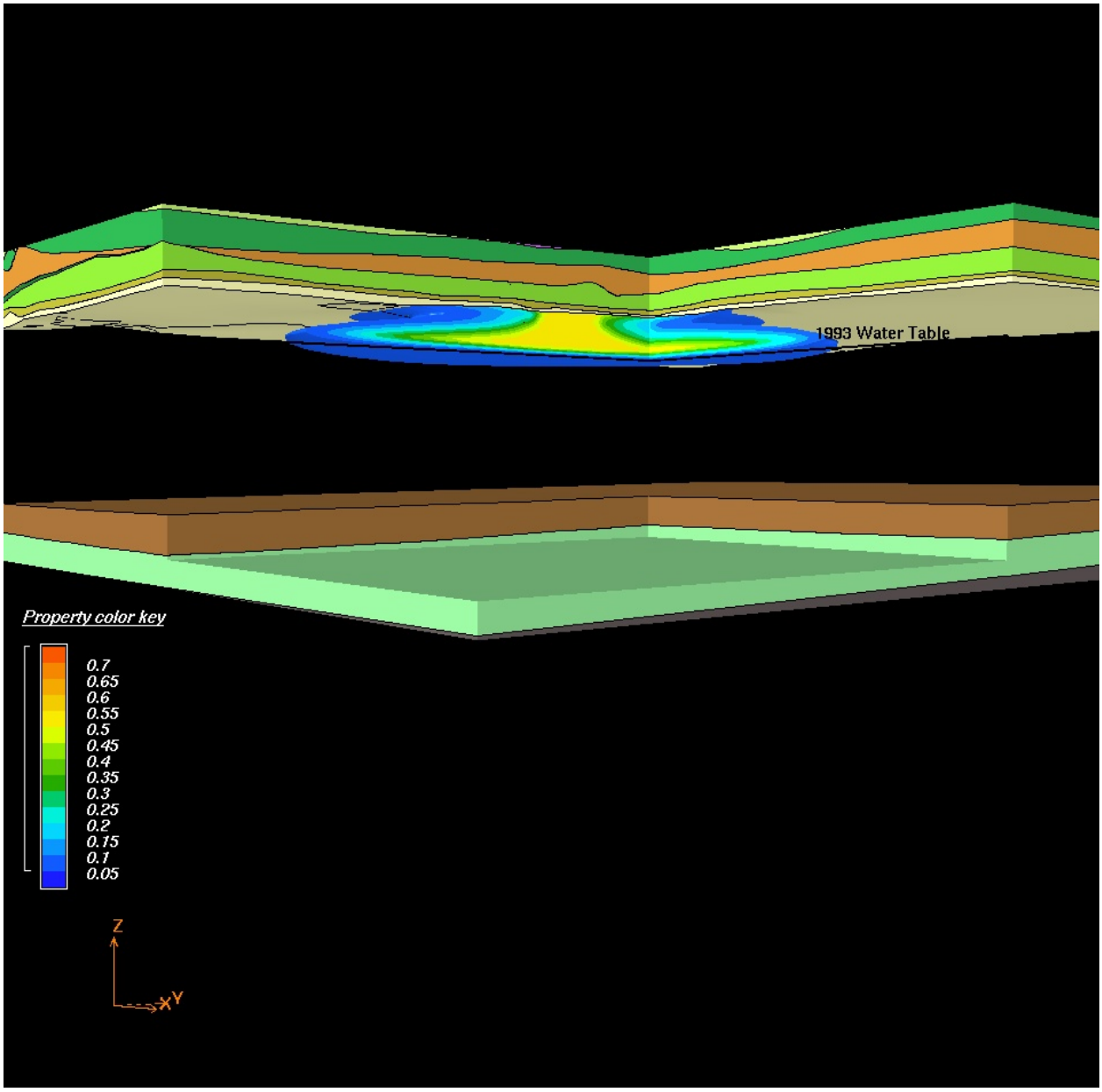

Figure 6.7. Dissolved Gaseous DNAPL Concentrations (g/L) in the Ringold E Unit at 1993 (Base Case)

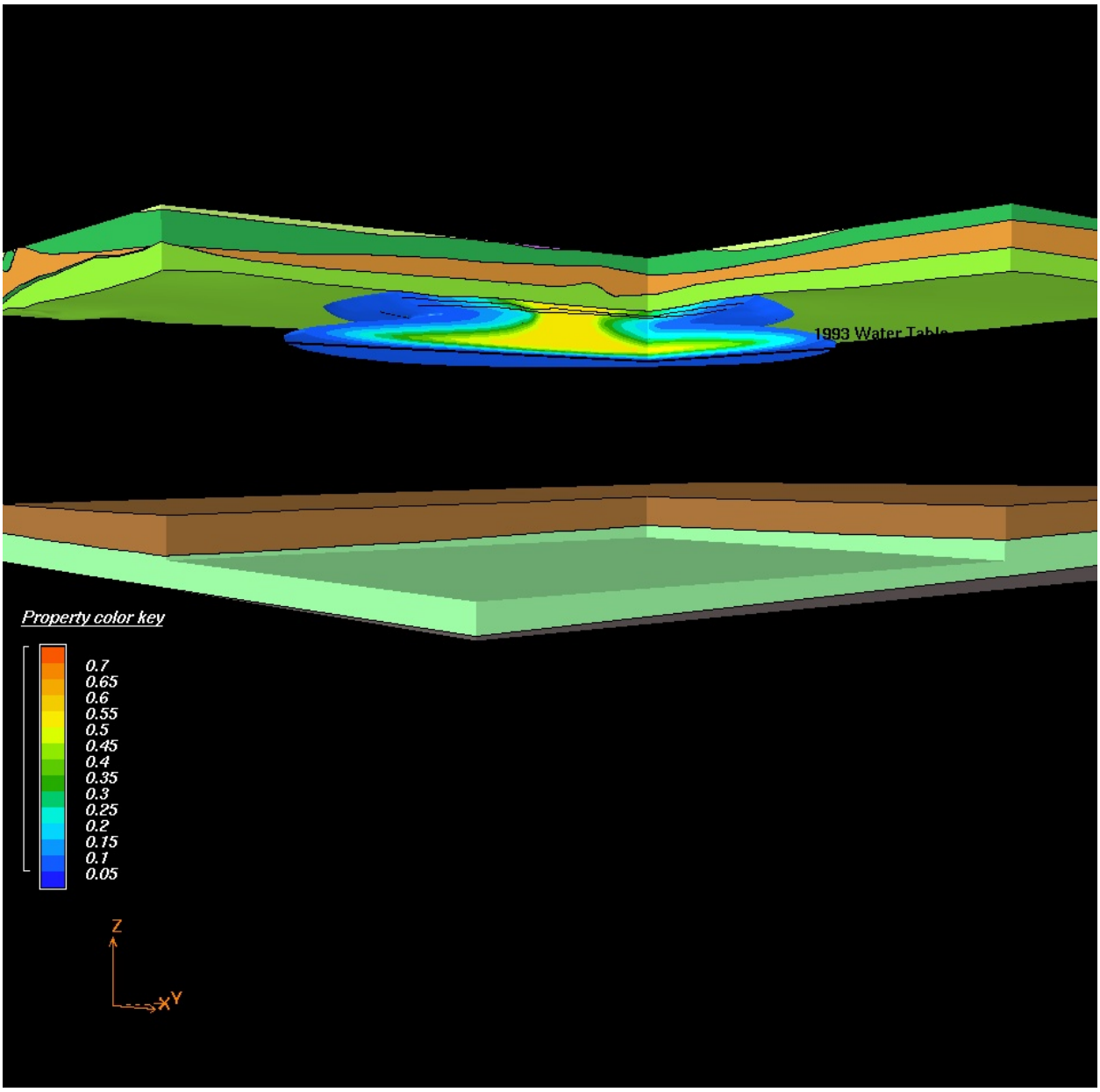

Figure 6.8. Dissolved Gaseous DNAPL Concentrations (g/L) in the Ringold E and Cold Creek Silt and Carbonate Layers at 1993 (Base Case)

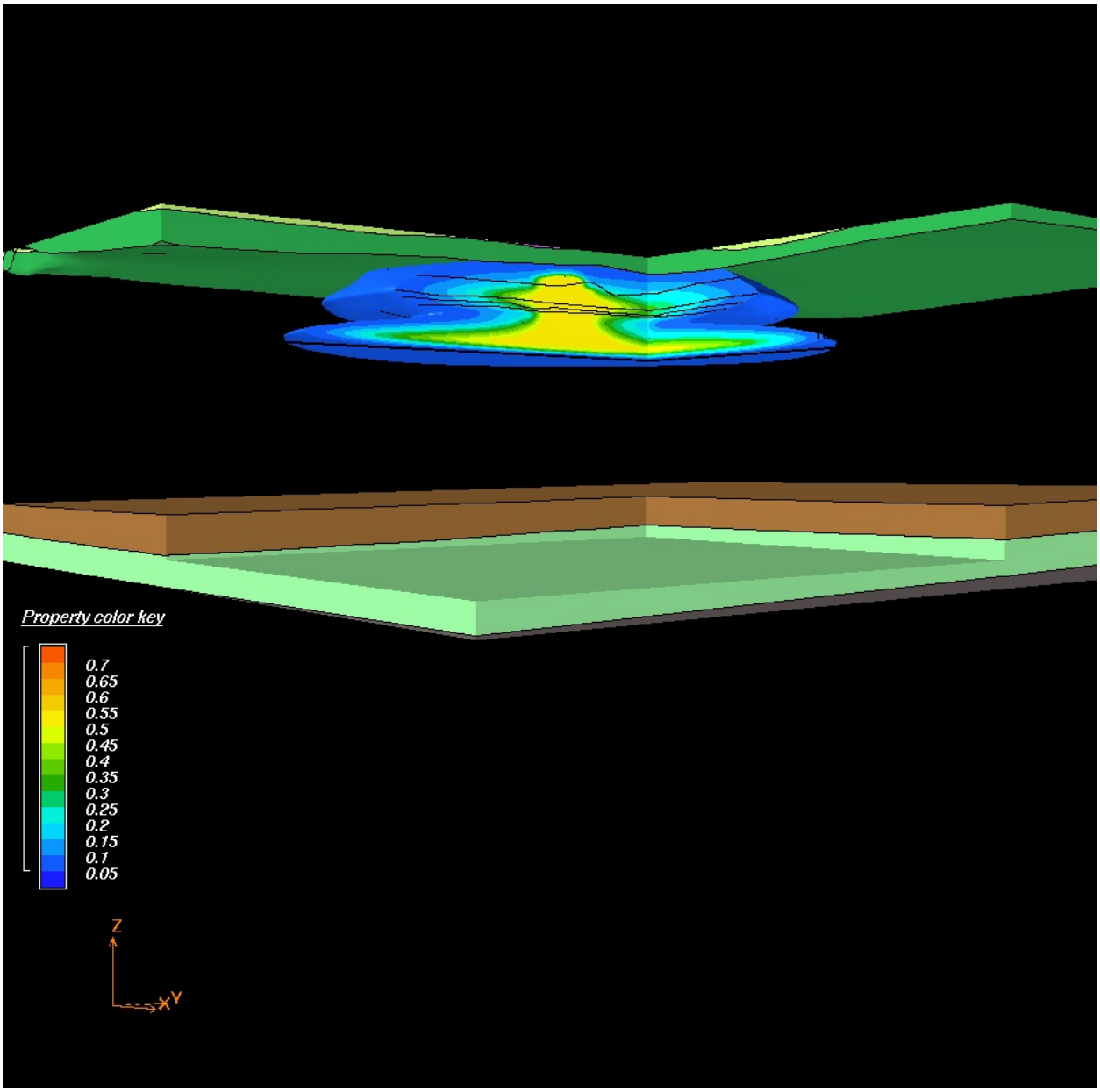

Figure 6.9. Dissolved Gaseous DNAPL Concentrations (g/L) in the Ringold E, Cold Creek, and Hanford Layers at 1993 (Base Case)

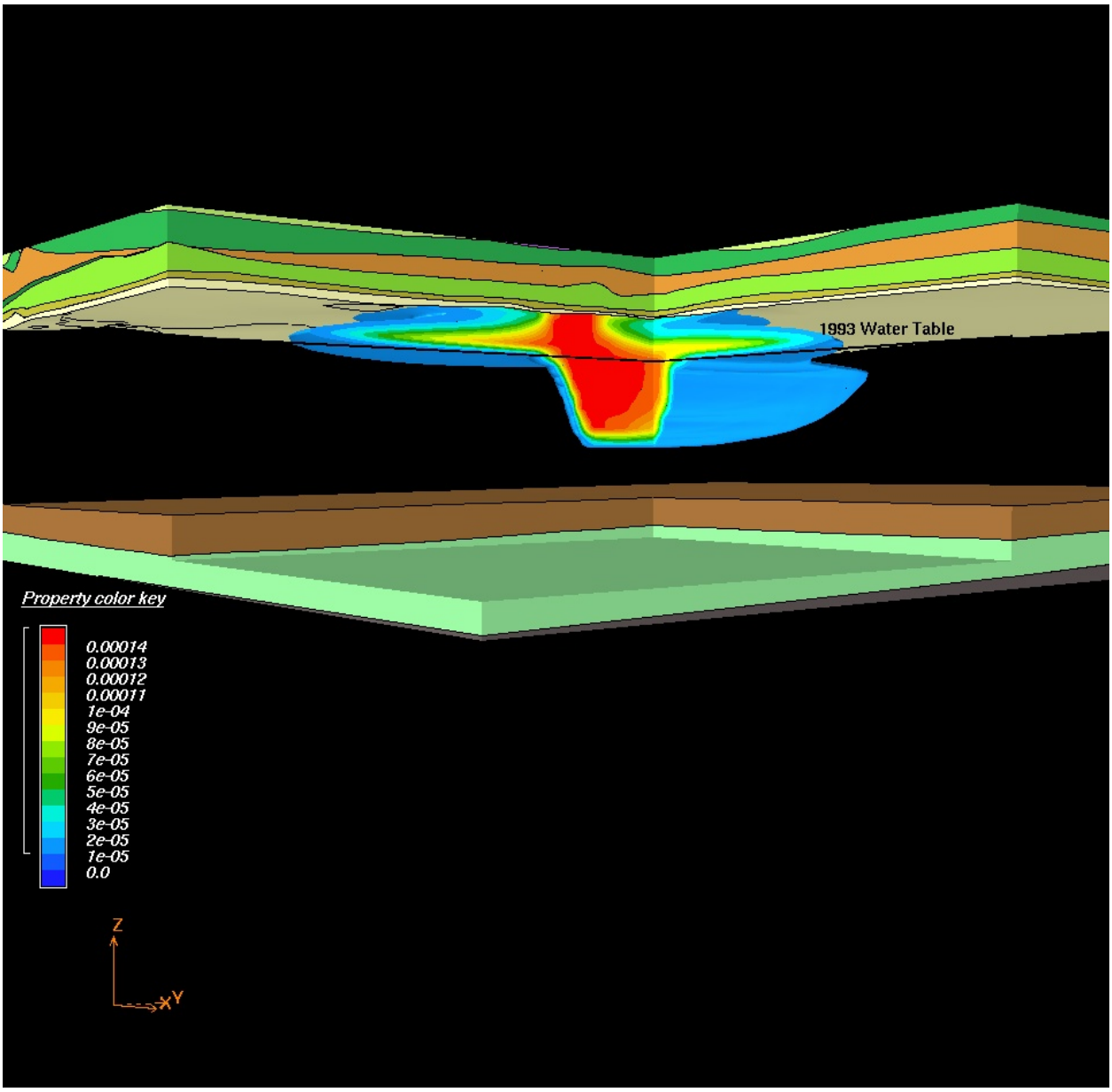

Figure 6.10. Sorbed DNAPL Concentrations (kg/kg) in the Ringold E Unit at 1993 (Base Case)

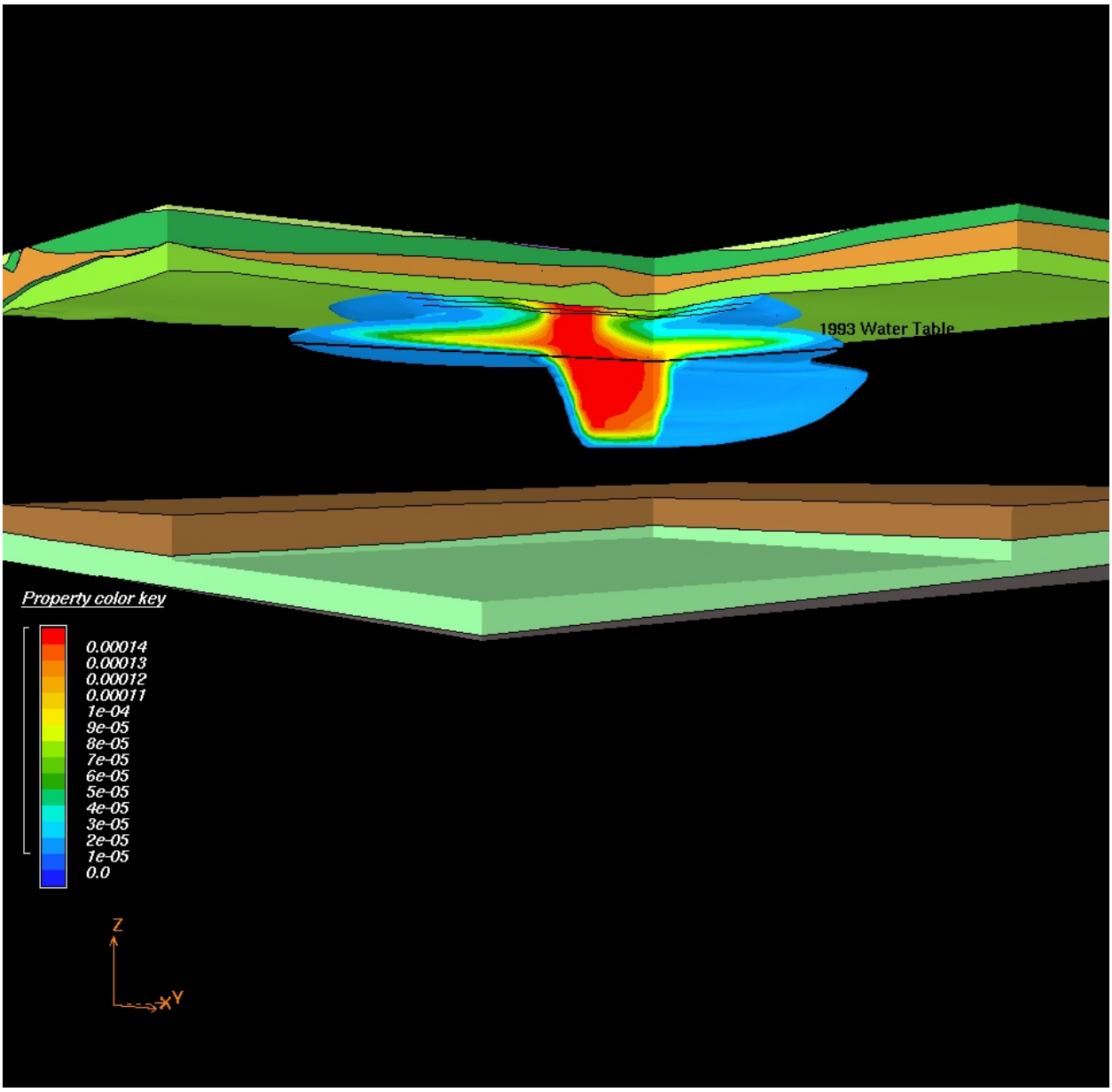

Figure 6.11. Sorbed DNAPL Concentrations (kg/kg) in the Ringold E and Cold Creek Layers at 1993 (Base Case)

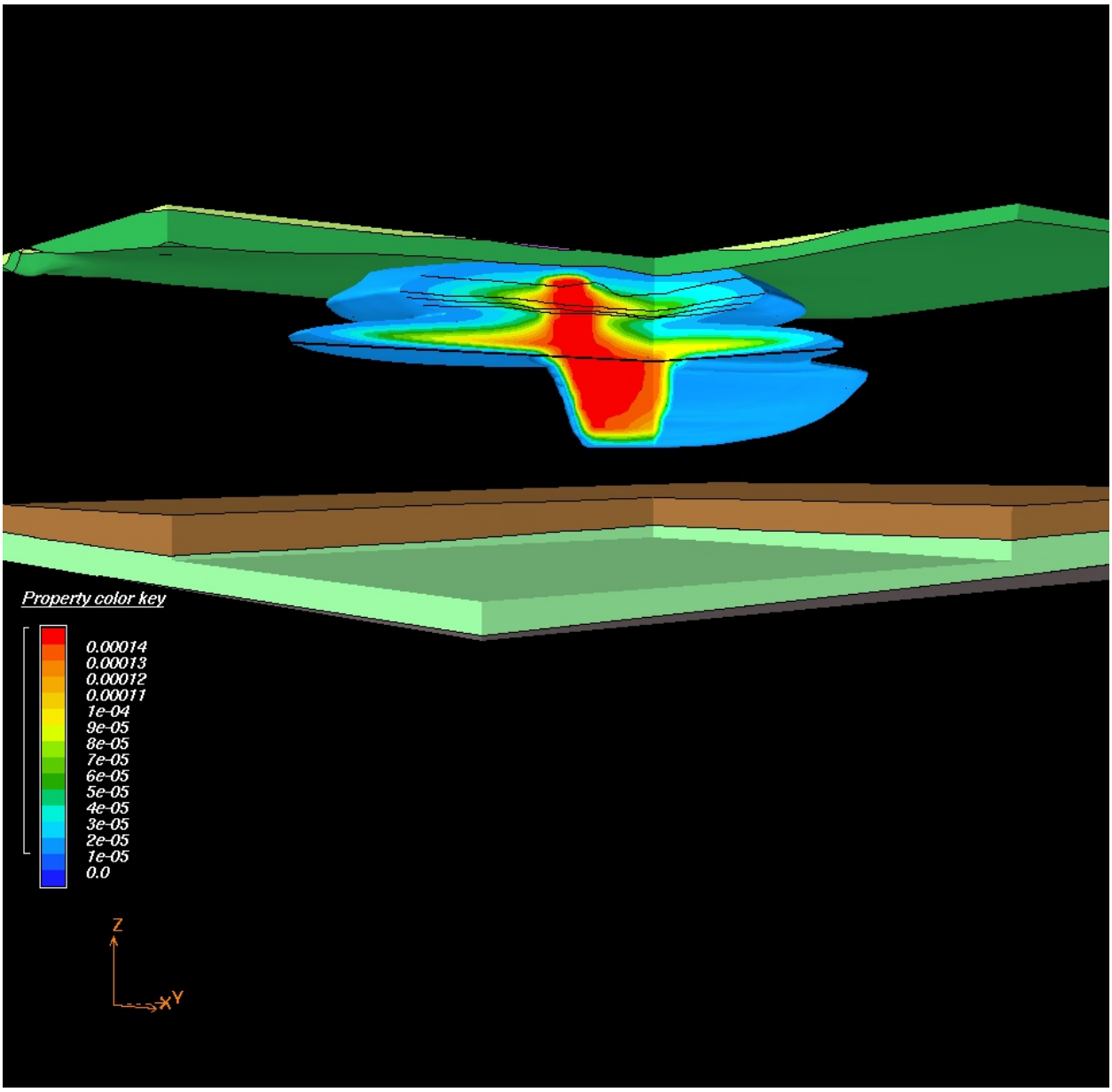

Figure 6.12. Sorbed DNAPL Concentrations (kg/kg) in the Ringold E, Cold Creek, and Hanford Units at 1993 (Base Case)

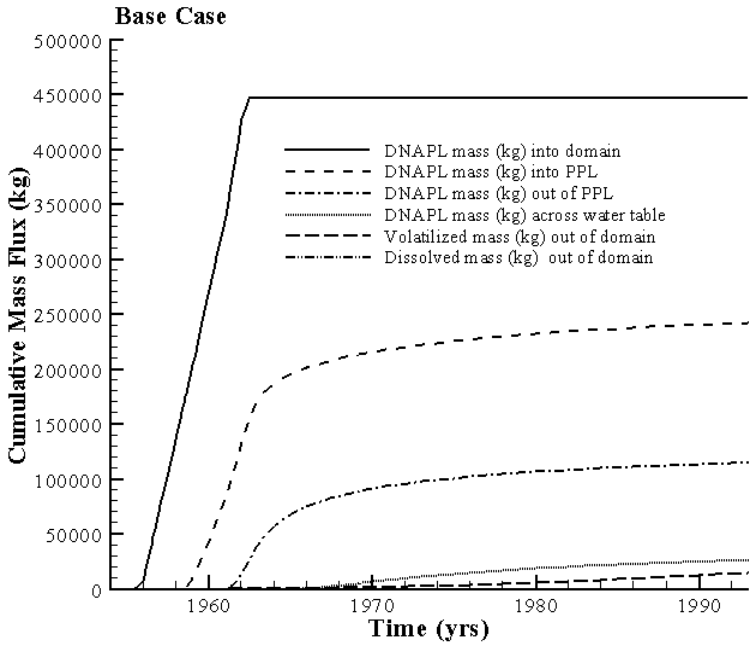

Figure 6.13. Cumulative DNAPL and Dissolved Mass Fluxes (Base Case). In the legend, PPL is used to indicate the Cold Creek unit.

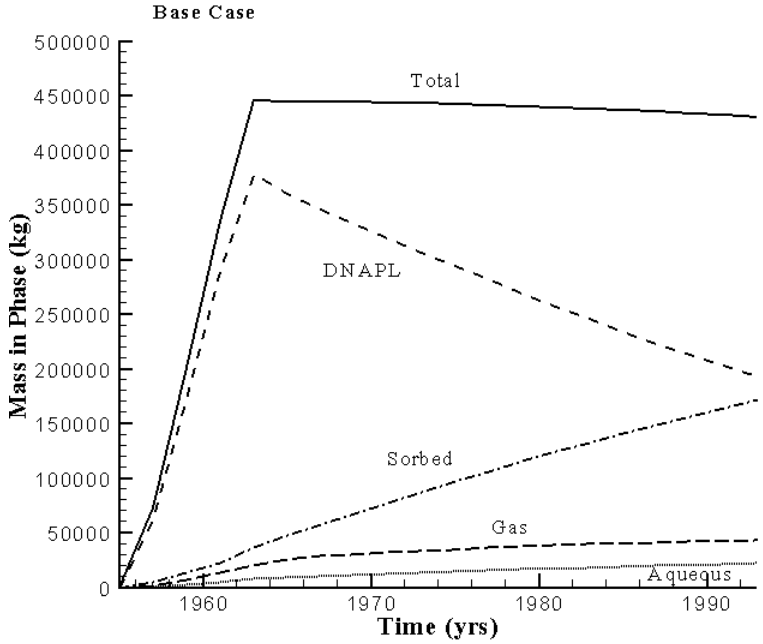

Figure 6.14. Volatile Organic Compound (VOC) Mass Distribution Over the NAPL, Sorbed, Aqueous and Gaseous Phases (Base Case)

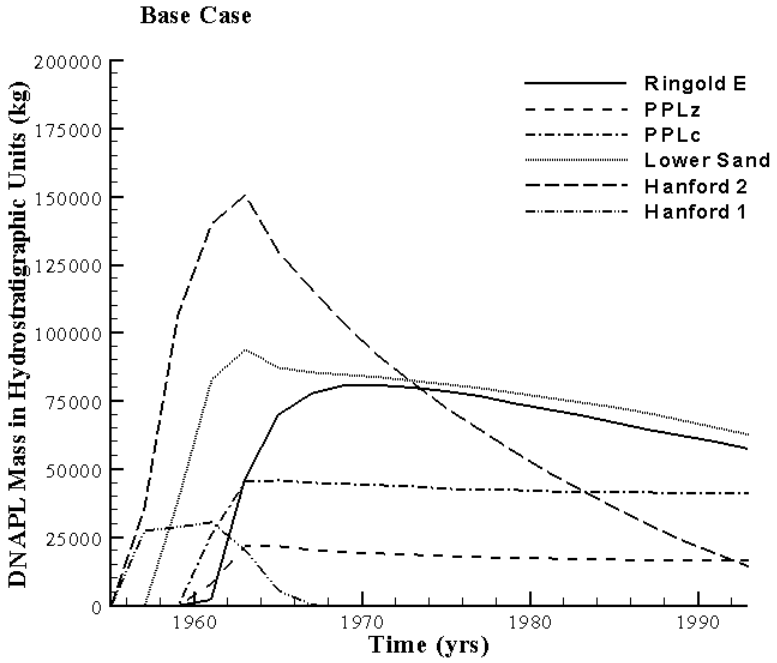

Figure 6.15. DNAPL Mass Distribution Over the Hydrostratigraphic Units (Base Case). In the legend, PPLz is used to indicate the Cold Creek silt and PPLc is used to indicate the Cold Creek carbonate.

6.2 Sensitivity Simulations

Results of all 22 sensitivity analysis simulations are described in this section. The results are compared against the results from the Base Case simulation. A comparison of the individual sensitivity simulation results is presented in Section 6.3.

6.2.1 Simulation 1

In this simulation, the total amount of disposed DNAPL was increased to 5.80E5 kg. An overview of the DNAPL body at 1993 is shown in Figure 6.16. Selective cumulative mass fluxes are shown in Figure 6.17. Mass distributions over the fluid phases and hydrostratigraphic units are presented in Figures 6.18 and 6.19, respectively. The shape of the curves for the cumulative mass fluxes for Simulation 1 and the Base Case are similar, although more DNAPL entered the domain, the Cold Creek unit, and the water table. The first kilogram of DNAPL reached the water table after 7.1 years. The Cold Creek silt and carbonate layers were also able to retain more DNAPL as a result of spreading. The amount of DNAPL in these units was approximately 160,000 kg at 1993. The simulation predicts that in 1993 DNAPL was still draining from the Hanford 2 sand into the lower sand. From the lower sand, DNAPL moves into the Cold Creek silt layer. The reduction of DNAPL mass in the Ringold E is the result of DNAPL dissolution. The maximum DNAPL saturation at 1993 is 0.106. The location of the maximum saturation is in the Cold Creek silt.

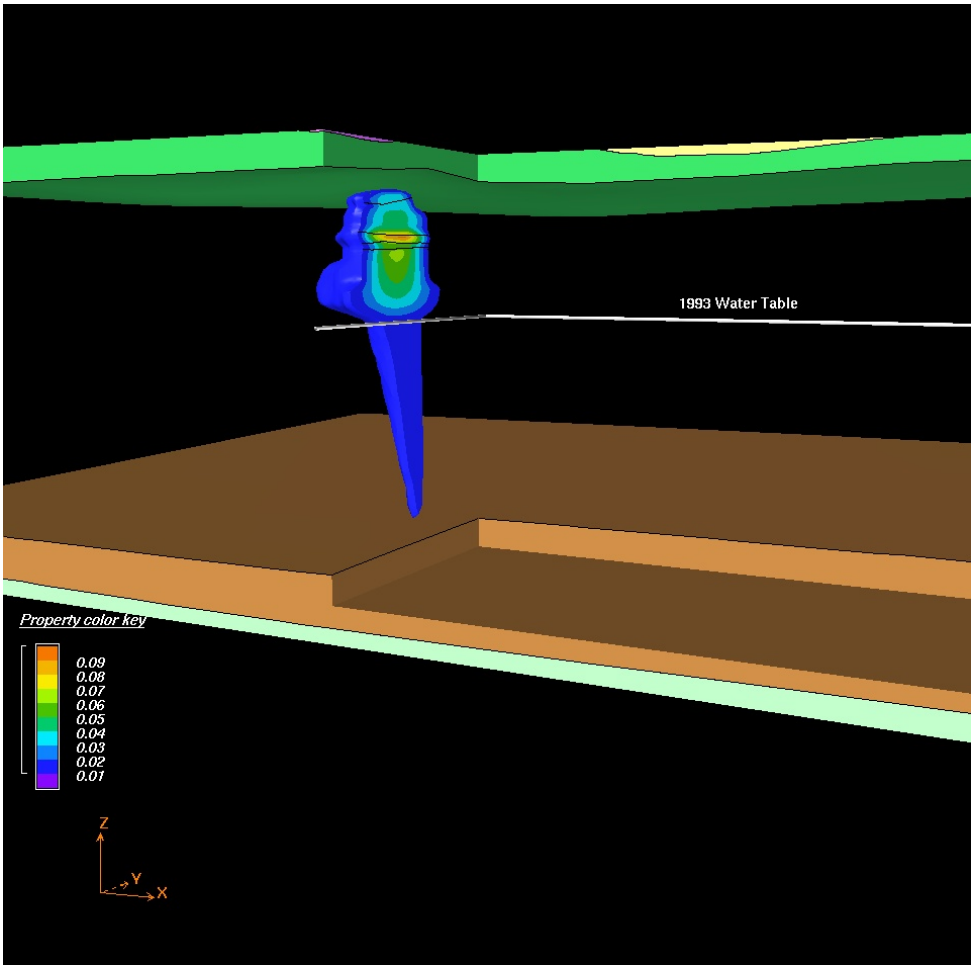

Figure 6.16. DNAPL Body in the Ringold E, Cold Creek, and Hanford Units at 1993 (Simulation 1)

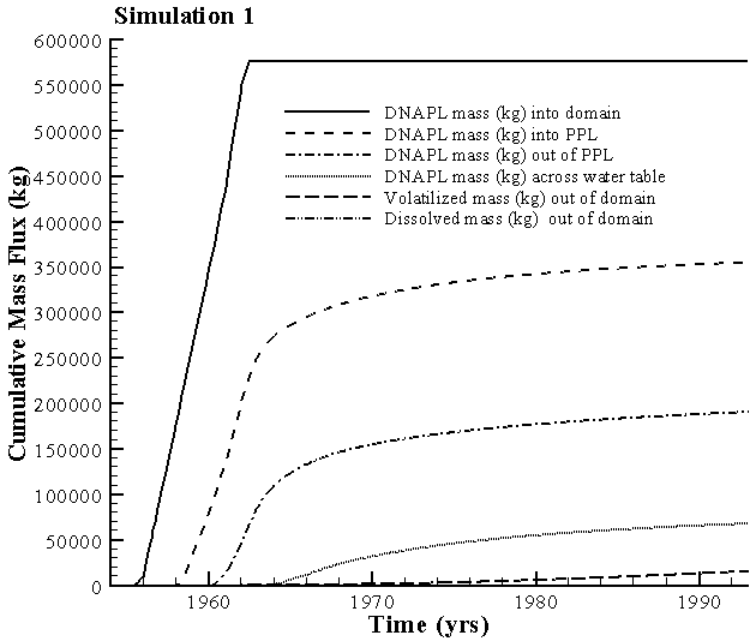

Figure 6.17. Cumulative DNAPL and Dissolved Mass Fluxes (Simulation 1). In the legend, PPL is used to indicate the Cold Creek unit.

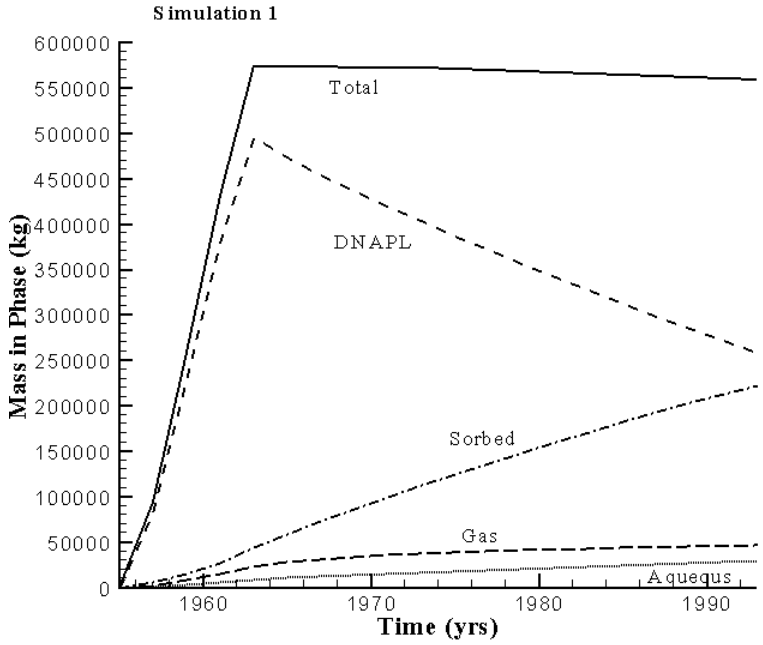

Figure 6.18. Volatile Organic Compound (VOC) Mass Distribution Over the NAPL, Sorbed, Aqueous, and Gaseous Phases (Simulation 1)

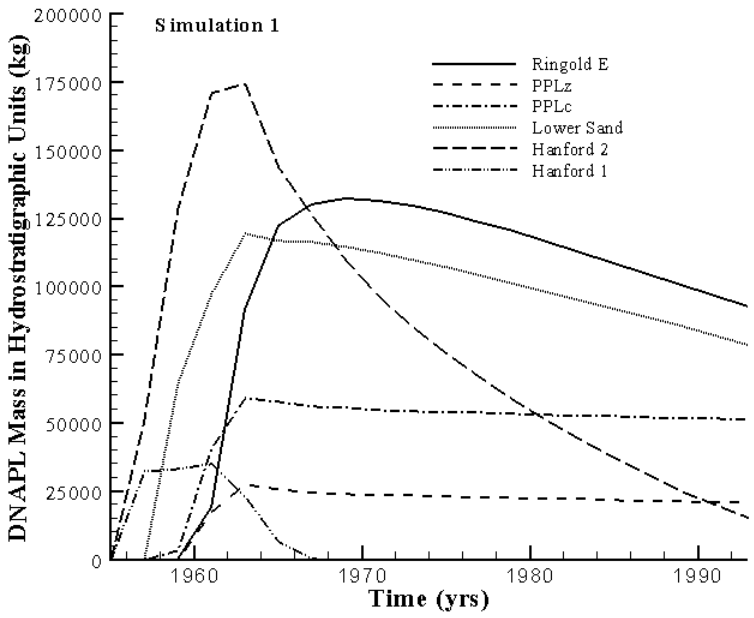

Figure 6.19. DNAPL Mass (kg) Distribution Over the Hydrostratigraphic Units (Simulation 1). In the legend, PPLz is used to indicate the Cold Creek silt and PPLc is used to indicate the Cold Creek carbonate.

6.2.2 Simulation 2

In this simulation, the total amount of disposed DNAPL was reduced to 1.61E5 kg. An overview of the DNAPL body at 1993 is shown in Figure 6.20. This figure shows that the DNAPL's lowest location is in the unsaturated part of the Ringold E units. The disposed amount was not sufficient enough to make it to the water table. Selective cumulative mass fluxes are shown in Figure 6.21. Mass distributions over the fluid phases and hydrostratigraphic units are presented in Figures 6.22 and 6.23, respectively. The maximum DNAPL saturation at 1993 is 0.096. The location of the maximum saturation is in the Cold Creek silt.

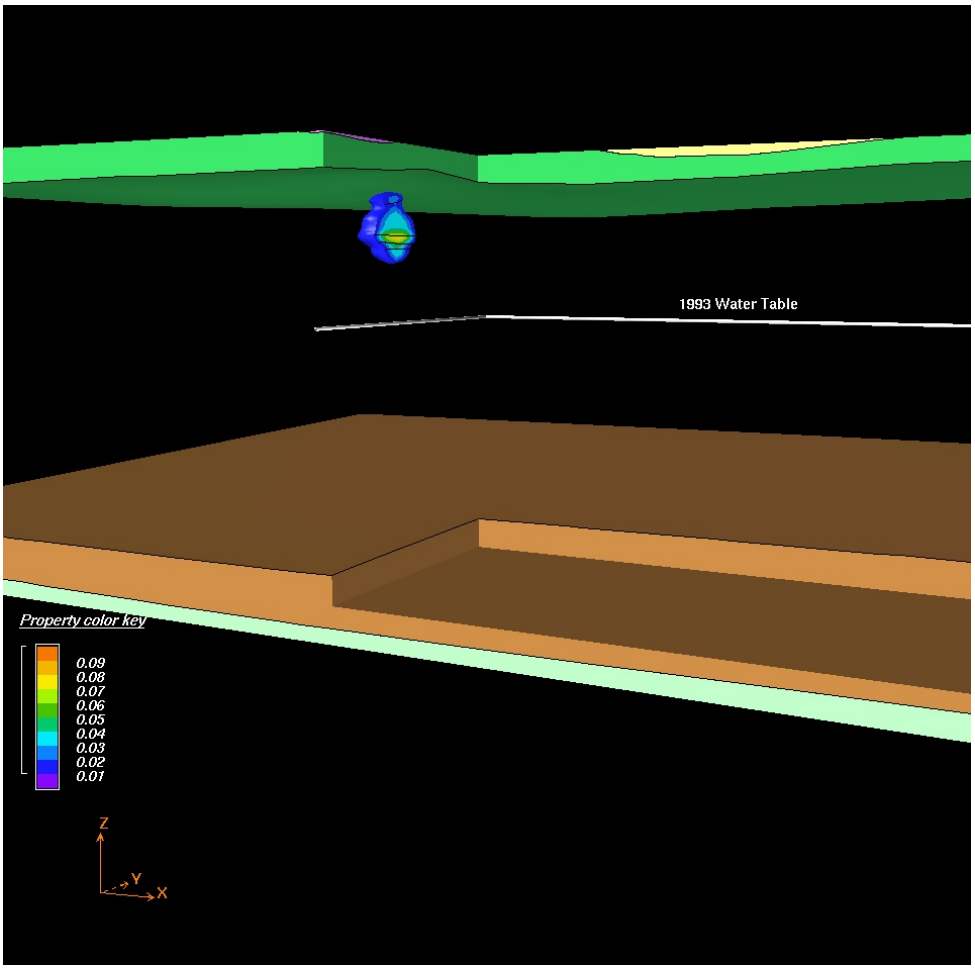

Figure 6.20. DNAPL Body in the Ringold E, Cold Creek, and Hanford Units at 1993 (Simulation 2)

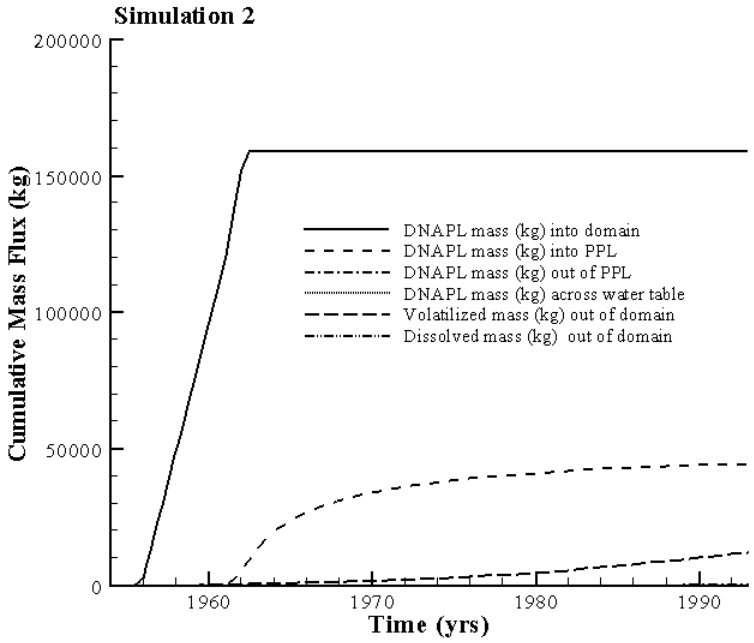

Figure 6.21. Cumulative DNAPL and Dissolved Mass Fluxes (Simulation 2). In the legend, PPL is used to indicate the Cold Creek unit.

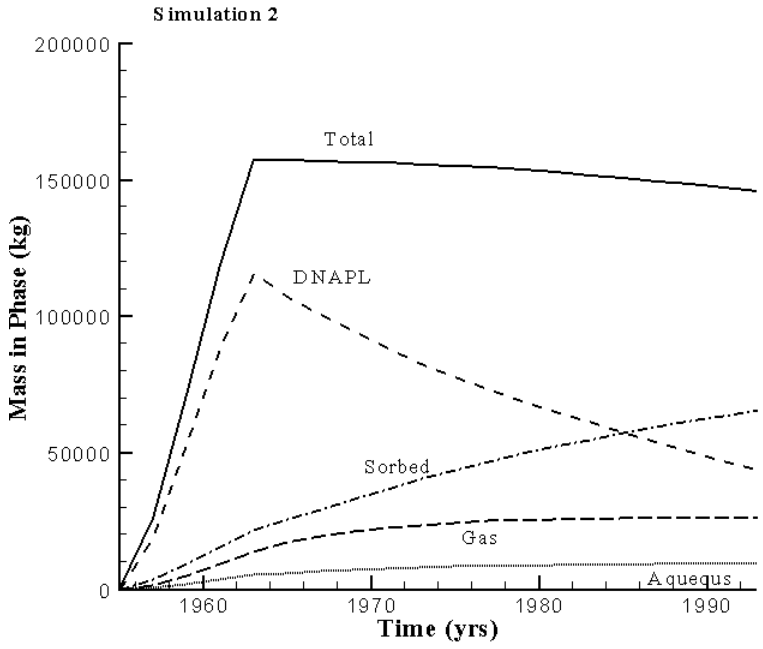

Figure 6.22. Volatile Organic Compound (VOC) Mass Distribution Over the NAPL, Sorbed, Aqueous, and Gaseous Phases (Simulation 2)

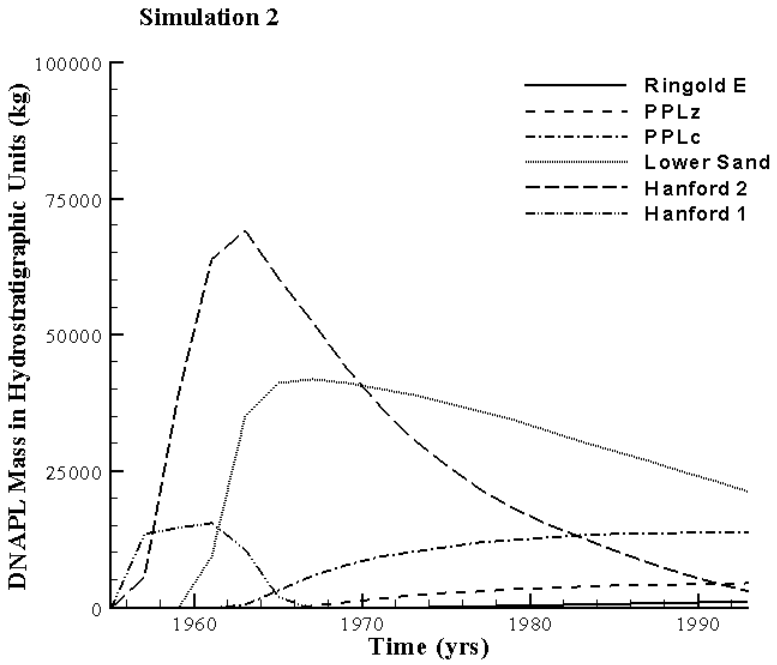

Figure 6.23. DNAPL Mass (kg) Distribution Over the Hydrostratigraphic Units (Simulation 2). In the legend, PPLz is used to indicate the Cold Creek silt and PPLc is used to indicate the Cold Creek carbonate.

6.2.3 Simulation 3

In this simulation, the properties of the DNAPL were those of pure CT. An overview of the DNAPL body at 1993 is shown in Figure 6.24. This figure looks similar to Figure 6.13 for the Base Case. Selected cumulative mass fluxes are shown in Figure 6.25. Mass distributions over the fluid phases and hydrostratigraphic units are presented in Figures 6.26 and 6.27, respectively. A comparison of these figures and the related figures for the Base Case show only marginal differences. The maximum DNAPL saturation at 1993 is 0.094. The location of the maximum saturation is in the Cold Creek silt.

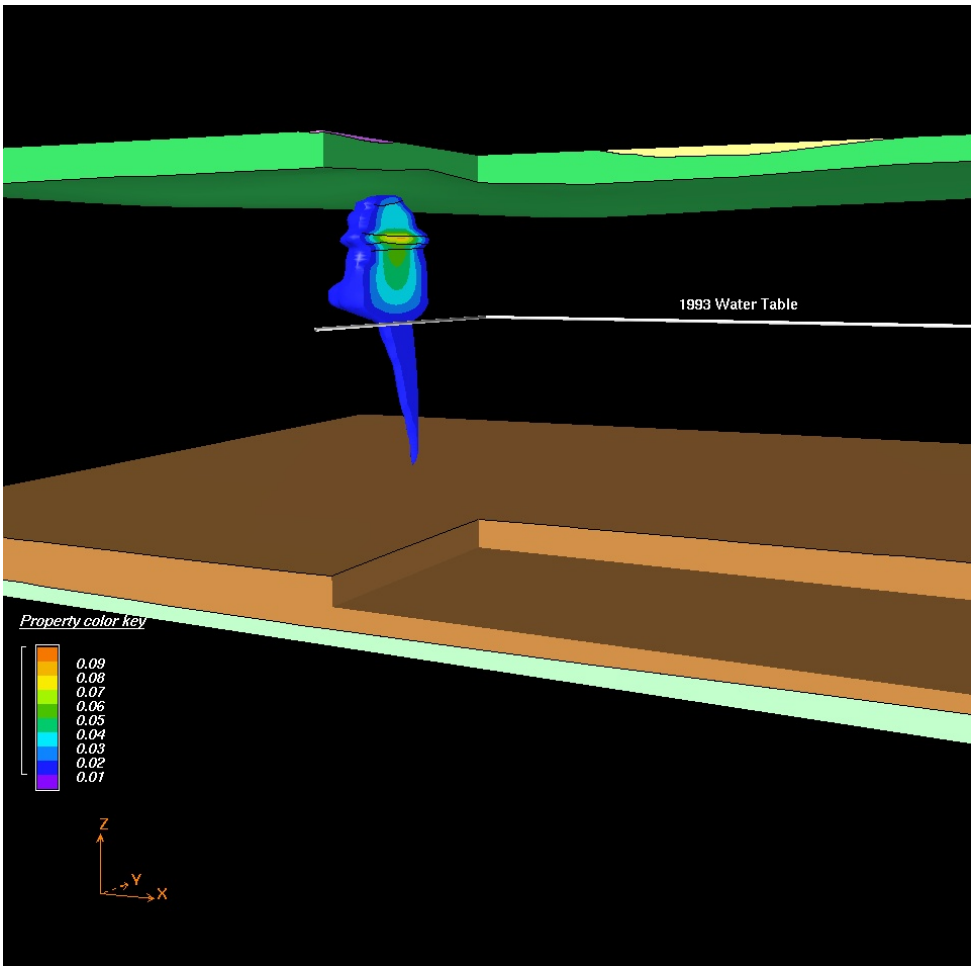

Figure 6.24. DNAPL Body in the Ringold E, Cold Creek, and Hanford Units at 1993 (Simulation 3)

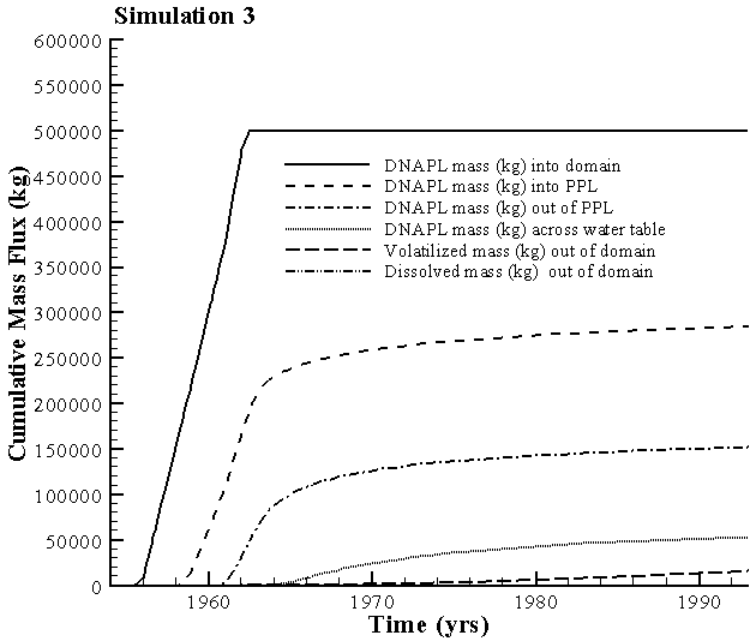

Figure 6.25. Cumulative DNAPL and Dissolved Mass Fluxes (Simulation 3). In the legend, PPL is used to indicate the Cold Creek unit.

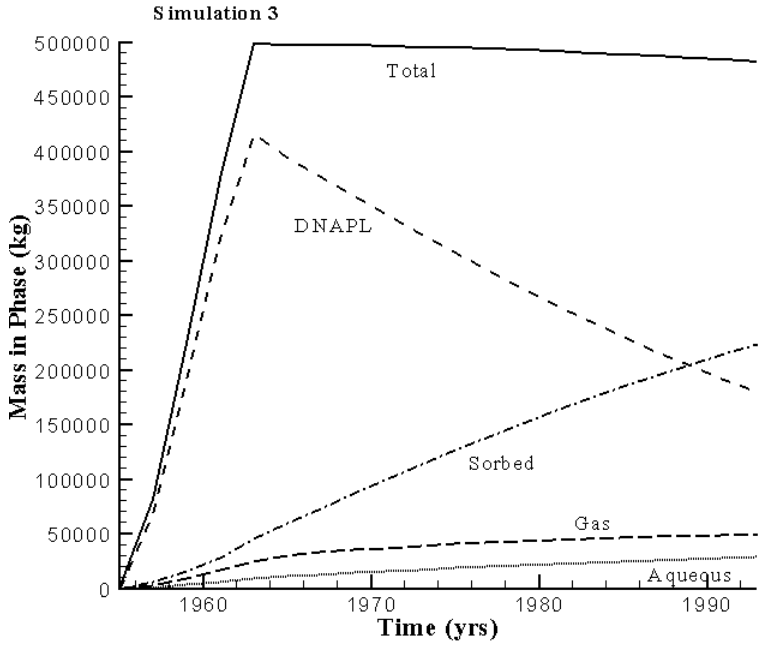

Figure 6.26. Volatile Organic Compound (VOC) Mass Distribution Over the NAPL, Sorbed, Aqueous, and Gaseous Phases (Simulation 3)

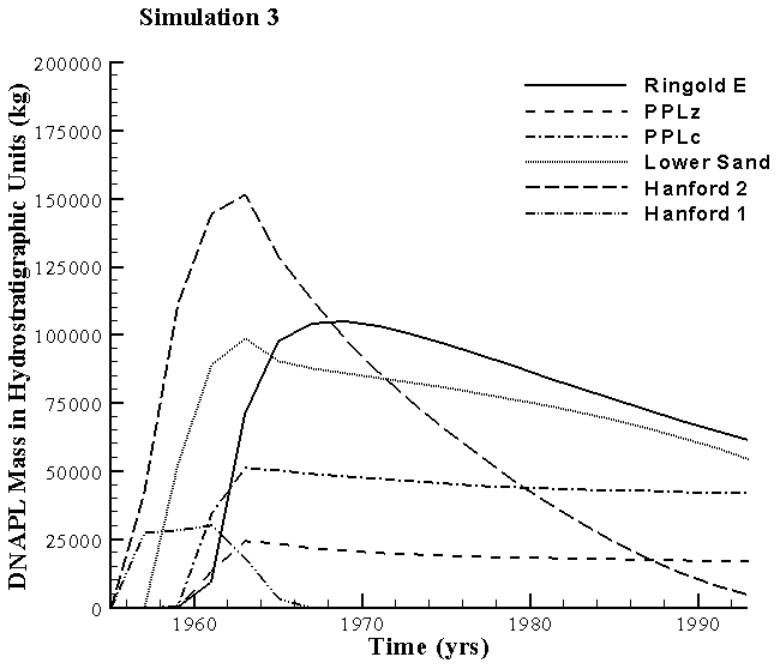

Figure 6.27. DNAPL Mass (kg) Distribution Over the Hydrostratigraphic Units (Simulation 3). In the legend, PPLz is used to indicate the Cold Creek silt and PPLc is used to indicate the Cold Creek carbonate.

6.2.4 Simulation 4

In this simulation, the DNAPL composition represents the lowest estimate of the CT fraction. An overview of the DNAPL body at 1993 is shown in Figure 6.28. This figure shows that the overall shape of the DNAPL body is similar to the Base Case but that the DNAPL penetrates less deep below the water table. Selective cumulative mass fluxes are shown in Figure 6.29. Mass distributions over the fluid phases and hydrostratigraphic units are presented in Figures 6.30 and 6.31, respectively. The travel time for the first kilogram to reach the water table was 11.9 years. At 1993, 59% of the original DNAPL inventory remained in the vadose zone. The maximum DNAPL saturation at 1993 is 0.117. The location of the maximum saturation is in the Cold Creek silt.

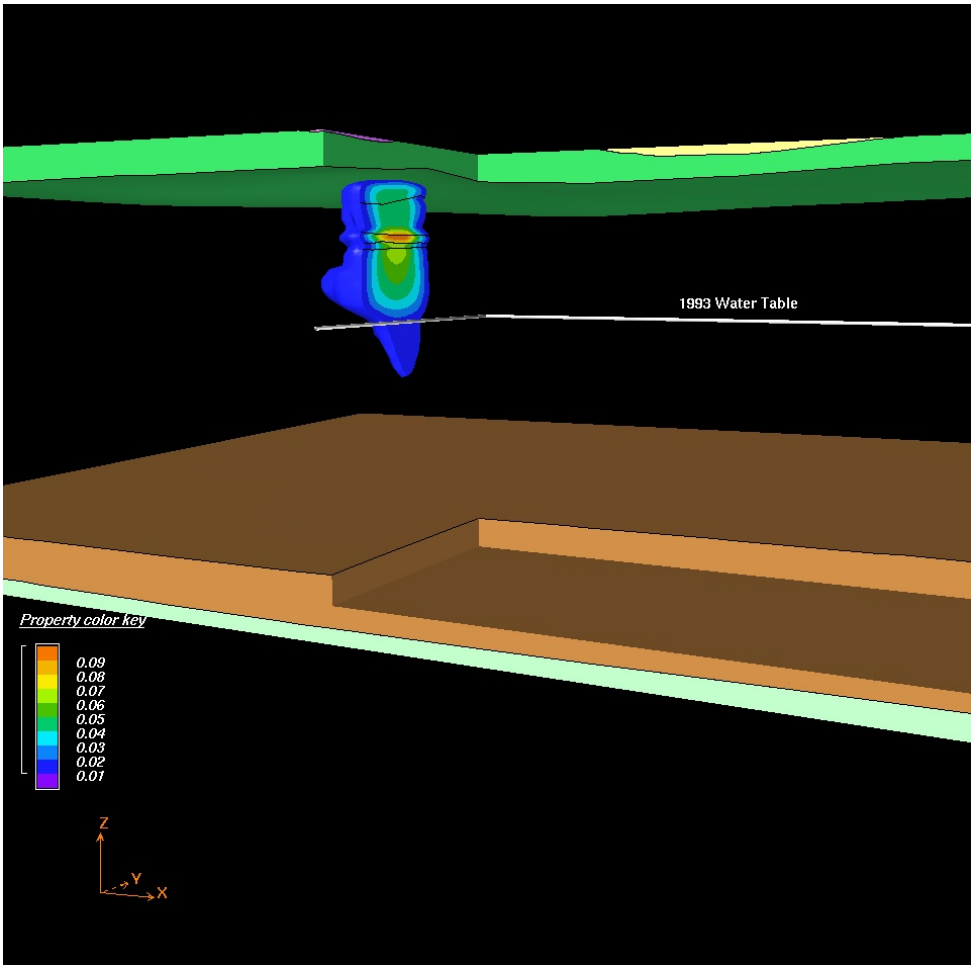

Figure 6.28. DNAPL Body in the Ringold E, Cold Creek, and Hanford Units at 1993 (Simulation 4)

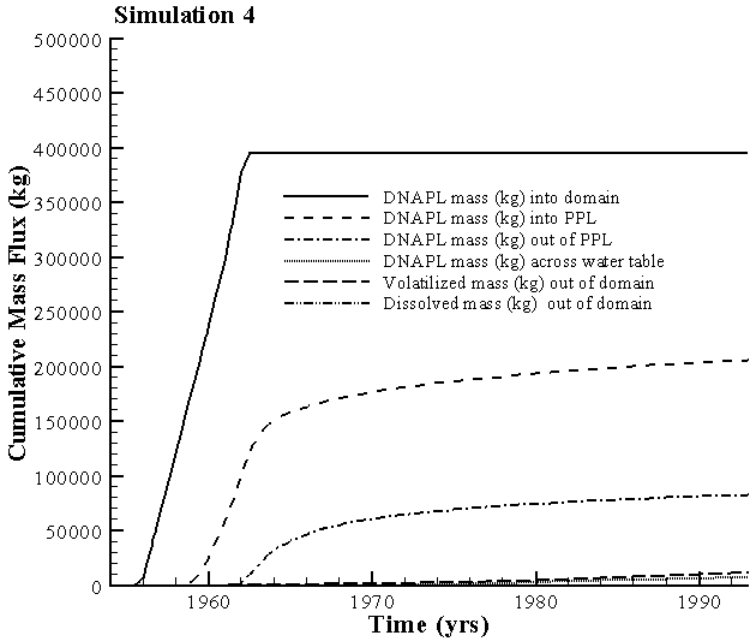

Figure 6.29. Cumulative DNAPL and Dissolved Mass Fluxes (Simulation 4). In the legend, PPL is used to indicate the Cold Creek unit.

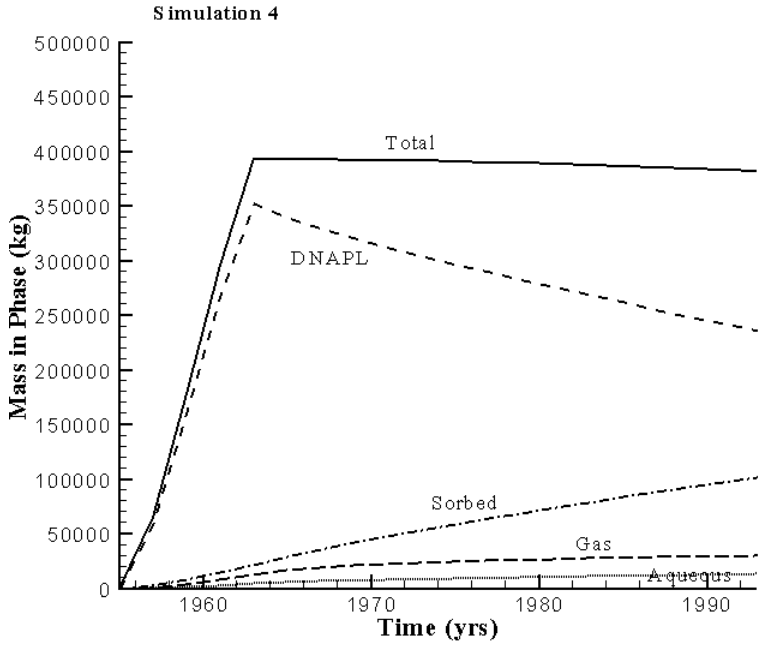

Figure 6.30. Volatile Organic Compound (VOC) Mass Distribution Over the NAPL, Sorbed, Aqueous, and Gaseous Phases (Simulation 4)

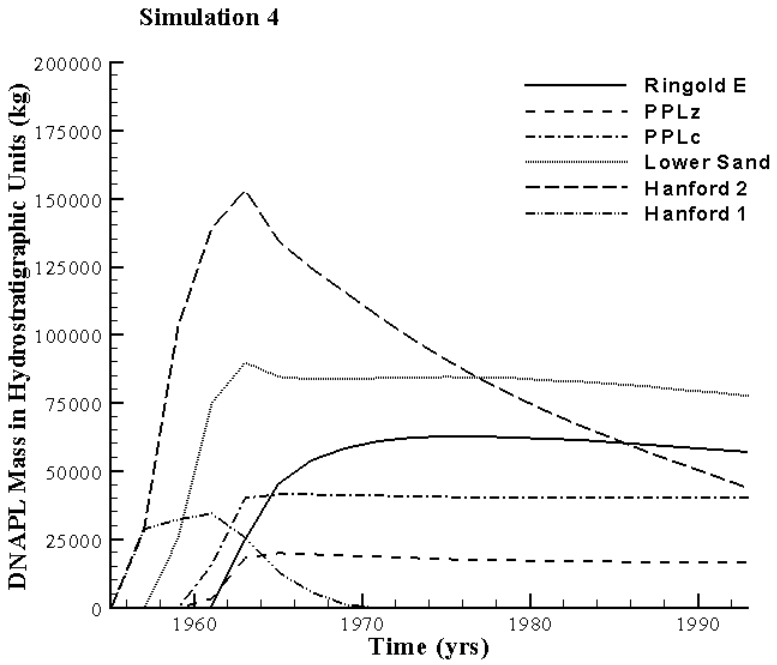

Figure 6.31. DNAPL Mass (kg) Distribution Over the Hydrostratigraphic Units (Simulation 4). In the legend, PPLz is used to indicate the Cold Creek silt and PPLc is used to indicate the Cold Creek carbonate.

6.2.5 Simulation 5

In this simulation, the DNAPL is allowed to infiltrate through an area 20% of 216 Z-9 disposal site footprint. An overview of the DNAPL body at 1993 is shown in Figure 6.32. Selective cumulative mass fluxes are shown in Figure 6.33. Mass distributions over the fluid phases and units are presented in Figures 6.34 and 6.35, respectively. The simulation results are close to the Base Case results, indicating that reducing the footprint to 20% or the original size does not considerably affect the multi-phase behavior. The travel time for the first kilogram to reach the water table was 8.2 years. At 1993, 43% of the original DNAPL inventory remained in the vadose zone. The maximum DNAPL saturation at 1993 is 0.104. The location of the maximum saturation is in the Cold Creek silt.

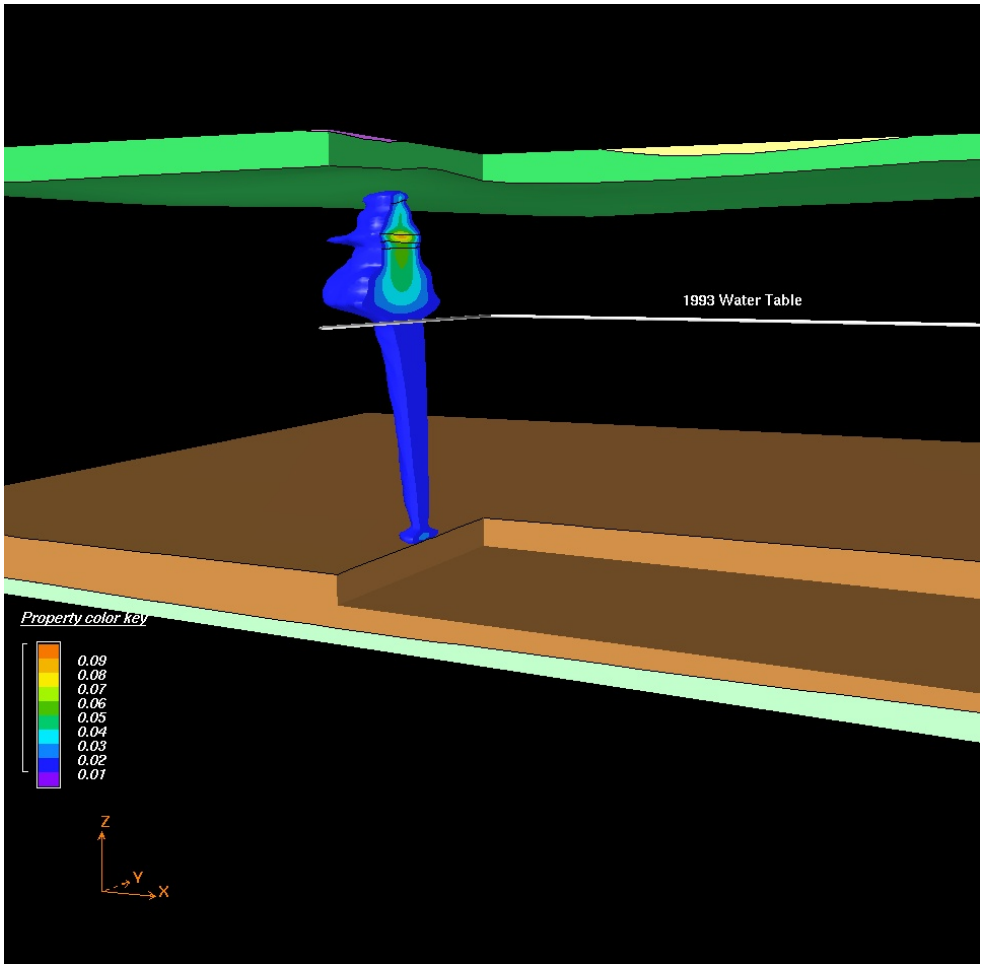

Figure 6.32. DNAPL Body in the Ringold E, Cold Creek, and Hanford Units at 1993 (Simulation 5)

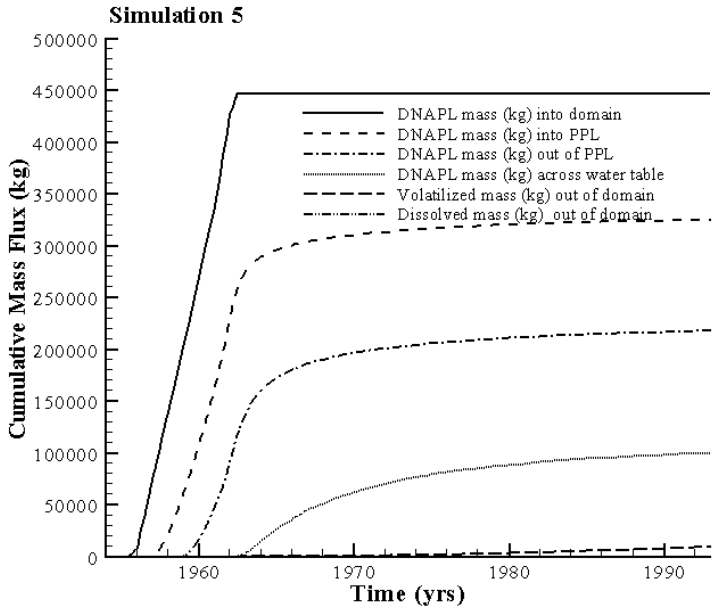

Figure 6.33. Cumulative DNAPL and Dissolved Mass Fluxes (Simulation 5). In the legend, PPL is used to indicate the Cold Creek unit.

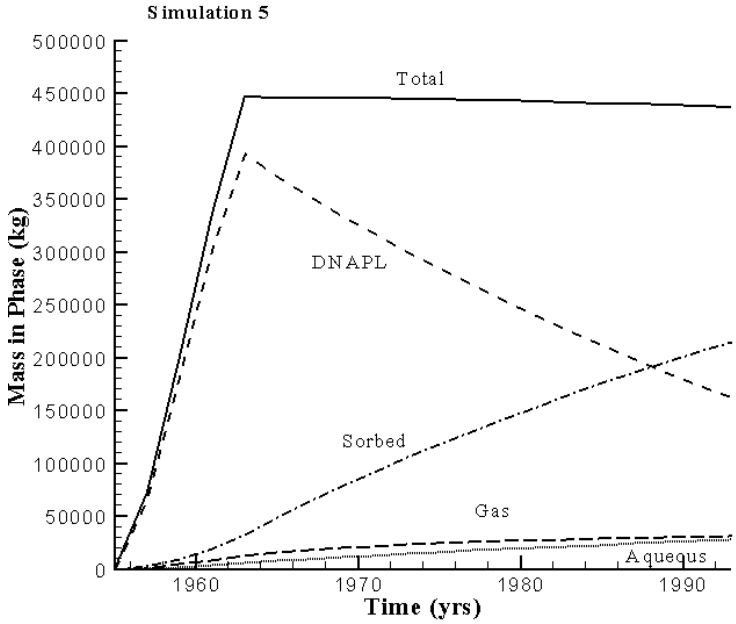

Figure 6.34. Volatile Organic Compound (VOC) Mass Distribution Over the NAPL, Sorbed, Aqueous, and Gaseous Phases (Simulation 5)

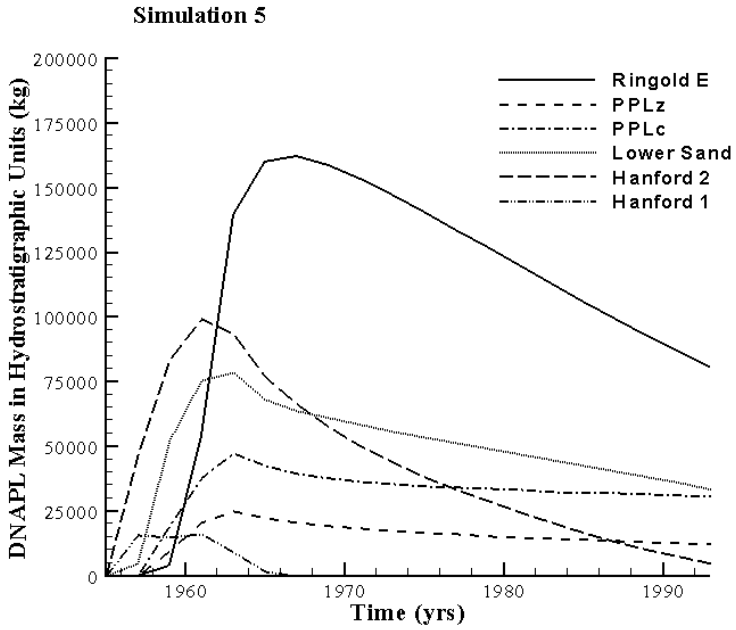

Figure 6.35. DNAPL Mass (kg) Distribution Over the Hydrostratigraphic Units (Simulation 5). In the legend, PPLz is used to indicate the Cold Creek silt and PPLc is used to indicate the Cold Creek carbonate.

6.2.6 Simulation 6

In this simulation, the DNAPL the infiltration rates are increased by a factor 4, for one week per month only. The total inventory did not change. An overview of the DNAPL body at 1993 is shown in Figure 6.36. Selective cumulative mass fluxes are shown in Figure 6.37. Mass distributions over the fluid phases and units are presented in Figures 6.38 and 6.39, respectively. The simulation results are very close to the Base Case results, indicating that the altered infiltration regime does not affect the multi-phase behavior. The travel time for the first kilogram to reach the water table was 9.4 years. At 1993, 36% of the original DNAPL inventory remained in the vadose zone. The maximum DNAPL saturation at 1993 is 0.104. The location of the maximum saturation is in the Cold Creek silt.

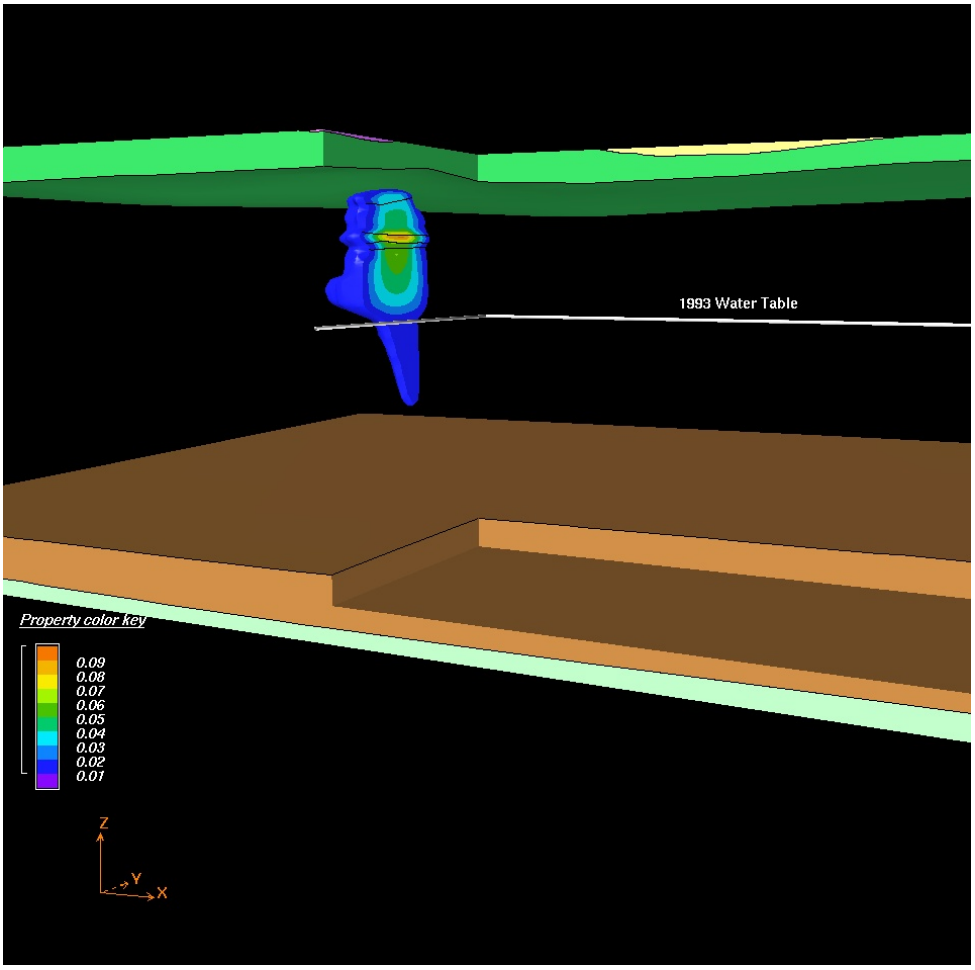

Figure 6.36. DNAPL Body in the Ringold E, Cold Creek, and Hanford Units at 1993 (Simulation 6)

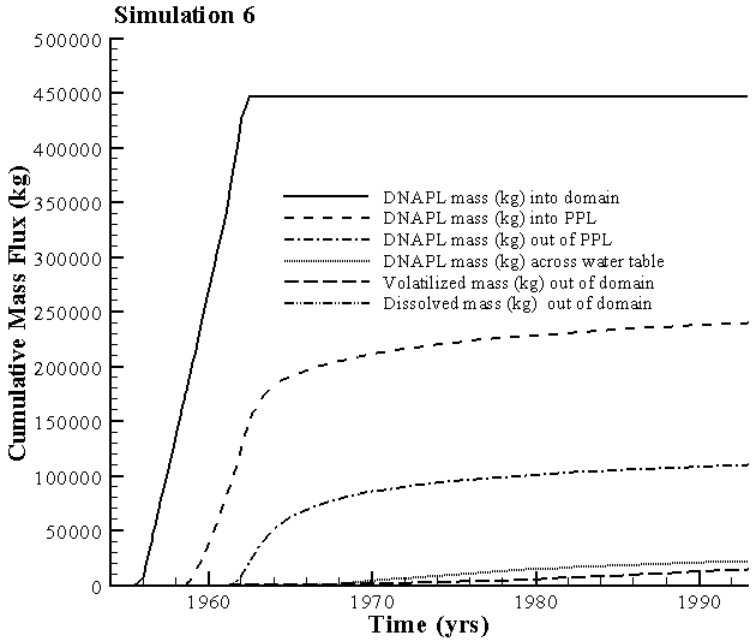

Figure 6.37. Cumulative DNAPL and Dissolved Mass Fluxes (Simulation 6). In the legend, PPL is used to indicate the Cold Creek unit.

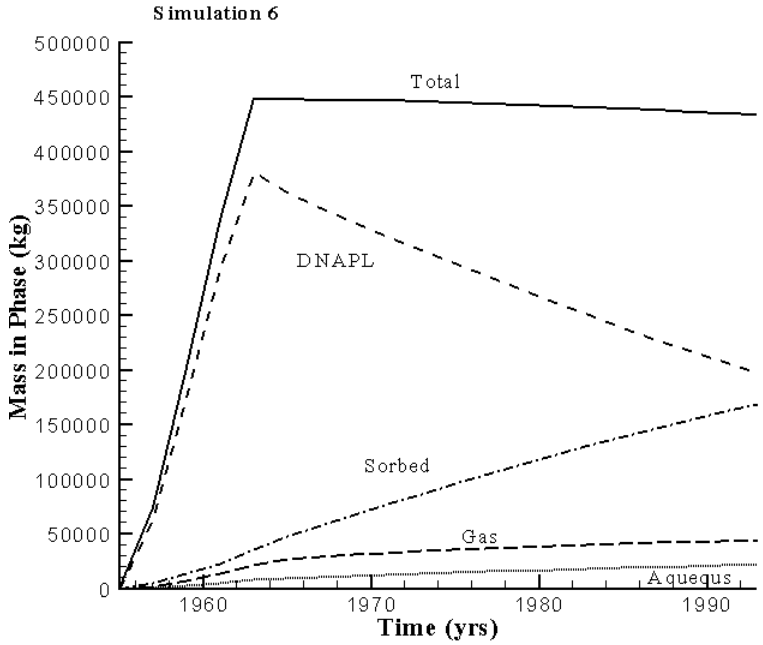

Figure 6.38. Volatile Organic Compound (VOC) Mass Distribution Over the NAPL, Sorbed, Aqueous, and Gaseous Phases (Simulation 6)

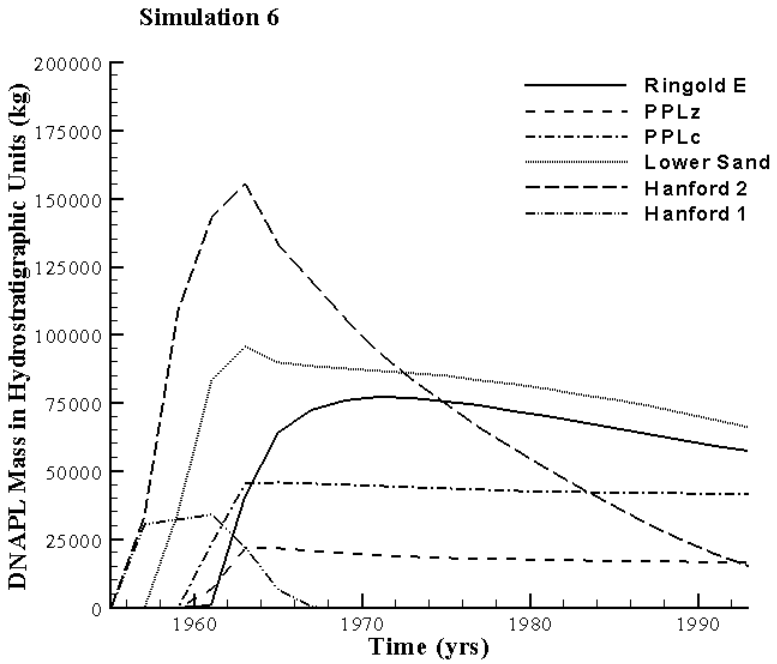

Figure 6.39. DNAPL Mass (kg) Distribution Over the Hydrostratigraphic Units (Simulation 6). In the legend, PPLz is used to indicate the Cold Creek silt and PPLc is used to indicate the Cold Creek carbonate.

6.2.7 Simulation 7

This simulation is a combination of Simulation 5 and 6. An overview of the DNAPL body at 1993 is shown in Figure 6.40. The figure shows that DNAPL moves down all the way to the Ringold Mud and it starts to pool on top of this low permeability unit. Selective cumulative mass fluxes are shown in Figure 6.41. Mass distributions over the fluid phases and hydrostratigraphic units are presented in Figures 6.42 and 6.43, respectively. The combination of the smaller footprint and the increased infiltration rates caused the DNAPL to move faster in the vertical direction. Compared to the Base Case, about three times as much DNAPL moved across the water table. The travel time for the first kilogram to reach the water table was 6.4 years. At 1993, 28% of the original DNAPL inventory remained in the vadose zone. The maximum DNAPL saturation at 1993 is 0.103. The location of the maximum saturation is in the Cold Creek silt.

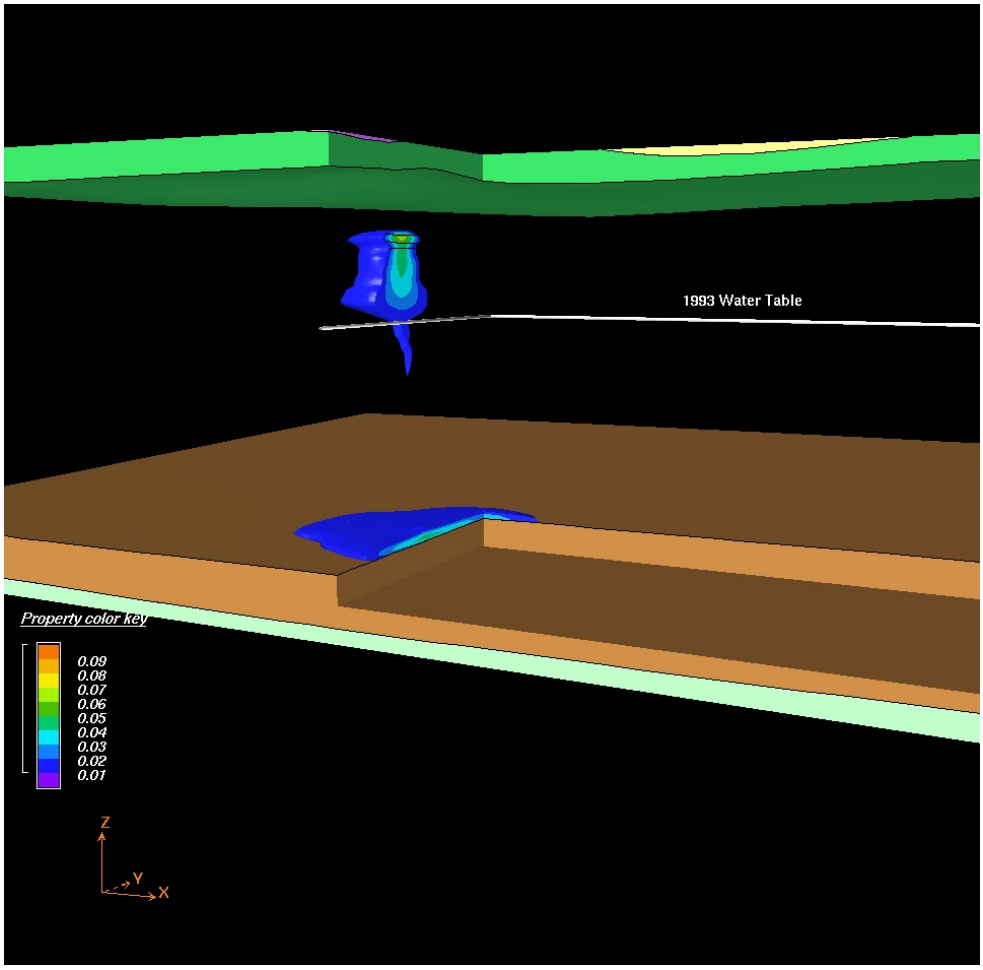

Figure 6.40. DNAPL Body in the Ringold E, Cold Creek, and Hanford Units at 1993 (Simulation 7)

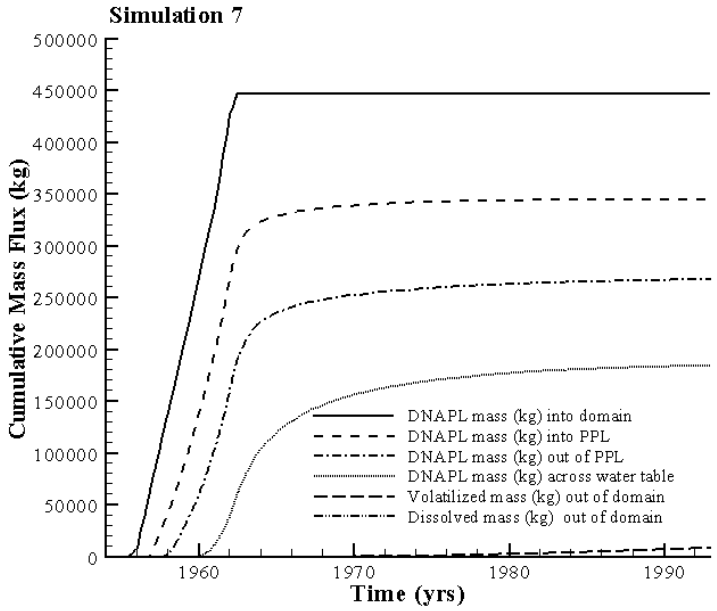

Figure 6.41. Cumulative DNAPL and Dissolved Mass Fluxes (Simulation 7). In the legend, PPL is used to indicate the Cold Creek unit.

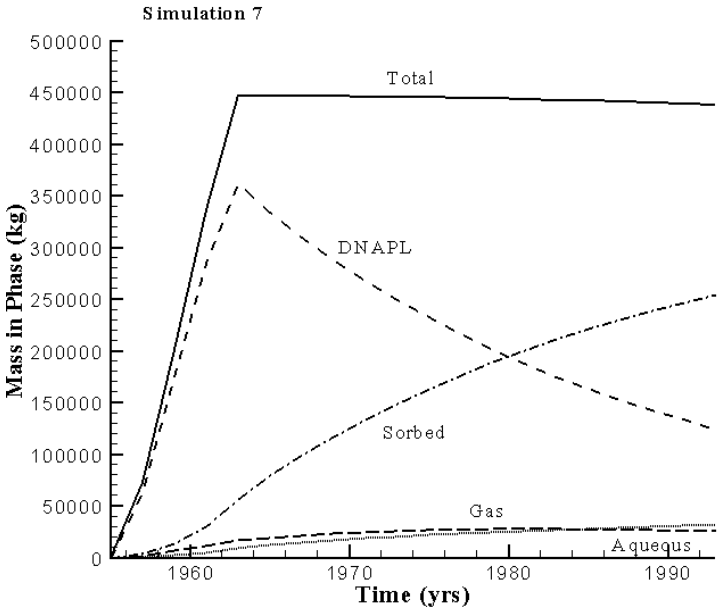

Figure 6.42. Volatile Organic Compound (VOC) Mass Distribution Over the NAPL, Sorbed, Aqueous, and Gaseous Phases (Simulation 7)

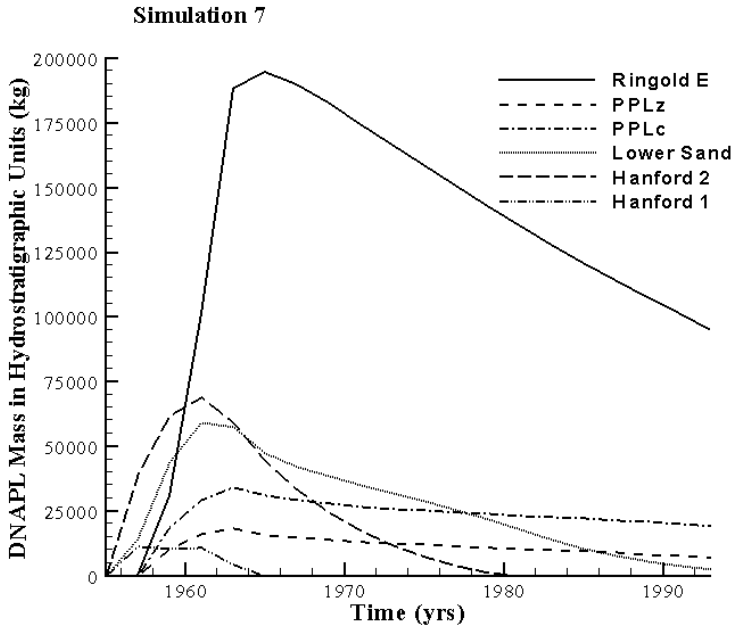

Figure 6.43. DNAPL Mass (kg) Distribution Over the Hydrostratigraphic Units (Simulation 7). In the legend, PPLz is used to indicate the Cold Creek silt and PPLc is used to indicate the Cold Creek carbonate.

6.2.8 Simulation 8

This simulation uses a Van Genuchten-Mualem configuration of the model. An overview of the DNAPL body at 1993 is shown in Figure 6.44. Selective cumulative mass fluxes are shown in Figure 6.45. This figure gives the impression that DNAPL has not moved across the water table. However, at this point in time over 92,000 kg has moved across the water table. Most of this DNAPL has already been dissolved and sorbed to the porous media. Mass distributions over the fluid phases and hydrostratigraphic units are presented in Figures 6.46 and 6.47, respectively. The travel time for the first kilogram to reach the water table was 6.7 years. At 1993, 30% of the original DNAPL inventory remained in the vadose zone. The maximum DNAPL saturation at 1993 is 0.076. The location of the maximum saturation is in the Cold Creek silt. The use of the Van Genuchten parameters causes a more rapid vertical movement due to the lack of a distinct nonwettting fluid entry pressure.

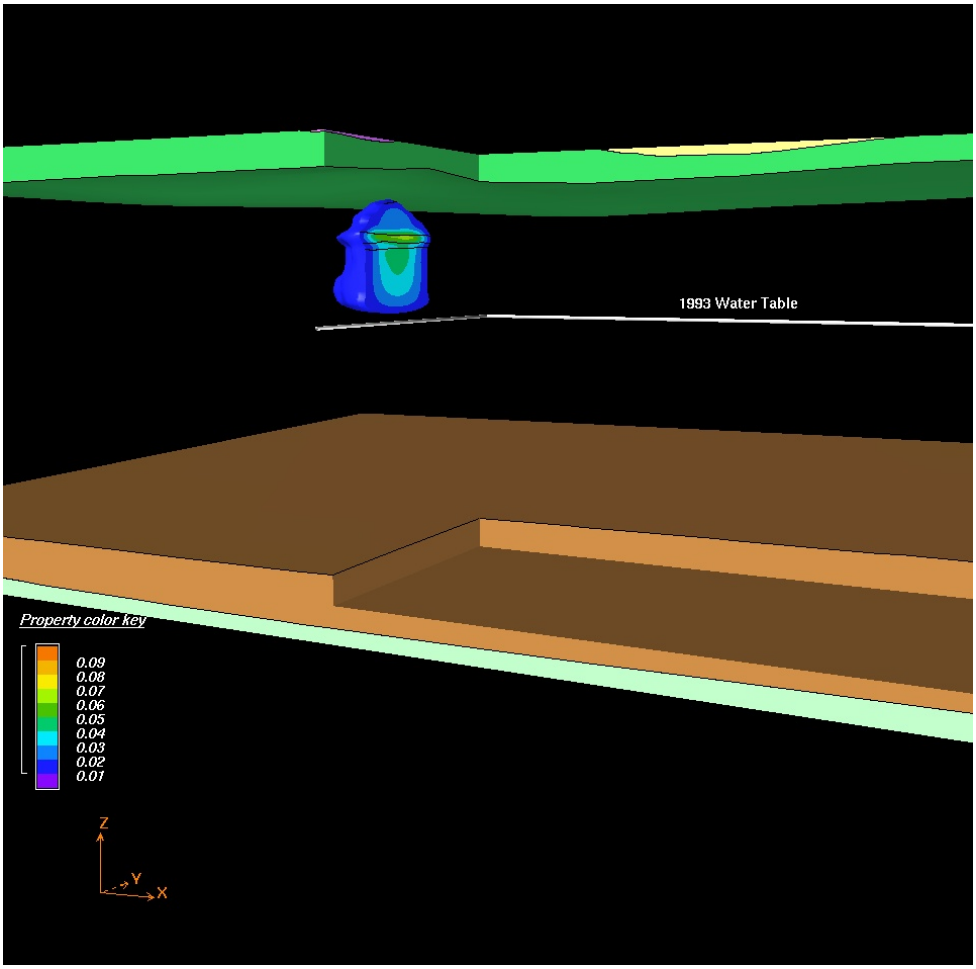

Figure 6.44. DNAPL Body in the Ringold E, Cold Creek, and Hanford Units at 1993 (Simulation 8)

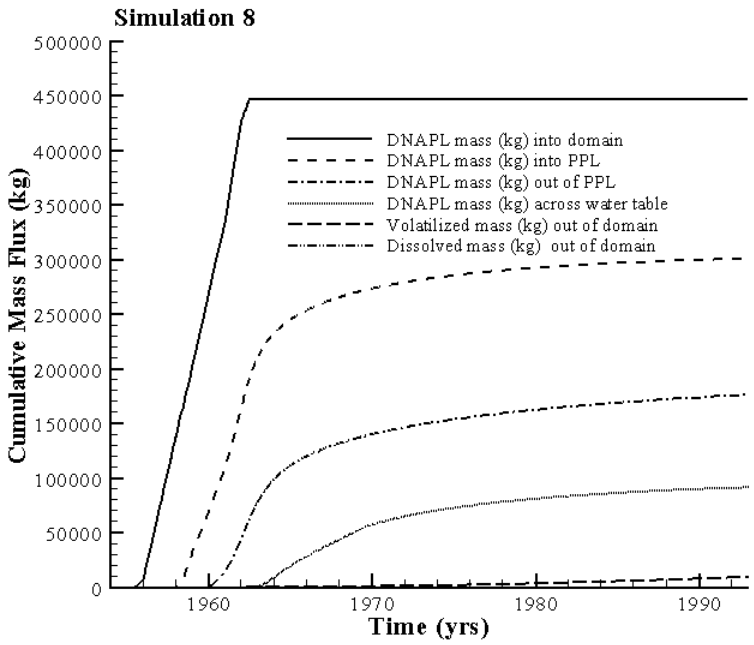

Figure 6.45. Cumulative DNAPL and Dissolved Mass Fluxes (Simulation 8). In the legend, PPL is used to indicate the Cold Creek unit.

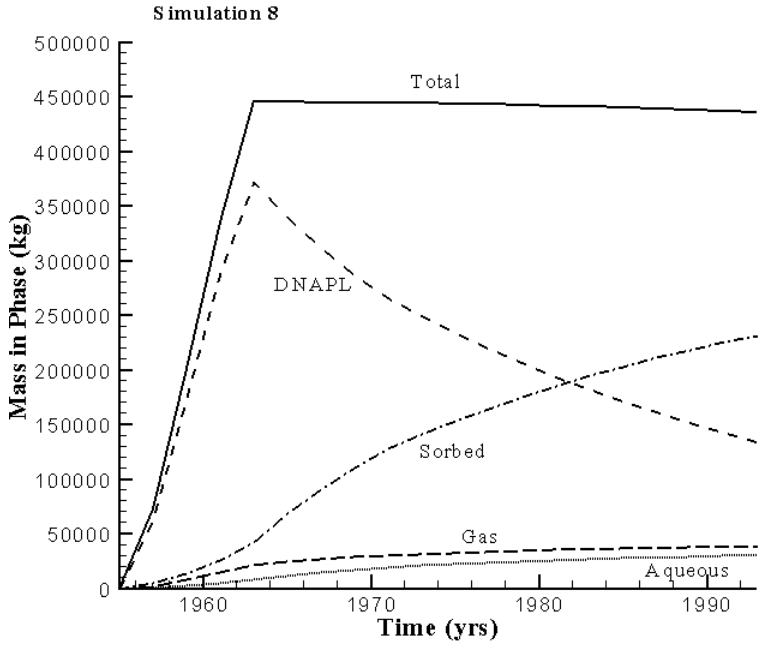

Figure 6.46. Volatile Organic Compound (VOC) Mass Distribution Over the NAPL, Sorbed, Aqueous, and Gaseous Phases (Simulation 8)

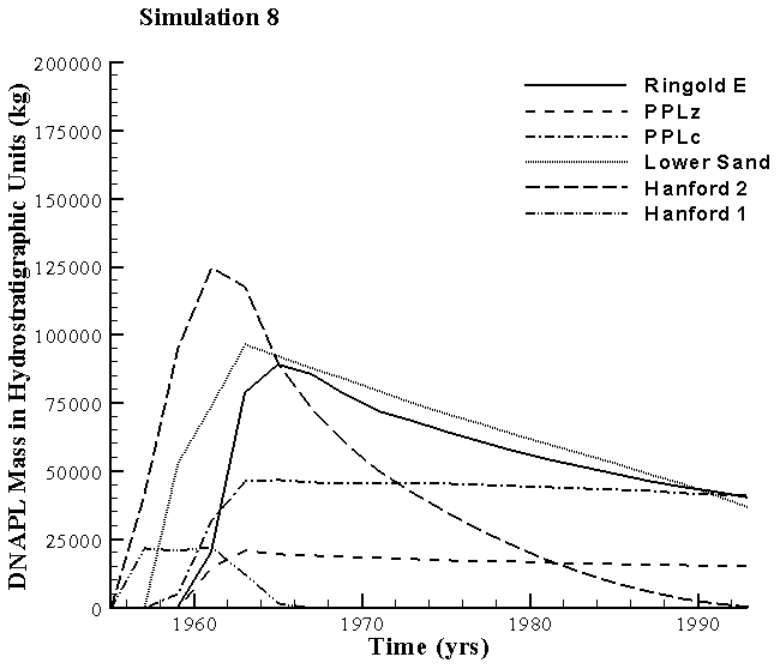

Figure 6.47. DNAPL Mass (kg) Distribution Over the Hydrostratigraphic Units (Simulation 8). In the legend, PPLz is used to indicate the Cold Creek silt and PPLc is used to indicate the Cold Creek carbonate.

6.2.9 Simulation 9

In this simulation, the nonwetting fluid entry pressures are increased by a factor 2. An overview of the DNAPL body at 1993 is shown in Figure 6.48. The figure shows that a relatively small amount of DNAPL crossed the water table. Selective cumulative mass fluxes are shown in Figure 6.49. Mass distributions over the fluid phases and hydrostratigraphic units are presented in Figures 6.50 and 6.51, respectively. The travel time for the first kilogram to reach the water table was 19.5 years. At 1993, 47% of the original DNAPL inventory remained in the vadose zone. Only 1,912 kg moved across the water table at 1993. The maximum DNAPL saturation at 1993 is 0.108. The location of the maximum saturation is in the Cold Creek silt.

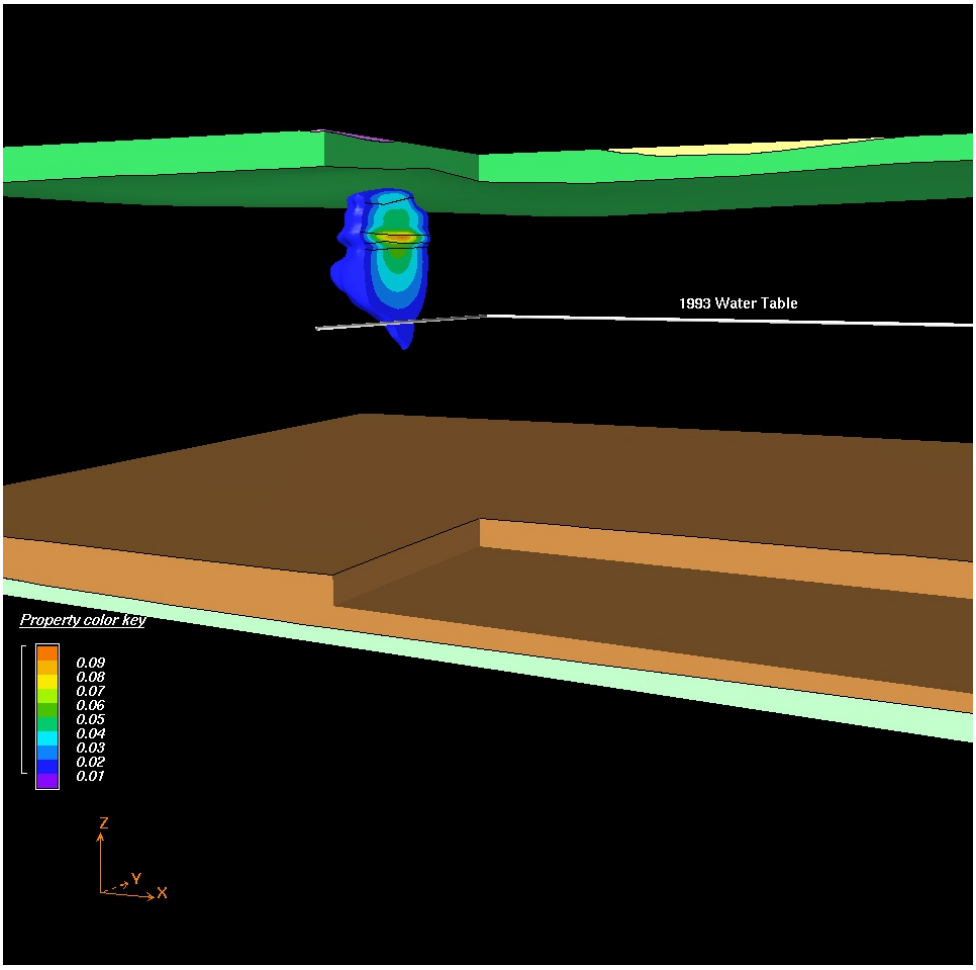

Figure 6.48. DNAPL Body in the Ringold E, Cold Creek, and Hanford Units at 1993 (Simulation 9)

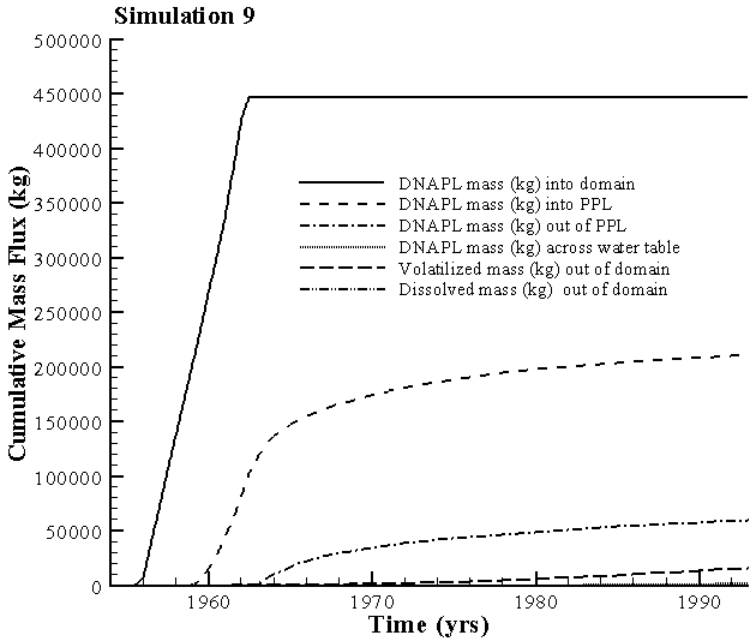

Figure 6.49. Cumulative DNAPL and Dissolved Mass Fluxes (Simulation 9). In the legend, PPL is used to indicate the Cold Creek unit.

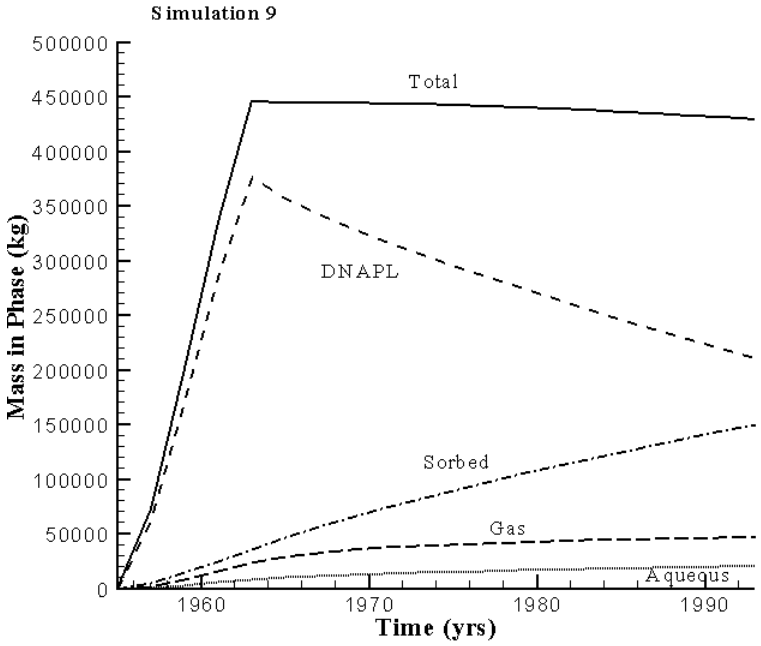

Figure 6.50. Volatile Organic Compound (VOC) Mass Distribution Over the NAPL, Sorbed, Aqueous, and Gaseous Phases (Simulation 9)

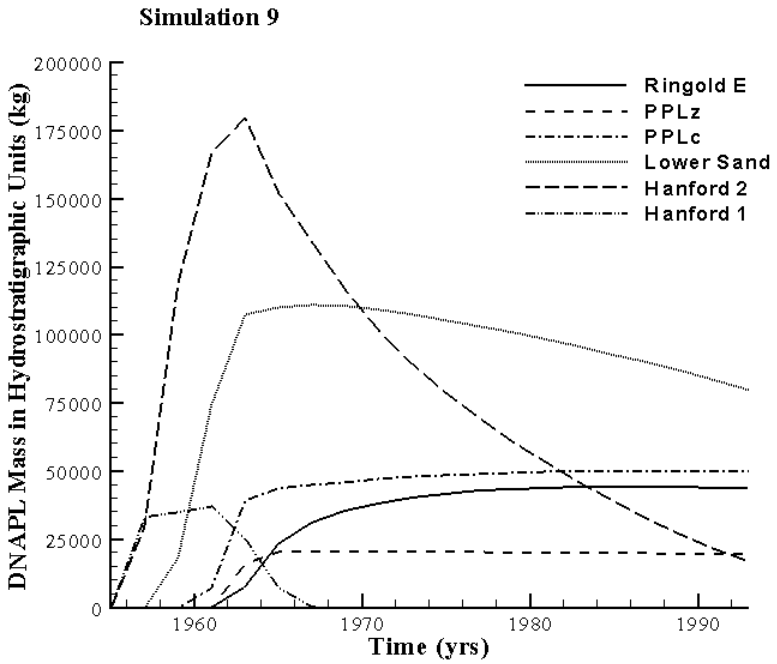

Figure 6.51. DNAPL Mass (kg) Distribution Over the Hydrostratigraphic Units (Simulation 9). In the legend, PPLz is used to indicate the Cold Creek silt and PPLc is used to indicate the Cold Creek carbonate.

6.2.10 Simulation 10

In this simulation, the nonwetting fluid entry pressures were decreased by a factor 2. An overview of the DNAPL body at 1993 is shown in Figure 6.52. The figure shows that DNAPL is pooling on top of the Ringold Mud. Selective cumulative mass fluxes are shown in Figure 6.53. Mass distributions over the fluid phases and hydrostratigraphic units are presented in Figures 6.54 and 6.55, respectively. The travel time for the first kilogram to reach the water table was 6.8 years. At 1993, 38% of the original DNAPL inventory remained in the vadose zone. A total of more than 76,000 kg of DNAPL moved across the water table at 1993. The maximum DNAPL saturation at 1993 is 0.101. The location of the maximum saturation is in the Cold Creek silt.

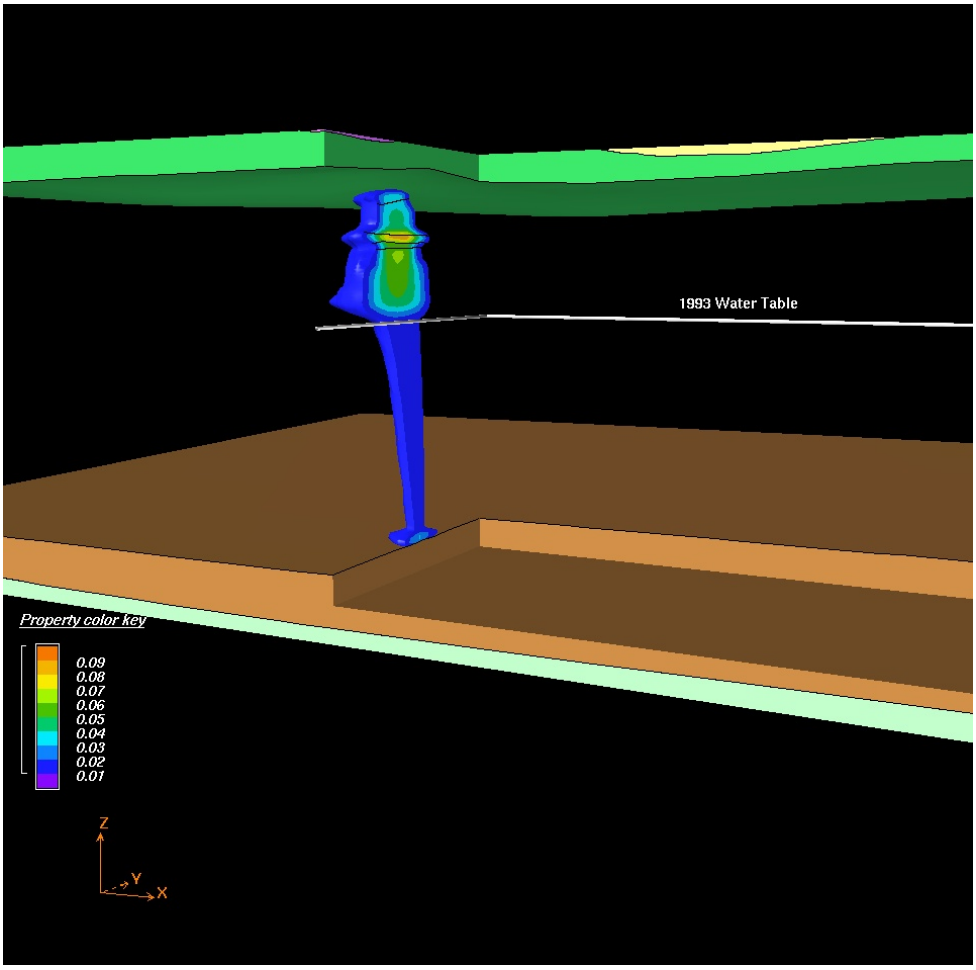

Figure 6.52. DNAPL Body in the Ringold E, Cold Creek, and Hanford Units at 1993 (Simulation 10)

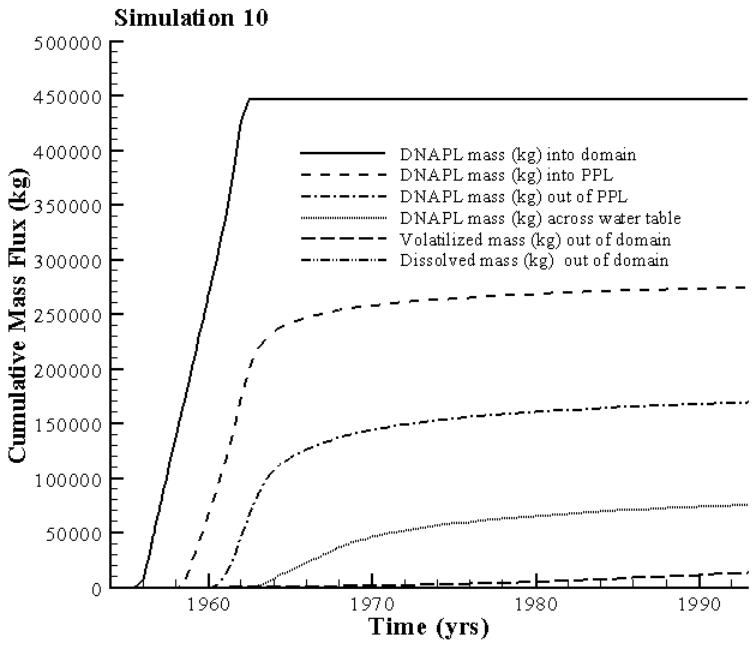

Figure 6.53. Cumulative DNAPL and Dissolved Mass Fluxes (Simulation 10). In the legend, PPL is used to indicate the Cold Creek unit.

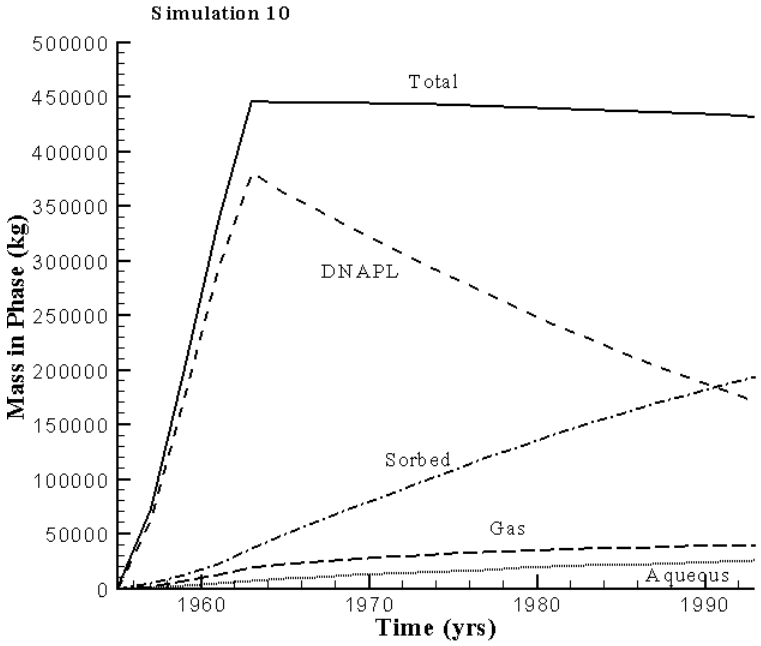

Figure 6.54. Volatile Organic Compound (VOC) Mass Distribution Over the NAPL, Sorbed, Aqueous, and Gaseous Phases (Simulation 10)

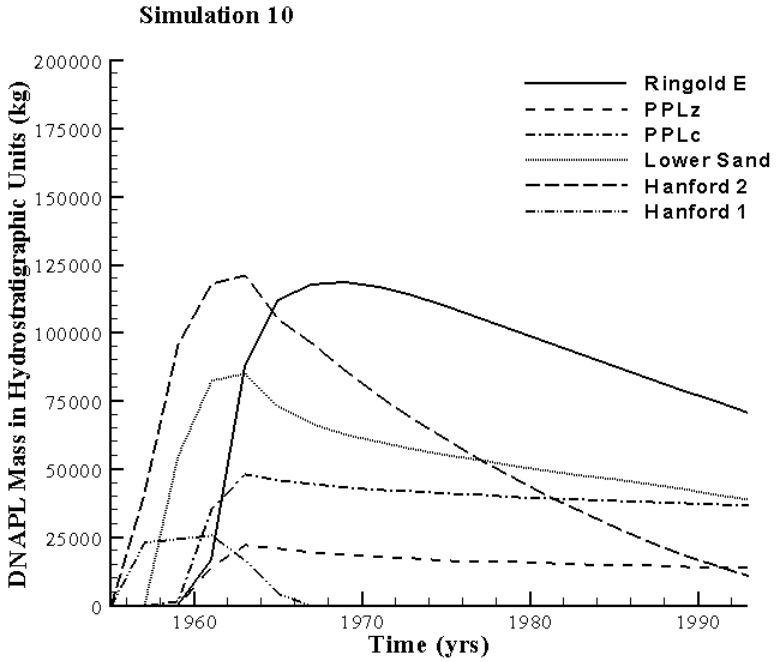

Figure 6.55. DNAPL Mass (kg) Distribution Over the Hydrostratigraphic Units (Simulation 10). In the legend, PPLz is used to indicate the Cold Creek silt and PPLc is used to indicate the Cold Creek carbonate.

6.2.11 Simulation 11

In this simulation, the pore geometry factor was increased by a factor 2. An overview of the DNAPL body at 1993 is shown in Figure 6.56. Selective cumulative mass fluxes are shown in Figure 6.57. Mass distributions over the fluid phases and hydrostratigraphic units are presented in Figures 6.58 and 6.59, respectively. The travel time for the first kilogram to reach the water table was 4.1 years. At 1993, 30% of the original DNAPL inventory remained in the vadose zone. A total of more than 109,000 kg of DNAPL moved across the water table at 1993. The maximum DNAPL saturation at 1993 is 0.086. The location of the maximum saturation is in the Cold Creek silt.

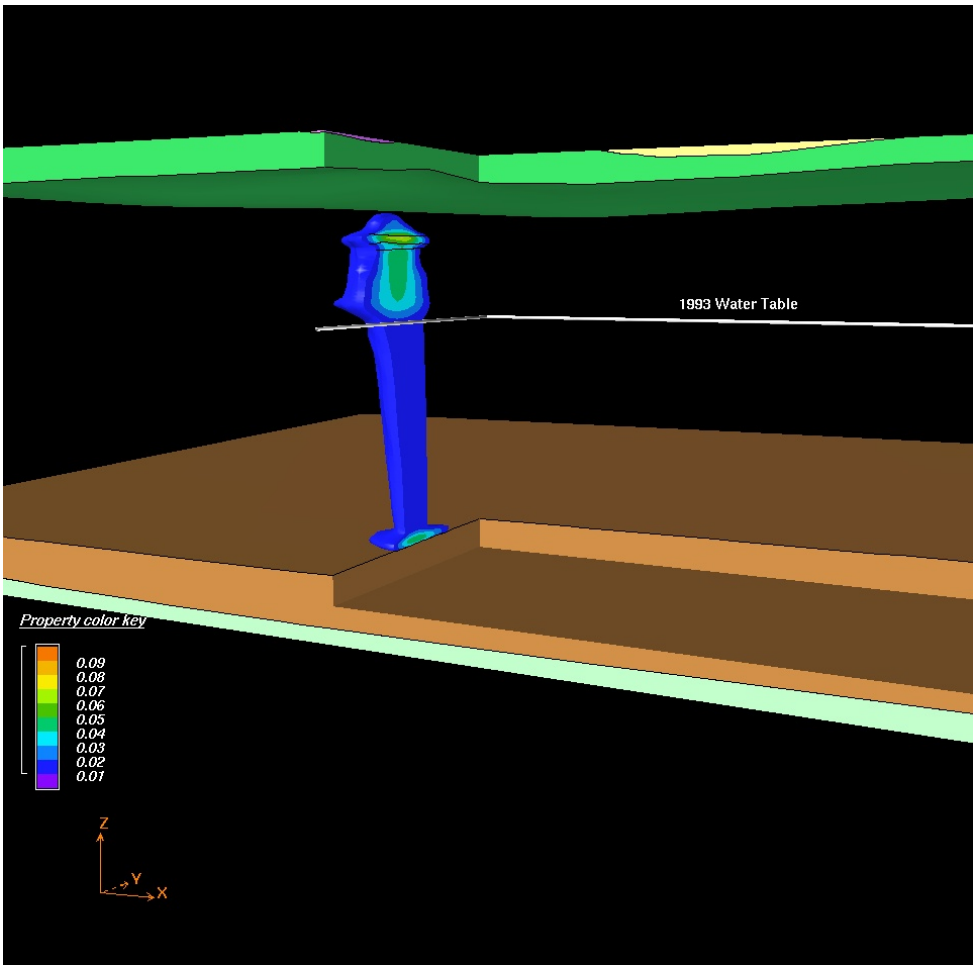

Figure 6.56. DNAPL Body in the Ringold E, Cold Creek, and Hanford Units at 1993 (Simulation 11)

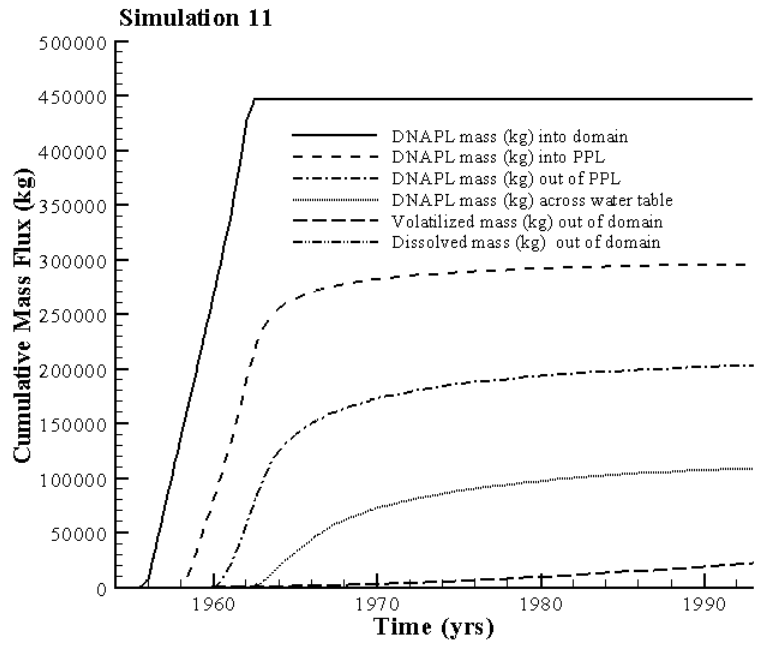

Figure 6.57. Cumulative DNAPL and Dissolved Mass Fluxes (Simulation 11). In the legend, PPL is used to indicate the Cold Creek unit.

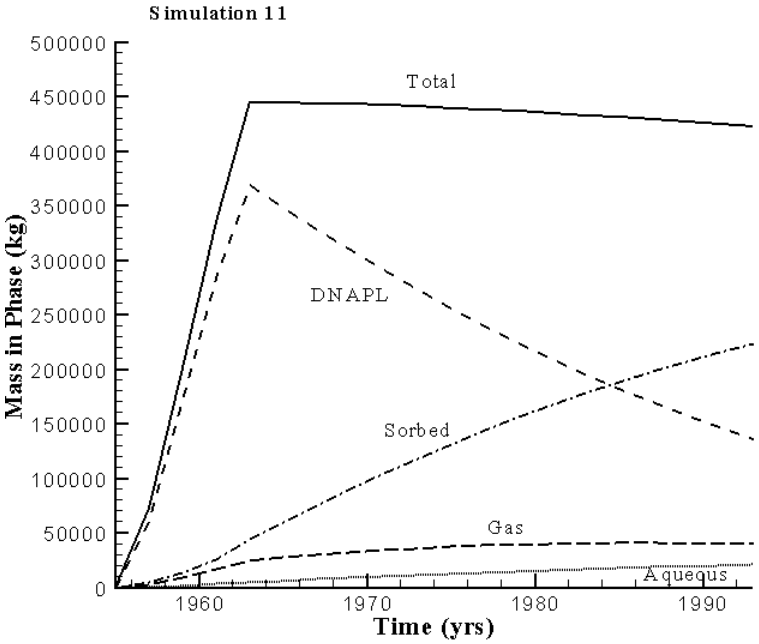

Figure 6.58. Volatile Organic Compound (VOC) Mass Distribution Over the NAPL, Sorbed, Aqueous, and Gaseous Phases (Simulation 11)

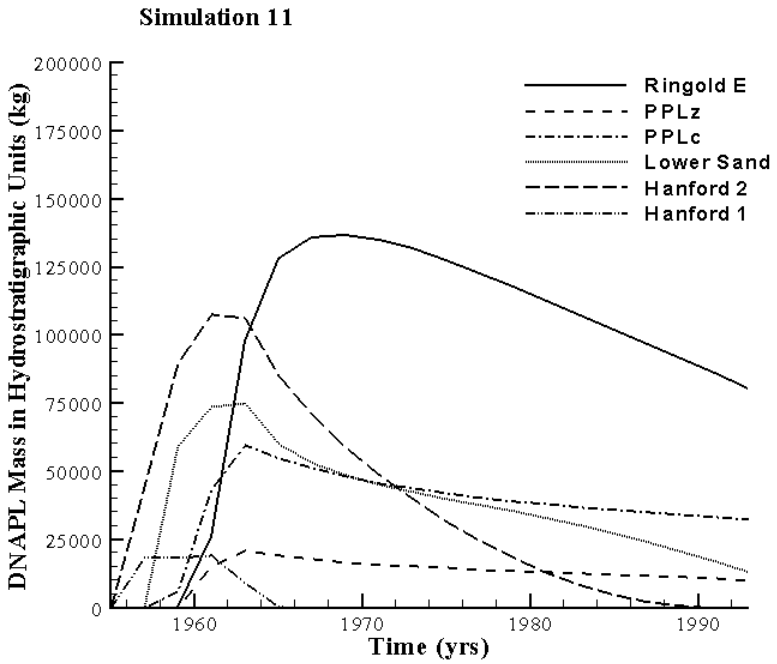

Figure 6.59. DNAPL Mass (kg) Distribution Over the Hydrostratigraphic Units (Simulation 11). In the legend, PPLz is used to indicate the Cold Creek silt and PPLc is used to indicate the Cold Creek carbonate.

6.2.12 Simulation 12

In this simulation, the pore geometry factor was decreased by a factor 2. An overview of the DNAPL body at 1993 is shown in Figure 6.60. Selective cumulative mass fluxes are shown in Figure 6.61. Mass distributions over the fluid phases and hydrostratigraphic units are presented in Figures 6.62 and 6.63, respectively. No DNAPL moved across the water table before 1993. At 1993, 59% of the original DNAPL inventory remained in the vadose zone. The maximum DNAPL saturation at 1993 is 0.117. The location of the maximum saturation is in the Cold Creek silt.

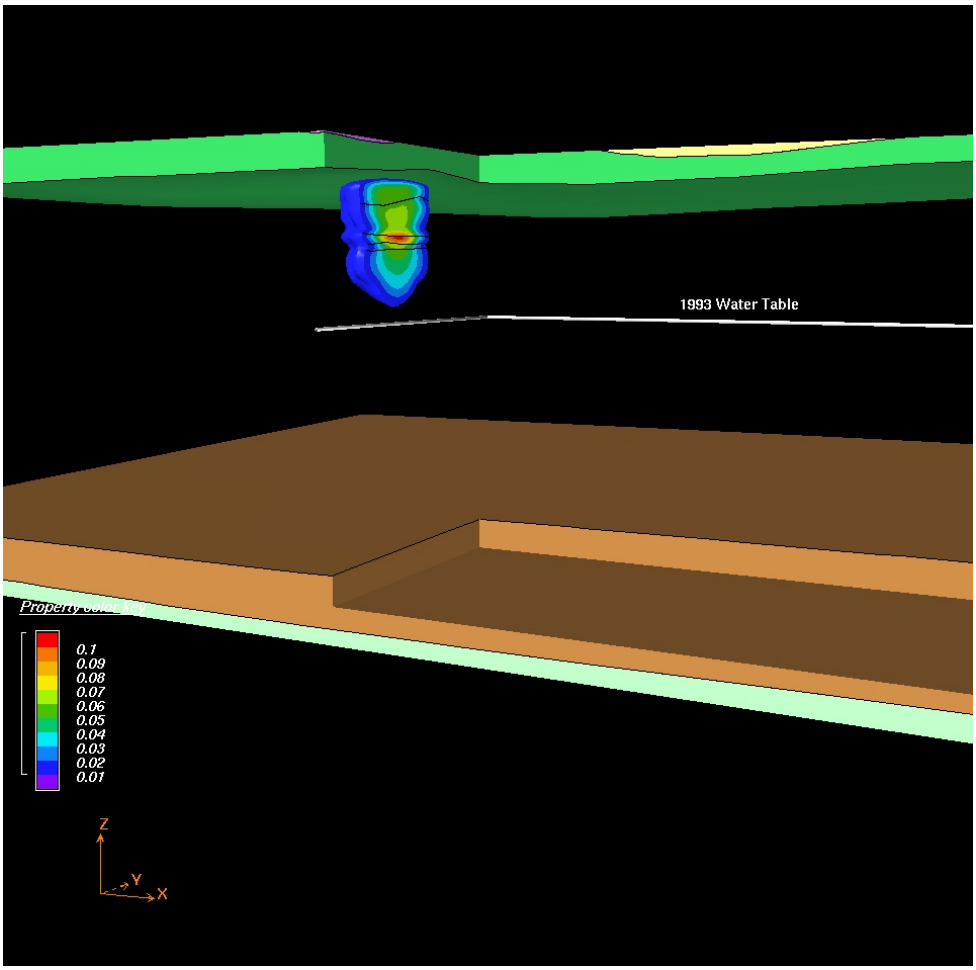

Figure 6.60. DNAPL Body in the Ringold E, Cold Creek, and Hanford Units at 1993 (Simulation 12)

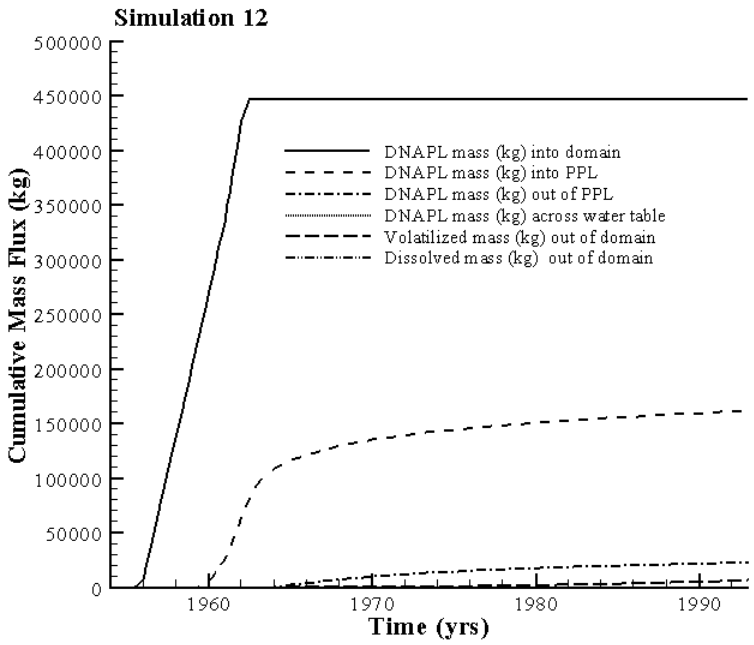

Figure 6.61. Cumulative DNAPL and Dissolved Mass Fluxes (Simulation 12). In the legend, PPL is used to indicate the Cold Creek unit.

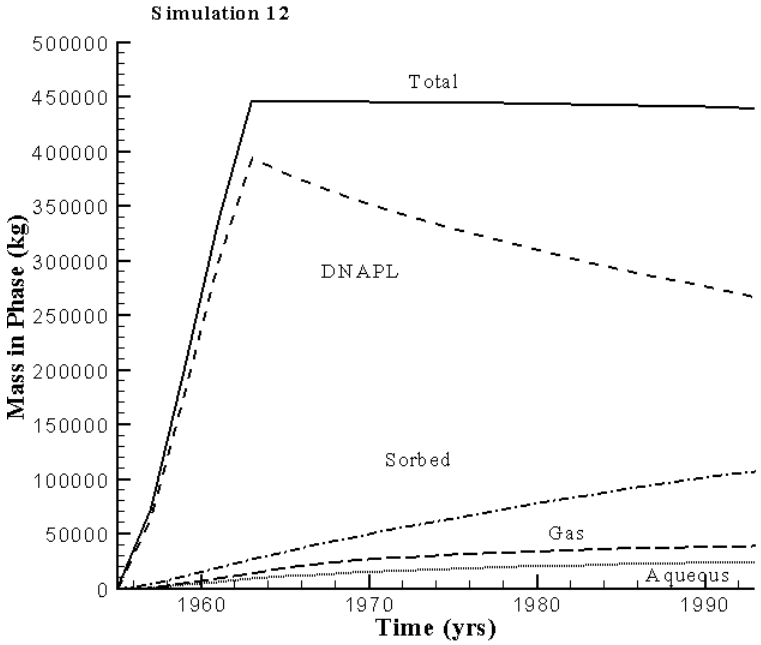

Figure 6.62. Volatile Organic Compound (VOC) Mass Distribution Over the NAPL, Sorbed, Aqueous, and Gaseous Phases (Simulation 12)

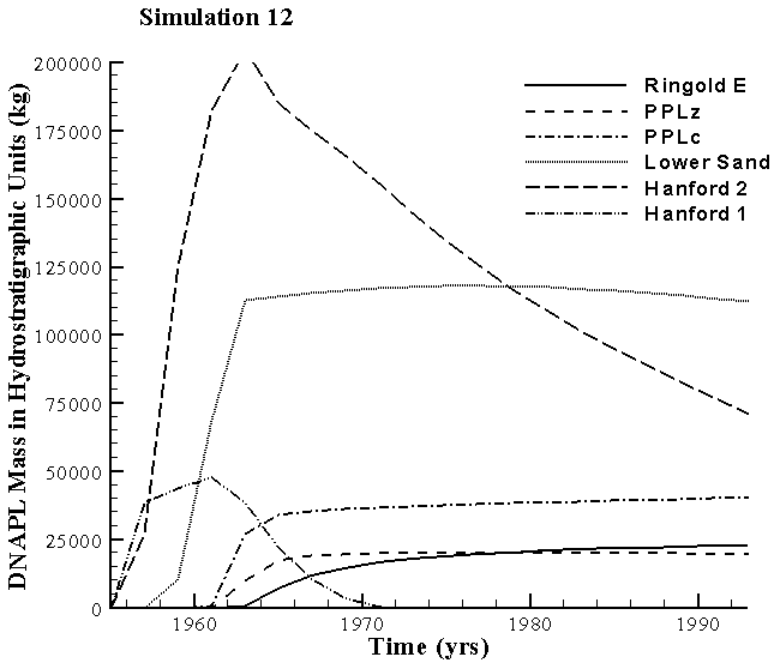

Figure 6.63. DNAPL Mass (kg) Distribution Over the Hydrostratigraphic Units (Simulation 12). In the legend, PPLz is used to indicate the Cold Creek silt and PPLc is used to indicate the Cold Creek carbonate.

6.2.13 Simulation 13

In this simulation, the permeability values were increased by a factor 10. An overview of the DNAPL body at 1993 is shown in Figure 6.64. Selective cumulative mass fluxes are shown in Figure 6.65. Mass distributions over the fluid phases and hydrostratigraphic units are presented in Figures 6.66 and 6.67, respectively. The travel time for the first kilogram to reach the water table was 8.5 years. At 1993, 19% of the original DNAPL inventory remained in the vadose zone. A total of more than 19,000 kg of DNAPL moved across the water table at 1993, which is less than for the Base Case. The reduction is the result of the more pronounced lateral movement of the DNAPL body, compared to the Base Case, as a result of the increased permeabilities. The maximum DNAPL saturation at 1993 is 0.086. The location of the maximum saturation is in the Cold Creek silt.

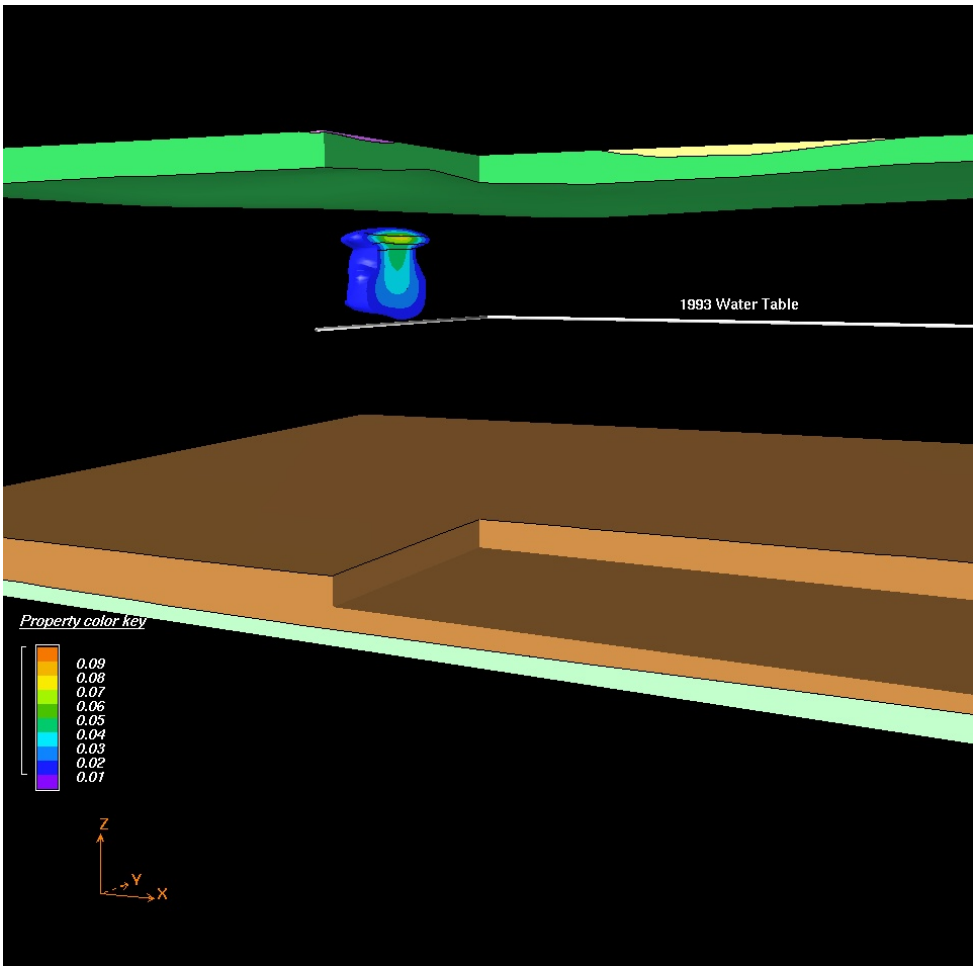

Figure 6.64. DNAPL Body in the Ringold E, Cold Creek, and Hanford Units at 1993 (Simulation 13)

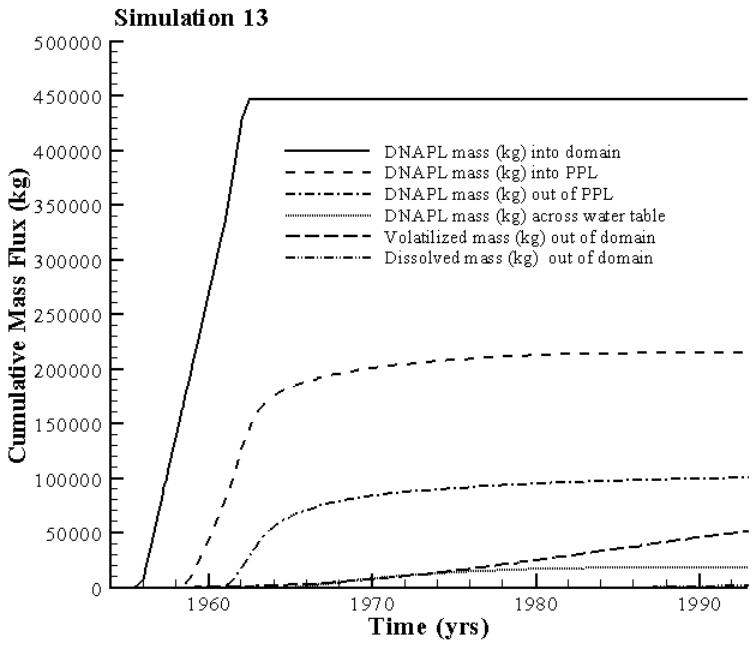

Figure 6.65. Cumulative DNAPL and Dissolved Mass Fluxes (Simulation 13). In the legend, PPL is used to indicate the Cold Creek unit.

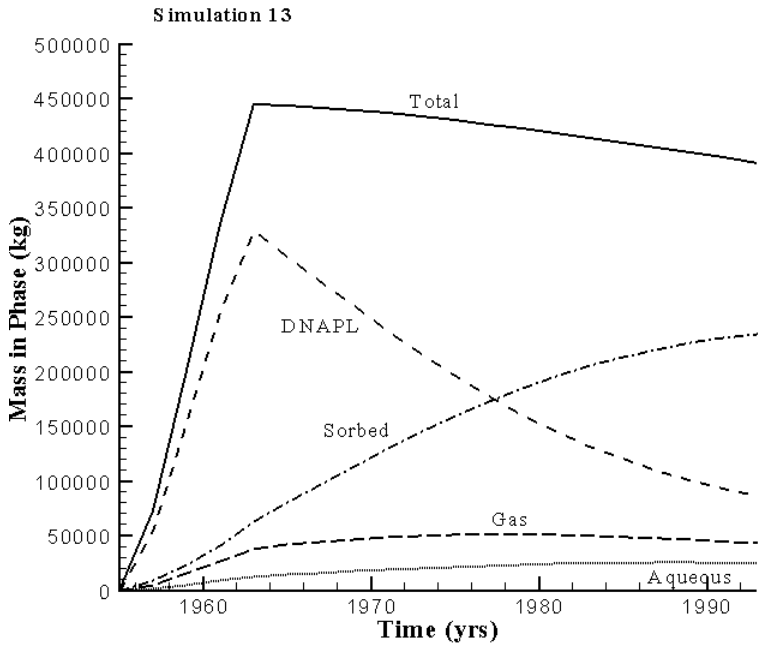

Figure 6.66. Volatile Organic Compound (VOC) Mass Distribution Over the NAPL, Sorbed, Aqueous, and Gaseous Phases (Simulation 13)

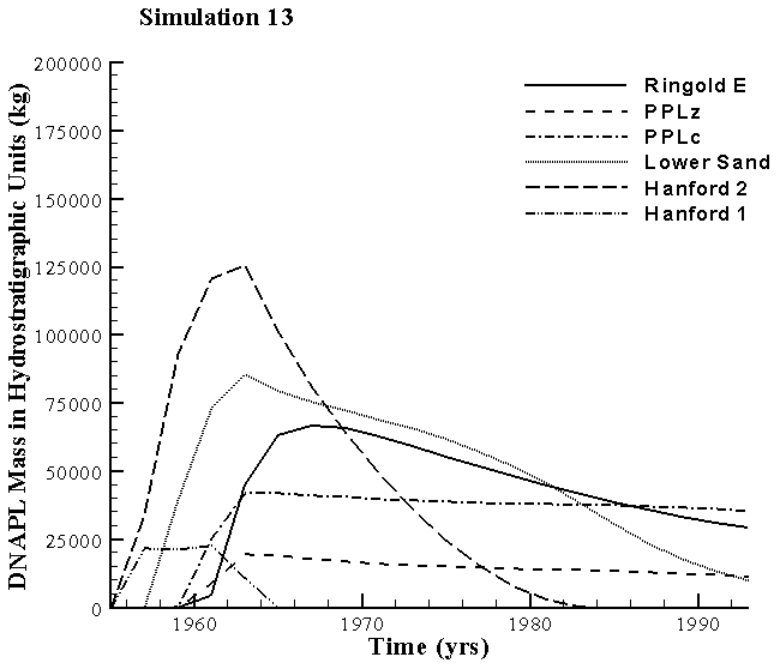

Figure 6.67. DNAPL Mass (kg) Distribution Over the Hydrostratigraphic Units (Simulation 13). In the legend, PPLz is used to indicate the Cold Creek silt and PPLc is used to indicate the Cold Creek carbonate.

6.2.14 Simulation 14

In this simulation, the permeability values were reduced by a factor 10. An overview of the DNAPL body at 1993 is shown in Figure 6.68. No DNAPL moved across the water table at 1993. Selected cumulative mass fluxes are shown in Figure 6.69. Mass distributions over the fluid phases and hydrostratigraphic units are presented in Figures 6.70 and 6.71, respectively. At 1993, 65% of the original DNAPL inventory remained in the vadose zone. The maximum DNAPL saturation at 1993 is 0.161. The location of the maximum saturation is in the Cold Creek silt.

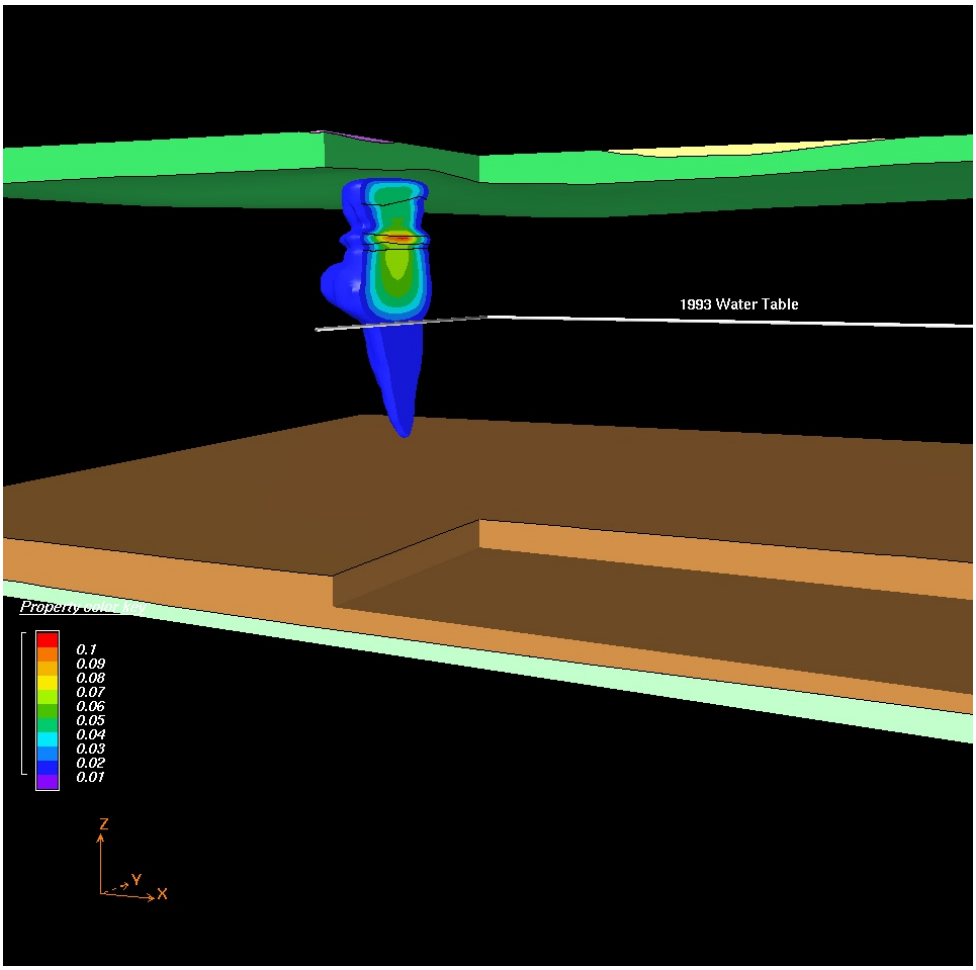

Figure 6.68. DNAPL Body in the Ringold E, Cold Creek, and Hanford Units at 1993 (Simulation 14)

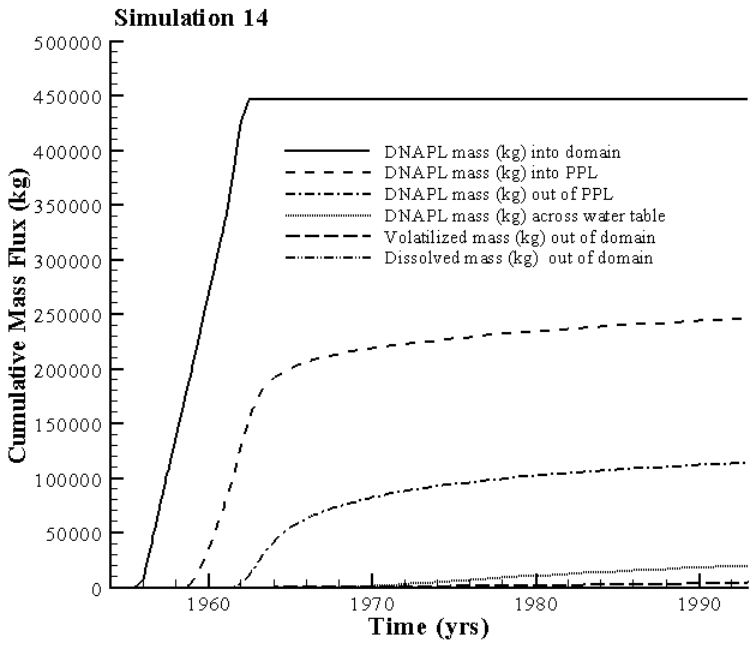

Figure 6.69. Cumulative DNAPL and Dissolved Mass Fluxes (Simulation 14). In the legend, PPL is used to indicate the Cold Creek unit.

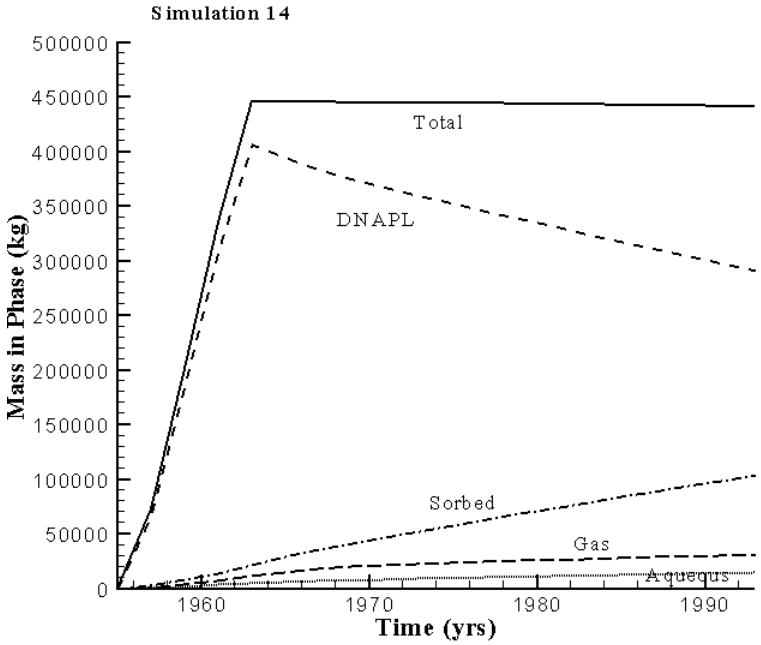

Figure 6.70. Volatile Organic Compound (VOC) Mass Distribution Over the NAPL, Aqueous, and Gaseous Phases (Simulation 14)

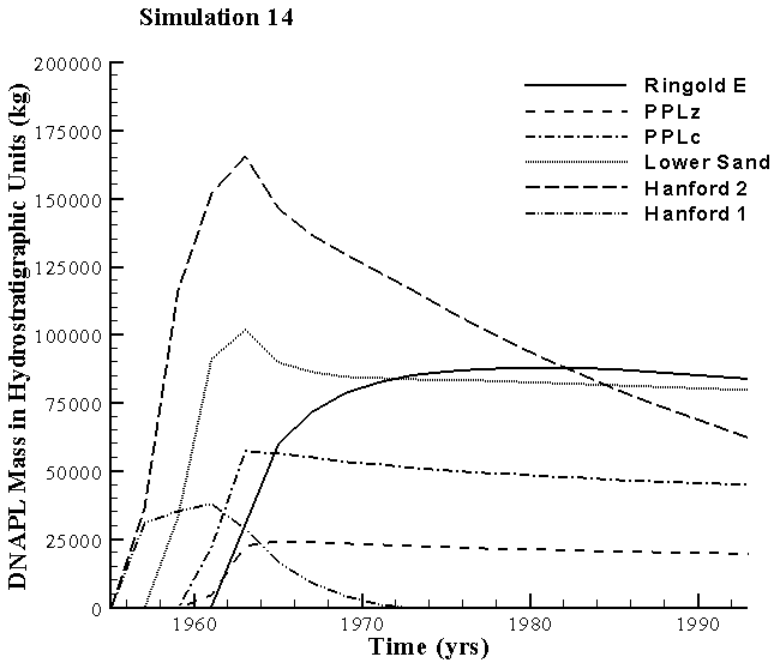

Figure 6.71. DNAPL Mass (kg) Distribution Over the Hydrostratigraphic Units (Simulation 14). In the legend, PPLz is used to indicate the Cold Creek silt and PPLc is used to indicate the Cold Creek carbonate.

6.2.15 Simulation 15

In this simulation, the anisotropy rate is 1:1. An overview of the DNAPL body at 1993 is shown in Figure 6.72. According to Chamness et al. (1991)[1] and Zhang et al. (2003), isotropic simulations are not appropriate for Hanford vadose zone simulations. These kinds of simulations tend to exaggerate vertical movement. The travel time for the first kilogram to reach the water table was 6.3 years. At 1993, only 25% of the original DNAPL inventory remained in the vadose zone. A total of more than 86,000 kg of DNAPL moved across the water table at 1993. Selective cumulative mass fluxes are shown in Figure 6.73. Mass distributions over the fluid phases and hydrostratigraphic units are presented in Figures 6.74 and 6.75, respectively. The maximum DNAPL saturation at 1993 is 0.051. The location of the maximum saturation is in the Cold Creek silt.

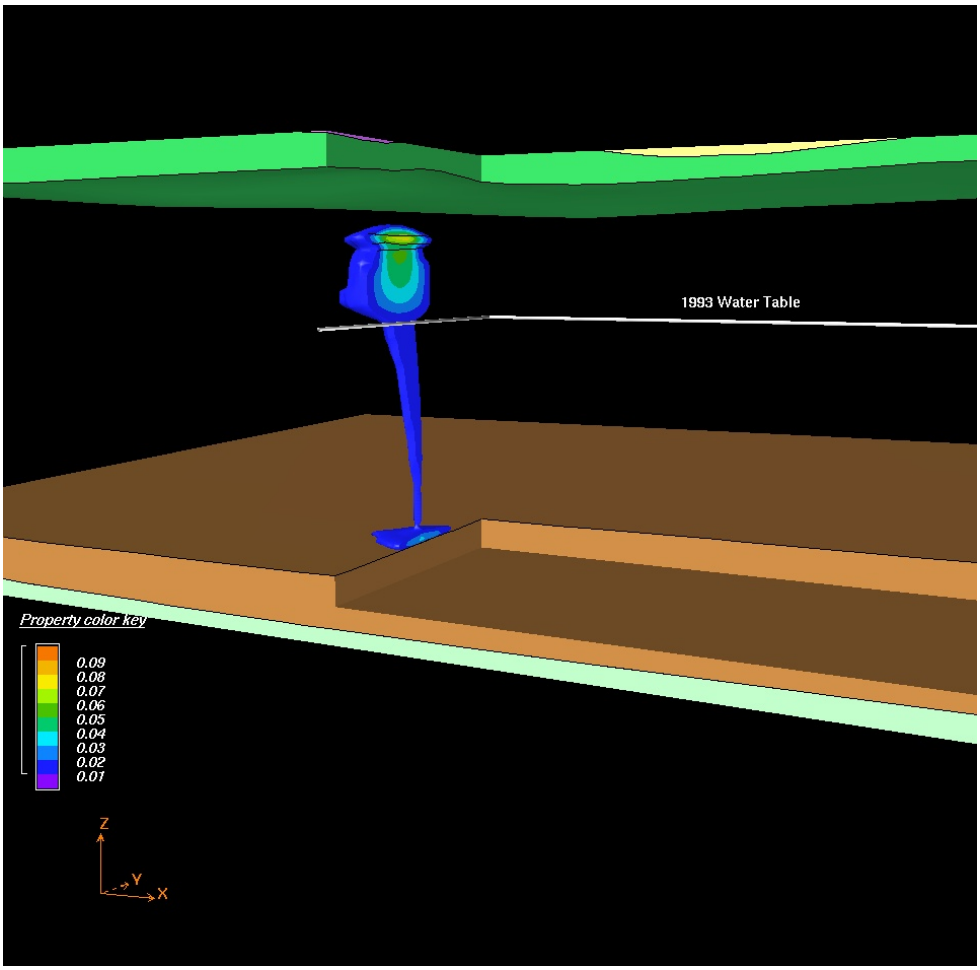

Figure 6.72. DNAPL Body in the Ringold E, Cold Creek, and Hanford Units at 1993 (Simulation 15)

[1] Letter Report from MA Chamness, ML Rockhold, and BN Bjornstad (Pacific Northwest National Laboratory) to U.S. Department of Energy, *A Hydrogeologic Study for Construction of a Percolations Pond*, dated 1991.

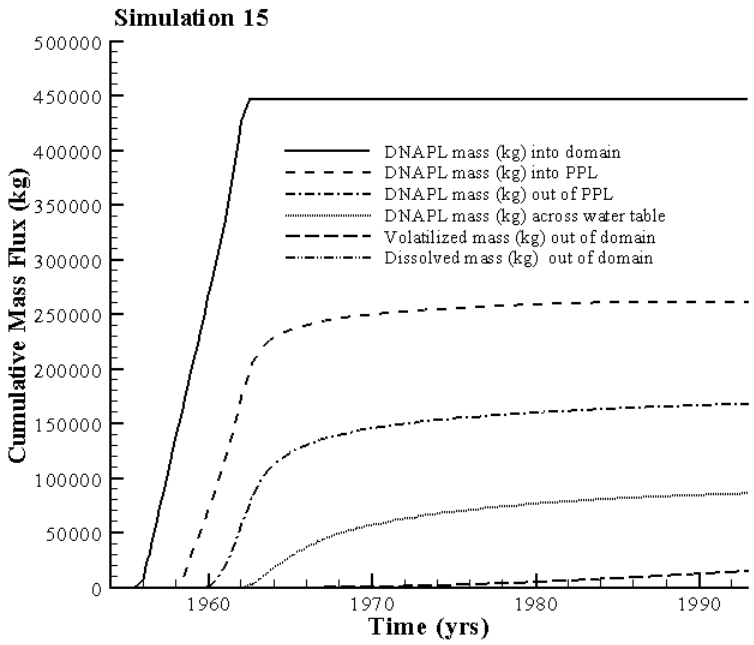

Figure 6.73. Cumulative DNAPL and Dissolved Mass Fluxes (Simulation 15). In the legend, PPL is used to indicate the Cold Creek unit.

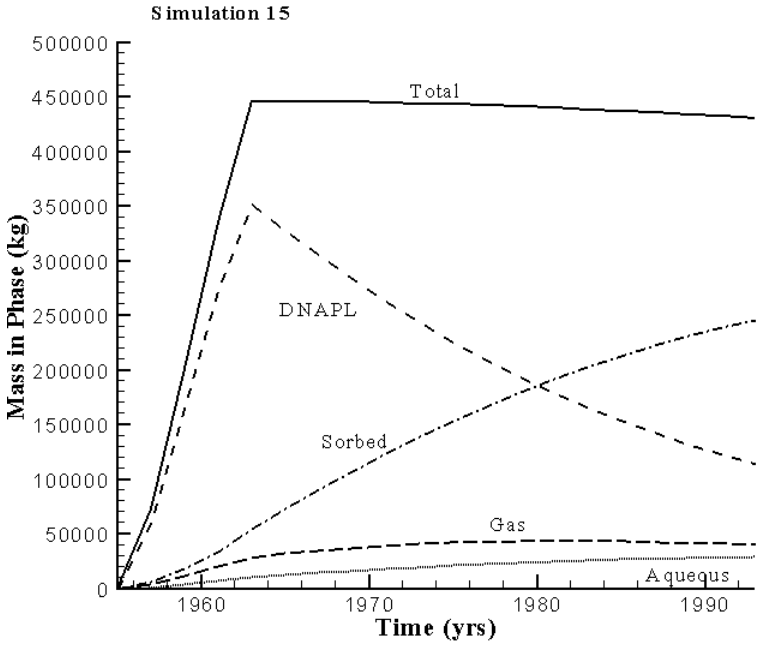

Figure 6.74. Volatile Organic Compound (VOC) Mass Distribution Over the NAPL, Sorbed, Aqueous, and Gaseous Phases (Simulation 15)

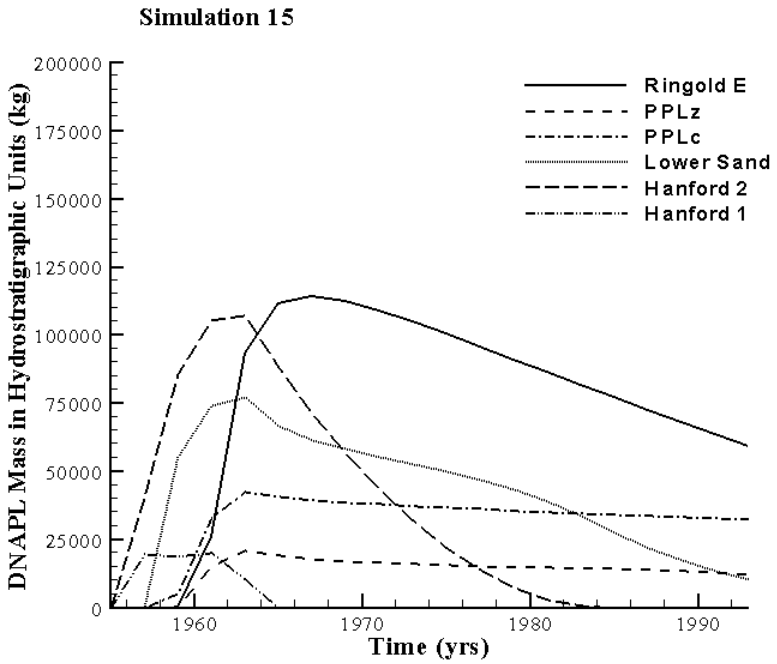

Figure 6.75. DNAPL Mass (kg) Distribution Over the Hydrostratigraphic Units (Simulation 15). In the legend, PPLz is used to indicate the Cold Creek silt and PPLc is used to indicate the Cold Creek carbonate.

6.2.16 Simulation 16

In this simulation, the anisotropy ratio is increased to 20:1. An overview of the DNAPL body at 1993 is shown in Figure 6.76. No DNAPL moved across the water table at 1993. Selective cumulative mass fluxes are shown in Figure 6.77. Mass distributions over the fluid phases and hydrostratigraphic units are presented in Figures 6.78 and 6.79, respectively. The maximum DNAPL saturation at 1993 is 0.121. The location of the maximum saturation is in the Cold Creek silt.

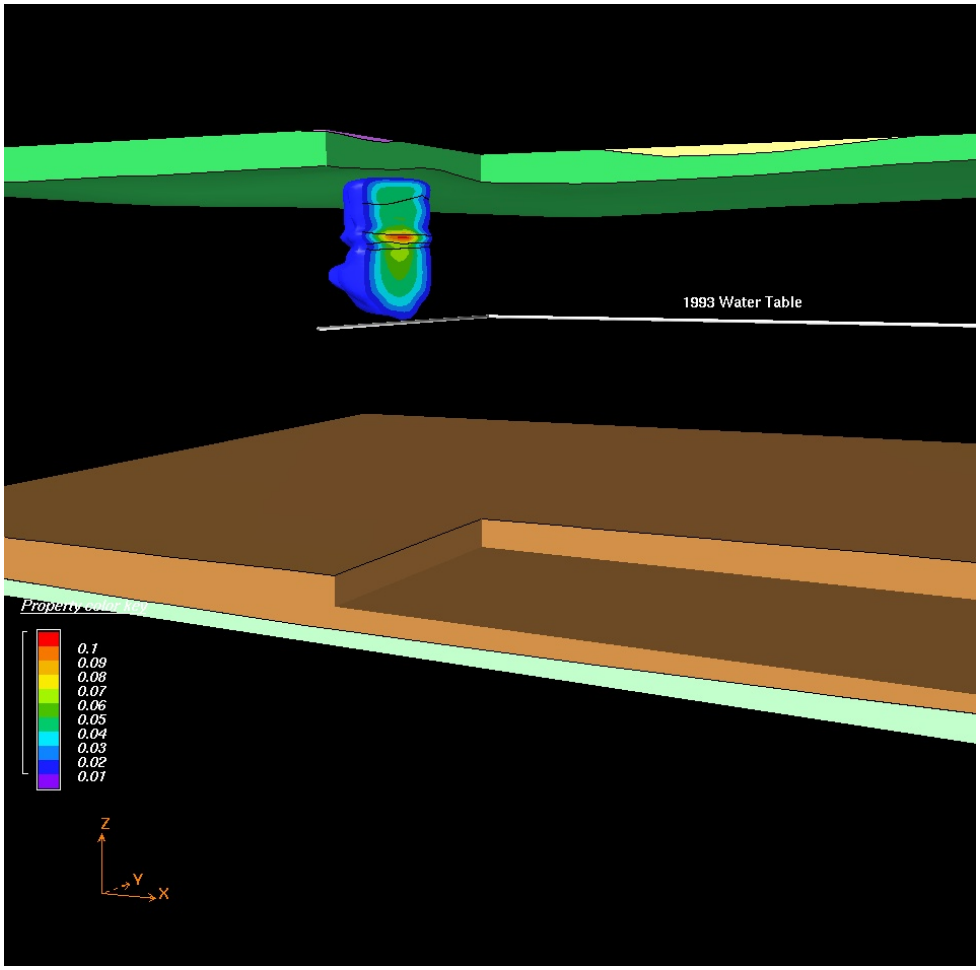

Figure 6.76. DNAPL Body in the Ringold E, Cold Creek, and Hanford Units at 1993 (Simulation 16)

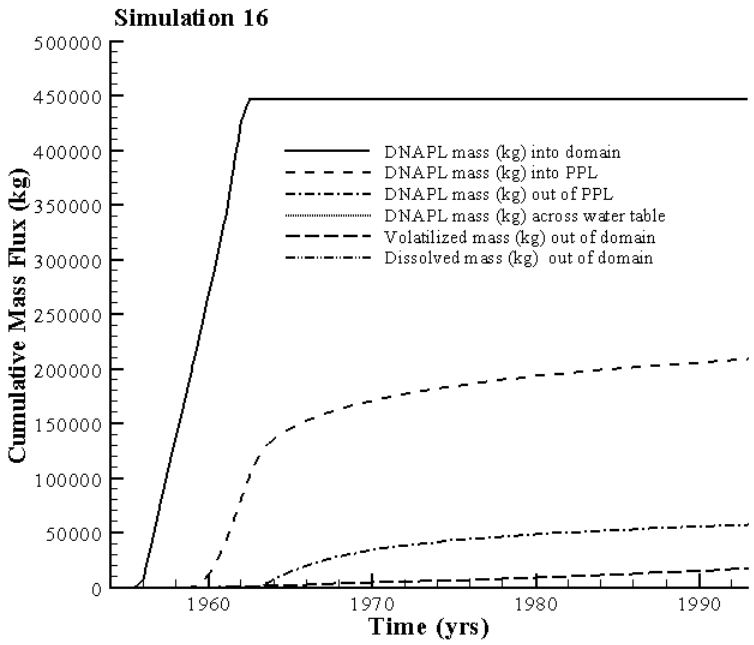

Figure 6.77. Cumulative DNAPL and Dissolved Mass Fluxes (Simulation 16). In the legend, PPL is used to indicate the Cold Creek unit.

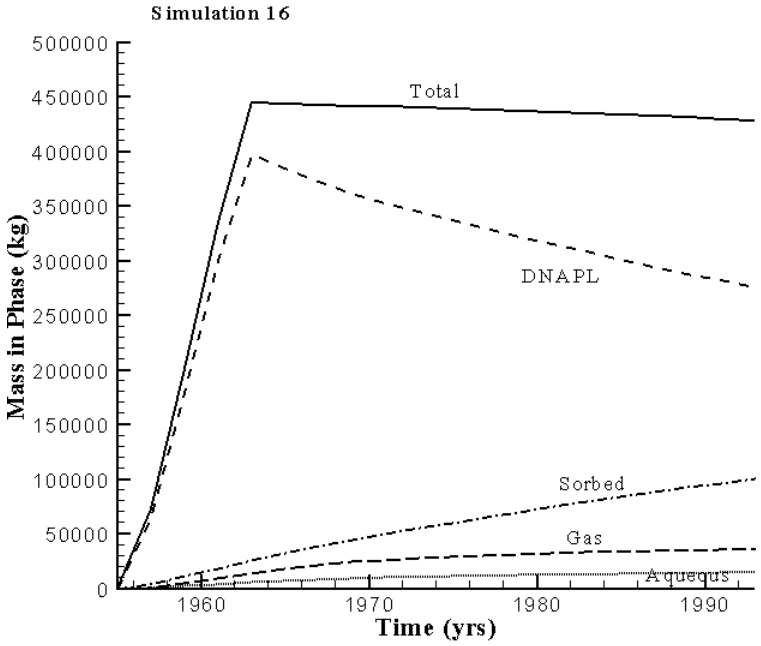

Figure 6.78. Volatile Organic Compound (VOC) Mass Distribution Over the NAPL, Aqueous, and Gaseous Phases (Simulation 16)

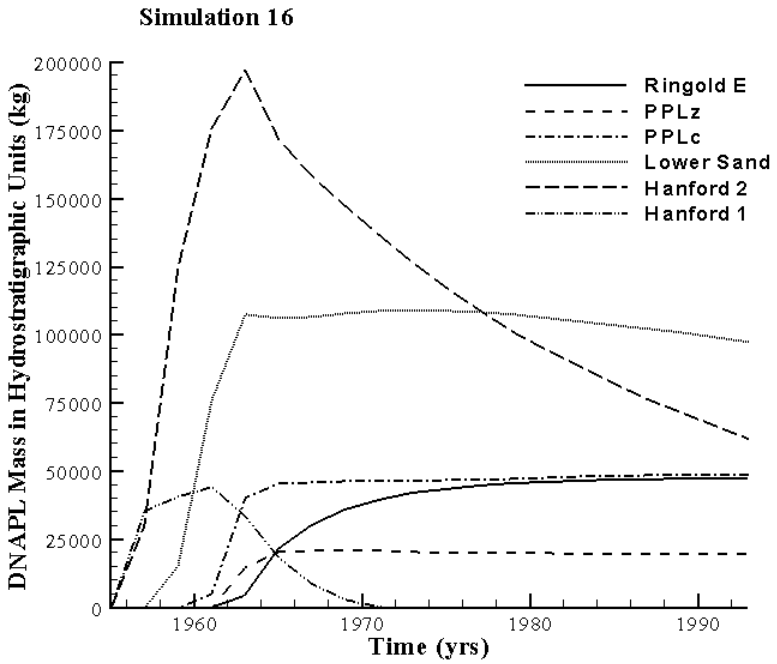

Figure 6.79. DNAPL Mass (kg) Distribution Over the Hydrostratigraphic Units (Simulation 16). In the legend, PPLz is used to indicate the Cold Creek silt and PPLc is used to indicate the Cold Creek carbonate.

6.2.17 Simulation 17

In this simulation, the new theory to compute residual DNAPL saturation has been applied using measured maximum residual NAPL saturations for 4 units and an assumed value of 0.1 for the rest of the units. This theory is described in detail in Appendix A. An overview of the DNAPL body at 1993 is shown in Figure 6.80. Selective cumulative mass fluxes are shown in Figure 6.81. Mass distributions over the fluid phases and hydrostratigraphic units are presented in Figures 6.82 and 6.83, respectively. The travel time for the first kilogram to reach the water table was 9.3 years. At 1993, 44% of the original DNAPL inventory remained in the vadose zone. A total of 16,803 kg of DNAPL moved across the water table at 1993. The maximum DNAPL saturation at 1993 is 0.149 which is larger than for simulation without the formation of residual saturation. The location of the maximum saturation is in the Cold Creek silt.

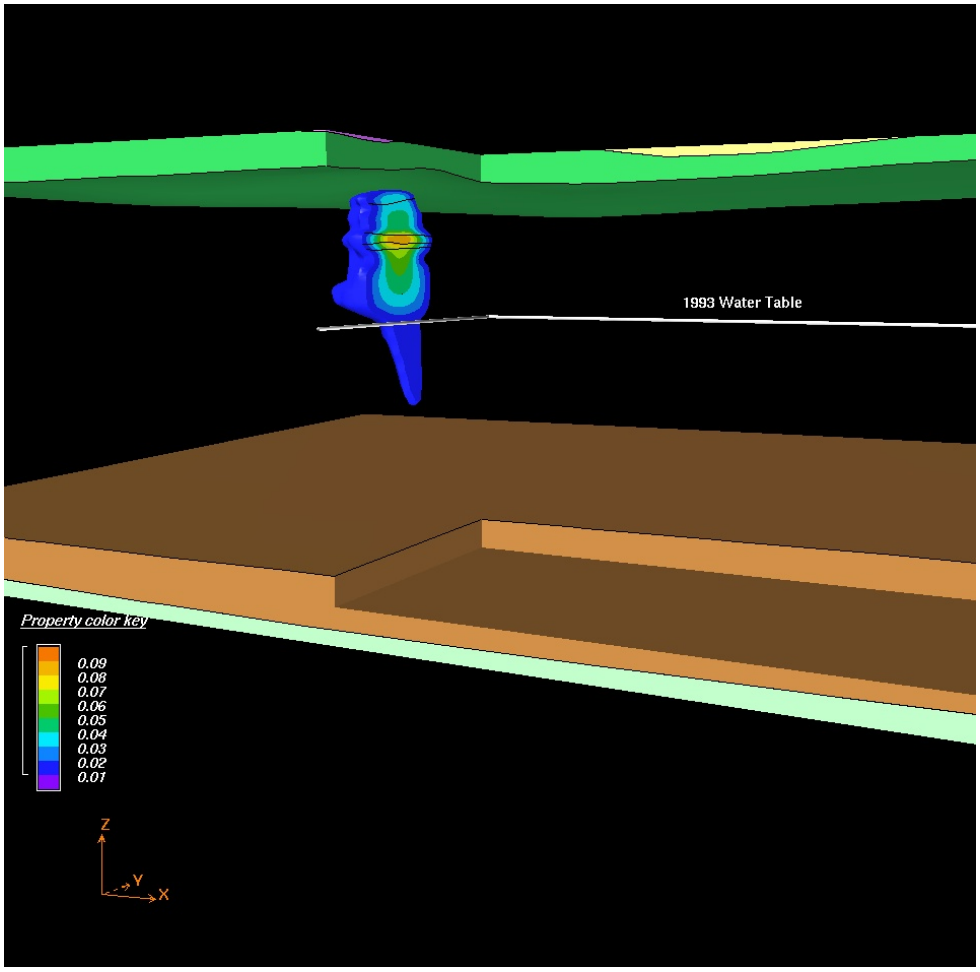

Figure 6.80. DNAPL Body in the Ringold E, Cold Creek, and Hanford Units at 1993 (Simulation 17)

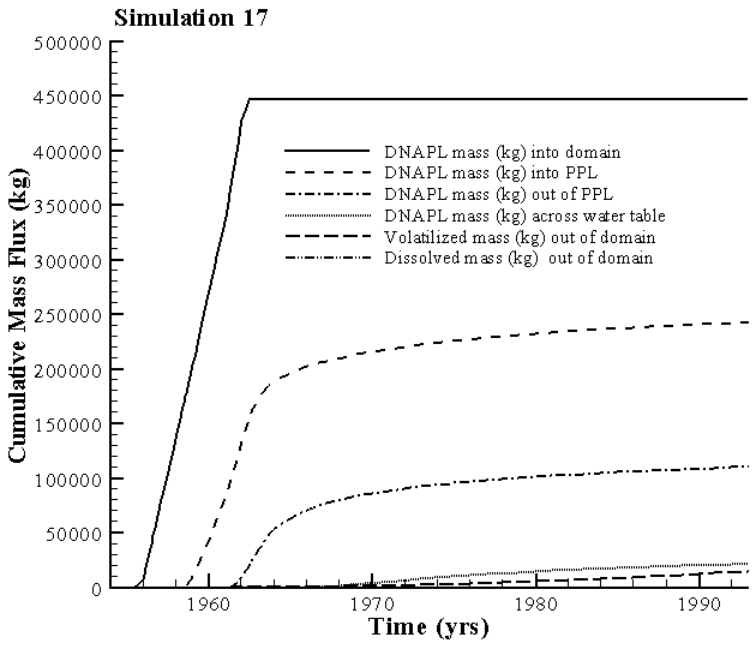

Figure 6.81. Cumulative DNAPL and Dissolved Mass Fluxes (Simulation 17). In the legend, PPL is used to indicate the Cold Creek unit.

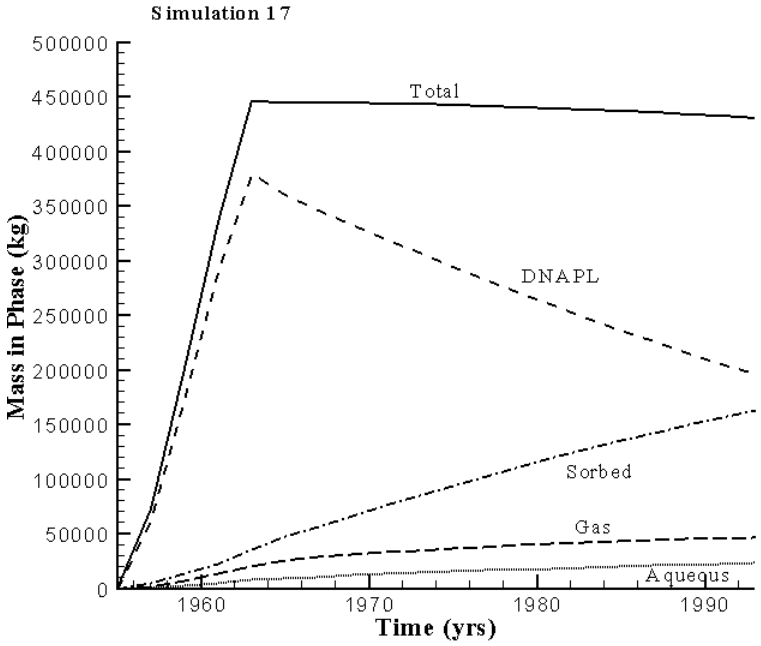

Figure 6.82. Volatile Organic Compound (VOC) Mass Distribution Over the NAPL, Sorbed, Aqueous, and Gaseous Phases (Simulation 17)

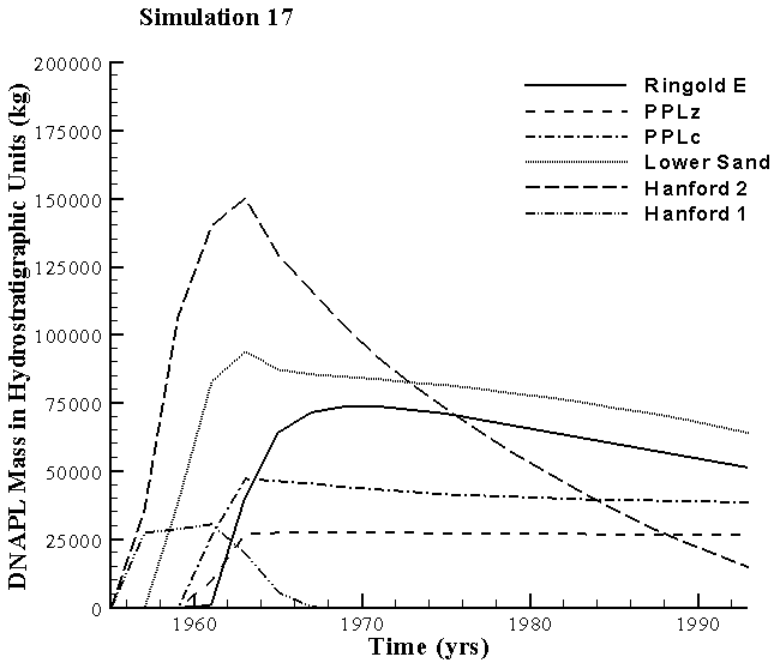

Figure 6.83. DNAPL Mass (kg) Distribution Over the Hydrostratigraphic Units (Simulation 17). In the legend, PPLz is used to indicate the Cold Creek silt and PPLc is used to indicate the Cold Creek carbonate.

6.2.18 Simulation 18

In this simulation, the new theory to compute residual DNAPL saturation has been applied using the measured and assumed maximum residual NAPL saturation values times 1.25. An overview of the DNAPL body in 1993 is shown in Figure 6.84. Selective cumulative mass fluxes are shown in Figure 6.85. A total of about 11,000 kg of DNAPL moved across the water table. Mass distributions over the fluid phases and hydrostratigraphic units are presented in Figures 6.86 and 6.87, respectively. The maximum DNAPL saturation at 1993 is 0.195. The location of the maximum saturation is in the Cold Creek silt.

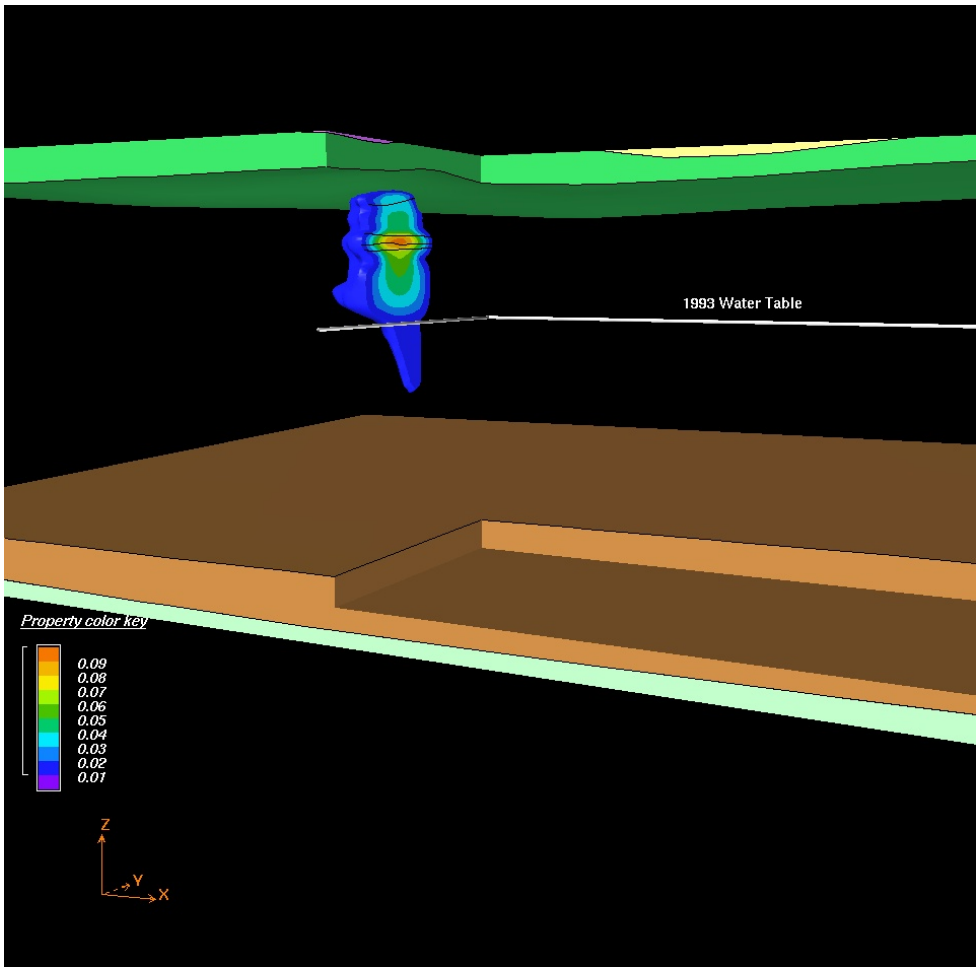

Figure 6.84. DNAPL Body in the Ringold E, Cold Creek, and Hanford Units at 1993 (Simulation 18)

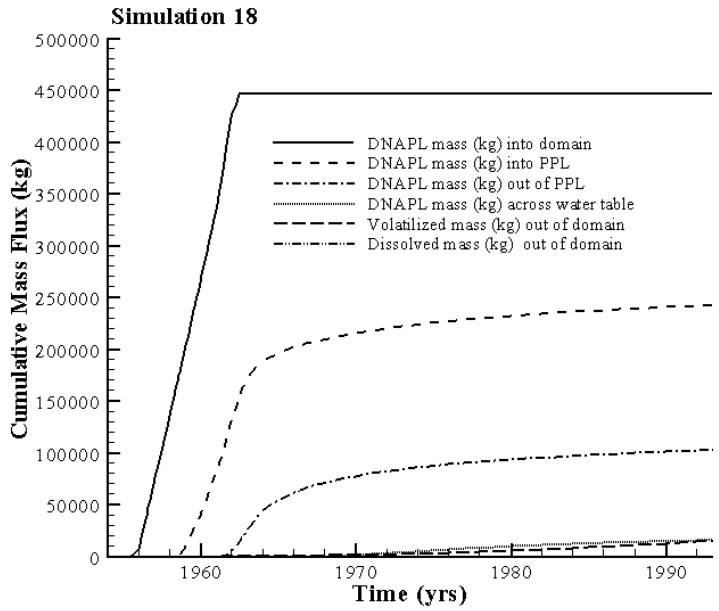

Figure 6.85. Cumulative DNAPL and Dissolved Mass Fluxes (Simulation 18). In the legend, PPL is used to indicate the Cold Creek unit.

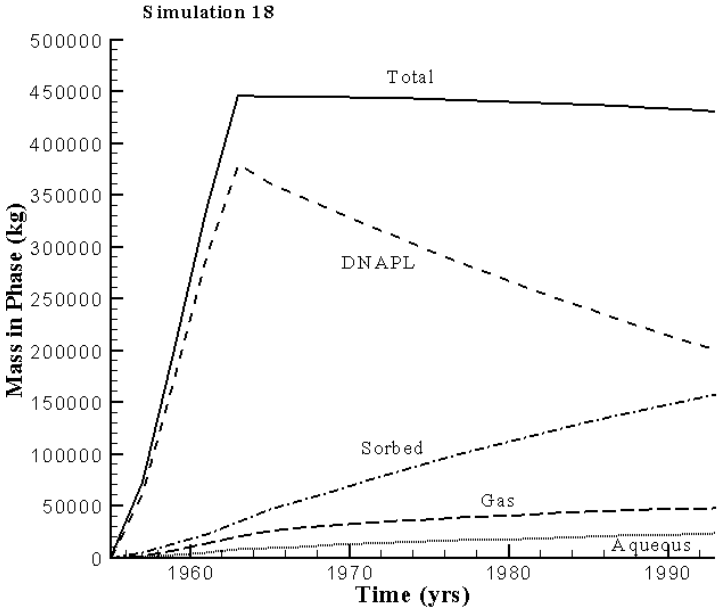

Figure 6.86. Volatile Organic Compound (VOC) Mass Distribution Over the NAPL, Sorbed, Aqueous, and Gaseous Phases (Simulation 18)

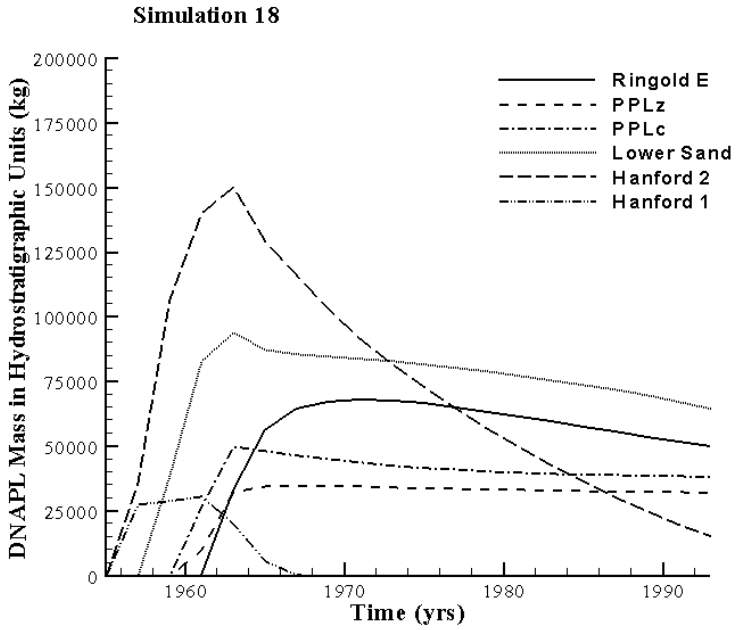

Figure 6.87. DNAPL Mass (kg) Distribution Over the Hydrostratigraphic Units (Simulation 18). In the legend, PPLz is used to indicate the Cold Creek silt and PPLc is used to indicate the Cold Creek carbonate.

6.2.19 Simulation 19

In this simulation, the porosity was increased by a factor 1.25. An overview of the DNAPL body at 1993 is shown in Figure 6.88. Selective cumulative mass fluxes are shown in Figure 6.89. Mass distributions over the fluid phases and hydrostratigraphic units are presented in Figures 6.90 and 6.91, respectively. The travel time for the first kilogram to reach the water table was 14.4 years. At 1993, 49% of the original DNAPL inventory remained in the vadose zone. Just 5,748 kg of DNAPL moved across the water table at 1993. The maximum DNAPL saturation at 1993 is 0.101. The location of the maximum saturation is in the Cold Creek silt.

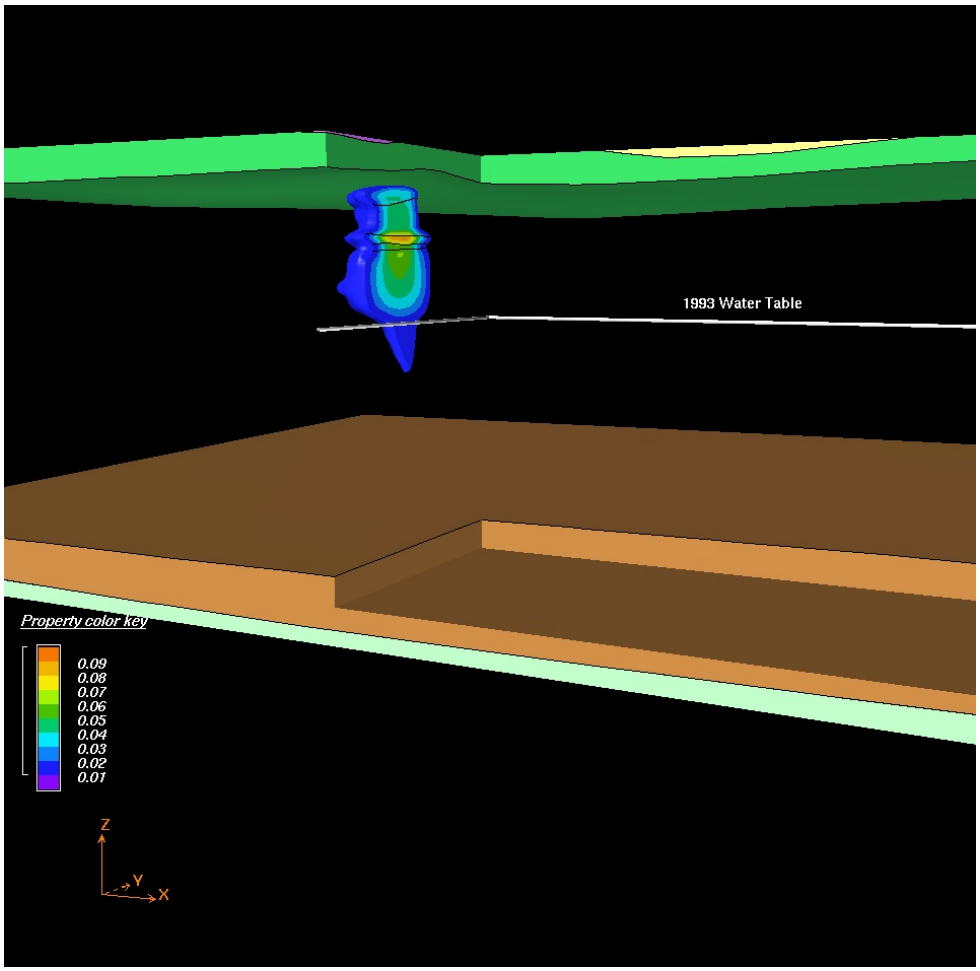

Figure 6.88. DNAPL Body in the Ringold E, Cold Creek, and Hanford Units at 1993 (Simulation 19)

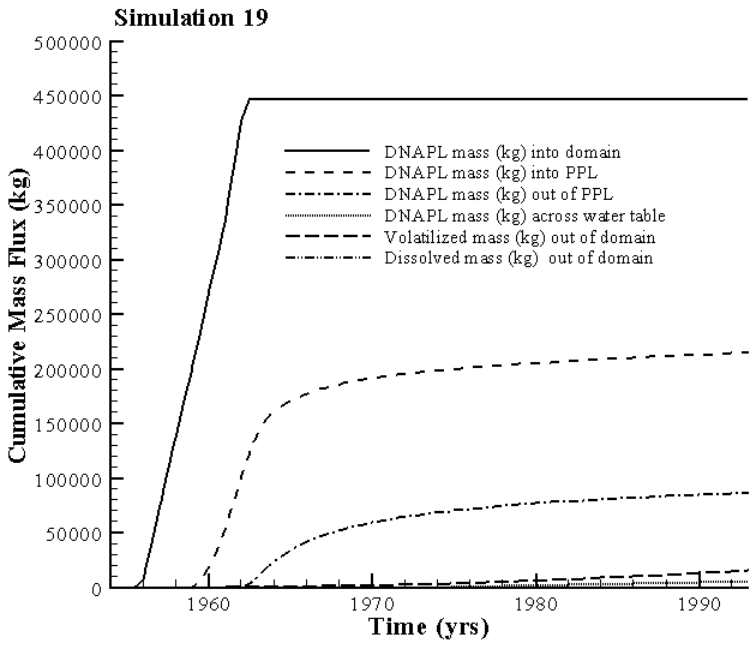

Figure 6.89. Cumulative DNAPL and Dissolved Mass Fluxes (Simulation 19). In the legend, PPL is used to indicate the Cold Creek unit.

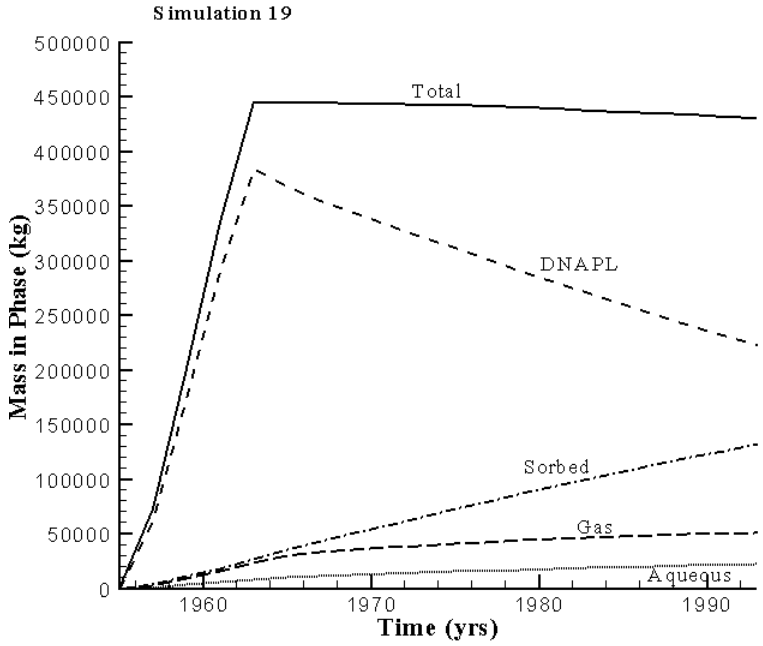

Figure 6.90. Volatile Organic Compound (VOC) Mass Distribution Over the NAPL, Sorbed, Aqueous, and Gaseous Phases (Simulation 19)

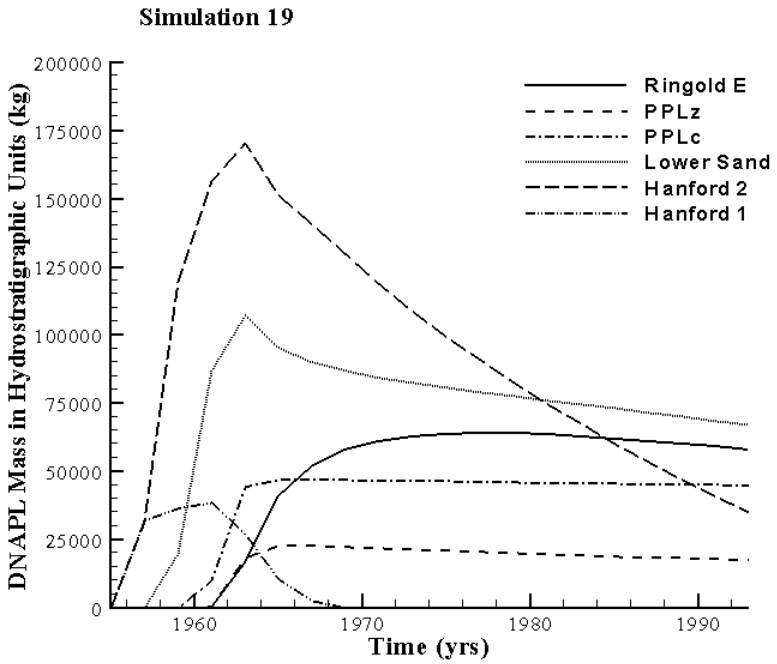

Figure 6.91. DNAPL Mass (kg) Distribution Over the Hydrostratigraphic Units (Simulation 19). In the legend, PPLz is used to indicate the Cold Creek silt and PPLc is used to indicate the Cold Creek carbonate.

6.2.20 Simulation 20

In this simulation, the porosity was decreased by a factor 0.75. An overview of the DNAPL body at 1993 is shown in Figure 6.92. Selective cumulative mass fluxes are shown in Figure 6.93. Mass distributions over the fluid phases and hydrostratigraphic units are presented in Figures 6.94 and 6.95, respectively. The travel time for the first kilogram to reach the water table was 6.5 years. At 1993, 32% of the original DNAPL inventory remained in the vadose zone. A total of more than 60,000 kg of DNAPL moved across the water table at 1993. The maximum DNAPL saturation at 1993 is 0.099. The location of the maximum saturation is in the Cold Creek silt.

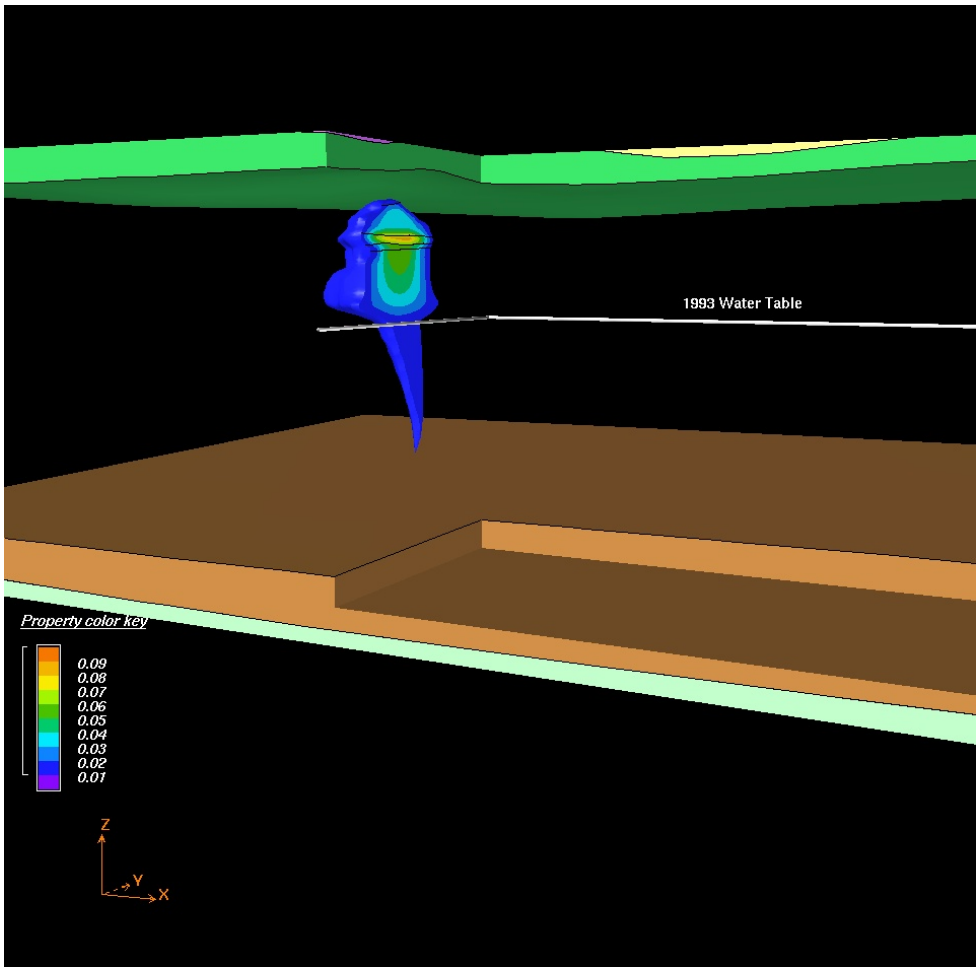

Figure 6.92. DNAPL Body in the Ringold E, Cold Creek, and Hanford Units at 1993 (Simulation 20)

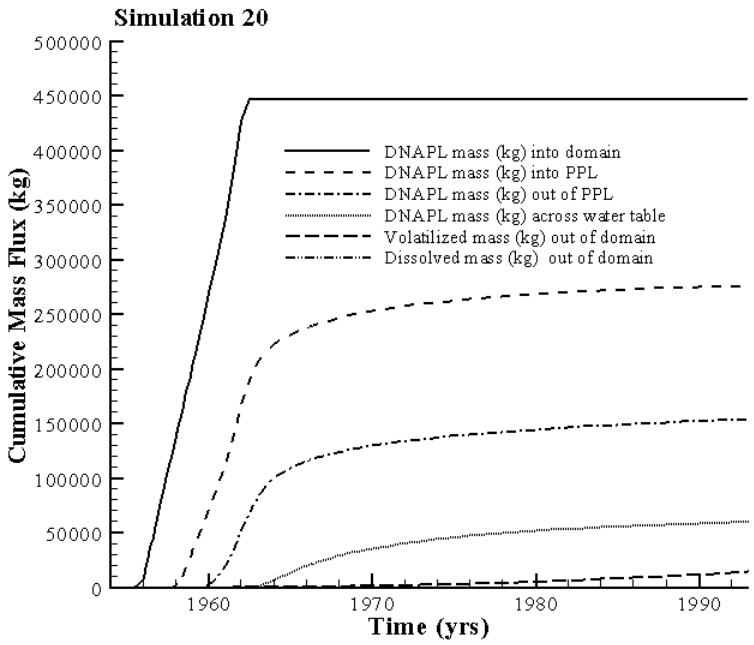

Figure 6.93. Cumulative DNAPL and Dissolved Mass Fluxes (Simulation 20). In the legend, PPL is used to indicate the Cold Creek unit.

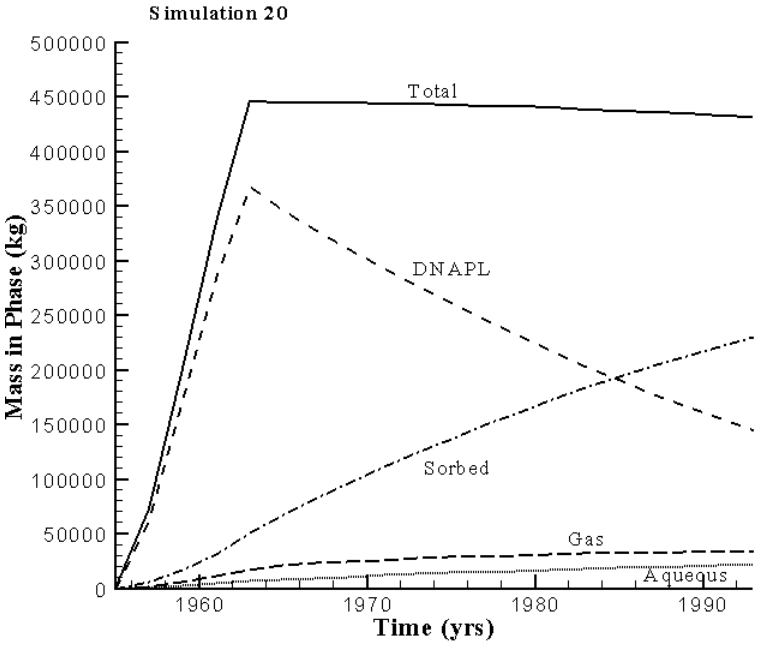

Figure 6.94. Volatile Organic Compound (VOC) Mass Distribution Over the NAPL, Sorbed, Aqueous, and Gaseous Phases (Simulation 20)

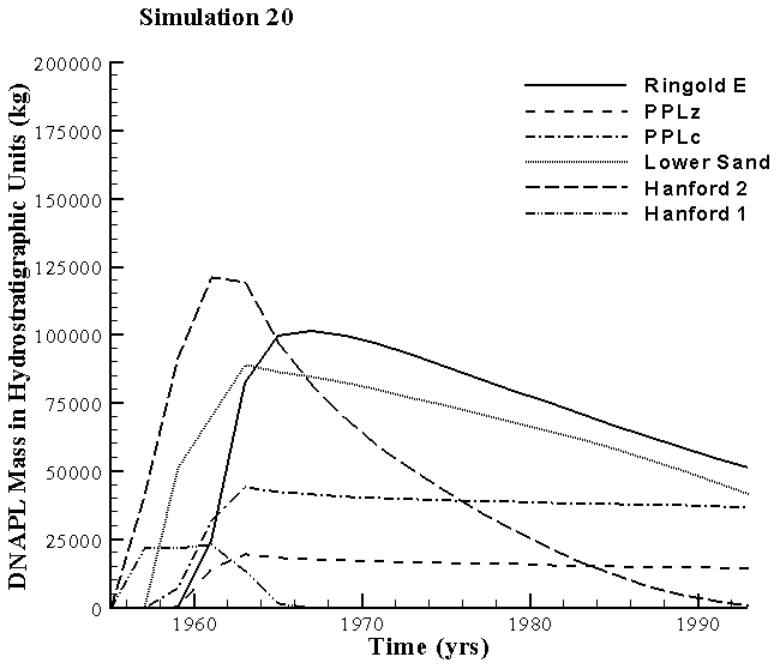

Figure 6.95. DNAPL Mass (kg) Distribution Over the Hydrostratigraphic Units (Simulation 20). In the legend, PPLz is used to indicate the Cold Creek silt and PPLc is used to indicate the Cold Creek carbonate.

6.2.21 Simulation 21

In this simulation, the linear K_d factor was reduced to 0.1 mL/g. An overview of the DNAPL body at 1993 is shown in Figure 6.96. Selected cumulative mass fluxes are shown in Figure 6.97. Mass distributions over the fluid phases and hydrostratigraphic units are presented in Figures 6.98 and 6.99, respectively. The travel time for the first kilogram to reach the water table was 8.5 years. At 1993, 45% of the original DNAPL inventory remained in the vadose zone. A total of more than 29,000 kg of DNAPL moved across the water table at 1993. The maximum DNAPL saturation at 1993 is 0.103. The location of the maximum saturation is in the Cold Creek silt.

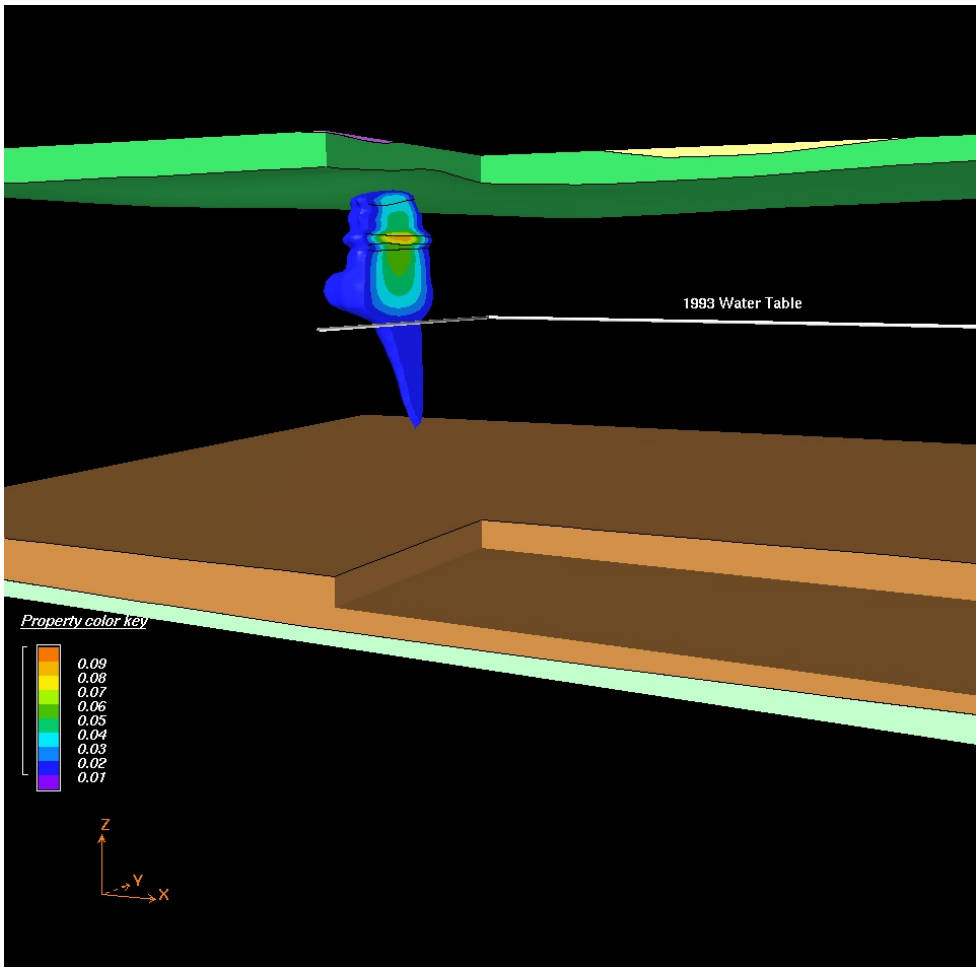

Figure 6.96. DNAPL Body in the Ringold E, Cold Creek, and Hanford Units at 1993 (Simulation 21)

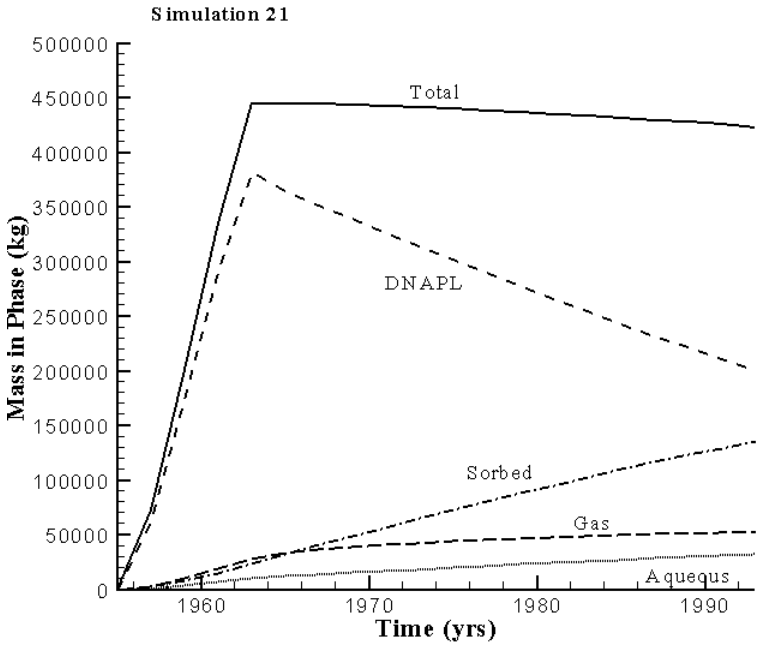

Figure 6.97. Cumulative DNAPL and Dissolved Mass Fluxes (Simulation 21). In the legend, PPL is used to indicate the Cold Creek unit.

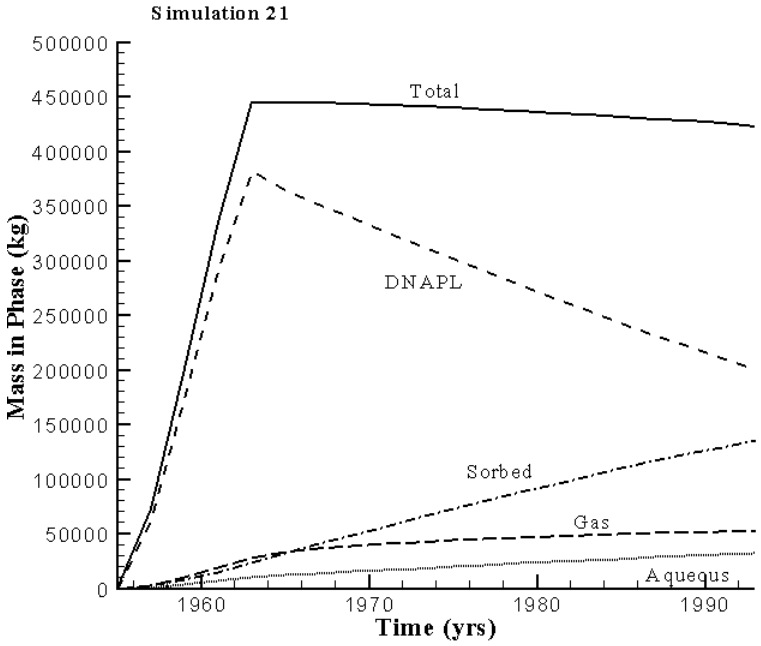

Figure 6.98. Volatile Organic Compound (VOC) Mass Distribution Over the NAPL, Sorbed, Aqueous, and Gaseous Phases (Simulation 21)

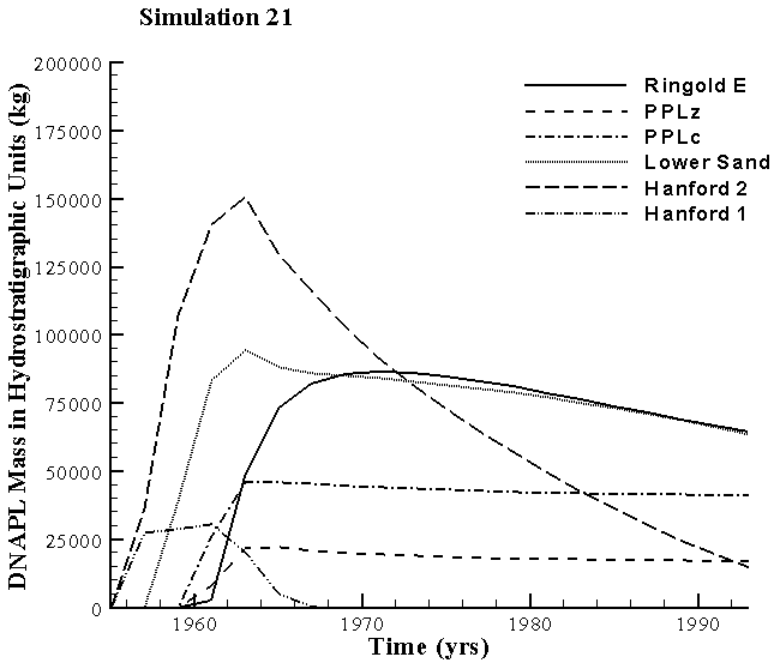

Figure 6.99. DNAPL Mass (kg) Distribution Over the Hydrostratigraphic Units (Simulation 21). In the legend, PPLz is used to indicate the Cold Creek silt and PPLc is used to indicate the Cold Creek carbonate.

6.2.22 Simulation 22

In this simulation, the linear K_d factor was increased to 0.4 mL/g. An overview of the DNAPL body at 1993 is shown in Figure 6.100. Selected cumulative mass fluxes are shown in Figure 6.101. Mass distributions over the fluid phases and hydrostratigraphic units are presented in Figures 6.102 and 6.103, respectively. The travel time for the first kilogram to reach the water table was 9.3 years. At 1993, 40% of the original DNAPL inventory remained in the vadose zone. A total of more than 21,000 kg of DNAPL moved across the water table at 1993. The maximum DNAPL saturation at 1993 is 0.098. The location of the maximum saturation is in the Cold Creek silt.

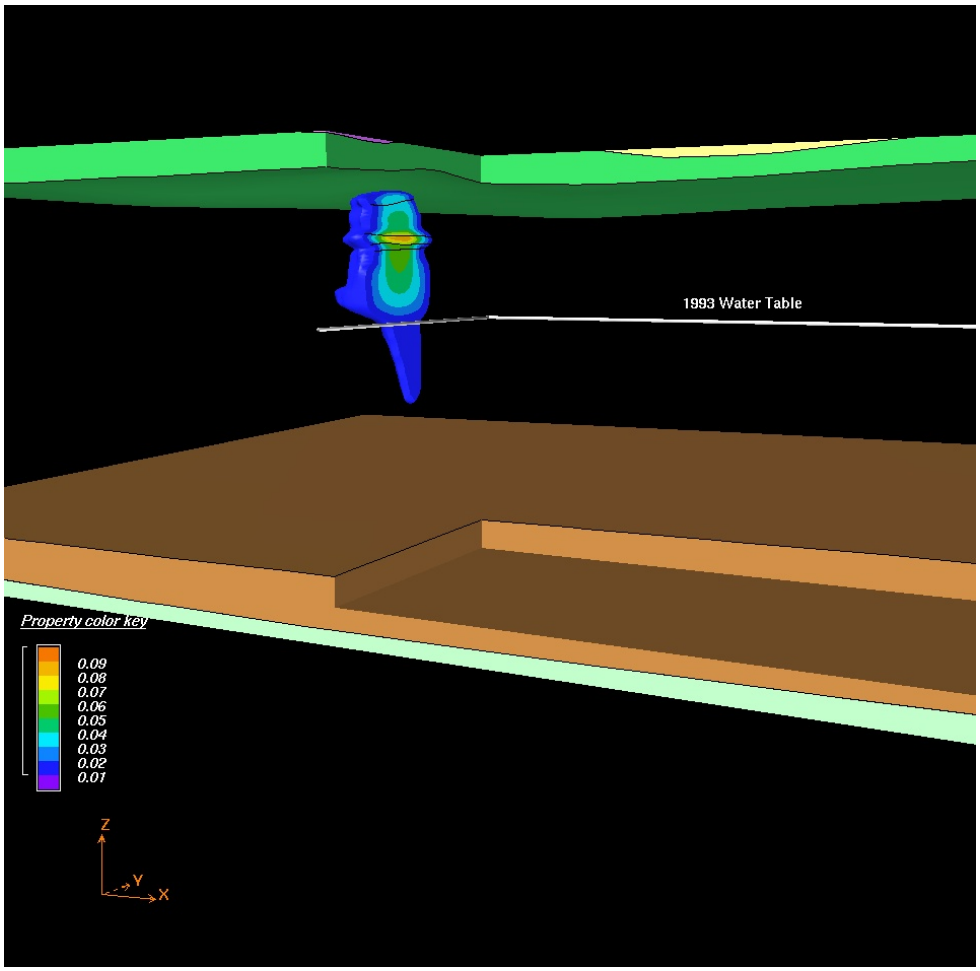

Figure 6.100. DNAPL Body in the Ringold E, Cold Creek, and Hanford Units at 1993 (Simulation 22)

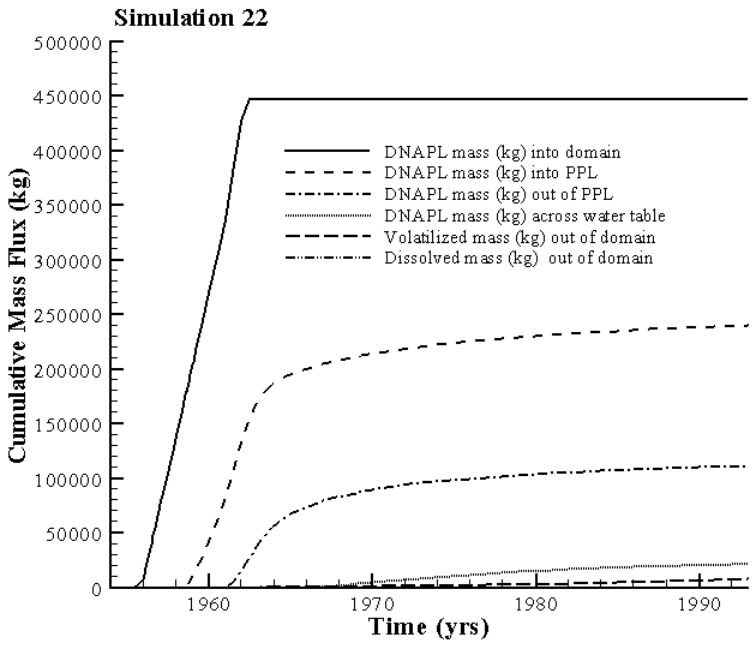

Figure 6.101. Cumulative DNAPL and Dissolved Mass Fluxes (Simulation 22). In the legend, PPL is used to indicate the Cold Creek unit.

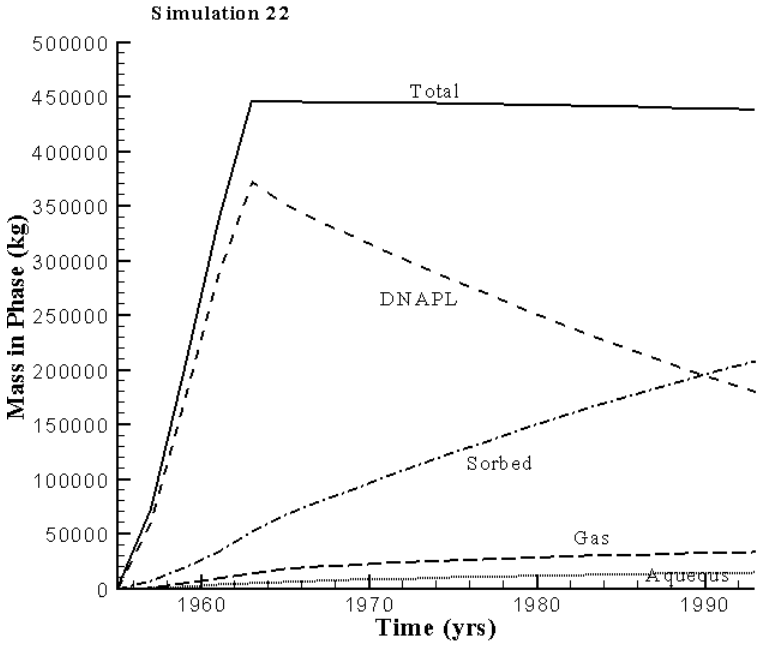

Figure 6.102. Volatile Organic Compound (VOC) Mass Distribution Over the NAPL, Sorbed, Aqueous, and Gaseous Phases (Simulation 22)

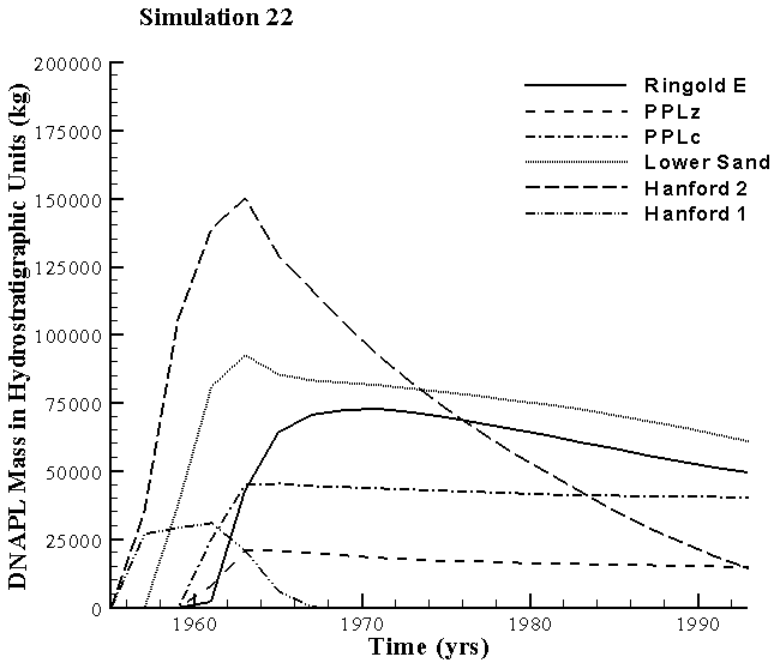

Figure 6.103. DNAPL Mass (kg) Distribution Over the Hydrostratigraphic Units (Simulation 22). In the legend, PPLz is used to indicate the Cold Creek silt and PPLc is used to indicate the Cold Creek carbonate.

6.3 Comparison of Simulation Results

Comparisons between the results of the individual sensitivity analysis simulations and the Base Case results have been discussed in Section 6.2. In this section, comparisons between all simulations are described. Most comparisons are made for 1993, the year when SVE was initiated at the site. Table 6.1 shows the DNAPL mass in the vadose zone at 1993 and the percentage of the total inventory. Simulation 13, with the increased permeability values, showed the lowest percentage (19%), while the highest percentage (65%) was obtained in Simulation 14, where the Base Case permeability values were divided across the board by a factor 10. Simulation 8 and 15 also showed rapid vertical DNAPL movement through the Cold Creek unit into the water table, resulting in only a small fraction remaining in the vadose zone. Other low estimates are produced by Simulation 8 (30%) and Simulation 11 (30%). Simulation 8 used the van Genuchten-Mualem retention parameters, which resulted in a more rapid vertical movement compared to the Base Case because a distinct positive nonwetting fluid entry pressure is not recognized in this model. The assumptions behind Simulations 8 and 15 are not likely and the computed results have to be interpreted as such. Not taking into account these simulations, the percentages of DNAPL in the vadose zone at 1993 vary from 19% to 65% of the initial inventory corresponding to 0.87E5 kg to 2.91E5 kg. The DNAPL mass in the vadose zone is potentially available for SVE remediation, although extraction for the Cold Creek unit might be more difficult.

Table 6.2 shows the time it takes for the first kilogram of DNAPL to move across the water table. In Simulations 2 (smaller DNAPL inventory), 12 (smaller Brooks-Corey pore geometry factor), and 16 (smaller permeability), no DNAPL was moved across the water table before 1993. For all other simulations, the arrival time varied from 4.1 to 19.5 years. The amount of DNAPL that moved across the water table is the highest in Simulation 11.

Normalized spatial moments of the simulated DNAPL plumes were calculated to provide a quantitative basis for comparing the results of the different simulation cases (Freyberg 1986). The *ijk*th moment of the NAPL mass distribution in space was defined as

$$M_{ijk}(t) = \int_{-\infty}^{\infty} \int_{-\infty}^{\infty} \int_{-\infty}^{\infty} \rho_n \phi S_n(x,y,z,t) x^i y^j z^k \, dx dy dz \tag{6.1}$$

where ρ_n is the mass density of the NAPL, ϕ is the porosity, S_n is the NAPL saturation, and x, y, and z are the spatial coordinates. The integrals in Equation (6.1) were evaluated over the extent of the three-dimensional model domain.

The zeroth, first, and second (i + j + k = 0, 1, or 2, respectively) spatial moments of the NAPL plumes were computed. These moments provide measures of the total NAPL mass, the location of the center of mass, and spread about the center of mass. The zeroth moment, M_{000}, is equal to the total mass in the domain. The first moment, normalized by the zeroth moment, defines the location of the center of mass (x_c, y_c, z_c):

$$x_c = \frac{M_{100}}{M_{000}} \qquad y_c = \frac{M_{010}}{M_{000}} \qquad y_c = \frac{M_{001}}{M_{000}} \tag{6.2}$$

The second moment about the center of mass defines a spatial covariance tensor (Freyberg 1986):

$$\sigma = \begin{bmatrix} \sigma_{xx} & \sigma_{xy} & \sigma_{xz} \\ \sigma_{yx} & \sigma_{yy} & \sigma_{yz} \\ \sigma_{zx} & \sigma_{zy} & \sigma_{zz} \end{bmatrix}$$

$$\sigma_{xx} = \frac{M_{200}}{M_{000}} - x_c^2 \qquad \sigma_{yy} = \frac{M_{020}}{M_{000}} - y_c^2 \qquad \sigma_{zz} = \frac{M_{002}}{M_{000}} - z_c^2 \tag{6-3}$$

$$\sigma_{xy} = \sigma_{yx} = \frac{M_{110}}{M_{000}} - x_c y_c \qquad \sigma_{xz} = \sigma_{zx} = \frac{M_{101}}{M_{000}} - x_c z_c \qquad \sigma_{yz} = \sigma_{zy} = \frac{M_{011}}{M_{000}} - y_c z_c$$

The components of the covariance tensor are directly related to the spread of the NAPL plume about its center of mass. In Table 6.3, the zeroth and first order moments are shown, while in Table 6.4 an overview is presented of the second order diagonal moments. The moments are computed for 1993.

Disregarding the results from Simulation 8 and 15, the first moments show that the center of mass in the x and y direction has not significantly shifted from the center of the 216-Z-9 trench. In general, the shift in the x direction is less than 1 m, while the shift in the y direction is less than 3 m. This means that in the horizontal plane, the center of mass is located directly under the disposal site. With the exception of Simulations 7, 8, 11, and 15, the vertical centers of mass are located either in the lower sand or Cold Creek unit. Simulations 7 and 11 show considerable DNAPL movement below the Cold Creek unit and the center of mass is located in the Ringold E formation. The standard deviations of the second order diagonal moments are shown in Table 6.2. According to this analysis, approximately 95% of the DNAPL mass is predicted to be located between the center of mass and plus or minus two times the computed standard deviation in Table 6.2. The large second order horizontal moments for Simulation 8 and 15 are further indications that these simulations produce nonrealistic results. For all other cases, the standard deviations of the horizontal second order moments are less than 10.0 m. The vertical standard deviations of the second order moments are relatively high for Simulation 7, 10, 11, and 25. In these four simulations, relatively large amounts of DNAPL moved through the unsaturated part of the Ringold E and across the water table. As a result, the DNAPL body is more elongated in the vertical direction than for the other simulations.

Table 6.1. Total DNAPL Mass Inventory and DNAPL Mass in Vadose Zone at 1993, as a Percentage of Total Inventory

Simulation	Total DNAPL Mass Inventory (kg)	DNAPL Mass (kg) in Vadose Zone at 1993	DNAPL Mass (kg) in Vadose Zone at 1993 as a Percentage of Inventory
Base Case	4.50E5	1.93e5	43
1	5.80E5	2.59E5	45
2	1.61E5	0.44E5	27
3	5.04E5	1.80E5	36
4	3.98E5	2.36E5	59
5	4.50E5	1.62E5	36
6	4.50E5	1.97E5	44
7	4.50E5	1.24E5	28
8	4.50E5	1.34E5	30
9	4.50E5	2.10E5	47
10	4.50E5	1.72E5	38
11	4.50E5	1.37E5	30
12	4.50E5	2.67E5	59
13	4.50E5	0.87E5	19
14	4.50E5	2.91E5	65
15	4.50E5	1.14E4	25
16	4.50E5	2.75E5	61
17	4.50E5	1.97E5	44
18	4.50E5	2.00E5	44
19	4.50E5	2.22E5	49
20	4.50E5	1.45E5	32
21	4.50E5	2.01E5	45
22	4.50E5	1.81E5	40

Table 6.2. Total DNAPL Mass Inventory, Time for DNAPL to Reach the Water Table, and DNAPL Mass Transported Across the Water Table at 1993

Simulation	Total DNAPL Mass Inventory (kg)	Time (yr) for DNAPL to Reach Water Table	DNAPL Mass (kg) Moved Across Water Table at 1993
Base Case	450,616	9.0	26,744
1	580,382	7.4	68,490
2	161,138	-	-
3	503,704	7.6	53,378
4	398,160	11.9	7,694
5	450,616	8.2	36,821
6	450,616	9.4	22,599
7	450,616	5.4	134,909
8	450,616	6.7	92,109
9	450,616	19.5	1,912
10	450,616	6.8	76,017
11	450,616	4.1	109,815
12	450,616	-	-
13	450,616	8.5	19,170
14	450,616	10.5	20,701
15	450,616	6.3	86,508
16	450,616	-	-
17	450,616	9.3	16,803
18	450,616	11.5	11,286
19	450,616	14.4	5,748
20	450,616	6.5	60,225
21	450,616	8.5	29,425
22	450,616	9.3	21,932

Table 6.3. Zero and First Order Moments of DNAPL Mass at 1993. (The center of 216-Z-9 Trench is at x = 0 m, y = 0 m, and z = 195 m. The Cold Creek unit below the trench is approximately located between z = 158 m and z = 169 m.)

Simulation	M_{000}	x_c (m)	y_c (m)	z_c (m)
Base Case	1.93E5	-0.29	0.23	167
1	2.59E5	-0.31	0.70	164
2	0.44E5	-0.29	0.08	172
3	1.80E5	-0.34	0.56	165
4	2.36E5	-0.16	0.09	170
5	1.62E5	-0.11	0.41	157
6	1.97E5	-0.21	0.33	167
7	1.24E5	-0.31	1.84	129
8	1.34E5	-0.94	1.28	166
9	2.10E5	-0.20	0.10	170
10	1.72E5	-0.33	1.19	161
11	1.37E5	-0.42	3.06	146
12	2.67E5	-0.07	0.08	174
13	0.87E5	-0.54	0.33	165
14	2.91E5	-0.16	0.13	169
15	1.14E4	-0.27	2.30	154
16	2.75E5	-0.25	0.01	173
17	1.97E5	-0.27	0.10	170
18	2.00E5	-0.26	0.01	171
19	2.22E5	-0.21	0.03	170
20	1.45E5	-0.42	0.68	164
21	2.01E5	-0.26	0.26	167
22	1.81E5	-0.31	0.16	168

Table 6.4. Standard Deviations of Second Order Moments of DNAPL Mass at 1993. (The center of 216-Z-9 trench is at x = 0 m, y = 0 m, and z = 195 m. The Cold Creek unit below the trench is approximately located between z = 158 m and z = 169 m.)

Simulation	$\sqrt{\sigma_{xx}}$ (m)	$\sqrt{\sigma_{yy}}$ (m)	$\sqrt{\sigma_{zz}}$ (m)
Base Case	5.8	6.8	11.4
1	6.4	7.9	16.0
2	2.6	4.5	3.9
3	5.7	7.1	13.3
4	5.9	7.1	10.5
5	6.4	7.9	12.8
6	5.8	6.9	11.0
7	8.1	8.0	23.0
8	7.7	14.8	12.0
9	6.1	7.1	8.1
10	5.3	7.1	20.5
11	5.5	8.1	29.3
12	5.4	6.8	7.0
13	5.7	6.8	7.3
14	5.9	7.1	13.3
15	5.8	8.2	25.4
16	5.7	7.1	8.6
17	5.7	6.8	7.9
18	5.6	6.9	7.1
19	5.3	6.4	10.0
20	6.3	7.9	12.6
21	6.0	7.1	11.7
22	5.5	6.6	10.8

6.4 SVE Simulation Results

The SVE scheme, discussed in Section 5.2, was applied to the Base Case simulation. The CT distribution over the phases, in the period from 1954 through 2004, is shown in Figure 6.104. The plot shows that the SVE process is very effective in removing CT from the vadose zone. Within a few years, the CT in the domain is reduced from about 440,000 to 50,000 kg. The remaining CT is located in the saturated zone dissolved in the aqueous phase and sorbed to the solid phase. Figure 6.105 demonstrates in more detail the rapid decline of the CT distribution over the phases for the period 1990 – 2004,

coinciding with SVE extraction. The DNAPL distribution over the porous media as a function of time has been shown in Figure 6.106 for the period 1954 - 2004 and Figure 6.107 for the period 1990 – 2004. The figures show that other than from the Cold Creek carbonate, CT removal occurs rapidly from all layers. The cumulative CT mass extraction (Figure 6.108) shows that most the CT is extracted during the first 2-3 years of operation.

The SVE process at the 216 Z-9 trench has extracted approximately 53,000 kg of CT. The detailed simulations show that the SVE, when based on CT equilibrium partitioning between the various phases, was quite effective. Applying the averaged extraction rates over the periods when the extraction system was active, yield an almost complete removal of the CT in the DNAPL, sorbed to the solid phase, and dissolved in the aqueous and gas phases. The imposed rates were sufficient to remove DNAPL from the Cold Creek unit. The Base Case simulation results in too much mass being extracted relative to what was observed in the field. There are several possible reasons for this discrepancy, including differences between the actual and simulated 1) flow rates, 2) fluid-media properties, and 3) disposal history (volumes, rates, and timing). Differences may also be due, in part, to the fact that the current simulations are based on equilibrium phase partitioning; thus any rate-limited (kinetic) mass transfer effects are not accounted for. Furthermore, the current simulations assume that the porous media is uniform within any of the defined hydrostratigraphic units. In reality, however, it is well know that these units are very heterogeneous.

A few scoping studies were completed to investigate whether the cumulative removed CT mass could be reduced by making simple but reasonable changes in the pumping and porous media parameters. When a constant 30% bleeding percentage was imposed on the extraction rates, the cumulative mass removed over the entire period decreased from 390,000 to 230,000 kg (Figure 6.108). Combining a 30% bleeding with reduced Cold Creek unit permeability values (by a factor 10) results in a cumulative extracted mass of about 50,000 kg (Figure 6.109). The latter amount compares favorably with the mass extracted at the field site. The scoping simulations demonstrate that reasonable changes in input parameters will yield considerable reductions in the extracted CT mass, compared to the base case. In addition, the effects of smaller-scale heterogeneities and kinetic volatilization on SVE extraction need to be evaluated in the future.

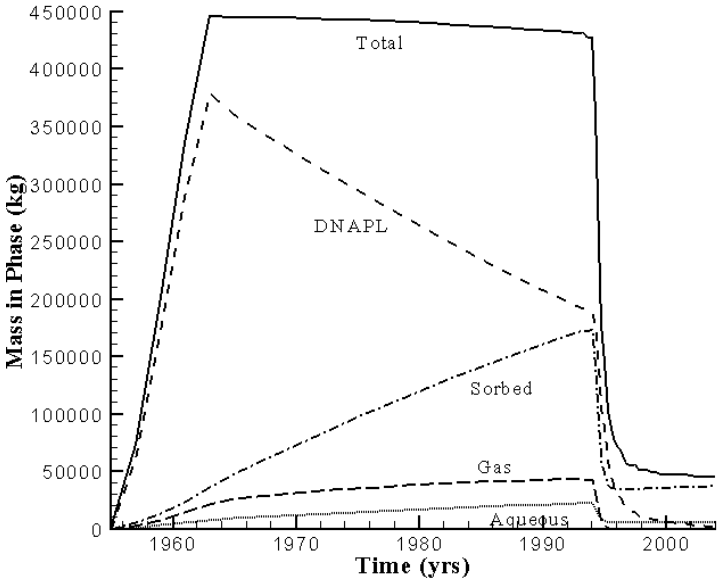

Figure 6.104. Phase Distribution of CT over the DNAPL, Sorbed, Gas, and Aqueous Phases from 1954 – 2004

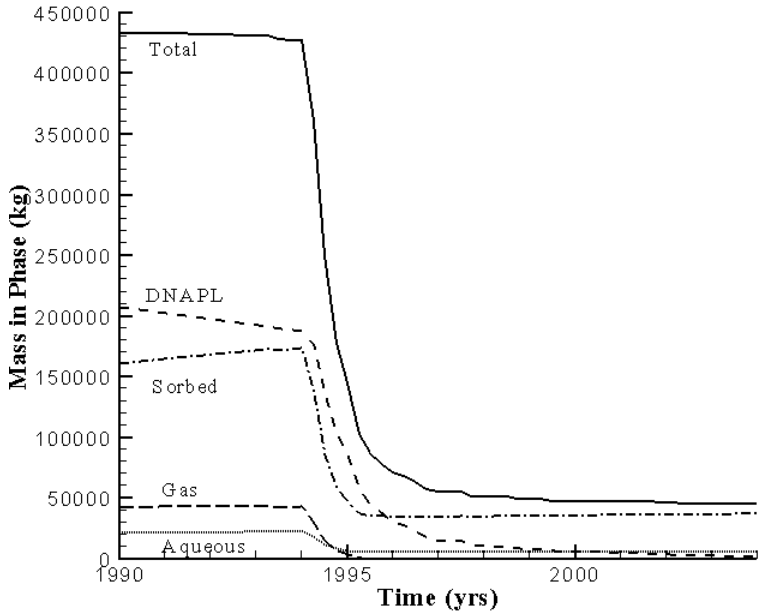

Figure 6.105. Phase Distribution of CT over the DNAPL, Sorbed, Gas, and Aqueous Phases from 1990 – 2004.

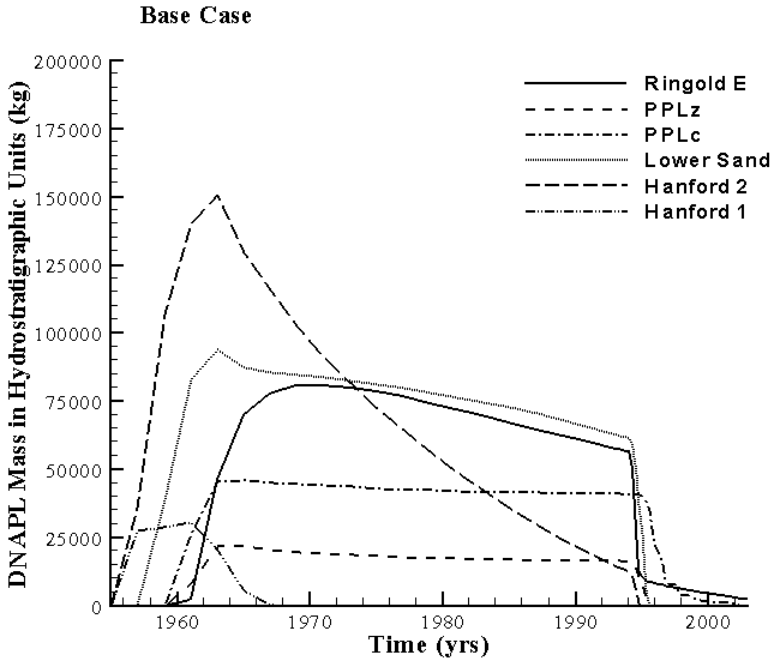

Figure 6.106. Phase Distribution of CT over the Various Porous Media from 1954 to 2004. In the legend, PPLz is used to indicate the Cold Creek silt and PPLc is used to indicate the Cold Creek carbonate.

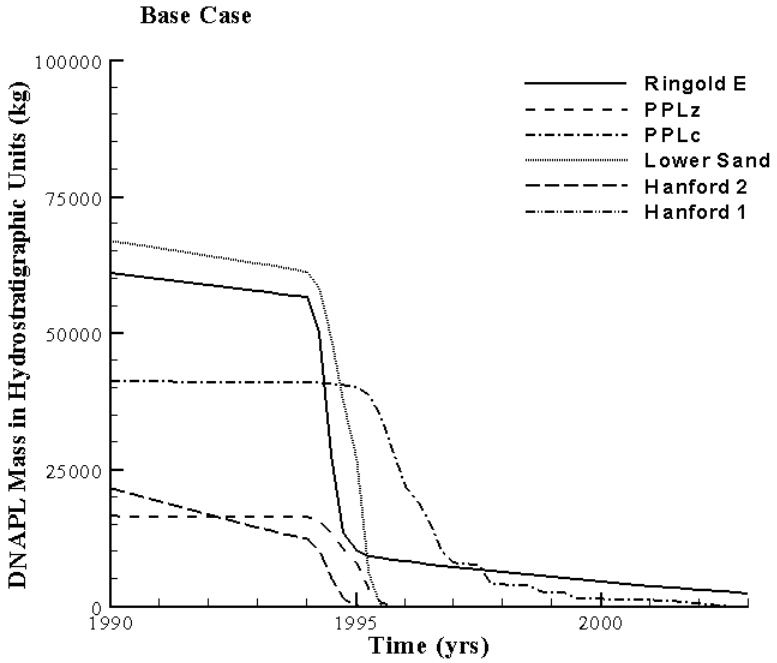

Figure 6.107. Phase Distribution of CT over the Various Porous Media from 1990 – 2004

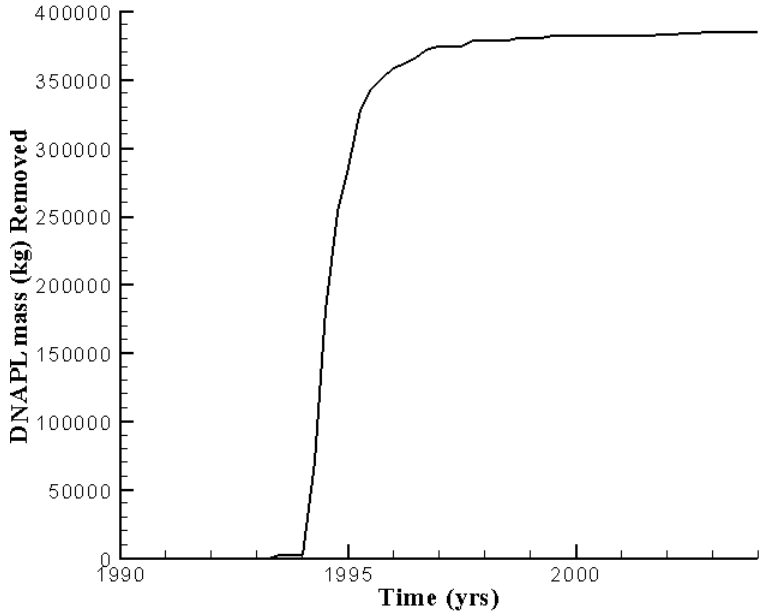

Figure 6.108. Extracted CT as a Function of Time (Base Case)

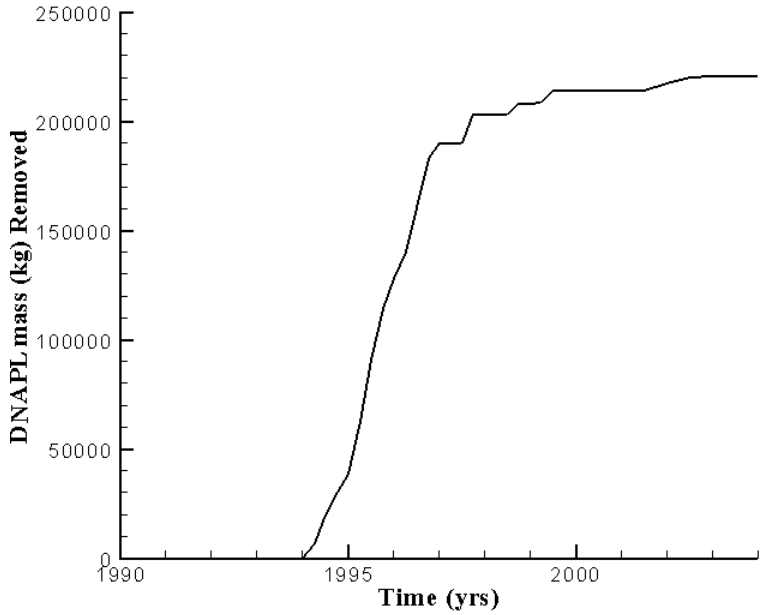

Figure 6.109. Extracted CT (kg) as a Function of Time for a Bleeding Percentage of 30% for the Entire Period

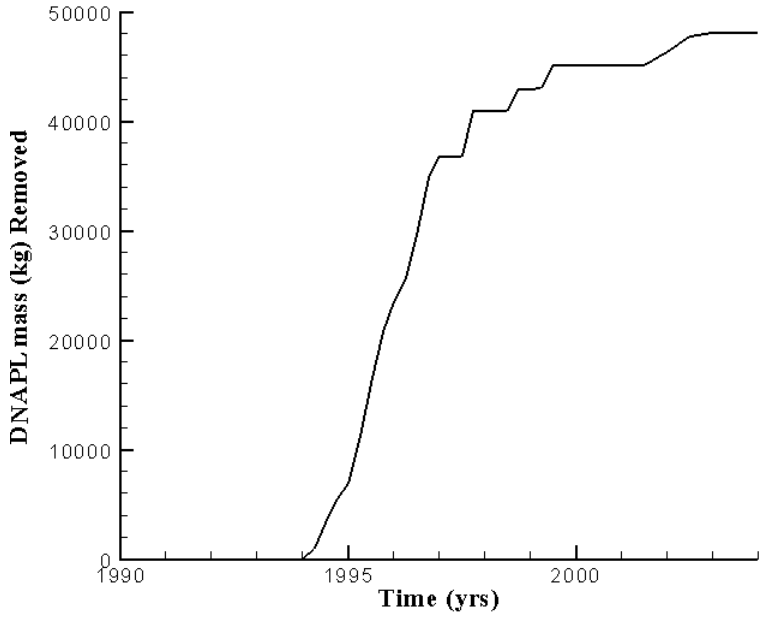

Figure 6.110. Extracted CT (kg) as a Function of Time for a Bleeding Percentage of 30% for the Entire Period in Combination with a Factor Ten Reduction of the Cold Creek Unit Permeability Values

7.0 Summary and Conclusions

Simulations using the multi-fluid flow model STOMP simulator (White and Oostrom 2003) were conducted to estimate how disposed DNAPL migrates in the vadose zone. Simulations targeted migration of DNAPL consisting of CT and co-disposed organics in the subsurface beneath the 216-Z-9 trench as a function of the properties and distribution of subsurface sediments and of the properties and disposal history of the waste. The geological representation of the computational domain was extracted from a larger EarthVision™ model of the 200 West Area subsurface developed during FY 2002. The geologic model used in the modeling study consisted of 12 hydrostratigraphic units. The three-dimensional modeling was conducted to enhance the estimates of CT distribution in the vertical and lateral direction underneath the 216-Z-9 trench.

A total of 23 three-dimensional simulations were conducted to examine infiltration and redistribution of CT in the subsurface prior to implementation of remediation activities in 1993. The simulations consisted of one Base Case simulation and 22 sensitivity analysis simulations. The sensitivity analysis simulations investigated the effects of variations in 1) fluid composition; 2) disposal rate, area, and volume; 3) fluid retention; 4) permeability; 5) anisotropy; 6) sorption; 7) porosity; and 8) residual saturation formation on the movement and redistribution of DNAPL. The residual saturation formation theory (Lenhard et al. 2004) was developed within the DOE Science and Technology Program. The simulations were conducted for the period 1954 to 2003.

The computational domain dimensions were 440 m in the west-east (x) direction, 540 m in the south-north (y) direction, and 147 m in the vertical (z) direction. The Base Case simulation used best estimates of CT and waste water total volumes and infiltration rates from the disposal site (Last and Rohay 1993). Retention parameters, porosities, and hydraulic conductivities for the units were obtained from Khaleel et al. 2001 and Khaleel and Freeman 1995. The relative permeability-saturation-pressure parameters were converted to equivalent Brooks-Corey-Burdine parameter data sets using Lenhard et al. (1989). Neumann boundary conditions were imposed for waste water and DNAPL for the 216-Z-9 trench area during the years that these liquids were disposed.

The results of the Base Case simulation show that at 1993, the year SVE began at the site, 43% of the original DNAPL inventory was still present in the vadose zone as a DNAPL. Most of the vadose zone DNAPL was located in the Lower Sand and Cold Creek unit. The maximum DNAPL saturation at this time was approximately 0.10 and was located in the Cold Creek silt layer. In this simulation, it took 8.5 years for the first kilogram of DNAPL to reach the water table. At 1993, about 27,000 kg had moved across the water table.

A moment analysis showed that the center of mass for DNAPL in the subsurface at 1993 has only shifted 0.29 m in the x direction and 0.23 m in the y direction from the centerline of the 216-Z-9 trench. The center of mass in the vertical direction is located in the Cold Creek silt layer. The second order moment analysis showed that 95% of the mass was expected to be within 11.6, 13.6, and 22.8 m of the center of mass in the x, y, and z direction, respectively. This analysis indicated that most of the liquid

DNAPL in the vadose zone is located underneath the footprint of the disposal facility with the majority of the mass is within the Lower Sand and Cold Creek unit under the conditions of the Base Case simulation.

A considerable amount of DNAPL volatilized in the vadose zone. Because the vapors are denser than ambient air due to large percentage of CT, the vapors tend to sink rapidly above and below the Cold Creek unit. The sinking vapors are forced to spread laterally on top of the fairly moist Cold Creek silt layer and on top of the water table. As a result, the dense vapor plumes spread laterally relatively fast. During this process, CT partitions into the upper regions of the ground water through phase partitioning. The fast lateral spreading of the CT vapors and the subsequent contamination of the ground water affects large volumes of water. This contamination process could occur almost anywhere in the domain. This phenomenon can only be investigated through a simulator recognizing an active gas phase, including density-driven advection. Three-phase simulators using a passive gas phase or ignoring density-driven advection are not appropriate to simulate behavior of a volatile DNAPL such as the organic liquids disposed at the Hanford Site.

Some of the simulations in the sensitivity analysis showed unrealistic results. The simulation using the van Genuchten retention parameters and the simulation with isotropic permeability distribution predicted rapid vertical movement of DNAPL with considerable pooling below the water table on top of the Ringold Mud. The van Genuchten relations do not recognize a distinct positive nonwetting fluid entry pressure, causing DNAPL to move rapidly downward. Based on arguments of Chamness et al. (1991)[1] and Zhang et al. (2003) the assumption of isotropic conditions for Hanford vadose zone porous materials is not appropriate. The summary of results does not include results from these two simulations. The other simulations all show that a considerable amount of the original inventory remained behind in the vadose zone at 1993. The estimates of vadose zone DNAPL at 1993 range from 19 to 65 %. Of the simulations that predict DNAPL to move across the water table, the arrival time of the first kilogram of DNAPL ranged from 4.1 to 19.5 years after the first disposal of DNAPL in 1955. The arrival times are a strong function of the imposed hydraulic properties.

A moment analysis for the sensitivity cases showed that most of the centers of mass in the lateral direction have shifted less than 1 m in the x-direction and less than 3 m in the y-direction by 1993. In the vertical direction, the centers of mass were located either just above or in the Cold Creek units. Maximum saturations were usually less than 0.10, except for the simulations where the new residual saturation formation theory was used. In these cases, the maximum saturations are close to 0.2. For all simulations, the maximum saturations were found in the Cold Creek silt layer. These rather uniform results indicate that the remaining DNAPL in the vadose zone is likely located directly underneath the disposal facility, with the majority of the mass in the Lower Sand and the Cold Creek unit.

The results show that groundwater contamination is caused by DNAPL movement across the water table and by partitioning of CT vapors from the gas phase into the aqueous phase. Even for the

[1] Letter Report from MA Chamness, ML Rockhold, and BN Bjornstad (Pacific Northwest National Laboratory) to U.S. Department of Energy, *A Hydrogeologic Study for Construction of a Percolations Pond*, dated 1991.

simulations where DNAPL was not able to penetrate the water table, large gaseous CT plumes were formed in the units above the Cold Creek unit and in the unsaturated Ringold E unit between the Cold Creek unit and the water table. As a result, large ground water plumes were formed through the partitioning process. The lateral extent of the ground water plumes appears to be independent of the simulation.

Initial simulations were conducted to investigate the effect of the SVE on the DNAPL in the subsurface of the 216 Z-9 trench. The SVE process at the 216 Z-9 Trench has extracted approximately 53,000 kg of CT. Daily records of pumping rates for the 216-Z-9 well network, its hours of operation on each day, and the on-line well intervals were used in conjunction with information on the current screened intervals for each well in the 216-Z-9 well field to generate time-averaged flow rates which were applied as sink terms to represent SVE in STOMP. No attempt was made in the model simulations to account for any physical changes that might have occurred to any given well during the course of the SVE operations. The detailed simulations show that the SVE, when based on CT equilibrium partitioning between the various phases, was quite effective. Applying the averaged extraction rates over the periods when the extraction system was active, yield an almost complete removal of the CT in the DNAPL, sorbed to the solid phase, and dissolved in the aqueous and gas phases. The imposed rates were sufficient to remove DNAPL from the Cold Creek unit. The Base Case simulation results in too much mass being extracted, relative to what was observed in the field. There are several possible reasons for this discrepancy, including differences between the actual and simulated 1) flow rates, 2) fluid-media properties, and 3) disposal history (volumes, rates, and timing). Differences may also be due, in part, to the fact that the current simulations are based on equilibrium phase partitioning; thus any rate-limited (kinetic) mass transfer effects are not accounted for. Furthermore, the current simulations assume that the porous media is uniform within any of the defined hydro-stratigraphic units. In reality, however, it is well know that these units are very heterogeneous.

The simulations show that the Cold Creek silt and carbonate layers have a large impact on DNAPL movement. Considerable amounts of CT were predicted to be retained in the Cold Creek silt and carbonate layers in 1993. The gas phase plume in the vadose is always predicted to much more extensive than the zone containing actual DNAPL. In the Cold Creek unit, the CT is still able to volatilize and move downward where groundwater contamination could take place. The simulation results also clearly demonstrate that the CT mixture has not moved away from the footprint of the disposal facility. In most simulations, CT is predicted to enter the water table as a separate phase of through gaseous transport and subsequent partitioning into the aqueous phase.

In summary, the modeling results led to the following conclusions that can be used to update the conceptual model of CT distribution in the subsurface.

- *Where is CT expected to accumulate?* CT DNAPL accumulates in the finer-grain layers of the vadose zone but does not appear to pool on top of these layers.

- *Where would continuing liquid CT sources to groundwater be suspected?* Migration of DNAPL CT tends to be preferentially vertically downward below the disposal area. Lateral movement of DNAPL CT is not likely. However, significant lateral migration of vapor CT occurs.

- *Where would DNAPL contamination in groundwater be suspected?* Sufficient CT and co-disposed liquids were introduced to the subsurface for DNAPL CT to migrate at least through the Cold Creek unit and, in some sensitivity cases, to migrate across the water table. For the Base Case simulation, 43% of the original DNAPL inventory (450,000 kg) was still present in the vadose zone as a DNAPL in 1993. Most of this DNAPL was located just above and within the Cold Creek units. At 1993, about 27,000 kg (6% of the inventory) of DNAPL had moved across the water table.

- *What is the estimated distribution and state of CT in the vadose zone?* The amount of DNAPL CT that accumulated in the vadose zone by 1993 ranges from 19% to 65% of the total disposed in the sensitivity simulations. The majority of the mass at 1993 was typically DNAPL or sorbed phase. The center of mass for CT in the vadose zone was typically directly beneath the disposal area and within the Cold Creek unit.

- *How does SVE affect the distribution of CT in the vadose zone?* SVE effectively removes CT from the permeable layers of the vadose zone. SVE previously applied in the 216-Z-9 trench area has likely removed a large portion of CT initially present in the permeable layers within the large radius of influence of the extraction wells. Finer grain layers with more moisture content are less effected by SVE and contain the CT remaining in the vadose zone.

8.0 References

Aldrich RC. 1984. *Radioactive Liquid Wastes Discharged to Ground in the 200 Areas During 1983*. RHO-HS-SR-83-3 4QLIQ, Rockwell Hanford Company, Richland, Washington.

Aldrich RC. 1985. *Radioactive Liquid Wastes Discharged to Ground in the 200 Areas During 1984*. RHO-HS-SR-84-3 4Q-LI, Rockwell Hanford Company, Richland, Washington.

Aldrich RC. 1986. *Radioactive Liquid Wastes Discharged to Ground in the 200 Areas During 1985*. RHO-HS-SR-85-3 4QLIQ, Rockwell Hanford Company, Richland, Washington.

Aldrich RC. 1987. *Radioactive Liquid Wastes Discharged to Ground in the 200 Areas During 1986*. RHO-HS-SR-86-3 4QLIQ, Rockwell Hanford Company, Richland, Washington.

Aldrich RC and GJ Sliger. 1981. *Radioactive Liquid Wastes Discharged to Ground in the 200 Areas During 1980*. RHO-CD-80-34-4Q, Rockwell Hanford Company, Richland, Washington.

Anderson JD. 1976. *Input and Decayed Values of Radioactive Liquid Wastes Discharged to the Ground in the 200 Areas Through 1975*. ARH-CD-745, Atlantic Richfield Hanford Company, Richland, Washington.

Anderson JD and BE Poremba. 1978. *Radioactive Liquid Waste Discharged to Ground in the 200 Areas During 1977*. RHO-CD-34 4Q, Rockwell Hanford Company, Richland, Washington.

Anderson JD and BE Poremba. 1979. *Radioactive Liquid Waste Discharged to Ground in the 200 Areas During 1978*. RHO-CD-78-34-4Q, Rockwell Hanford Company, Richland, Washington.

Brooks RH and AT Corey. 1964. "Hydraulic Properties of Porous Media." *Hydrol. Pap. 3*, Civil Engineering Department, Colorado State University, Fort Collins, Colorado.

Brown MJ, MJ P'Pool, and SP Thomas. 1990. *Westinghouse Hanford Company Effluent Discharges and Solid Waste Management Report for Calendar Year 1989: 200/600 Areas*. WHC-EP-0141-2, Westinghouse Hanford Company, Richland, Washington.

Burdine NT. 1953. "Relative Permeability Calculations from Pore-Size Distribution Data." *Petr. Trans., Am. Inst. Mining Metall. Eng*. 198:71-77.

Connelly MP, BH Ford, and JV Borghese. 1992. *Hydrogeologic Model for the 200 West Groundwater Aggregate Area*. WHC-SD-EN-TI-014, Rev. 0, Westinghouse Hanford Company, Richland, Washington.

Coony FM and SP Thomas. 1989. *Westinghouse Hanford Company Effluent Discharges and Solid Waste Management Report for Calendar Year 1988: 200/600 Areas*. WHC-EP-0141-1, Westinghouse Hanford Company, Richland, Washington.

Coony FM, DB Howe, and LJ Voigt. 1988. *Westinghouse Hanford Company Effluent Discharges and Solid Waste Management Report for Calendar Year 1987: 200/600/1100 Areas*. WHC-EP-0141, Westinghouse Hanford Company, Richland, Washington.

DOE. 2001. *Drilling, Sampling, and Analysis Plan for Installation of a Well Within the Vicinity of the Plutonium Finishing Plant*. U.S. Department of Energy, Richland Operations Office, Richland, Washington.

DOE. 2002. *Standardized Stratigraphic Nomenclature for Post-Ringold Formation Sediments Within the Central Pasco Basin*. DOE/RL-2002-39. U.S. Department of Energy, Richland, WA.

Driggers SA. 1994. *Summary of Canister Overheating Incident at the Carbon Tetrachloride Expedited Response Action Site*. WHC-SD-EN-TI-203, Rev. 0, Westinghouse Hanford Company, Richland, Washington.

Freyberg DL. 1986. "A Natural Gradient Experiment on Solute Transport in a Sand Aquifer, 2. Spatial Moments and the Advection and Dispersion of Nonreactive Tracers. *Water Resour. Res*. 22:2031-2046.

Fuchs MR, AG Law, and AL Schatz. 1986. *Results of the Separations Area Groundwater Monitoring Network for 1984*. RHO-RE-SR-85-24P, Rockwell Hanford Company, Richland, Washington.

Ho CK, RG Baca, SH Conrad, GA Smith, L Shyr, and TA Wheeler. 1999. *Stochastic Parameter Development for PORFLOW Simulations of the Hanford AX Tank Farm.* SAND98-2880, Sandia National Laboratories, Albuquerque, New Mexico.

Hofstee C, RC Walker, and JH Dane. 1998. "Infiltration and Redistribution of Perchloroethylene in Partially Saturated, Stratified Porous Media." *J. Contam. Hydrol.* 34:293-313.

Khaleel R and EJ Freeman. 1995. *Variability and Scaling of Hydraulic Properties for 200 Area Soils, Hanford Site*. WHC-EP-0883, Westinghouse Hanford Company, Richland, Washington.

Khaleel R, TE Jones, AJ Knepp, FM Mann, DA Myers, PM Rogers, RJ Serne, and MI Wood. 2001. *Modeling Data Package for S-SX Field Investigation Report (FIR)*. RPP-6296 Rev. 0, CH2MHILL Hanford Group, Inc., Richland, WA.

Klinkenberg LJ. 1941. "The Permeability of Porous Media to Liquids and Gases." *Drilling and Production Practice*, 200-213, American Petroleum Institute, New York.

Last GV, DG Horton, BN Bjornstad, TJ Gilmore, R Mackley, and C Strickland. 2002. *Prototype Geologic Database and User's Guide, FY02 Status Report*. CP-17090, Fluor Hanford, Richland, Washington.

Last GV and VJ Rohay. 1993. *Refined Conceptual Model for the Volatile Organic Compounds-Arid Integrated Demonstration and 200 West Area Carbon Tetrachloride Expedited Response Action*. PNL-8597, Pacific Northwest Laboratory, Richland, Washington.

Lenhard RJ. 1994. "Scaling Fluid Content-Pressure Relations of Different Fluid Systems in Porous Media." In *Proc. 14th Annual American Geophysical Union Hydrology Days*, HJ Morel-Seytoux (ed.), Hydrology Days Publ., Atherton, California.

Lenhard RJ, M Oostrom, and JH Dane. 2004. "A Constitutive Model for Air-NAPL-Water Flow in the Vadose Zone Accounting for Immobile Non-Occluded (Residual) NAPL in Strongly Water-Wet Porous Media." *J. of Contaminant Hydrology* 73:283-304

Lenhard RJ, JC Parker, and S Mishra. 1989. "On the correspondence between Brooks-Corey and van Genuchten models" *J. of Irrigation and Drainage Engineering* 115:744-751

Leverett MC. 1941. "Capillary Behavior in Porous Solids." *Trans. Soc. Pet. Eng. AIME* 142:152-169.

Mirabella JE. 1977. *Radioactive Liquid Wastes Discharged to Ground in the 200 Areas During 1976.* ARH-CD-743 4Q, Atlantic Richfield Hanford Company, Richland, Washington.

Mualem Y. 1976. "A New Model for Predicting the Hydraulic Conductivity of Unsaturated Porous Media." *Water Resour. Res*. 12:513-522.

Oostrom M and RJ Lenhard. 1998. "Comparison of relative permeability-saturation-pressure parametric models for infiltration and redistribution of a light nonaqueous phase liquid in sandy porous media." *Adv. in Water Resour*. 21:145-157.

Oostrom M and RJ Lenhard. 2003. "Carbon Tetrachloride Flow Behavior in Unsaturated Hanford Caliche Material: An Investigation of Residual NAPL." *Vadose Zone J*. 2: 25-33.

Oostrom M, C Hofstee, and JH Dane. 1997. "Light Nonaqueous-Phase Liquid Movement in a Variably Saturated Sand." *Soil Science Society of America J*. 61:1547-1554.

Oostrom M, C Hofstee, RC Walker, and JH Dane. 1999. "Movement and Remediation of Trichloro-ethylene in a Saturated, Heterogeneous Porous Medium. 1. Spill Behavior and Initial Dissolution." *J. of Contaminant Hydrol*. 37:159-178.

Oostrom M, C Hofstee, RJ Lenhard, and TW Wietsma. 2003. Flow behavior and residual saturation formation of injected carbon tetrachloride in unsaturated heterogeneous porous media. J. of Contaminant Hydrology. 64: 93-112.

Piepho MG. 1996. *Numerical Analysis of Carbon Tetrachloride Movement in the Saturated and Unsaturated Zones in the 200 West Area, Hanford Site*. BHI-00459, Bechtel Hanford, Inc., Richland, Washington.

Rohay VJ. 2002. *Performance Evaluation Report for Soil Vapor Extraction Operations at the Carbon Tetrachloride Site, February 1992 – September 2001*. BHI-00720, Rev. 6, Bechtel Hanford, Inc., Richland, Washington.

Rohay VJ. 1997. *Rebound Study Report for the Carbon Tetrachloride Soil Vapor Extraction Site, Fiscal Year 1997*. BHI-01105, Rev. 0, Bechtel Hanford, Inc., Richland, Washington.

Rohay, VJ, KJ Swett, and GV Last. 1994. *Conceptual Model of the Carbon Tetrachloride Contamination in the 200 West Area at the Hanford Site*. WHC-SD-EN-TI-248, Rev. 0, Westinghouse Hanford Company, Richland, Washington.

Schroth MH, JD Istok, JS Selker, M Oostrom, and MD White. 1998. "Multifluid Flow in Bedded Porous Media: Laboratory Experiments and Numerical Simulations." *Adv. in Water Resour*. 22:169-183.

Sliger GJ. 1980. *Radioactive Liquid Wastes Discharged to Ground in the 200 Areas During 1979*. RHO-CD-79-34-4Q, Rockwell Hanford Company, Richland, Washington.

Sliger GJ. 1982. *Radioactive Liquid Wastes Discharged to Ground in the 200 Areas During 1981*. RHO-HS-SR-81-3, Rockwell Hanford Company, Richland, Washington.

Sliger GJ. 1983. *Radioactive Liquid Wastes Discharged to Ground in the 200 Areas During 1972*. RHO-HS-SR-82-3-4Q-LI, Rockwell Hanford Company, Richland, Washington.

Westinghouse Hanford Company (WHC). 1990. *Liquid Effluent Study Final Project Report*. WHC-EP-0367, prepared for the U.S. Department of Energy, Office of Environmental Restoration and Waste Management by Westinghouse Hanford Company, Richland, Washington.

Westinghouse Hanford Company (WHC). 1992a. *Environmental Releases for Calendar Year 1990*. WHC-EP-0527, Westinghouse Hanford Company, Richland, Washington.

Westinghouse Hanford Company (WHC). 1992b. *Environmental Releases for CY 1991*. WHC-EP-0527-1, Westinghouse Hanford Company, Richland, Washington.

Westinghouse Hanford Company (WHC). 1993. *Environmental Releases for Calendar Year 1992*. WHC-EP-0527-2, Westinghouse Hanford Company, Richland, Washington.

White MD and M Oostrom. 2000. *STOMP, Subsurface Transport Over Multiple Phases. Version 2.0. Theory Guide.* PNNL-12030, Pacific Northwest National Laboratory, Richland, Washington.

White MD and M Oostrom. 2003. *STOMP, Subsurface Transport Over Multiple Phases. Version 3.0. User's Guide.* PNNL-14286, Pacific Northwest National Laboratory, Richland, Washington.

White MD, M Oostrom, and RJ Lenhard. 2004. "A Practical Model for Mobile, Residual, and Entrapped NAPL in Porous Media." *Ground Water* 42:734-746

Zhang ZF, AL Ward, and GW Gee. 2003. "A Tensorial Connectivity-Tortuosity Concept to Describe the Unsaturated Hydraulic Properties of Anisotropic Soils." *Vadose Zone J*. 2:313-321.

Appendix

Residual Saturation Description

Appendix

Residual Saturation Description

Residual saturation is a term used by modelers in the hydrologic and petroleum sciences to describe different phenomena or processes. Use of this term can be confusing unless supporting information is given, such as the wettability of the porous medium. When applied to water in strongly water-wet porous media, the residual-water saturation is the water saturation at which the water relative permeability decreases to zero. Theoretically, it refers to the water contained in the smallest pore spaces (pore wedges, pores) and as films on solid surfaces. It is the minimum water content that can be obtained by water (liquid) drainage when there are no restrictions to drainage (e.g., capillary breaks, impermeable layers). In the petroleum industry, the residual-water saturation is also referred to as the irreducible-water saturation.

When applied to nonaqueous phase liquid (NAPL) in strongly water-wet porous media, the term 'residual NAPL' has been used to describe the NAPL saturation that becomes occluded by water as water displaces NAPL into larger pore spaces during water imbibition. In strongly water-wet porous media, the NAPL is a nonwetting fluid. Typically, the vadose zone is assumed to be strongly water wet. Residual NAPL has also been applied to mixed- and oil-wet porous media in the petroleum industry. In those systems, the residual-NAPL saturation is similar in concept to the residual-water saturation in strongly water-wet porous media (NAPL is contained in the smallest pore spaces available), because it is the wetting fluid in the oil-wet pore spaces. Additionally, residual NAPL has been applied to describe the NAPL saturation in the vadose zone that does not drain from the pore spaces when no drainage restrictions exist. In strongly water-wet porous media, the residual NAPL in the vadose zone is a nonwetting fluid. Residual NAPL is a term that is used by various disciplines (e.g., petroleum versus vadose-zone hydrologists) to describe different processes. It has been used to describe either a nonwetting or a wetting fluid and is conceptualized as being continuous, discontinuous, or both throughout the pore spaces. In all cases, however, the residual NAPL is considered to be immobile.

In the following discussions, we will employ the definition of residual NAPL used by vadose-zone hydrologists for strongly water-wet porous media. We will call NAPL that is occluded by water trapped NAPL and NAPL that is not trapped by water but does not drain from the pore spaces residual NAPL. Trapped NAPL could also be called occluded residual NAPL and residual NAPL could be called 'non-occluded residual NAPL.' Both forms of NAPL (trapped and residual) are assumed to be immobile. Residual NAPL can be discontinuous and/or continuous throughout the pore spaces, but trapped NAPL is always discontinuous.

Residual and trapped NAPL are important because they are long-term sources of groundwater contamination. Two research groups (Wipfler and van der Zee 2001; van Geel and Roy 2002) have recently proposed amendments to existing multi-fluid constitutive theory in order to predict the residual-NAPL saturation. In the model proposed by Wipfler and van der Zee (2001), a critical NAPL pressure is defined from knowledge of a critical total-liquid saturation and fluid and porous medium properties. The

critical total-liquid saturation is considered to be unique for each set of fluids and porous medium. The critical NAPL pressure defines the transition from free (mobile) NAPL to residual (immobile) NAPL. Wipfler and van der Zee (2001) do not address relative permeability relations. Van Geel and Roy (2002) conducted a series of saturation-pressure (S-P) measurements to investigate residual NAPL, and they utilized their data to develop a model to predict the residual-NAPL saturation. Their model is based on knowledge of the maximum residual-NAPL saturation, the apparent total-liquid saturation, and the apparent total-liquid saturation at the saturation-path reversal from the primary wetting S-P curve to a drainage S-P scanning curve. Their predictive equation does not explicitly include the water saturation. By defining the total-NAPL saturation to be the sum of free-, trapped-, and residual-NAPL saturations, they indirectly address relative permeability relations. When all of the NAPL becomes residual and trapped, the NAPL relative permeability goes to zero because the free-NAPL saturation is zero.

In this section, a model is presented to account for the effects of immobile, non-water-occluded NAPL (residual NAPL) on NAPL behavior in the subsurface. The model differs from that of Wipfler and van der Zee (2001) because free and residual NAPL can co-exist in the pore spaces. In their model, free and residual NAPL cannot co-exist. Our model differs from that of van Geel and Roy (2002) because we think that the water saturation is an important variable and should be explicitly included in any equation for predicting residual NAPL. Our model is developed to be consistent with the hysteretic constitutive theory for k-S-P relations developed by Parker and Lenhard (1987) and Lenhard and Parker (1987). We test the modified S-P relations by calculating residual-NAPL saturations for the experimental conditions reported in van Geel and Roy (2002) and compare those predictions to van Geel and Roy's measurements. Additionally, we demonstrate the use of the modified model for a scenario involving NAPL imbibition and subsequent drainage to its residual value.

Our objective is to improve existing multifluid constitutive theory (i.e., k-S-P relations) so that the effects of trapped and residual NAPL on subsurface contamination and cleanup can be predicted. However, we first want to give a conceptual understanding of residual NAPL, as we will use it in our model.

We hypothesize that NAPL in small pores and small pore wedges can be considered to be immobile because 1) the pore dimensions are small and any advection of NAPL through those spaces would be negligible or 2) the pore spaces are dead-end channels that are unable to conduct NAPL. We also hypothesize that NAPL adjacent to water films that are adsorbed to solid particles do not effectively contribute to NAPL advection and can be considered to be immobile, especially if the water films are thin. We reason that there is no significant slippage along the NAPL-water interface after the NAPL wets water films. Therefore, the NAPL at the interface should move at the same velocity as the water at the interface, which would likely be negligible relative to the velocity of NAPL at the centers of the pores.

Once the small pores and pore wedges are filled with NAPL and the NAPL films are formed, the NAPL in those spaces becomes practically immobile. Therefore, the residual NAPL forms during NAPL imbibition, not during drainage. We consider that NAPL in small pores and pore wedges and as films on water surfaces cannot be mobile during NAPL imbibition, but immobile during drainage. After forming, the residual NAPL does not contribute to NAPL advection whether the NAPL is imbibing or draining. In a pore system filled with NAPL, some NAPL can potentially move and some NAPL is assumed to be

immobile. The NAPL that can potentially move we call 'free' NAPL and the non-water-occluded NAPL assumed to be immobile we call residual NAPL.

We will modify the hysteretic, multifluid k-S-P model of Parker and Lenhard (1987) and Lenhard and Parker (1987), which is valid for air-NAPL-water systems in strongly water-wet porous media where water is the wetting fluid and air and NAPL are nonwetting fluids with NAPL being more wetting than air. The intent is to minimize changes to the existing model so that coding the improvements will not be a major undertaking, but the use of the model in flow and transport simulators will yield results that more accurately reflect NAPL behavior in the field.

It is appropriate first to give definitions of saturation terms that will be used in the model, because both apparent and effective saturations are used and readers may not be familiar with the existing model. An apparent saturation is a scaled fluid saturation that is corrected (adjusted) for trapped fluids. An effective saturation is a scaled saturation that is not corrected for trapped fluids. Typically, an effective saturation refers to a single fluid form (e.g., water, trapped air), whereas an apparent saturation includes multiple fluid forms, because it accounts for trapped fluids. Apparent saturations are used to obtain a more accurate description of the distribution of fluids in the pore spaces. The apparent water saturation is predicted from the NAPL-water capillary pressure and the water saturation-path history. The apparent total-liquid saturation is predicted from the air-NAPL capillary pressure and the total-liquid saturation-path history. The trapped and non-trapped saturations are determined from the apparent saturations and saturation-path histories. Readers are referred to and Parker and Lenhard (1987) and Lenhard and Parker (1987) for further discussion of effective and apparent saturations.

The apparent water saturation is defined as

$$\overline{\overline{S}}_w = \frac{S_w + S_{ot} + S_{atw} - S_{wr}}{1 - S_{wr}} \tag{A.1}$$

where S_w is the water saturation, S_{ot} is the trapped-NAPL saturation (occluded by water), S_{atw} is the trapped-air saturation in water (occluded by water), and S_{wr} is the residual-water saturation, which is assumed to be immobile and the value of which is independent of the water saturation-path history. The trapped-NAPL saturation in water (S_{ot}) includes the trapped air in the trapped NAPL that is occluded by water.

The apparent total-liquid saturation is defined as

$$\overline{\overline{S}}_l = \frac{S_w + S_o + S_{at} - S_{wr}}{1 - S_{wr}} \tag{A.2}$$

where S_o is the total-NAPL saturation and S_{at} is the total trapped-air saturation. The total trapped-air saturation (S_{at}) is the sum of trapped-air saturations occluded by water and occluded by the NAPL, i.e.,

$$S_{at} = S_{atw} + S_{ato} \tag{A.3}$$

where S_{ato} is the trapped-air saturation occluded by the NAPL, which is not also occluded by water (not the trapped air in the trapped NAPL). The values of S_{ot}, S_{atw}, and S_{at} in Equations (A.1) and (A.2) are functions of the water and total-liquid saturation-path histories. Equations (A.1)-(A.3) are given for the convenience of the reader; the definitions of the apparent water and total-liquid saturations are unchanged from the existing model.

The modifications to the constitutive theory are presented in two sections. The first section describes changes to the S-P submodel and the second section describes changes to the k-S submodel. We refer to the S-P relations described in Parker and Lenhard (1987) and the k-S relations described in Lenhard and Parker (1987) as the 'existing' models.

A.1 S-P Submodel

The major modification to the existing S-P model is to divide the non-water-occluded NAPL into free (mobile) and residual (immobile) components and to predict the residual component using the total-liquid and water saturation-path histories. In the existing model, the total-NAPL saturation consists of two components: free- and trapped-NAPL saturations. The free-NAPL saturation is mobile and the trapped-NAPL saturation is immobile. In our modification, we define the total-NAPL saturation to consist of three components: free-, trapped-, and residual-NAPL saturations. The free-NAPL saturation is the portion of the NAPL that is continuous and mobile with regard to NAPL advection. The trapped-NAPL saturation is the portion of the NAPL that is contained in discontinuous immobile ganglia occluded by water. The residual-NAPL saturation is the portion of the NAPL that is not occluded by water, but is immobile. We redefine the total-NAPL saturation as

$$S_o = S_{of} + S_{ot} + S_{or} \tag{A.4}$$

where S_{of} is the free-NAPL saturation, S_{ot} is the trapped-NAPL saturation, and S_{or} is the residual-NAPL saturation. The symbol S_{or} in the existing model is used to denote the maximum amount of water-occluded NAPL with co-existing trapped air for a given water saturation-path history. Using symbols consistent with this manuscript, the symbol S_{or} in the existing model should be replaced with S_{otm}. Van Geel and Roy (2002) used the same definition for total-NAPL saturation (S_o) that we use in Equation (A.4). To determine the total-NAPL saturation (S_o), each component on the right-hand side of Equation (A.4) needs to be calculated based on the total-liquid and water saturation-path histories and the NAPL-water and air-NAPL capillary pressures. The total-NAPL saturation (S_o) does not approach zero when the free-NAPL saturation (S_{of}) approaches zero.

We theorize that the residual-NAPL saturation depends largely on two factors. The first factor is related to the volume of pore space occupied by NAPL, while the second factor is related to the size of

the pores containing the NAPL. We propose that these factors affect the value of the residual-NAPL saturation in a nonlinear manner. Accordingly, we propose that the residual-NAPL saturation can be predicted using a power function of the form

$$\bar{S}_{or} = A\, B^{\lambda}\, C^{\eta} = \frac{S_{or}}{1 - S_{wr}} \tag{A.5}$$

where $\bar{S}_{or}$ is the effective residual-NAPL saturation, A is a calibration term that reflects the maximum residual-NAPL saturation possible for a porous medium, B is a factor related to the volume of pore space occupied by NAPL, C is a factor related to the size of the pores containing the NAPL, and λ and η are power law exponents.

The calibration term (A) in Equation (A.5) is the maximum residual-NAPL saturation (S_{orm}) that can be obtained in a porous medium. It is porous medium and fluid specific. We will use the B and C terms in Equation (A.5) to scale the maximum residual-NAPL saturation (the A term) to predict the effective residual-NAPL saturation for given conditions. The maximum residual-NAPL saturation (S_{orm}) can be measured by draining water to its residual-water saturation in a two-phase NAPL-water fluid system that is initially water saturated, followed by draining NAPL to its residual-NAPL saturation. For spreading NAPLs (NAPLs for which the sum of the NAPL-water and air-NAPL interfacial tensions is equal to or less than the air-water interfacial tension), the NAPL will form a film (will spread) on the water surfaces when the maximum residual-NAPL saturation (S_{orm}) is measured. For nonspreading NAPLs (NAPLs for which the sum of the NAPL-water and air-NAPL interfacial tensions is greater than the air-water interfacial tension), the NAPL will form lenses on the water surfaces when the maximum residual-NAPL saturation (S_{orm}) is measured. We reason that the different behavior of spreading and nonspreading NAPLs in porous media can be addressed via the calibration term (A) in Equation (A.5). Measurement systems similar to those described by Lenhard and Parker (1988), Busby et al. (1995), and van Geel and Roy (2002) can be used to determine the maximum residual-NAPL saturation (S_{orm}). After S_{orm} is measured, it must be scaled to yield an effective saturation using

$$A = \bar{S}_{orm} = \frac{S_{orm}}{1 - S_{wr}} \tag{A.6}$$

The term B in Equation (A.5) is a measure of the volume fraction of pore space occupied by NAPL. An expression for B must ensure that it has a value of zero when the residual-NAPL saturation (S_{or}) is zero and that it will reach its maximum value when S_{or} is at its maximum. Accordingly, we propose the relationship

$$B = \frac{\bar{\bar{S}}_{l}^{\max} - \bar{\bar{S}}_{w}}{1 - \bar{\bar{S}}_{w}} \tag{A.7}$$

where $\bar{\bar{S}}_{l}^{\max}$ is the historic maximum apparent total-liquid saturation in an air-NAPL-water fluid system. Using Equation (A.7), B is zero when the apparent water saturation ($\bar{\bar{S}}_{w}$) is equal to the historic

maximum apparent total-liquid saturation ($\overline{\overline{S}}_l^{\max}$), which occurs when either NAPL imbibes into a two-phase air-water system or when all of the NAPL becomes trapped in water. In both cases, conditions are such that the residual-NAPL saturation (S_{or}) is zero. The apparent water saturation ($\overline{\overline{S}}_w$) can never be greater than the historic maximum apparent total-liquid saturation ($\overline{\overline{S}}_l^{\max}$), because it would mean that the apparent water saturation is greater than the apparent total-liquid saturation ($\overline{\overline{S}}_l$), which is physically impossible. The largest residual-NAPL saturation (S_{or}) for a given water saturation path will occur when the historic maximum apparent total-liquid saturation ($\overline{\overline{S}}_l^{\max}$) approaches 1. For the conditions that pertain to measuring the maximum residual-NAPL saturation (S_{orm}), B = 1 and represents a maximum value. When conducting numerical simulations, the historic maximum apparent total-liquid saturation ($\overline{\overline{S}}_l^{\max}$) needs to be updated after every time step for each node.

The term C in Equation (A.5) is a measure of the size (radii) of the pores containing the NAPL. We use this measure to estimate the volume of NAPL that is immobile in thin films or lenses on water surfaces. Again, this term must be zero when the residual-NAPL saturation (S_{or}) is zero and must have a maximum value when S_{or} is a maximum. For the former constraint, immobile NAPL in thin films or lenses on water surfaces will only be zero when the apparent water saturation ($\overline{\overline{S}}_w$) is 1, or when a two-phase air-water system exists. For the latter constraint, the maximum value of immobile NAPL in thin films or lenses on water surfaces should theoretically occur when the apparent water saturation ($\overline{\overline{S}}_w$) is 0 – the water saturation (S_w) is equal to the residual-water saturation (S_{wr}). An expression that meets these constraints is

$$C = \left(1 - \overline{\overline{S}}_w\right) \tag{A.8}$$

Substituting expressions for A, B, and C (Equations [A.6], [A.7], and [A.8]) into Equation (A.5), the following equation for predicting the effective residual-NAPL saturation as a function of saturation-path history is obtained:

$$\overline{S}_{or} = \overline{S}_{orm}\left(\frac{\overline{\overline{S}}_l^{\max} - \overline{\overline{S}}_w}{1 - \overline{\overline{S}}_w}\right)^{\lambda}\left(1 - \overline{\overline{S}}_w\right)^{\eta} \tag{A.9}$$

To determine the power law exponent λ in Equation (A.9), we hypothesize that immobile NAPL in pore wedges and in small pores will increase as the volume of pore space that contains NAPL increases. As the NAPL invades larger-sized pores, small pores can become accessible to the NAPL that otherwise would not be accessible. However, the rate of increase in residual NAPL will decrease as the volume of pore space that contains NAPL becomes larger (the volume of pore space in pore wedges and in small pores relative to the total pore volume will decrease as NAPL invades larger pores). Consequently, we propose using $\lambda = 0.5$ as a first approximation. To determine the power law exponent η in Equation (A.9), we hypothesize that the volume of immobile NAPL in thin films or lenses on water surfaces will be greater when NAPL is in smaller radii pore spaces relative to larger radii pore spaces (more surface area

in a given volume). As smaller radii pores become accessible to the NAPL because of water drainage, then the volume of immobile NAPL in thin films or lenses on water surfaces will increase at an increasing rate. Accordingly, we propose using $\eta = 2$ based on the hypothesis that the increase in the volume of NAPL present in thin films or as lenses on water surfaces as the apparent water saturation ($\overline{\overline{S}}_w$) becomes smaller follows a pattern similar to the variation of tortuosity as the water saturation decreases, as proposed by Burdine (1953). Substituting the proposed values for λ and η in Equation (A.9), the following predictive equation for the effective residual-NAPL saturation is

$$\overline{S}_{or} = \overline{S}_{orm}\left(\overline{\overline{S}}_l^{\max} - \overline{\overline{S}}_w\right)^{0.5}\left(1 - \overline{\overline{S}}_w\right)^{1.5} \qquad \text{(A.10)}$$

The only other modification needed for the existing model addresses air entrapment. In the existing model, trapped air is a function of the total-NAPL saturation. In our modification, we assume that all trapped air in the NAPL (i.e., S_{ato}) is trapped only by the free NAPL and not by any residual NAPL. Therefore, trapped air in NAPL should be a function of the free-NAPL saturation and not the total-NAPL saturation.

A.2 k-S Submodel

Using the modifications in the S-P model, k-S relations can be predicted using an approach similar to that used in the existing model. Predictions of the water and air relative permeabilities are identical to those in the existing model. The major modification is in the determination of the NAPL relative permeability (k_{ro}). The key assumption is that all of the residual NAPL is contained in pore spaces indexed between the apparent water saturation ($\overline{\overline{S}}_w$) and the sum of the apparent water saturation and the effective residual-NAPL saturation ($\overline{\overline{S}}_w + \overline{S}_{or}$). This assumption is necessary to obtain an expedient method to predict the NAPL relative permeability. If we knew how the residual NAPL is distributed throughout the pore spaces indexed between the historic maximum apparent total-liquid saturation ($\overline{\overline{S}}_l^{\max}$) and the apparent water saturation ($\overline{\overline{S}}_w$), then we could develop a protocol for estimating the NAPL relative permeability (k_{ro}) that reflects the distribution of discontinuous and continuous residual NAPL in porous media. In the absence of a well-defined theory describing the distribution of residual NAPL, we have used the above assumption as a first approximation.

Applying the above assumption to Mualem's (1976) integral expression for relative permeability to account for effects of residual NAPL and trapped air on the NAPL relative permeability (k_{ro}), the integral expression becomes

$$k_{ro} = \bar{S}_{of}^{0.5} \left\{ \frac{\int_{\bar{S}_w + \bar{S}_{or}}^{\bar{\bar{S}}_l} \frac{d\bar{S}_e}{h(\bar{S}_e)} - \int_0^{\bar{S}_{ato}} \frac{d\bar{S}_{ato}}{h(\bar{S}_e)}}{\int_0^1 \frac{d\bar{S}_e}{h(\bar{S}_e)}} \right\}^2 \tag{A.11}$$

where $\bar{S}_{ato}$ is the effective trapped-air saturation in the free NAPL, $\bar{S}_e$ is the effective porosity in which the flow of the fluid under consideration can potentially occur, and $h(\bar{S}_e)$ is a surrogate for the pore-size distribution of the porous medium. The limits of integration are chosen so that the integration of the relative permeability integral is performed only over the pore space containing mobile NAPL. Both the effective free-NAPL saturation term (tortuosity term) and the integrals in the numerator of Equation (A.11) will approach zero as the free-NAPL saturation (S_{of}) approaches zero. In the model proposed by van Geel and Roy (2002), only the tortuosity term approaches zero as S_{of} approaches zero.

Following Lenhard and Parker (1987), the integral on the right-hand side in the numerator of Equation (A.11), which corrects for obstruction of NAPL flow by the trapped air in the free NAPL, can be expressed in terms of $\bar{S}_e$ for different saturation-path histories. For saturation-path histories for which all of the free NAPL is in pores that were previously occupied by air in the air-NAPL-water system ($\bar{\bar{S}}_w + \bar{S}_{or} \geq \bar{\bar{S}}_l^{\min}$), the transformation yields

$$\int_0^{\bar{S}_{ato}} \frac{d\bar{S}_{ato}}{h(\bar{S}_e)} = \frac{\bar{S}_{aro}}{1 - \bar{\bar{S}}_l^{\min}} \int_{\bar{S}_w + \bar{S}_{or}}^{\bar{\bar{S}}_l} \frac{d\bar{S}_e}{h(\bar{S}_e)} \tag{A.12}$$

where $\bar{S}_{aro}$ is the effective maximum trapped-air saturation that resulted from advancing air-NAPL interfaces, and $\bar{\bar{S}}_l^{\min}$ is the historic minimum apparent total-liquid saturation. The effective maximum trapped-air saturation ($\bar{S}_{aro}$) is a function of the historic minimum apparent total-liquid saturation ($\bar{\bar{S}}_l^{\min}$).

For saturation-path histories for which only some of the free NAPL is in pores that were previously occupied by air in the air-NAPL-water system and the remainder of the free NAPL is in smaller pores that were previously occupied by air in the air-water system ($\bar{\bar{S}}_w + \bar{S}_{or} < \bar{\bar{S}}_l^{\min}$ and $\bar{\bar{S}}_l^{\min} \geq {}^{\Delta}\bar{S}_w^{aw}$), the transformation yields

$$\int_0^{\bar{S}_{ato}} \frac{d\bar{S}_{ato}}{h(\bar{S}_e)} = \frac{\bar{S}_{arw}}{1-{}^{\Delta}\bar{S}_w^{aw}} \int_{\Psi}^{\bar{\bar{S}}_l^{\min}} \frac{d\bar{S}_e}{h(\bar{S}_e)} + \frac{\bar{S}_{aro}}{1-\bar{\bar{S}}_l^{\min}} \int_{\bar{\bar{S}}_l^{\min}}^{\bar{\bar{S}}_l} \frac{d\bar{S}_e}{h(\bar{S}_e)} \tag{A.13}$$

where $\bar{S}_{arw}$ is the effective maximum trapped-air saturation that resulted from advancing air-water interfaces, ${}^{\Delta}\bar{S}_w^{aw}$ is the effective water saturation at the saturation-path reversal from the main S-P path to a scanning water imbibition path in a two-phase air-water fluid system, and Ψ is the maximum of either $\bar{\bar{S}}_w + \bar{S}_{or}$ or ${}^{\Delta}\bar{S}_w^{aw}$.

For saturation-path histories for which only some of the free NAPL is in pores that were previously occupied by air in the air-NAPL-water system and the remainder of the free NAPL is in smaller pores that were never occupied by air in either the air-water or air-NAPL-water systems ($\bar{\bar{S}}_w + \bar{S}_{or} < \bar{\bar{S}}_l^{\min}$ and $\bar{\bar{S}}_l^{\min} < {}^{\Delta}\bar{S}_w^{aw}$), the transformation yields

$$\int_0^{\bar{S}_{ato}} \frac{d\bar{S}_{ato}}{h(\bar{S}_e)} = \frac{\bar{S}_{aro}}{1-\bar{\bar{S}}_l^{\min}} \int_{\Omega}^{\bar{\bar{S}}_l} \frac{d\bar{S}_e}{h(\bar{S}_e)} \tag{A.14}$$

where Ω is the maximum of either $\bar{\bar{S}}_w + \bar{S}_{or}$ or $\bar{\bar{S}}_l^{\min}$.

Following van Genuchten (1980), closed-form expressions for the NAPL relative permeability (k_{ro}) of different saturation-path histories that account for residual NAPL are obtained by substituting Equations (A.12-A.14) into Equation (A.11) and integrating.

For the condition $\bar{\bar{S}}_w + \bar{S}_{or} \geq \bar{\bar{S}}_l^{\min}$, the solution is

$$k_{ro} = \bar{S}_{of}^{0.5} \left\{ \left[1-\left(\bar{\bar{S}}_w + \bar{S}_{or}\right)^{1/m}\right]^m \left(1-\frac{\bar{S}_{aro}}{1-\bar{\bar{S}}_l^{\min}}\right) - \left(1-\bar{\bar{S}}_l^{1/m}\right)^m \left(1-\frac{\bar{S}_{aro}}{1-\bar{\bar{S}}_l^{\min}}\right) \right\}^2 \tag{A.15}$$

where m is a parameter of the van Genuchten (1980) S-P equation.

For the condition $\bar{\bar{S}}_w + \bar{S}_{or} < \bar{\bar{S}}_l^{\min}$ and $\bar{\bar{S}}_l^{\min} \geq {}^{\Delta}\bar{S}_w^{aw}$, the solution is

$$k_{ro} = \bar{S}_{of}^{0.5} \left\{ \begin{array}{r} \left[1 - \left(\bar{\bar{S}}_w + \bar{S}_{or}\right)^{1/m}\right]^m - \left(1 - \bar{\bar{S}}_l^{1/m}\right)^m \left(1 - \dfrac{\bar{S}_{aro}}{1 - \bar{\bar{S}}_l^{\min}}\right) \\ - \left[1 - \left(\bar{\bar{S}}_l^{\min}\right)^{1/m}\right]^m \left[\dfrac{\bar{S}_{aro}}{1 - \bar{\bar{S}}_l^{\min}} - \dfrac{\bar{S}_{arw}}{1 - {}^{\Delta}\bar{S}_w^{aw}}\right] \\ - \left(1 - \Psi^{1/m}\right)^m \left(\dfrac{\bar{S}_{arw}}{1 - {}^{\Delta}\bar{S}_w^{aw}}\right) \end{array} \right\}^2 \qquad \text{(A.16)}$$

For the condition $\bar{\bar{S}}_w + \bar{S}_{or} < \bar{\bar{S}}_l^{\min}$ and $\bar{\bar{S}}_l^{\min} < {}^{\Delta}\bar{S}_w^{aw}$, the solution is

$$k_{ro} = \bar{S}_{of}^{0.5} \left\{ \begin{array}{r} \left[1 - \left(\bar{\bar{S}}_w + \bar{S}_{or}\right)^{1/m}\right]^m - \left(1 - \bar{\bar{S}}_l^{1/m}\right)^m \left(1 - \dfrac{\bar{S}_{aro}}{1 - \bar{\bar{S}}_l^{\min}}\right) \\ - \left(1 - \Omega^{1/m}\right)^m \left(\dfrac{\bar{S}_{aro}}{1 - \bar{\bar{S}}_l^{\min}}\right) \end{array} \right\}^2 \qquad \text{(A.17)}$$

A stepwise approach to evaluating the above conditional statements is needed when determining the NAPL relative permeability (k_{ro}) in order to minimize the number of conditional statements that must be evaluated. The conditional statement $\bar{\bar{S}}_w + \bar{S}_{or} \geq \bar{\bar{S}}_l^{\min}$ needs to be evaluated first, followed by the second conditional statement ($\bar{\bar{S}}_w + \bar{S}_{or} < \bar{\bar{S}}_l^{\min}$ and $\bar{\bar{S}}_l^{\min} \geq {}^{\Delta}\bar{S}_w^{aw}$), and subsequently by the last statement ($\bar{\bar{S}}_w + \bar{S}_{or} < \bar{\bar{S}}_l^{\min}$ and $\bar{\bar{S}}_l^{\min} < {}^{\Delta}\bar{S}_w^{aw}$). For saturation-path histories other than $\bar{\bar{S}}_w + \bar{S}_{or} > \bar{\bar{S}}_l^{\min}$, the apparent total-liquid saturation ($\bar{\bar{S}}_l$) will become equal to the historic minimum apparent total-liquid saturation ($\bar{\bar{S}}_l^{\min}$) before $\bar{\bar{S}}_l$ becomes equal to $\bar{\bar{S}}_w + \bar{S}_{or}$ as $\bar{\bar{S}}_l$ approaches $\bar{\bar{S}}_w + \bar{S}_{or}$. When $\bar{\bar{S}}_l$, $\bar{\bar{S}}_l^{\min}$, and $\bar{\bar{S}}_w + \bar{S}_{or}$ are equal to each other, which means that all of the NAPL becomes residual NAPL, then the first conditional statement will apply. The first conditional statement will always hold when the apparent total-liquid saturation ($\bar{\bar{S}}_l$) is equal to the sum of the apparent water saturation and the effective residual-NAPL saturation ($\bar{\bar{S}}_l = \bar{\bar{S}}_w + \bar{S}_{or}$). The predicted NAPL relative permeability (k_{ro}) will be zero for this condition [see Equation (A.15) for the condition $\bar{\bar{S}}_l = \bar{\bar{S}}_w + \bar{S}_{or}$]. For the other solutions given by Equations (A.16) and (A.17), the NAPL relative permeability (k_{ro}) will never be zero because the apparent total-liquid saturation ($\bar{\bar{S}}_l$) can never be equal to the sum of the apparent water saturation and the effective residual-NAPL saturation ($\bar{\bar{S}}_l = \bar{\bar{S}}_w + \bar{S}_{or}$) for these saturation-path histories.

Key elements of the proposed model are 1) some portion of the NAPL is predicted to remain in the pore spaces as residual NAPL unless all of it is entrapped by imbibing water, 2) the residual NAPL saturation is a function of the saturation-path history (not a constant), and 3) the NAPL relative permeability (k_{ro}) will approach zero as the free-NAPL saturation (S_{of}) approaches zero. To calculate fluid saturations using the revised constitutive model in numerical models, the apparent total-liquid saturation ($\overline{\overline{S}}_l$) is first determined from the air-NAPL capillary pressure and the total-liquid saturation-path history. From the apparent total-liquid saturation and the saturation-path histories, the total-liquid (S_l) and total trapped-air (S_{at}) saturations are determined. Next, the apparent water saturation ($\overline{\overline{S}}_w$) is determined from the NAPL-water capillary pressure and the water saturation-path history. From the apparent water saturation and the saturation-path histories, the water (S_w) and trapped-NAPL (S_{ot}) saturations, as well as the trapped-air saturation that resulted from advancing air-water interfaces (S_{atw}), are determined.

The next step is to determine if the apparent total-liquid saturation ($\overline{\overline{S}}_l$) needs to be adjusted because of a limiting condition. For water drainage paths, the apparent total-liquid saturation ($\overline{\overline{S}}_l$) should never be less than the sum of the apparent water saturation and the effective residual-NAPL saturation of the previous time step, because residual NAPL is immobile and should not change between time steps during drainage. If it is ($\overline{\overline{S}}_l < \overline{\overline{S}}_w + \overline{S}_{or}$), then the apparent total-liquid saturation is set equal to the sum of the apparent water saturation at the current time step and the effective residual-NAPL saturation of the previous time step ($\overline{\overline{S}}_l = \overline{\overline{S}}_w + \overline{S}_{or}$). The corresponding total-liquid (S_l) and total trapped-air (S_{at}) saturations are then recalculated. For water imbibition paths, the apparent total-liquid saturation ($\overline{\overline{S}}_l$) should never be less than the apparent water saturation ($\overline{\overline{S}}_w$). If it is, then the apparent total-liquid saturation is set to equal the apparent water saturation ($\overline{\overline{S}}_l = \overline{\overline{S}}_w$) and the total-liquid (S_l) and total trapped-air (S_{at}) saturations are recalculated. When the apparent total-liquid saturation equals the apparent water saturation ($\overline{\overline{S}}_l = \overline{\overline{S}}_w$), then all of the NAPL will be trapped ($S_o = S_{ot}$).

The next step is to calculate the effective residual-NAPL saturation ($\overline{S}_{or}$) at the current time step. From calculations in earlier steps, all other saturations (S_{ato}, S_{of}, S_{or}, S_o, etc.) can be determined. These values can be used to evaluate mass balances and determine relative permeabilities. The final step is to update the historic saturations $\overline{\overline{S}}_w^{\min}$ (used to determine S_{ot}), $\overline{\overline{S}}_l^{\min}$, and $\overline{\overline{S}}_l^{\max}$. Because an air-NAPL-water fluid system exists, the effective water saturation at the saturation-path reversal from the main S-P path to a scanning water imbibition path in a two-phase air-water fluid system ($^{\Delta}\overline{S}_w^{aw}$) is fixed and does not need to be updated; it was established prior to NAPL imbibition.

It is expected that the presented modifications will yield more accurate predictions of NAPL behavior in the vadose zone. The revised model is applicable to NAPLs less dense than water (LNAPLs) and NAPLs more dense than water (DNAPLs). Although we have stated that the revised model pertains to the vadose zone (an air-NAPL-water fluid system), it can be used, like the existing model, to predict fluid behavior in two-phase air-water and NAPL-water systems. The model can be also used for both

spreading and nonspreading NAPLs, because the different behavior should be accounted for by the calibration term ($\bar{S}_{orm}$) in Equation (A.10).

A.3 References

Busby RD, RJ Lenhard, and D.E. Rolston. 1995. "An Investigation of Saturation-Capillary Pressure Relations in Two- and Three-Fluid Systems for Several NAPLs in Different Porous Media" *Groundwater* 33: 570578.

Lenhard RJ and JC Parker. 1987. "A Model for Hysteretic Constitutive Relations Governing Multiphase Flow, 2. Permeability-Saturation Relations." *Water Resour. Res*. 23:2197-2206.

Lenhard RJ and JC Parker. 1988. "Experimental Validation of the Theory of Extending Two-Phase Saturation-Pressure Relations to Three-Phase Systems for Monotonic Drainage Paths." *Water Resour. Res*. 24:373-380.

Mualem Y. 1976. "A New Model for Predicting the Hydraulic Conductivity of Unsaturated Porous Media." *Water Resour. Res*. 12:513-522.

Parker JC and RJ Lenhard. 1987. "A Model for Hysteretic Constitutive Relations Governing Multiphase Flow 1. Saturation-Pressure Relations." *Water Resour. Res*. 23:2187-2196.

van Geel PJ and SD Roy. 2002. "A Proposed Model to Include a Residual NAPL Saturation in a Hysteretic Capillary Pressure-Saturation Relationship." *J. Contam. Hydrol.* 58:79-110.

van Genuchten M Th. 1980. "A Closed-Form Equation for Predicting the Hydraulic Conductivity of Unsaturated Soils." *Soil Sci. Soc. Am. J.* 44:892-898.

Wipfler EL and SEATM van der Zee. 2001. "A Set of Constitutive Relationships Accounting for Residual NAPL in the Unsaturated Zone." *J. Contam. Hydrol.* 50:53-77.

Distribution

No. of Copies

OFFSITE

Wes Bratton
Vista Engineering

ONSITE

4 **DOE Richland Operations Office**

B. L. Foley	A6-38
J. G. Morse	A6-38
K. M. Thompson	A6-38
A. C. Tortoso	A6-38

9 **Fluor Hanford, Inc.**

J. V. Borghese	E6-35
M. E. Byrnes	E6-35
D. B. Erb	E6-35
T. W. Fogwell	E6-35
B. H. Ford	E6-35
S. W. Petersen	E6-35
V. J. Rohay	E6-35
L. C. Swanson	E6-35
M. E. Todd-Robertson	E6-35

No. of Copies

U.S. Environmental Protection Agency

D. E. Faulk	T4-04

Washington State Department of Ecology

D. Goswami	H0-57

9 **Pacific Northwest National Laboratory**

R. W. Bryce	E6-35
M. D. Freshley	K9-33
C. T. Kincaid	K9-33
G. V. Last	K6-81
M. Oostrom (3)	K9-33
M. L. Rockhold	K9-36
P. D. Thorne	K9-33
M. J. Truex (2)	K6-96